SPECIAL FIBERS IN DIELECTRIC METAMATERIALS FOR HIGH CAPACITY MODE DIVISION MULTIPLEXING OAM-BASED

CLAUDIA MILENA SERPA IMBETT

UNIVERSIDAD PONTIFICIA BOLIVARIANA
ESCUELA DE INGENIERÍAS
DOCTORADO EN INGENIERÍA
MEDELLÍN
2017

SPECIAL FIBERS IN DIELECTRIC METAMATERIALS FOR HIGH CAPACITY MODE DIVISION MULTIPLEXING OAM-BASED

CLAUDIA MILENA SERPA IMBETT

Trabajo de grado para optar al titulo de Doctor en Ingenieria

Director
Hugo Enrique Hernandez Figueroa, PhD
Codirector
Ferney Orlando Amaya Fernandez, PhD

UNIVERSIDAD PONTIFICIA BOLIVARIANA
ESCUELA DE INGENIERÍAS
DOCTORADO EN INGENIERÍA
MEDELLÍN
2017

Nota de aceptación

Firma
Nombre:
Presidente del jurado

Firma
Nombre:
Jurado

Firma
Nombre:
Jurado

Medellín, June 22, 2017

To my beloved son Thomas, my dearest niece Mariana and my beloved mom Zirza!

AGRADECIMIENTOS

To my God.

To my mom, Zirza for being my unconditional support and for always to be with me.

To my beloved family Thomas, Mariana, Zirza, Liseth, my brothers, my grandfathers, and the endless list of relatives that I know that are very happy with my achievement.

To my advisor, Prof. Hugo Enrique Hernandez Figueroa, for his friendship and excellent scientific orientation. My endless thankful for trusting to me, and guiding me in this very important time of my life. Your work always will be valuable for me.

To Lucas Heitzman-Gabrielli, thank you for all friendly support, teachings, suggestions and for the contribution to the improvement of this manuscript.

To my co-advisor, Prof. Ferney Amaya-Fernandez, and also to Roberto Hincapie, and Cristina Gomez, thanks for all the support.

To Jorge Diego Marconi, thanks for all scientific discussions and support during these last years. Beyond this, I won a great friend forever, and this is priceless to me. Thank you for never give up me, because your details were very important to the success of this work.

To Mateus Corato-Zanarella, thanks for his support in the implementation of the simulations and data processing, and for all very fruitful discussions around this work. Your contributions are part of the success of this work.

To my friends Jeison, Javier, Sebastian, Diego, Tomas, Jose Angel, Jimy, Dalia, Katherine, Andrea, and the long list of friends for the company, generosity, and support in all of this last years.

To Universidad Pontificia Bolivariana - Monteria Campus for receiving me. Thank you,

Monteria, my city of birth for receiving me again. Working at Monteria after my Ph.D. is a fulfilled dream, so I hope to be an inspiration to Monteria‘s people, and in special for that Electronic Engineer students follow the scientific road. My endless thankfulness to my working group Fabian, Richard, Jhon, Jorge, Rosa, Roger, Saul, Jhon Fredy Ana Milena for their support these last months. You have become my new family.

To FEEC/UNICAMP for being my second home during last years. I and my son, Thomas, were very happy in UNICAMP, so we keep up the nicest remembers of our years there.

To Universidad Pontificia Bolivariana Medellin - Campus for the support of all years in the development of this doctoral work.

To Colciencias in Colombia and CAPES in Brazil for the scholarships and all the financial supports.

CONTENTS

Pág.

LIST OF FIGURES

LIST OF TABLES

Pág.

GLOSARIO

EDFA: *erbium-doped-fiber-amplifiers*

WDM: *wavelength-division-multiplexing*

SMF: *single-mode fibers*

SNR: *signa- to-noise-ratio*

LMA: *large modal area*

PBGF: *photonic bandgap fibers*

SDM: *space division multiplexing*

MDM: *mode division multiplexing*

MCF: *multicore fiber*

MMF: *multimode fiber*

FMF: *few-mode fiber*

OAM: *orbital angular momentum*

SAM: (*spin angular momentum*)

CVB: *cylindrical vector beam* (CVB)

HG: *Hermite-Gaussian-like beams*

MIMO: *multiple-input multiple-output*

DSP: *digital signal processing*

HOM: *Higher-order modes*

SLM: *Spatial light modulator*

S^2: *Spatial and spectral resolved image*

TO: *Transformation Optics*

SO: *Spin-orbit*

AA: Anti-aligned

A: Aligned

RESUMEN

Abstract

High modal coupling in multimode fibers is perhaps one of the most critical barriers unlocking the all-photonic systems multiplexed by modes. Regarding multimode vortex fibers that propagate modes with orbital angular momentum (OAM) the degeneracy amongst modes is a problem that prevents the exploitation of the infinite-dimensional basis allowed by OAM states. In this work, we propose the use of dielectric metamaterials in vortex fibers. Metamaterials in waveguides have been demonstrated to be helpful in modifying the modal behavior in photonic structures. We propose a new class of vortex fibers with a modified cladding made of metamaterial to lift the degeneracy between OAM modes, increasing thus the number of stable OAM states. We also show a better purity of the OAM modes in the vortex solid fiber using the proposed metamaterial, reaching a reduction of approximately -30 dB between the TE_{01} and OAM_1 modes when the fiber is bending up to 1 cm. Besides, we achieve additional non-degenerate modes in the air-core vortex fiber using this metamaterial cladding, which means an increase of available independent OAM states.

Finally, we show the main challenges still open in this technology, and that arise from the results of this doctoral work, such as tailoring dispersion in vortex fibers, design of vortex fibers in polymer/plastic to be used in other applications of short lengths (less than 100 m), the coupling of OAM modes to chips in planar waveguides.

Resumen

El alto acoplamiento modal en fibras multimodo es quizás una de la barrera más crítica para desbloquear los sistemas fotónicos multiplexados por modos. En cuanto a las fibras de vórtice multimodo que propaga modos con momento cinético orbital (OAM), la degeneración entre modos es un problema que impide la explotación de la base de dimensión infinita permitida por los estados de OAM. En este trabajo se propone el uso de metamateriales dieléctricos en fibras de vortice. Se ha demostrado que los metamateriales en guías de ondas son útiles para modificar el comportamiento modal en estructuras fotónicas. Proponemos una nueva clase de fibras vortices con un revestimiento modificado de metamaterial para elevar la degeneración entre modos OAM, aumentando así el número de estados OAM estables. También mostramos una mejor pureza de los modos OAM en la fibra sólida de vórtice usando el metamaterial propuesto, alcanzando una reducción de aproximadamente -30 dB entre los modos TE_{01} y OAM_1 cuando la fibra se dobla hasta 1 cm. Además, conseguimos modos adicionales no degenerados en la fibra de vórtice de núcleo de aire utilizando este revestimiento metamaterial, lo que significa un aumento de los estados de OAM independientes disponibles.

Finalmente, se muestran los principales desafíos que todavía se abren en esta tecnología, y que surgen de los resultados de este trabajo de doctorado, como la adaptación de la dispersión en fibras vortices, el diseño de fibras vortices en polímero o plástico para otras aplicaciones de longitudes cortas (distancias menores de 100 m), el acoplamiento de modos OAM a chips usando guías de ondas planares.

PALABRAS CLAVE:

Keywords: Optical Communication, Space Division Multiplexing, Optical Modes, Orbital Angular Momentum of light, Vortex fiber.

Palabras claves: Comunicaciones Opticas, Multiplexación por division de espacio, Momentum angular orbital de la luz, fibra vortex.

1. INTRODUCTION

1.1. OPTICAL FIBER COMMUNICATION AND SPACE-DIVISION MULTIPLEXING

The *Erbium-doped-fiber-amplifiers (EDFA)* and the *wavelength-division-multiplexing (WDM)* technologies developed in the 1990's have enabled the transmission of huge amount of data in the current global optical communication systems. Internet applications such as *video-on-demand* (VOD), high definition TV, ultrahigh-definition video transmission and digital cinema have generated an exponential growth for the demand of bandwidth in the optical communication networks [20–24], increasing demand will achieve the theoretical capacity limit of standard *silica single mode fibers* (SMF) given by the nonlinear Shannon limit.

Considering a wavelength range of about 400 nm (from 1200 up to 1600 nm, or 50 THz) with a channel *signal to noise ratio* (SNR) of 20 dB, and a spectral efficiency (SE) of 6.6 bit $s^{-1}Hz^{-1}$, the value of the capacity limit for SMF is ∼300 Tbps [25, 26]. The detrimental effects due to nonlinearities and losses can be reduced by using new special fibers with *large modal area* (LMA) [27, 28], and low loss, or with hollow core *photonic bandgap fibers* (PBGF) [2]. However, these fibers do not have enough low nonlinearity and loss to improve significantly the capacity of fiber channels [26].

Another explored option consisting of to optimize the channel capacity through modulation formats as a way to increase the data carrying capacity. Researchers have explored every available degree of freedom: time, wavelength, polarization and phase (*quadrature*) in order to exploit as much as possible the installed fiber infrastructure. Those efforts have resulted in commercial systems that, nowadays, are operating near the Shannon limit.

The problem is that assuming a traffic growth from 30% to 60% per year, in a period from 5 to 10 years, will be necessary commercial systems operating beyond the Shannon limit (See Figure 1.1a). This leads to the imminent "*optical networks capacity crunch*" (See Figure 1.1b). In order to avoid this collapse, the scientific community has been looking for other options, one of them considering the old idea that fibers can easily support hundreds of spatial modes. This multiplexing technology is so called as *space division multiplexing* (SDM), which has become in the most promise candidate to overcome capacity crunch of optical networks [2].

SDM is the theme of the present doctoral work. The nomenclature SDM includes two different concepts. In the former, the idea is related with the transmission of information through several parallel fibers, or through *multicore fibers* (MCFs). In the latter, the technique involves the use of multiple data pathways by using the same fiber, which is in other words, the transmission of information in several modes, either by using *multimode fibers* (MMF) or *few mode fibers (FMF)* (all-solid or hollow-core), instead of SMF (See Figure 1.2). This is called *mode division multiplexing* (MDM), offering a great potential to increase the capacity of optical fiber networks because allows, like WDM, to use a single fiber to transmit multiple independent channels [2].

In MDM, each mode can carry an independent data channel, allowed by the orthogonality amongst them. There are several types of orthogonal modal basis sets that are potential candidates for such MDM systems. One of them is based on the *orbital angular momentum* (OAM) of light. Others are based on *cylindrical vector beams* (CVBs), and *Hermite-Gaussian-like beams* (HG) generated by different linear combinations of CVBs, which are know as linearly polarized modes (*LP*-basis) [29]. These sets are supported by multimode fibers of different kinds for short and long links, as was recently demonstrated in several works [30, 31]. This new technology presents two options: *(i)* The use of complicated specially designed fibers to support either OAM or HGs with low-crosstalk, but without *multiple-input multiple-output* (MIMO) *digital signal processing* (DSP) [3]; *(ii)* The use of simple FMF that support HGs or CVBs with higher crosstalk, but assisted by MIMO DSP to separate the channels/modes [31]. Both options have been explored last years, however, in order to reach an all-photonic communication system is recommended to avoid the MIMO DSP.

One of the main challenges to make SDM technology more attractive is related with the development of capacities to allow the integration with other technologies such as WDM. Integration capacity is based on the concept of "*optical parallelism*" [32], which

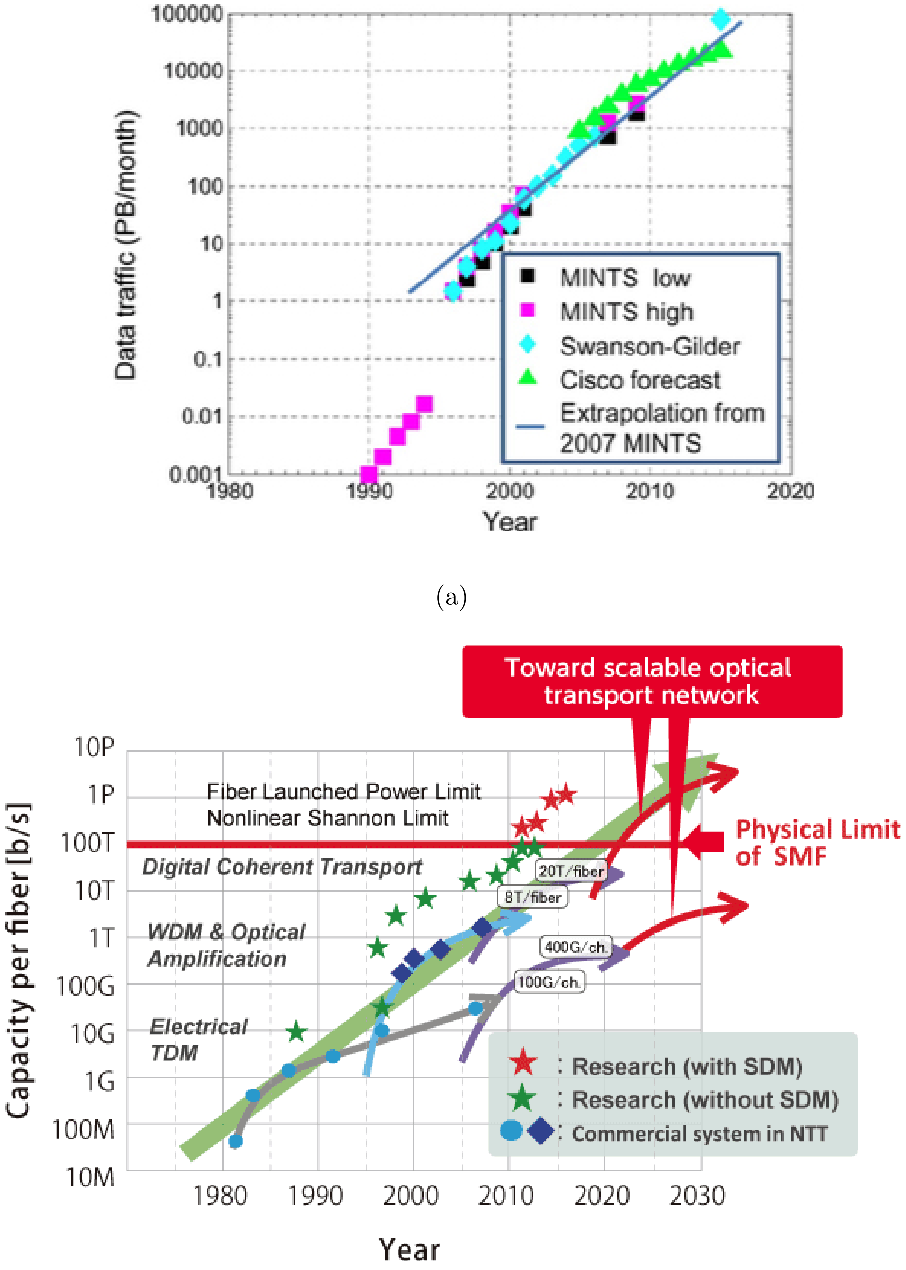

(a)

(b)

Figure 1.1: **(a)** North American Internet traffic in Petabytes/month according to several studies, such as Minnesota Internet Traffic Study (MINTS) and Cisco: (See Figure 1 in [1]).© 2012 IEEE. With permission, from [1]. **(b)** Capacity evolution for different communication systems (See Figure 1 in [2]). © 2013 IEEE. With permission, from [2].

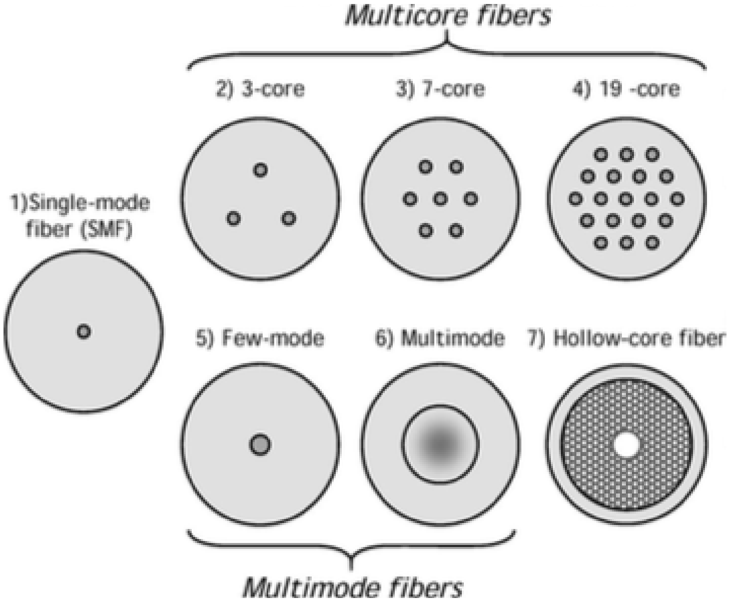

Figure 1.2: Cross sections of a singlemode fiber and fibers supporting spatial multiplexing. ©2012 IEEE. With permission, from [1]

was introduced, in the past for the quadrature modulation formats, where the phase and the amplitude of the signal are independently modulated, in one or in the two possible states of light polarization [33].

The WDM technique can be considered within the concept of parallelism in the frequency dimension. Multiple carries are grouped to form a single logical interface which integrates multiple technologies (for instance, WDM and PolMux), it is defined the so-called super-channel. Using super-channel technologies, optical interfaces rates of terabits per second and beyond are feasible today ([33], pag. 32). However, even considering all this improvements, the capacity can be increased by a maximum factor of approximately five. Undoubtedly, this will be a critical stopgap solution in the near future, but the point is that none of these techniques would provide a sustainable path to overcome the optical capacity crunch.

To increase the optical capacity in the optical networks for the next several decades, the optical parallelism must be extended to another physical dimensions, and the only dimension not exploited yet is "*the space*". A possible adoption of SMD in future optical networks can be made following one of these two "*integration*" visions: A fully-SDM system and an upgrade-path vision. *i)* The "*grand vision*" of an ultrahigh capacity, fully-SDM systems. *ii)* The "*upgrade-path*" vision, where SDM components and links operating with other technologies like SDM, are gradually added to the existing SDM-infrastructure.

The "*grand vision*" is based on the use of flexible devices for actively multiplexing or demultiplexing the desired spatial channels as much as possible. The "*upgrade vision*" is based on the gradual replacement of the existing infrastructure [33], of specific fiber optical communications or free-space links. The key here is not scalability but compatibility, however, in this vision low-crosstalk solutions are extremely important to obtain a "*hybrid*-SDM" network, without the necessity of MIMO DSP. This vision is very interesting because could be implemented quite soon. For instance, it would be possible with the partial replacement of the installed infrastructure in access networks with high congestion without changing the surrounding network, or installing hybrid SDM systems between optical and free-space links. It should be possible this upgrade through the more compact solution like integrated devices [34, 35]. The "*integration*" is key for the success of the SDM technology being a priority in both, incremental upgrades and fully SDM systems.

While SMD looks like offering promising results, this new technology have a limitations arising by the mode coupling in MMF. Modes in a MMF are ideally orthogonal to each other and no coupling amongst them is expected. Besides, different modes have different effective indices or propagation velocities. However, the refractive index profile in a real fiber is perturbed for the diameter induced variations during the fabrication, and also the fiber bending changes the effective index of the modes and the field distributions, leading to values of the overlap integral different from zero [36], which means a loss of orthogonality. Also, inhomogeneity of the material can create birefringence that causes mode coupling for the non-degenerate or near degenerate modes. Finally, the refractive index can change in the longitudinal z axis creating mode coupling (distributed along z) if the spatial frequency of the perturbation matches the beat length between two modes (see for example grating based mode couplers in [37]).

In the case of multiple optical paths (modes or cores) traveling in a fiber, there are two basic tradeoff solutions: *(i) Strong-coupling regime* (typically greater than 1 km): This scheme could be implemented in fibers with a large number of modes, which could share, for instance, the same optical amplifier, but with the drawbacks of the complexity of the MIMO-DSP schemes for mitigating mode coupling unavoidable increasing as the number of modes increasing. The fiber design is more complex in order to reach a low modal differential group delay, and more complex mode couplers are required. An example of this kind of fiber is the FMF with step or parabolic index [38]. Couplers and switches are designed on chips based on Si-technology in order to make post-processing of the optical signal. In this case, it is necessary to analyze carefully the control of the crosstalk and the losses for the fiber to chip couplers. *(ii) weak-coupling regime* (typically less than 1 km) where the crosstalk is smaller, and may be implemented in fibers with simpler design, but with the drawbacks of limited number of spatial paths. Crosstalk could be compensated with methods that use computationally intensive adaptive optics feedback algorithms [39]. These methods "*back off*" the effect of mode coupling by sending a desired superposition of modes at the input, so that desired output mode can be obtained. This approach is limited, since mode coupling is a random process that can change on the order of a millisecond in conventional fibers [39], therefore, the adaptation of this method can be problematic in long-haul systems, where the signal delay can be tens of milliseconds [40]. On the other hand, there are different kinds of low crosstalk fibers such as the MCF with a long (almost 1 km) beat length between cores, the multimode *photonic bandgap fiiber* (PBGF) with a high difference between the modal effective indices [30], and multimode fibers with an special index profile, which is sculpted for a OAM state propagation over long lengths [41]. These special fibers are well-know as vortex fibers, and have allowed OAM propagation in tipically distance of around 1 km [3], and recently, in 2016 of up to 13.4 km [42]. The PBGFs were another option to increase optical channel capacity due to the low nonlinearity. However, recently have been shown that this low nonlinearity is not enough for a significant increasing of the capacity [26, 43]. Multimode PBGFs have attracted the interest of the scientific community because appear as the best option to implement SDM scheme with low latency [44] in data center networks. Somewhat unconventional transmission at 2.08 μm has also been demonstrated in 290 m-long photonic crystal fibers, though still with high losses (4.5 dB/km) [45].

Vortex fibers can be used to transmit multiple independent OAM modes encoding information in all the modes. We show in Figure 1.3 the set up of one of the most recent experiment reported by [3]. In this experiment, they use a continuous wave laser operating at 1550 nm was modulated using a 50 GBaud QPSK signal, and subsequently split into four arms of standard single mode fiber of different lengths to produce a sufficient delay in order to obtain four decorrelated data channels. Two of the four channels were converted into the ℓ=±1 OAM modes (modes A and B in green and blue, respectively) using fork-holograms of topological charge ℓ=±1, created with a spatial light modulator (SLM-1). OAM modes was sending through QWP@45^o (Quarter Wave Plate) to produce two polarization states of light: $s = 1$ or $s = -1$ for the OAM modes. The other two polarization of LP_{01} or HE_{11} modes (C and D in red) were left unchanged. These mode are then propagated through 1.1 km of vortex fiber, as Figure 1.3 shows. With all four channels enabled simultaneously, the demultiplexing system sorts the modes according to their OAM (ℓ) and spin (s) values, using another SLM (SLM-2) and a combination of a QWP@45^o and a polarizer, respectively. The resulting output was mapped back into a conventional Gaussian-shaped beam with a planar phase, which was routed to a coherent receiver by coupling into an SMF [3].

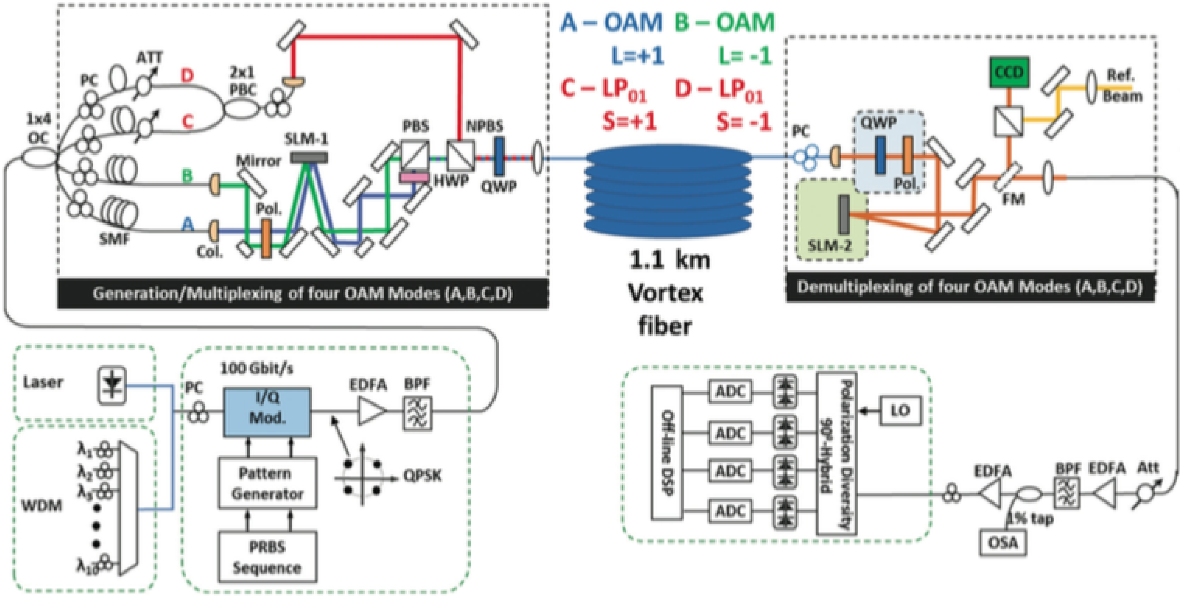

Figure 1.3: Experimental setup for a WDM-OAM multiplexing. From [3]. With permission from AAAS

Figure 1.4a shows a variety of spiral interference patterns that come to CCD camera at different wavelengths across C-bands, qualitatively indicative of broadband transmission of a pure OAM state obtained at the output of the 1.1 km vortex fiber in the setup shown in Figure 1.3. 2 OAM modes and 10 WDM channels (from 1546.64 to 1553.88 nm) observed in Figure 1.4b were transmitted for the OAM-WDM experiment. Transmission of 20 channels (OAM-MDM and WDM), resulted in a total transmission capacity of

1.6 Tbps under the FEC limit (Figure 1.4c shows typical constellation diagrams that were recorded).

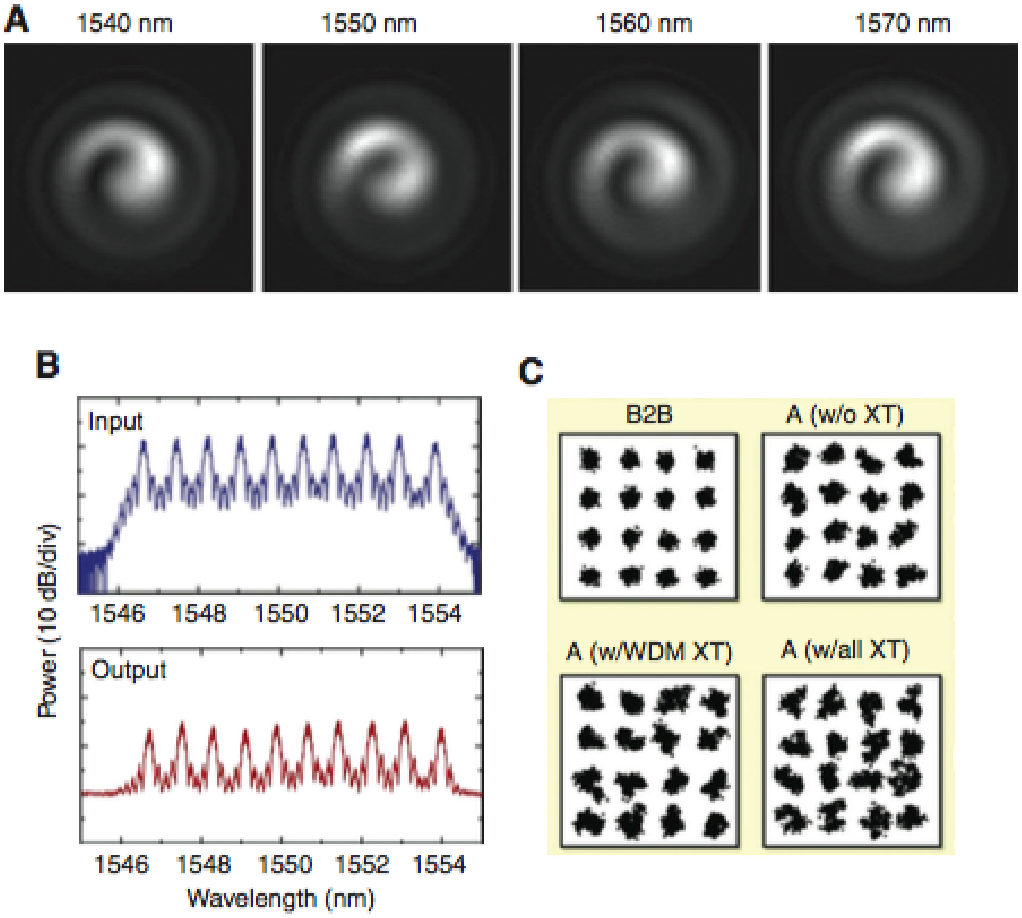

Figure 1.4: OAM-WDM experiment **(a)** Spiral interference patterns of OAM states. **(b)** 10 WDM channels across C-band. **(c)** Constellation diagrams of 16-QAM modulation (Back-to-back: B2B) for the demultiplexed $\ell = \pm 1$ mode at 1550-64 nm (Channel A). From [3]. With permission from AAAS

The aforementioned experiment show that the vortex fibers are a new possibility for a future network capacity increase. This special class of MMFs are capable of reducing mode coupling avoiding MIMO-DSP equalization. In this dissertation we present a new possibility of design still unexplored, which consists of the use of anisotropic metamaterials to "*lift*" the mode degeneracy amongst vector modes, reducing in this way the mode coupling. Before we go further into details of our proposal, we first introduce the orbital angular momentum of light.

Linear momentum of light $\boldsymbol{p}$ is one of the fundamental quantity in classical electrodynamics [46]. This is proportional to time average Poynting vector $\langle\mathbf{S}\rangle=\frac{1}{2}Re(\mathbf{ExH^*})$, where $\mathbf{E}$ is the electric field and $\mathbf{H}$ is the magnetic field. The Poynting vector associated with an electromagnetic plane wave is purely longitudinal (z-propagation direction), and linear momentum is parallel to it (see Figure 1.5a). However, a plane wave carries infinite energy, but this is not physically realizable. In practice, all generated optical beams have finite energy and are solution of the paraxial wave equation, leading to a non-vanishing component of the linear momentum in the transverse plane (henceforth named the azimuthal component of $\boldsymbol{p}\rightarrow p_\phi$ (see Figure 1.5b) [47]). Under this approximation, such a paraxial beam might posses a net *orbital angular momentum* (OAM) in the propagation direction as a consequence of having a transverse component of linear momentum [48].

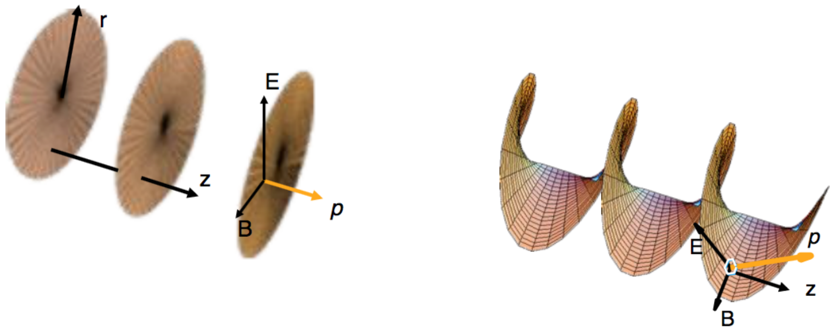

(a)p_ϕ=0

(b)p_ϕ≠0

Figure 1.5: **(a)** Linear momentum of light $\boldsymbol{p}$ associated with an electromagnetic plane wave in the free space (r→∞). p_ϕ=0. **(b)** Paraxial approximation of a generated optical beam which have an azimuthal component of linear momentum of light $p_\phi\neq0$. Adapted from [4]

In the paraxial approximation a value of $p_\phi\neq0$ leads a light field having an ℓ-dependent and azimuthally varying phase given by $e^{\ell\phi}$ in addition to e^{-ikz}. ℓ is an integer called as "*topological charge*", which counts the number of intwined helices (i.e., the number of 2π phase shifts along the circle around the beam axis). ℓ is assumed as positive, negative, or even a zero value, corresponding to clockwise or counterclockwise phase helices or a gaussian beam (i.e., no helix), respectively (see Figure 1.6 [4]).

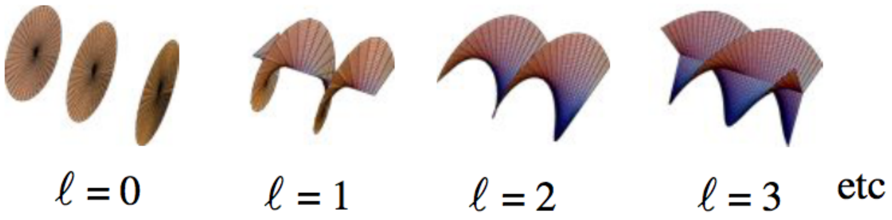

Figure 1.6: Light beams with different $+\ell$ values. Adapted from [4]

Angular momentum is imparted by spinning (*spin angular momentum* → SAM) (see Figure 1.7a) or orbiting around an axis (*orbital angular momentum* → OAM), (see Figure 1.7b) [5].

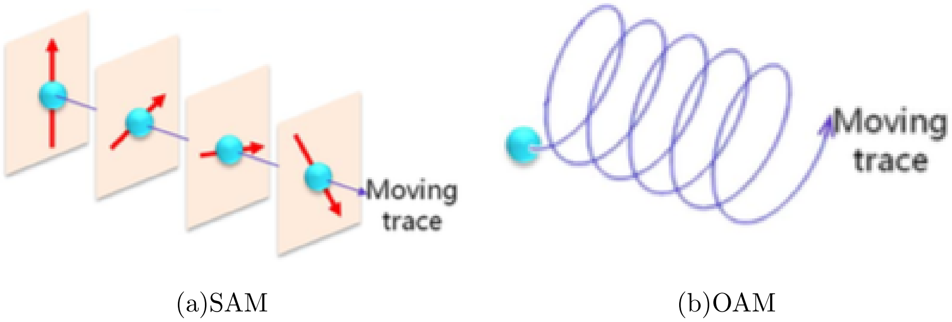

(a)SAM (b)OAM

Figure 1.7: **(a)** A spinning object carrying SAM and **(b)** and orbiting object carrying OAM. With permission from [5]. Copyright 2015 Optical Society of America

Then, a light beam may also posses these two types of angular momentum. The first one, the SAM is associated with circular polarization of light. This mechanical property of light was demonstrated by Poynting in 1909 (see Ref. [49]). He showed by use of a mechanical analogy, that circularly polarized light should exert a torque per unit area on a quarter-wave birefringent plate, equal to $\lambda/2\pi$ (λ is the wavelength) times the light energy per unit volume. When the energy of each photon crossing the surface is associated with $\hbar\omega$, we obtain the result that circularly polarized photons each carry $\hbar$ units of angular momentum. The effect was experimentally detected about twenty years after Poynting's death by Beth [50]. The second one, the OAM is associated with the azimuthal phase dependence of light $e^{i\ell\phi}$. These light beams carry OAM independent of the polarization state [4]. This OAM would have a value of $L=\ell\hbar$ per photon. Just as with circularly polarized light, the sign of the OAM momentum ($\pm\ell$) indicates its handedness with respect to the beam direction [51].

One can understand momentum of light properties without reference to photons. The total angular momentum of any light field could be considered in terms of a sum of spin (SAM) and orbital (OAM) contributions. These contribution are independent features of the optical field in the paraxial limit. The SAM contribution is associated with the polarization of the electric field (see Figure 1.8a), and the OAM contribution is caused by the azimuthal component of the Poynting vector $e^{\ell\phi}$, which gives a helical phase front resulting in a twisting of wave vector (see Figure 1.8b). These components produce an orbital angular momentum parallel to the beam axis. Because the momentum circulates about the beam axis, such beams are said to contain an optical vortex [51].

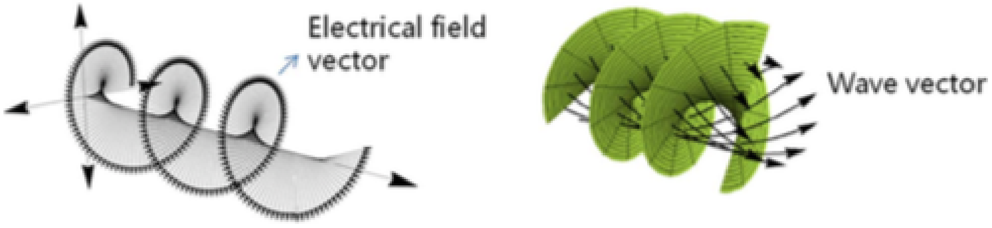

(a)   (b)

Figure 1.8: **(a)** A circular polarized light beam carrying SAM, and **(b)** Twisting of wave vector of an OAM-carrying light beam. With permission from [5]. Copyright 2015 Optical Society of America

The most common form of helically phased beam is the so-called Laguerre-Gaussian (LG) laser mode (see Figure 1.9) [51]. Other examples of beams that have non-zero OAM include free space Bessel, Mathieu, and Ince-Gaussian beams. These OAM beams have been used in widespread scientific and technological applications, such as optical twister, atom manipulation and free-space classical and quantum communications [52].

There are many approaches for creating OAM beams, the most common methods converts a Gaussian beam into OAM beam using a spiral phase plate, phase hologram with a spiral phase pattern or phase hologram with a "*fork*" pattern (see Figure 1.10). There are also different ways to detect an OAM beam, such as using a conjugated helical phase or using a plasmonic detector [5].

Besides, there are several works on creating OAM modes in fibers [53–55], however, in all these cases the fiber lengths were short, due to the fact that OAM modes are subject

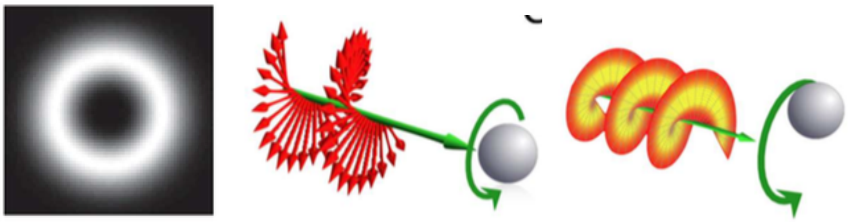

(a) (b)SAM interaction (c)OAM interaction

Figure 1.9: **(a)** Illustration of an intensity partner of a $LG_{p\ell}$ beam with ℓ=1: LG_{01}. **(b)** Circularly polarized LG_{01} beam, that carry *spin angular momentum* (SAM), which can rotate an object (gray sphere) around straight arrow green axis upon illumination. **(c)** LG_{01} beam can transfer *orbital angular momentum* (OAM) and also rotate an object under an "*orbit*" even at much higher rates. SAM and OAM interaction are described in details in [6]. With permission from ©Wikipedia

to mode coupling, inhibiting the possibility to obtain a pure OAM mode in long lengths. Recently, Ramachandran and its group in Boston University [3] have introduced a new class of fibers called vortex fibers to overcome this drawback, allowing OAM mode propagation for longer fiber lengths (13.4 km in 2016). These new class of MMFs has been used as a new alternative implementing MDM systems. However, even though mode coupling has been reduced, this is limited by the effective index separation of the vector modes within *almost degenerated groups*, enabled by the index profile of the vortex fiber. One can think that if the mode coupling is reduced even more, which means an increase in the effective index separation between vector modes, then there would have the possibility to send more OAM modes to longer fiber lengths. The focus of this dissertation is to propose a new approach of design of vortex fibers that consists of using metamaterials as cladding to reduce the mode coupling and increase the number of propagated OAM modes.

1.3. GOALS AND THESIS ORGANIZATION

Practical communication distances, over vortex fibers, have been achieved only for special case of the lowest order $\pm\ell = 1$ that yield 2-OAM states [3], and, recently for

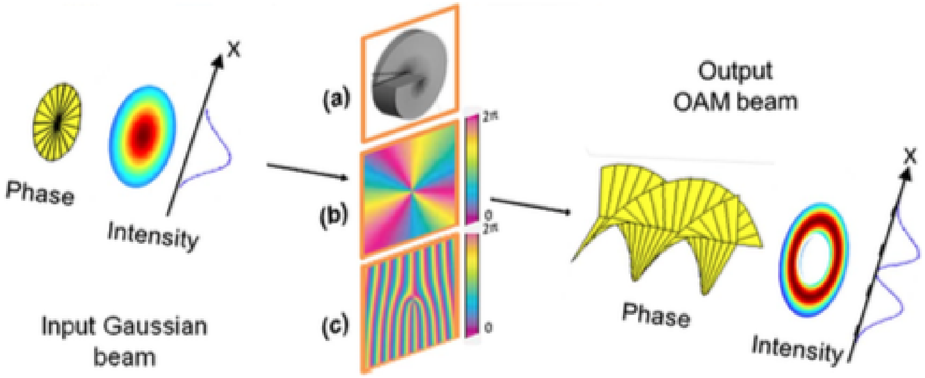

Figure 1.10: Three approaches to convert a Gaussian beam into an OAM beam.**(a)** A spiral phase plate. **(b)** A phase hologram with a spiral phase pattern, or **(c)** a phase hologram with a "*fork*" pattern. ©2015 IEEE. With permission from [5]

[42] $\pm\ell = 6, 7, 8$ that yield 12-OAM states. Modal coupling amongst OAM modes that comes from degeneracies of the vector modes prevents the exploitation of the infinite-dimensional basis allowed by OAM states. Our proposal of vortex fibers with cladding in metamaterials is conceived as a way to tackle this problem by achieving both a lifting in the degeneracy between vector modes within a group, as well as the increase in the number of independent OAM modes.

This dissertation is organized into 6 chapters. Besides this introductory chapter which is intended to provide a brief background and outline of the study, the contents of rest of the chapters are organized as follows: we start in Chapter 2 introducing the mathematical description of MMFs using electromagnetic theory in order to explain the physical origin of the degeneracies amongst vector modes, then in Chapter 3 we explain how the OAM modes can exist in fibers, and which are the conditions necessary for uncoupled propagation. In chapter 4 we show the numerical simulations of vortex fibers with solid and air-core [3,9]. In chapter 5, we study the dielectric metamaterials, and the fabrication techniques. Here, we also explain our designs of vortex fiber with a cladding in metamaterial to increase the number of available OAM modes, and also confine and reduce the coupling strengths under perturbations like the bends. Finally, we discuss the future works and perspective.

2. MULTIMODE FIBERS

In this chapter, we describe the electromagnetic theory of multimode fiber in a weakly guided approximation to obtain the expressions of the bound modes, as well as the origin of the degeneracies amongst vector modes. Understanding the phenomenology behind the degeneracies among modes will help to design other possible vortex fibers.

2.1. OPTICAL FIBER WAVEGUIDE THEORY

Optical fiber waveguides have been widely studied in the literature [7,56,57]. These are cylindrical waveguides with one or multiples cores of high refractive index surrounded by a cladding of low refractive index. In an ideal case, the cores have a circular shape, the cladding is limited in extent, and also it is assumed no changes across longitudinal dimension. The cladding refractive index is slightly lower compared with the core, in order to describe light propagation in a weakly guided approximation. In this subsection, we describe the propagation of light along optical fiber waveguides in regions sufficiently far from any source of excitation, where the spatial steady state is reached, so these spatial steady states are described by bound modes on the waveguide. Bound modes are solutions of the source-free Maxwell equation, and are formed by resonance conditions in the waveguide cross-section (see [7], pag. 209). These bound modes are called fiber modes, which constitute an orthogonal basis with eigenstates characterized with both the different values of *refractive effective indices:* n_{eff_j} or, equivalently *propagation constants:* β_j, and eigenvectors that give the transverse spatial distributions of the fiber modes.

Optical fibers can support a certain number of modes limited by the index contrast, light wavelength, and core size. There are two classes of fibers: one of them are the *singlemode fibers* (SMFs) that propagate the fundamental mode (HE_{11} or LP_{01}) with two polarizations, and the other is the *multimode fiber* (MMF) with large core radius or high contrast index to propagate the fundamental mode and also *higher order modes* (HOMs). MMFs with a step-index profile guide modes in "*groups*", where within each group modes have almost the same effective index (they typically have a difference of $\sim 10^{-6}$). These groups of modes are said "*almost degenerate*". This degeneracy could be lifted in certain fiber designs with the objective of achieving propagation of OAM modes [10]. A criterion to consider a lifting of the degeneracy consists of achieving a difference of effective index of around 10^{-4} between the modes within a group. This effect will be explained in next sections.

2.1.1. Homogeneous vector wave equations

Mathematical description of modes will be made following the Snyder&Love approach in [7]: sections 11-14. To describe a waveguide, we introduce cartesian axes *xy* that coincide with the transverse section, and *z* axis that coincides with longitudinal axis of the waveguide. The variation in refractive index over the waveguide cross-section is given by the profile *n(x,y)* with n_{co} being maximum refractive index of the core, and n_{cl} the refractive index of an uniform cladding, where $n_{co} > n_{cl}$ for the waveguide to provide guidance. If a waveguide has a refractive-index profile that does not vary along *z*, i.e. *n=n(x,y)*, then the waveguide is *translationally invariant*, therefore this fact enables us to express the modal fields (electric (equation (2.1)) and magnetic (equation (2.2)) fields) in the separable form:

$$\mathbf{E}_j(x, y, z) = \mathbf{e}_j(x, y)\mathrm{exp}(i\beta_j \mathrm{z}), \tag{2.1}$$

$$\mathbf{H}_j(x, y, z) = \mathbf{h}_j(x, y)\mathrm{exp}(i\beta_j \mathrm{z}), \tag{2.2}$$

where β_j is called the *propagation constant* or *eigenvalue* of the *jth*-mode. Generally each mode has a unique value of β_j. We assume that all fields contain the implicit time dependence $\exp(-i\omega \mathrm{t})$, where ω is the angular frequency associated with optical light wavelength λ.

The electric and magnetic fields $\mathbf{E}_j$ and $\mathbf{H}_j$ of a bound mode (eigenvector of the *jth*-mode) are source-free solutions of Maxwell's equations, or, equivalently, the homogeneous vector wave equations:

$$\{\nabla_t^2 + n^2k^2 - \beta_j^2\}\mathbf{e}_j = -\{\nabla_t + i\beta_j\hat{\mathbf{z}}\}\mathbf{e}_{\mathbf{t}j} \cdot \nabla_t \ln n^2, \tag{2.3}$$

$$\{\nabla_t^2 + n^2k^2 - \beta_j^2\}\mathbf{h}_j = \nabla_t \ln n^2 \times (\{\nabla_t + i\beta_j \hat{\mathbf{z}}\} \times \mathbf{h}_j), \tag{2.4}$$

that assumes $\mu = \mu_0$, $n{=}n(x,y)$ is the refractive index profile, $k{=}2\pi/\lambda$ is the free-space wavenumber, λ is the free-space wavelength, ∇_t^2 is the transverse Laplacian and $\nabla_{\mathbf{t}}$ is the transverse vector gradient operator with the subscript denoting the transverse components. Electric and magnetic fields can be expressed with cartesian or cylindrical components (see pag. 239 in Snyder&Love [7])

2.1.2. Nature of hybrid modes

The terms involving $\nabla_t \ln n^2$ in equations (2.3) and (2.4) couple various field components. This term describes polarization phenomena due to the waveguide structure and, it is responsible for the hybrid nature of the modal fields. A circular waveguide possesses hybrid modes denoted as: $HE_{l+1,m} and EH_{l-1,m}$. These modes can be understood using a local plane-wave interpretation. Consider a ray propagating in the core of the fiber, in general, this ray follows the helical or skewer trajectory in circular waveguides with step or graded-index profiles. Following the direction of the electric field vector along a skew ray path using the local plane-wave description, we conclude about the impossibility of maintaining either $e_{zj}{=}0$ or $h_{zj}{=}0$ because the direction of propagation rotates along the ray trajectory. Consequently, a skew ray needs mixes between *transverse electric* (TE) and *transverse magnetic* (TM) polarizations at each reflection, so that the corresponding modal fields couple both e_{zj} and h_{zj} field components, consistent with the definition of hybrid modes. Consequently, all hybrid mode are composed of skewed rays.

The $\nabla_t \ln n^2$ term in the vector wave equation (2.3) describes the rotation of the electric vector. The smaller $\nabla_t \ln n^2$ value, the greater the axial distance z which is required for the ray path to complete a full period. Consequently, regardless of how small the value of $\nabla_t \ln n^2$, the electric field vector must eventually rotate through 360^o.

To summarize, the waveguide structure has polarization properties by virtue of its cross-sectional geometry and refractive-index profile. These effects are built into the vector wave equations (2.3) and (2.4) through the $\nabla_t \ln n^2$ term, which is responsible for the hybrid modes. Ignoring this term completely disregards polarization properties of the waveguide structure and leads to the scalar wave equation with solutions of modes with *linear polarization* (*LP*-modes). (For physical explanation of hybrid modes see

Snyder&Love [7]: sections 11, pag. 225-226)

2.1.3. Modal parameteres

The modal fields of an optical waveguide depend on the refractive-index profile, the cross-sectional geometry, and the frequency or wavelength of the source of excitation. From these parameters, we can define dimensionless quantities to characterize the waveguide. The *waveguide or fiber parameter* V and *the profile height parameter* Δ are defined thus:

$$V = \frac{2\pi\rho}{\lambda}(n_{co}^2 - n_{cl}^2)^{1/2} \tag{2.5}$$

$$\Delta = \frac{1}{2}\left\{1 - \frac{n_{cl}^2}{n_{co}^2}\right\}, \tag{2.6}$$

where ρ is the core radius. A waveguide is said to be multimode if $V \gg 1$, when many bound modes can propagate. Otherwise, when V is sufficiently small so that only the two polarization states of the fundamental mode can propagate, the waveguide is said to be singlemode. For example, a circular fiber with a step-index profile is single-mode when $V < 2.405$.

2.1.4. Weakly guided approximation

The vector fields depicted in equations (2.1) and (2.2) are solution of the homogeneous vector wave equations (2.3) and (2.4), however, there are few known refractive-index profiles that lead to exact solutions for the modal fields. One of them is the step-profile index which is one of practical interest in fiber design. In this subsection, we show the modal field solutions using weakly guided approximation which considers $\Delta \ll 1$, or equivalently, $n_{co} \cong n_{cl}$. This approximation leads to a solution in terms of a scalar wave equation, instead of vector solutions of the vector wave equation (see a physical explanation in [7]: sections 13, pag. 282). Modal fields of weakly guiding waveguides can be derived by applying perturbation methods to Maxwell's equations (see section 32 in [7]), so the electric and magnetic fields **E** and **H** of individual bound modes (in this subsection we omit the modal subscript, since only individual modes are considered) of a waveguide are expressed as:

$$\mathbf{E}(x, y, z) = \mathbf{e}(x, y)\exp(i\beta\mathrm{z}) = (\mathbf{e_t} + \hat{\mathbf{z}}e_z)\exp(i\beta\mathrm{z}) \tag{2.7}$$

$$\mathbf{H}(x,y,z) = \mathbf{h}(x,y)\exp(i\beta \mathrm{z}) = (\mathbf{h_t} + \hat{\mathbf{z}}h_z)\exp(i\beta \mathrm{z}), \tag{2.8}$$

where subscripts t and z denote transverse and longitudinal components respectively. If $n_{co}{\cong}n_{cl}$, Δ can be rewritten as:

$$\Delta = \frac{1}{2}\left\{1 - \frac{n_{cl}^2}{n_{co}^2}\right\} \cong \frac{n_{co} - n_{cl}}{n_{co}}, \tag{2.9}$$

and the refractive index can be written thus:

$$n^2(x,y) = n_{co}^2\left\{1 - 2\Delta f(x,y)\right\} \tag{2.10}$$

where f=0 at the maximum index (center of the core) and f=1 in the cladding.

Ignoring polarization effects contained in the the ∇_tln n^2 term of the vector wave equation, each component of the transverse electric field $\mathbf{e_t}$ satisfies the scalar wave equation:

$$\{\nabla_t^2 + k^2n^2(x,y) - \tilde{\beta}^2\}\mathbf{e_t} = 0, \tag{2.11}$$

with components of the transverse magnetic field $\mathbf{h_t}$ given by:

$$\mathbf{h_t} = n_{co}\left(\frac{\epsilon_0}{\mu_0}\right)^{\frac{1}{2}}\hat{\mathbf{z}} \times \mathbf{e_t}, \tag{2.12}$$

where k=$2\pi/\lambda$, the free-space wavelength is λ. Although the cartesian components of $\mathbf{e_t}$ satisfy equation 2.11, their spatial dependence can be determined in any cylindrical coordinate systems, e.g. in cylindrical polar coordinates $\mathbf{e_t}$=$\mathbf{e_t}$*(r,ϕ)*. $\tilde{\beta}$ denotes the propagation constant for the scalar wave equation, as distinct from the exact propagation constant β for the vector wave equation (see Snyder&Love [7]: sections 13-4, pag. 284). Any solution of the scalar wave equation and its first derivatives are continuous everywhere. Together with the requirement that $\mathbf{e_t}$ be bounded, this property leads to an eigenvalue equation for the allowed values of $\tilde{\beta}$.

Taking into account waveguide polarization properties a correction $\delta\beta$ to the scalar propagation constant $\tilde{\beta}$ must be added . To determine $\delta\beta$ exactly we would have to solve the vector wave equation. However, the ∇_tln n^2 term is small for weakly guiding waveguides, so we use simple perturbation methods. For a waveguide with step-profile $\delta\beta$ is given by (see Snyder&Love [7]: sections 13-6, pag. 287):

$$\delta\beta \cong \frac{\rho(2\Delta)^{3/2}}{2V}\oint_l(\nabla_t\cdot\mathbf{e_t})\mathbf{e_t}\cdot\hat{\mathbf{n}}\mathrm{d}l \Bigg/ \int_{A_\infty}\mathbf{e_t^2}\mathrm{d}A \tag{2.13}$$

where A_∞ is the infinite cross-section of the waveguide, and l is the contour along the interface and $\hat{\mathbf{n}}$ is the unit outward normal on the waveguide cross-section.

In a weakly guiding waveguide, longitudinal components can be considered much smaller respect to transverse components. These components are expressed approximately in terms of $\mathbf{e_t}$ and $\mathbf{h_t}$ (see Snyder&Love [7] pag. 625):

$$e_z \cong \frac{i(2\Delta)^{\frac{1}{2}}}{V}(\rho\nabla_t \cdot \mathbf{e_t}), \tag{2.14}$$

$$h_z \cong \frac{i(2\Delta)^{\frac{1}{2}}}{V}(\rho\nabla_t \cdot \mathbf{h_t}), \tag{2.15}$$

2.2. MODES IN AN OPTICAL FIBER

Following the development of Snyder&Love [7] section 14-2 pag. 303, we consider a fiber of circular cross-section to solve the scalar wave equation derived from weakly guiding approximation (see equation (2.4)). We solve analytically by the separation of variables considering an step-index profile given in the equation (2.10), to obtain an approximate solution for the modal fields of the equations (2.7) and 2.8. Also, we will find the *propagation constants* (*eigenvalue*) $\tilde{\beta}$ for each mode, that are classified in terms of azimuthal (l) and radial (m) numbers → β_{lm}. For the case of l=0, the solutions can be separated into two classes that have either transverse electric (TE_{0m}), i.e e_z=0 (so called "*radial*" modes), or transverse magnetic (TM_{0m}) fields, i.e h_z=0 (so called "*meridional*" modes). In the case of $l \neq 0$, both electric and magnetic field have non-zero z-component, and depending on which one is more dominant are denoted as: $HE_{l+1,m}$ and $EH_{l-1,m}$. These modes are so-called *the hybrid modes.*

The solutions of the scalar wave equation (2.4) for a fiber of circular cross-section, of refractive-index profile *n(r)* and core radius ρ, have the separable form (see pag. 303 of Snyder&Love [7]) :

$$\Psi = F_l(r)cos(l\phi), \qquad \Psi = F_l(r)sin(l\phi), \tag{2.16}$$

where l=0,1..., ϕ and r are azimuthal and radial coordinates, respectively, and $F_l(r)$ satisfies the ordinary differential equation that comes from weakly guiding approximation:

$$\left\{\frac{\mathrm{d}^2}{\mathrm{d}r^2} + \frac{1}{r}\frac{\mathrm{d}}{\mathrm{d}r} + k^2n^2(r) - \frac{l}{r^2} - \beta^2\right\}\ F_l(r) = 0 \tag{2.17}$$

We use $n^2(R) = n_{co}^2\{1\text{-}2\Delta f(R)\}$, where the radial coordinate r is normalized by radius ρ, which denotes the core radius, thus $R = r/\rho$. This leads to:

$$\left\{\frac{\mathrm{d}^2}{\mathrm{d}R^2} + \frac{1}{R}\frac{\mathrm{d}}{\mathrm{d}R} - \frac{l}{R^2} + \tilde{U}^2 - V^2 f(R)\right\} \; F_l(R) = 0 \tag{2.18}$$

where $\tilde{U}$ contains the polarization correction $\delta\beta$ in a weakly guiding approximation:

$$\tilde{U}^2 \cong \rho(k^2 n_c^2 o - \tilde{\beta}^2)^{\frac{1}{2}}, \tag{2.19}$$

$$\tilde{\beta} \cong \beta + \delta\beta \tag{2.20}$$

This scalar wave equation has two solutions for each value of $\tilde{\beta}$ for its higher-order modes, corresponding to values of $l \geqslant 1$. Thus the direction of $\mathbf{e_t}$, takes the form:

$$\mathbf{e_t} = F_l[\{a\cos(l\phi) + b\sin(l\phi)\}\hat{\mathbf{x}} + \{c\cos(l\phi) + d\sin(l\phi)\}\hat{\mathbf{y}}] \tag{2.21}$$

where a, b, c and d are constants. There are four sets of values for these constants, corresponding to two pairs of orthogonally polarized modes (4-fold degenerate). Scalar wave equation for a circular waveguide depends on the polarization corrections through term $\tilde{U}$, if the equation (2.21) satisfies the scalar equation, the term of the polarization correction can be rewritten as (see pag. 305 of Snyder&Love [7]):

$$I_1 = \frac{(2\Delta)^{3/2}}{4\rho V}\frac{\int_0^\infty RF_l(\mathrm{d}F_l/\mathrm{d}R)(\mathrm{d}f/\mathrm{d}R)\mathrm{d}R}{\int_0^\infty RF_l^2\mathrm{d}R}, \tag{2.22}$$

$$I_2 = \frac{l(2\Delta)^{3/2}}{4\rho V}\frac{\int_0^\infty F_l^2(\mathrm{d}f/\mathrm{d}R)\mathrm{d}R}{\int_0^\infty RF_l^2\mathrm{d}R} \tag{2.23}$$

that indicates that polarization correction has different values within the same group of modes with the same azimuthal value (l), even if the fiber is perfectly circular. This will be very important to understand the development of special type of fiber for OAM propagation.

→ *Fundamental HE_{11} and HE_{1m} (l=0) modes*: Each mode has a transverse electric field whose electric field direction, or polarization, is parallel to one of an arbitrary pair of orthogonal directions in the fiber cross-section. Thus, the fundamental HE_{11} mode and HE_{1m} modes are always uniformly polarized. There is only one solution of the scalar wave equation for these modes, corresponding to l=0. For convenience we take one mode to be x-polarized and the other y-polarized. The transverse and also longitudinal fields of HE_{11} mode and HE_{1m} modes are shown in Table 2.1. The subscript t and z denote transverse and longitudinal components, respectively; and $\hat{\mathbf{x}}$, $\hat{\mathbf{y}}$ and $\hat{\mathbf{z}}$ are unit vectors parallel to cartesian axes.

Table 2.1: Transverse and longitudinal components of the fundamental HE_{11} mode and HE_{1m} (*l=0*) modes. With permission from [7], © Chapman and Hall, pag. 304.

Mode	$\mathbf{e}_{ti}$	$\mathbf{h}_{ti}$	$\mathbf{e}_{zi}$	$\mathbf{h}_{zi}$	$\delta\beta_i$
Even HE_{1m}	$\hat{\mathbf{x}}F_0$	$n_{co}\left(\frac{\epsilon_0}{\mu_0}\right)^{\frac{1}{2}}\hat{\mathbf{y}}F_0$	$i\frac{(2\Delta)^{\frac{1}{2}}}{V}G_0\cos\phi$	$in_{co}\left(\frac{\epsilon_0}{\mu_0}\right)^{\frac{1}{2}}\frac{(2\Delta)^{\frac{1}{2}}}{V}G_0\sin\phi$	I_1
Odd HE_{1m}	$\hat{\mathbf{y}}F_0$	$-n_{co}\left(\frac{\epsilon_0}{\mu_0}\right)^{\frac{1}{2}}\hat{\mathbf{x}}F_0$	$i\frac{(2\Delta)^{\frac{1}{2}}}{V}G_0\sin\phi$	$-in_{co}\left(\frac{\epsilon_0}{\mu_0}\right)^{\frac{1}{2}}\frac{(2\Delta)^{\frac{1}{2}}}{V}G_0\cos\phi$	I_1

→ *Higher-order modes* ($l\geqslant 1$). For each ($l\geqslant 1$), there are four modes. These modes are no longer uniformly polarized, i.e. the direction of e_{ti} depends on the position in the fiber cross-section. These mode are denote as $HE_{l+1,m}$. The HE_{1m} modes showed in the previous table are a particular case of the $HE_{l+1,m}$ modes when *l=0*. The transverse and longitudinal fields of these modes are shown in Tables 2.2 and 2.3.

Table 2.2: Transverse components of $HE_{l+1,m}$ modes. With permission from [7], © Chapman and Hall, pag. 304.

Mode	$\mathbf{e}_{ti}$	$\mathbf{h}_{ti}$
Even $HE_{l+1,m}$	$\{\hat{\mathbf{x}}\cos l\phi - \hat{\mathbf{y}}\sin l\phi\}F_l$	$n_{co}\left(\frac{\epsilon_0}{\mu_0}\right)^{\frac{1}{2}}\{\hat{\mathbf{x}}\sin l\phi + \hat{\mathbf{y}}\cos l\phi\}F_l$
TM_{0m} (*l=1*)	$\{\hat{\mathbf{x}}\cos l\phi + \hat{\mathbf{y}}\sin l\phi\}F_l$	$-n_{co}\left(\frac{\epsilon_0}{\mu_0}\right)^{\frac{1}{2}}\{\hat{\mathbf{x}}\sin\phi - \hat{\mathbf{y}}\cos\phi\}F_1$
Even $EH_{l-1,m}$ ($l\geqslant 1$)	$\{\hat{\mathbf{x}}\cos l\phi + \hat{\mathbf{y}}\sin l\phi\}F_l$	$-n_{co}\left(\frac{\epsilon_0}{\mu_0}\right)^{\frac{1}{2}}\{\hat{\mathbf{x}}\sin l\phi - \hat{\mathbf{y}}\cos l\phi\}F_l$
Odd $HE_{l+1,m}$	$\{\hat{\mathbf{x}}\sin l\phi + \hat{\mathbf{y}}\cos l\phi\}F_l$	$-n_{co}\left(\frac{\epsilon_0}{\mu_0}\right)^{\frac{1}{2}}\{\hat{\mathbf{x}}\cos l\phi - \hat{\mathbf{y}}\sin l\phi\}F_l$
TE_{0m} (*l=1*)	$\{\hat{\mathbf{x}}\sin l\phi - \hat{\mathbf{y}}\cos l\phi\}F_l$	$n_{co}\left(\frac{\epsilon_0}{\mu_0}\right)^{\frac{1}{2}}\{\hat{\mathbf{x}}\cos\phi + \hat{\mathbf{y}}\sin\phi\}F_1$
Odd $EH_{l-1,m}$	$\{\hat{\mathbf{x}}\sin l\phi - \hat{\mathbf{y}}\cos l\phi\}F_l$	$n_{co}\left(\frac{\epsilon_0}{\mu_0}\right)^{\frac{1}{2}}\{\hat{\mathbf{x}}\cos l\phi + \hat{\mathbf{y}}\sin l\phi\}F_l$

Table 2.3: Longitudinal components of $HE_{l+1,m}$ modes. With permission from [7], © Chapman and Hall, pag. 305.

Mode	$\mathbf{e}_{zi}$	$\mathbf{h}_{zi}$	$\delta\beta_i$
Even $HE_{l+1,m}$	$i\frac{(2\Delta)^{\frac{1}{2}}}{V}G_l^- \cos(l+1)\phi$	$in_{co}\left(\frac{\epsilon_0}{\mu_0}\right)^{\frac{1}{2}}\frac{(2\Delta)^{\frac{1}{2}}}{V}G_l^- \sin(l+1)\phi$	$I_1 - I_2$
TM_{0m} (*l*=*1*)	$i\frac{(2\Delta)^{\frac{1}{2}}}{V}G_1^+$	0	$2(I_1 + I_2)$
Even $EH_{l-1,m}$ (*l*⩾*1*)	$i\frac{(2\Delta)^{\frac{1}{2}}}{V}G_l^+ \cos(l-1)\phi$	$-in_{co}\left(\frac{\epsilon_0}{\mu_0}\right)^{\frac{1}{2}}\frac{(2\Delta)^{\frac{1}{2}}}{V}G_l^+ \sin(l-1)\phi$	$I_1 + I_2$
Odd $HE_{l+1,m}$	$i\frac{(2\Delta)^{\frac{1}{2}}}{V}G_l^- \sin(l+1)\phi$	$-in_{co}\left(\frac{\epsilon_0}{\mu_0}\right)^{\frac{1}{2}}\frac{(2\Delta)^{\frac{1}{2}}}{V}G_l^- \cos(l+1)\phi$	$I_1 - I_2$
TE_{0m} (*l*=*1*)	0	$in_{co}\left(\frac{\epsilon_0}{\mu_0}\right)^{\frac{1}{2}}\frac{(2\Delta)^{\frac{1}{2}}}{V}G_1^+$	0
Odd $EH_{l-1,m}$	$i\frac{(2\Delta)^{\frac{1}{2}}}{V}G_l^+ \sin(l-1)\phi$	$in_{co}\left(\frac{\epsilon_0}{\mu_0}\right)^{\frac{1}{2}}\frac{(2\Delta)^{\frac{1}{2}}}{V}G_l^+ \sin(l-1)\phi$	$I_1 + I_2$

, where $G_l^{\mp}$ is given by:

$$G_l^{\mp} = \frac{\mathrm{d}F_l}{\mathrm{d}R} \mp \frac{l}{R}F_l. \tag{2.24}$$

and F_l is a solution that depends on index profile $n(R)$.

$$n(R) = \begin{cases} n_{co}, & 0 \leqslant R \leqslant 1 \\ n_{cl}, & 1 \leqslant R \leqslant \infty \end{cases} \tag{2.25}$$

Assuming that the fiber is weakly guiding, we have a solution for equation (2.17). The *l*=*0* solution gives the radial dependence of the fundamental HE_{11} and remaining HE_{1m} modes, which are a Bessel function of the first kind J_0 for the core, and a modified Bessel function of the second kind K_0 for the cladding. The modal properties of the fundamental mode can be found in [7], pag. 313.

Besides, higher order modes ($l \geqslant 1$) have solutions of F_l and $G_l^{\pm}$ in terms of Bessel function and modified Bessel function of order l. Continuity of F_l and $\mathrm{d}F_l/\mathrm{d}R$ (i.e. boundary conditions of $\mathbf{H}$ and $\mathbf{E}$ in $R = 1$), leads to the eigenvalue equation for the propagation constant (β_j), or equivalently the effective index (n_{eff}) for each mode:

$$\tilde{U}\frac{J_{l+1}(\tilde{U})}{J_l(\tilde{U})} = \tilde{W}\frac{K_{l+1}(\tilde{W})}{K_l(\tilde{W})}, \tag{2.26}$$

$$\tilde{U}^2 + \tilde{W}^2 = V^2. \tag{2.27}$$

Finally, we find solutions to all four even and odd $HE_{l+1,m}$ and $EH_{l-1,m}$ modes, and TM_{0m} and TE_{01} modes when $l = 1$ (see pag. 319 in [7]). Numerical solution of the equations (2.26) and (2.27) leads to the modes in terms of $\tilde{U}$ and V parameters, as shown in Figure 2.1.

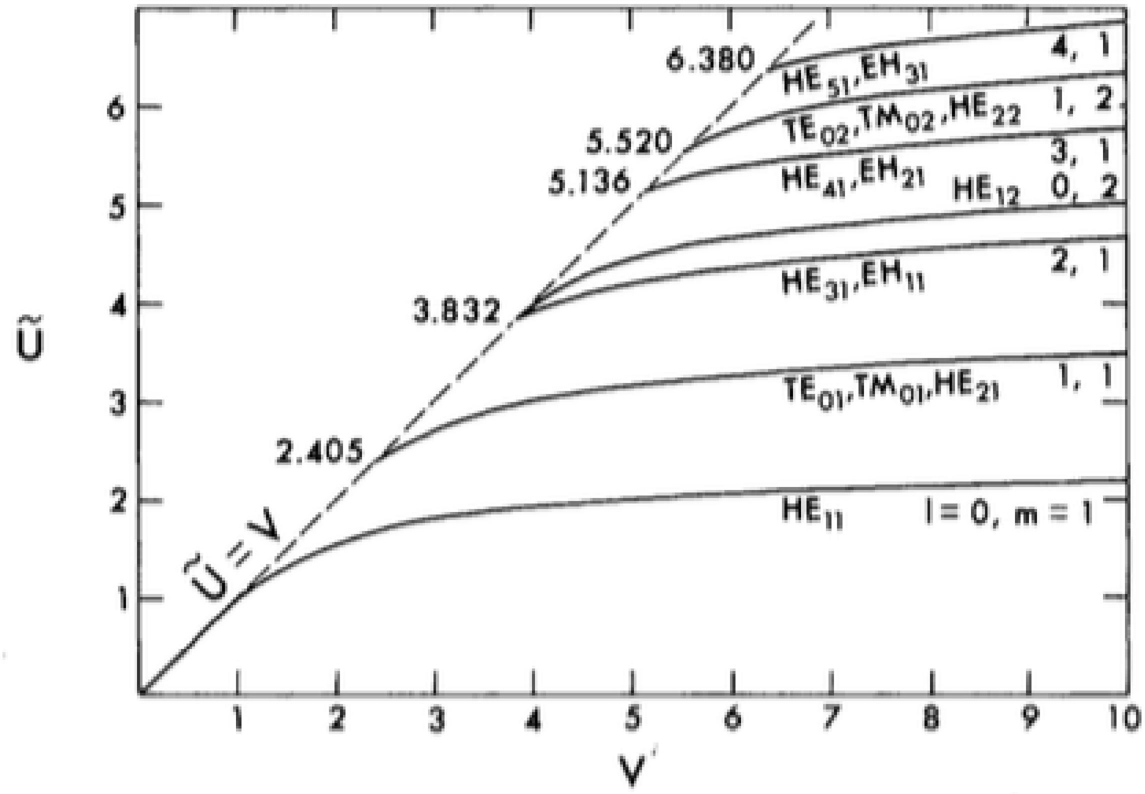

Figure 2.1: Numerical solutions of the eigenvalue equation 2.26, showing the mode labelling and the corresponding values of l and m. The values along the dashed line are the cutoff values of each modes. With permission from [7], © Chapman and Hall, pag 307

2.2.1. *Polarization correction*

In the case of step-index fiber, the modes belonging to a "*group*" that have almost the same propagation constant are considered as "*almost degenerate*", also meaning that the *polarization correction* ($\delta\beta$) value can be considered quite small (see polarization corrections in [7] pag. 319). As an example, Figure 2.2 shows the first-order group formed by TE_{01}, TM_{01}, $HE_{21}^{even,odd}$ modes with $l = 1$ and $m = 1$, and also the group formed by the two polarizations of the fundamental mode HE_{11}^{even} (x-polarized), HE_{11}^{odd} (y-polarized) modes with $l = 0$.

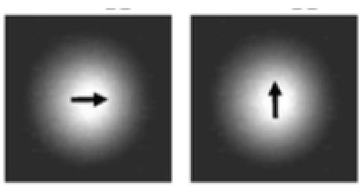

(a) HE_{11}^{even} HE_{11}^{odd}

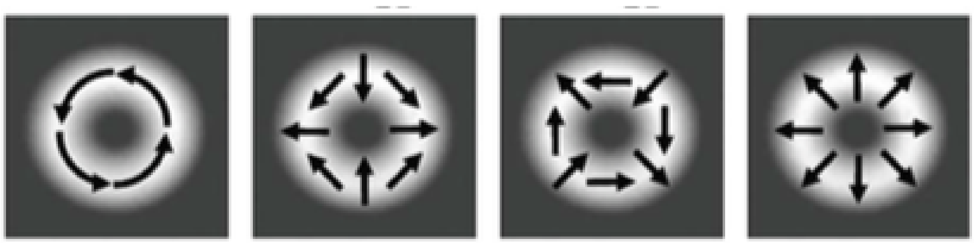

(b) TE_{01} HE_{21}^{odd} HE_{21}^{even} TE_{01}

Figure 2.2: First modes in a step index fiber. **(a)** Fundamental mode HE_{11} is "*linearly polarized (LP)*" and corresponds to the group with *l=0* **(b)** Higher order modes correspond to the group with *l=1.* These modes are no longer *LP*. Adapted from [8]

$\delta\beta$ is considered one of the most important parameters in the design of OAM fibers. OAM modes are derived from $HE_{l+1,m}$ and $EH_{l-1,m}$ modes, and might be used as independent channels as long as the degeneracy is lifted in the modes into the same group. As an example, the polarization correction between TM_{01} and HE_{21}^{even} modes is given by:

$$\delta\beta = -\frac{(2\Delta)^{3/2}}{\rho}\frac{\tilde{W}\tilde{U}^2}{V^3}\frac{K_1(\tilde{W})}{K_2(\tilde{W})}. \tag{2.28}$$

In general, for all modes of an step-index fiber there is an increase of $\delta\beta$ by increasing the refractive index contrast, and a reduction of this term by decreasing the fiber radius, as mode order increases (see Figure 2.3).

It is considered that the modes become in "*quasi non-degenerate*" as $\delta\beta$ increase. $\delta\beta$ is responsible for interference effect depending on z between pairs of modes with the same scalar propagation constant. As β can change with perturbations along z, then both the perturbations and the $\delta\beta$ are responsible for interference amongst modes of

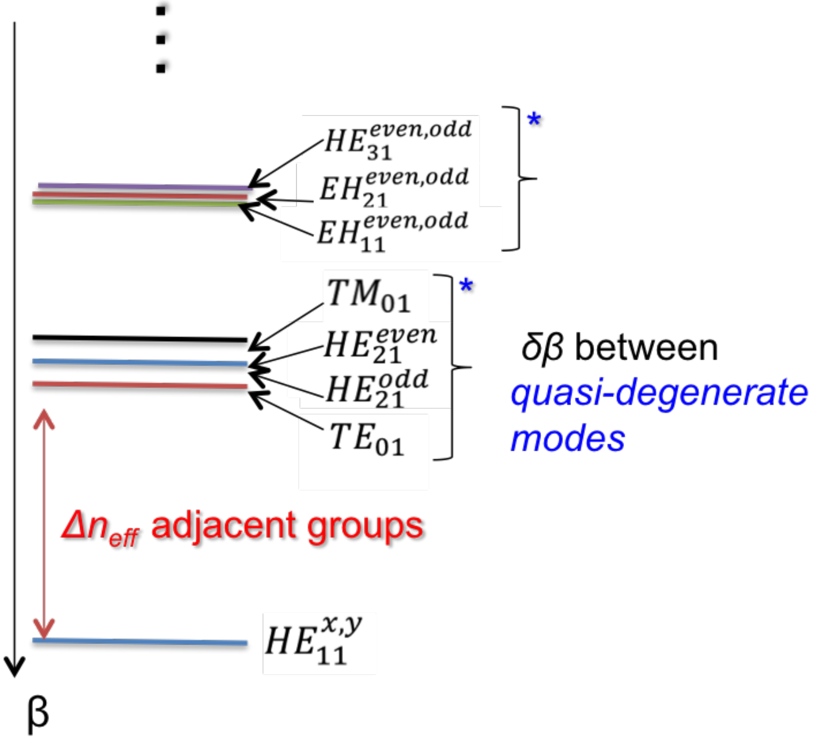

Figure 2.3: $\delta\beta$ and its dependence with the order of higher order modes

the same group, inhibiting thus the propagation of a unique mode without coupling with the others.

3. OAM MODES IN FIBERS AND MODE STABILITY

We show how a multimode fiber possesses vector modes that can be combined to give OAM modes. This is through a basis transformation that leads to modes with a non-zero azimuthal component of a Poynting vector proportional to $e^{i\ell\phi}$. In this chapter, we demonstrate how the OAM modes can exist in a fiber. We also discuss the conditions for uncoupled propagation of OAM modes in long lengths, when the fiber is under external perturbation such as bends.

3.1. OAM MODES IN FIBERS

3.1.1. Poynting vector, linear momentum and angular momentum of light

Using Mikonski definition [58], linear momentum density **p**, and angular momentum density **j**, of a light beam may be calculated from the electric and magnetic fields [59]:

$$\mathbf{p} = \epsilon_0 \mathbf{E} \times \mathbf{H} \tag{3.1}$$

$$\mathbf{j} = \epsilon_0 (\mathbf{r} \times \mathbf{E} \times \mathbf{H}) = \mathbf{r} \times \mathbf{p} = \epsilon_0 \mathbf{r} \times \mathbf{S} \tag{3.2}$$

with **r** as position and **S** is Poynting vector. The total angular momentum **J**, and angular momentum flux $\Phi_{\mathbf{j}}$ can be defined as:

$$\mathbf{J} = \int\int\int \mathbf{j} dV \tag{3.3}$$

$$\Phi_{\mathbf{j}} = \int\int \mathbf{j} dA \tag{3.4}$$

Let us define the time average of the angular momentum flux $\langle \Phi_{\mathbf{j}} \rangle$:

$$\langle \Phi_j \rangle = \int\int \langle \mathbf{j} \rangle dA, \tag{3.5}$$

as well as time average of the energy flux $\langle \Phi_{\mathcal{W}} \rangle$ in order to verify whether certain modes have OAM. From here, we follow the development showed in [11] pag. 17-20:

$$\langle \Phi_{\mathcal{W}} \rangle = \int \int \langle S_z \rangle dA, \tag{3.6}$$

In order to leave only z-component of the angular momentum density non-zero, the momentum density $\mathbf{j}$, or equivalently the Poynting vector should have only azimuthal components ϕ:

$$\langle j \rangle_z = \epsilon_0 \mathbf{r} \times \langle \mathbf{E} \times \mathbf{H} \rangle_\phi = \mathbf{r} \times \mathbf{p}_\phi = \epsilon_0 \mathbf{r} \times \langle S_\phi \rangle \tag{3.7}$$

where the time-averaged Poynting vector $\langle S \rangle = Re(\mathbf{S})$, with $\mathbf{S} = \frac{1}{2}\mathbf{E} \times \mathbf{H}^*$ still referred to as "Poynting vector" expressed directly in terms of the phasors.

Any angular momentum component in z direction, by definition, requires a component of linear momentum in the xy plane, i.e., light with transverse momentum components. This fact leads to an inexistent of components of angular momentum for both a *transverse plane wave* or a *transverse electromagnetic mode* (TEM), since the linear momentum of this wave/mode, is only in the propagation direction z, and there can not have any component of angular momentum in the same direction. Hence, an angular momentum in the z direction requires a component of electric or magnetic field also in the z direction. Consequently, the hybrid modes of an optical fiber with non-zero components of electric or magnetic field comprise a natural modal set for the generation and propagation of OAM modes.

3.1.2. OAM modes in fibers: the role of hybrid modes

Considering hybrid modes $HE^{even,odd}_{l+1,m}/EH^{even,odd}_{l-1,m}$:

$$HE^{even,odd}_{l+1,m} = F_{l,m}(r) \left\{ \begin{array}{c} \hat{\mathbf{x}} \cos l\phi - \hat{\mathbf{y}} \sin l\phi \\ \hat{\mathbf{x}} \sin l\phi + \hat{\mathbf{y}} \cos l\phi \end{array} \right\} e^{ik_{z,HE} \cdot z} \tag{3.8}$$

$$EH^{even,odd}_{l-1,m} = F_{l,m}(r) \left\{ \begin{array}{c} \hat{\mathbf{x}} \cos l\phi + \hat{\mathbf{y}} \sin l\phi \\ \hat{\mathbf{x}} \sin l\phi - \hat{\mathbf{y}} \cos l\phi \end{array} \right\} e^{ik_{z,EH} \cdot z} \tag{3.9}$$

where $F_{l,m}(r)$ is the mode's electric field envelope, where m is the radial mode number and m-1 the number of zeroes in F, and k_z is the longitudinal wave vector of the mode, related to the effective index by $k_z = 2\pi n_{eff}/\lambda$. $HE_{l+1,m}/EH_{l-1,m}$ even and odd solutions are degenerate with each other in circular fiber with conventional step/gradual index profile. However, $HE_{l+1,m}$ and $EH_{l-1,m}$ are not degenerate, which means that $k_{z,HE} \neq k_{z,EH}$. Hybrid modes are not used as independent channel in fiber communication links because are easily coupled among them under perturbations, moreover, it is very difficult to excite them by means of a external source circularly or linearly polarized because the polarization structure of these modes is spatially varying, as shown in Figure 3.1.

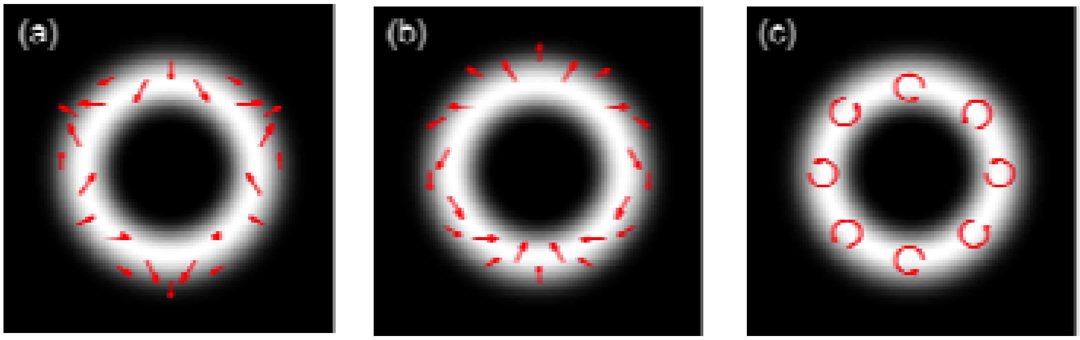

Figure 3.1: Plot of the electric field of **(a)**HE_{31}^{even} and **(b)**EH_{11}^{even} mode in an air-core fiber reported in [9] (similar polarization patterns exist for any weakly- guiding circular fiber) **(c)** Plot of the electric field of an OAM mode made of complex combinations of the HE_{31}^{even} and HE_{31}^{odd}. Note that the complicated spatially-dependent polarization has given way to a spatially uniform circular polarization. This figure was taken from Supplementary Materials in [9]. With permission from [9]. Copyright 2015 Optical Society of America.

Let us now focus on a specific complex linear combination between the pair of degenerate solutions (even and odd) of the hybrid modes $HE_{l+1,m}^{even,odd}$, $EH_{l-1,m}^{even,odd}$ with $\pi/2$ phase shift among them [60]:

$$V_{l,m}^{\pm} = HE_{l+1,m}^{even} \pm iHE_{l+1,m}^{odd} = \hat{\sigma^{\pm}} F_{l,m}(r) e^{\pm il\phi} e^{ik_{z,HE}.z} \tag{3.10}$$

$$W_{l,m}^{\pm} = EH_{l-1,m}^{even} \mp iEH_{l-1,m}^{odd} = \hat{\sigma^{\pm}} F_{l,m}(r) e^{\mp il\phi} e^{ik_{z,HE}.z} \tag{3.11}$$

where $\hat{\sigma^{\pm}} = \hat{x} \pm i\hat{y}$ indicates left and right handed circular polarizations, and l is named as ℓ or state of topological charge of OAM mode. This linear combination showed in equations (3.10) and (3.11) comes from observing azimuthal dependence of the phase $e^{\pm i\ell\phi}$. It is evident from equations (3.10) and (3.11) that these combination between fiber modes are OAM states, with $\ell = \pm l$ for $V_{l,m}^{\pm}$ and $\ell = \mp l$ for $W_{l,m}^{\pm}$. In addition, OAM modes have spatially uniform polarizations making easier their modal excitation compared with the complex modal excitation of hybrid modes, as is shown in Figure 3.1. The two classes of OAM states $V^{\pm}_{l,m}$ and $W^{\pm}_{l,m}$ are distinguished by comparing the handedness of OAM and circular polarization, with $V^{\pm}_{l,m}$ possessing spin angular momentum *(SAM)* and orbital angular momentum of the same handedness, and $W^{\pm}_{l,m}$ the opposite handedness. We refer to this two classification as "*spin-orbit aligned*" and "*spin-orbit anti-aligned*", respectively. We define four states derived from $V^{\pm}_{l,m}$ and $W^{\pm}_{l,m}$ of the same l,m as "*OAM family*" (see Supplementary Materials in [9]). However, before go further, let us show whether these OAM modes can exist in an optical fiber or not.

3.1.3. Can OAM modes exist in an optical fiber?

Following the development showed in [11] pag. 17-20, and considering $HE^{even}_{l+1,m}$ and $HE^{odd}_{l+1,m}$ modes, if we denote the electric field of these modes as $\mathbf{e_1}$ and $\mathbf{e_2}$, and magnetic fields as $\mathbf{h_1}$ and $\mathbf{h_2}$, the expression for this new mode can be written as:

$$\mathbf{e} = \mathbf{e_1} + i\mathbf{e_2} \tag{3.12}$$

$$\mathbf{h} = \mathbf{h_1} + i\mathbf{h_2} \tag{3.13}$$

Using a simple coordinate transformation from cartesian to cylindrical coordinates, and expressions for $HE^{even}_{l+1,m}$ and $HE^{odd}_{l+1,m}$ modes given by equations (3.8) and (3.9), we derive the radial and longitudinal components of the electric and magnetic fields as:

$$e_r = e^{i(l+1)\phi} F_l(R), \tag{3.14}$$

$$h_r = -in_{co} \left(\frac{\epsilon_0}{\mu_0}\right)^{\frac{1}{2}} e^{i(l+1)\phi} F_l(R), \tag{3.15}$$

$$e_z = i\frac{(2\Delta)^{\frac{1}{2}}}{V} G^{-}_{l} e^{i(l+1)\phi}, \tag{3.16}$$

$$h_z = n_{co} \left(\frac{\epsilon_0}{\mu_0}\right)^{\frac{1}{2}} \frac{(2\Delta)^{\frac{1}{2}}}{V} G^{-}_{l} e^{i(l+1)\phi}, \tag{3.17}$$

All quantities with $e^{i(l+1)\phi}$ dependence indicates that these modes might be OAM, similarly to free space case (Laguerre-Gaussian modes). Besides, it can be shown that the complex linear combination of the $EH^{even,odd}_{l-1,m}$ modes gives similar results as equation (3.17), except the OAM is $e^{i(l-1)\phi}$ and the SAM of these states are of the opposite signs.

From equation (3.17), we conclude that in an ideal fiber, OAM mode exists. However, we have considered a fiber as perfectly symmetric, assuming no longitudinal perturbations in the fiber profile. In a real fiber, random perturbations along z can induce coupling between spatial and polarization modes, causing possibility coupling amongst OAM modes. Let us explain in the follow subsection the conditions to guarantee uncoupled OAM propagation.

3.2. FIBER MODE COUPLING

Modes in an optical fiber form an orthogonal basis, and no coupling amongst them is expected. In an ideal scenario, a fiber cross-section is ideally circular and is assumed no change along the longitudinal axis (z). However, in a real fiber, the refractive index profile is perturbed by the diameter induced variations and inhomogeneity of the material during the fabrication process. Likewise, external perturbations like fiber bends, twist and microbending change the field distributions of the modes, leading to coupling amongst them, which means a loss of orthogonality [36].

Mode coupling effects were widely studied in the 70's by Marcuse in [61] (Chapter 3-5), but recently, these effects have become in relevant to develop MDM optical communication systems [37], for example, how this can influence the modal dispersion and mode dependent loss and gain in MDM systems [40].

To characterize the strength of the overall coupling, we consider a "*correlation length*", over which the local eigenvectors (modal field distribution) can be assumed constant. In the *weak-coupling regime*, the fiber length is not much longer than the correlation length. In the *strong-coupling regime*, the fiber length far exceeds the correlation length [62]. Depending on the strength of mode coupling, detection systems can be divided into direct and coherent. Direct detection is used in communication systems operating in *weak-coupling regime*, otherwise, if the communication system operates in *strong-coupling regime* the coherent detection is used in order to compensate the crosstalk that comes from mode coupling [62].

By the origin, mode coupling can be classified as "*distributed*", caused by random perturbations along propagation axis (z) in fibers, or "*discrete*", caused by the connections between dissimilar waveguides or fibers. We focus on the former; this is the most important for us because higher order modes within the same group or in near groups suffer mainly strong coupling.

Regarding SMFs, these support the propagation in two linear polarizations of the fundamental mode. These two polarizations have an effective index separation on the order of 10^{-7} [63], so external perturbations can easily couple one mode into another. Similarly, higher order modes are very sensitive to distributed mode coupling. There have been multiple efforts over the years to understand the relationship between effective index separation Δn_{eff} and mode coupling, especially in the context of understanding microbend losses in SMF [63]. However, the effects of mode coupling intimately depend on the electric field overlap between the modes of interest, and the form, symmetry, and strength of perturbation on a fiber (See the chapter 4 of the Marcuse's book [61]). Only some phenomenological rules have been developed for a limited number of cases [64]. One such rules have demonstrated that distributed mode coupling is inversely proportional to Δn_{eff}^{-p} , with $p \geq 4$ [65]. This has had broad experimental confirmation, providing a degree of reliability, is that $\Delta n_{eff} \geq 10^{-4}$ yields polarization maintaining fibers in which the orthogonal polarizations of the fundamental modes, which are "*almost degenerate*", remain stable for a length scale, or correlation length exceeding 100 m. Stability means both no coupling and no change in the modal field distribution of each individual mode in a specific propagation length ("*correlation length*"). Likewise, by adopting this criterion, the higher order modes belonging to the same group, which are also "*almost degenerate*", should stable in a scale of similar length, or even longer, as long as $\Delta n_{eff} \geq 10^{-4}$ amongst them [10].

3.2.1. Mode stability conditions

In particular, in a conventional MMF, the n_{eff} splitting between modes within a mode group is much too small to isolate the modes from one another. Each *LP* mode generated by linear combination of the vector modes ($HE_{l+1,m}$, $EH_{l-1,m}$, $TM_{0,m}$, $TE_{0,m}$) randomly shares power due to longitudinal inhomogeneities caused by fiber bends, geometry imperfections during manufacture, and stress-induced index perturbations. For this reason, in most MMFs, modes that are observed at the fiber output are in fact the linear combinations of the vector modes, and are considered *linearly polarized* (LP) states [36]. In Figure 3.2, for example, the LP_{11} pattern is formed by interference of two vector modes ($HE_{2,1}^{even,odd}$, $TM_{0,1}$, $TE_{0,1}$) with slightly different n_{eff}.

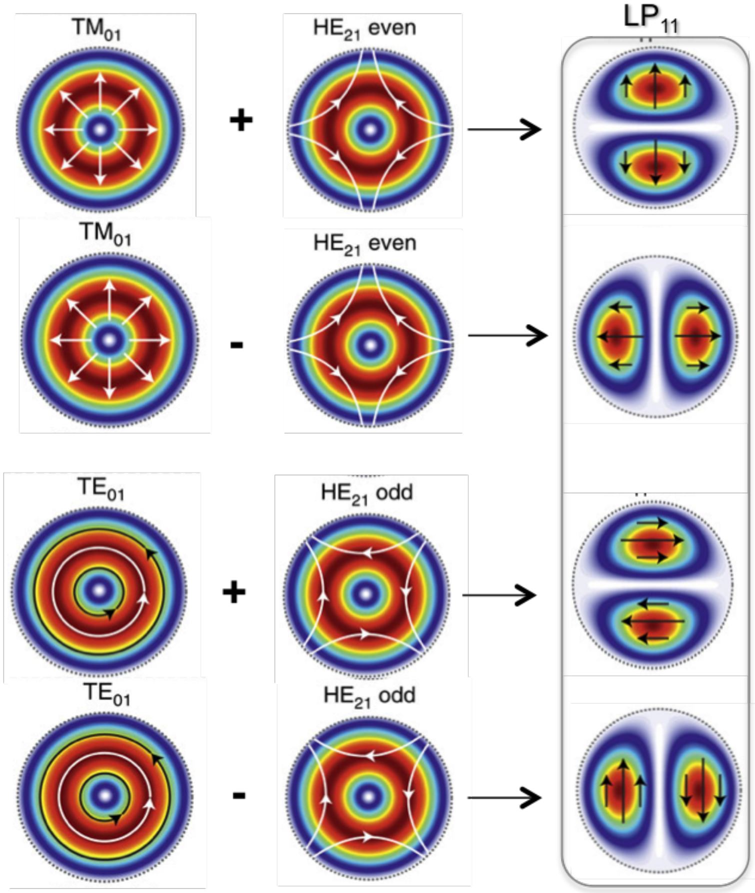

Figure 3.2: Modal intensity patterns for the first higher order mode group: LP_{11}-like modes of the LP_{11} group. Arrows show the polarization of the electric fields. $HE_{2,1}^{even,odd}$, TE_{01} and TM_{01} are simulated vector eigenmodes coming from exact vector solutions of the equation (2.18). This figure represents the unstable intensity patterns of LP_{11} modes due to intermodal mode coupling between vector eigenmodes. This pattern is commonly obtained at a fiber output [10].

This pattern is unstable which means that it is coupled with other vector modes, exhibiting changes in the modal field distribution, that are observed as rotations at the output of the fiber when perturbed. Note the striking similarity between the obtained interference and the LP_{11} mode obtained from the scalar mode solution, however, care must be exercised when using the nomenclature LP to describe these states [10]. This is the reason why in some papers these modes are called as LP-like modes. A true eigenmode (eigenvector) in a fiber is lengthwise invariant, that is, it would not change in size or shape, even should not rotate during the propagation in the fiber. The LP_{11} state shown in Figure 3.2 would switch its orientation as it propagates, even in a perfectly unperturbed straight fiber. This is because constructive and destructive interference lead to an LP_{11} pattern with 90 deg rotated intensity pattern, and light propagation in the constitutive vector modes in a fiber will necessarily lead to such beating with a beat length of $\lambda/\Delta n_{eff}$ [36]. These patterns are known as polarization vortexes caused by intermodal coupling phenomena, however their generation is limited to short lengths, so this kind of conventional MMFs and even others such as protonic crystal and multicore fibers do not allow propagation of polarization vortexes over reasonable long lengths. Likewise, OAM modes with $\ell = 1$, that are the linear combination of the $HE_{2,1}^{even,odd}$ can't coexist in these fibers due to coupling to degenerate TE_{01} and TM_{01} modes. Even OAM modes with $\ell > 1$ formed with no degenerate modes $HE_{l+1,m}$ and $EH_{l-1,m}$ modes neither would be propagated.

Following the phenomenological law proposed by [65] that indicates a strong exponential reduction in mode coupling by increasing the Δn_{eff} among modes, an example of a desired solution to enable propagation of OAM modes with $\ell = \pm 1, \pm 2$ derived from combinations of $HE_{2,1}^{even,odd}$ and $HE_{3,1}^{even,odd}$, $EH_{1,1}^{even,odd}$ modes is shown in Figure 3.3b.

These desired solutions have been widely studied in [9, 11], which look for inhibiting the coupling amongst *almost degenerate* modes within a specific group. Through a fiber of special index profile shown in [11] the degeneracy among first-order modes (LP_{11} group) is lifted, enabling propagation of OAM modes of $\ell = \pm 1$. Similarly, in [9] other special index profile that lifts the degeneracy of the highest-order mode is also shown, enabling the stable propagation of OAM modes of $\ell = \pm 5 \pm 6 \pm 7$. An increase of stable OAM modes brings as consequence an increase in system capacity. This doctoral work will show a new design of vortex fiber to improve the stability under external perturbation like bends, and also how to increase the number of stable OAM modes. Before going further, we will show a brief mathematical description of fiber mode coupling phenomenon.

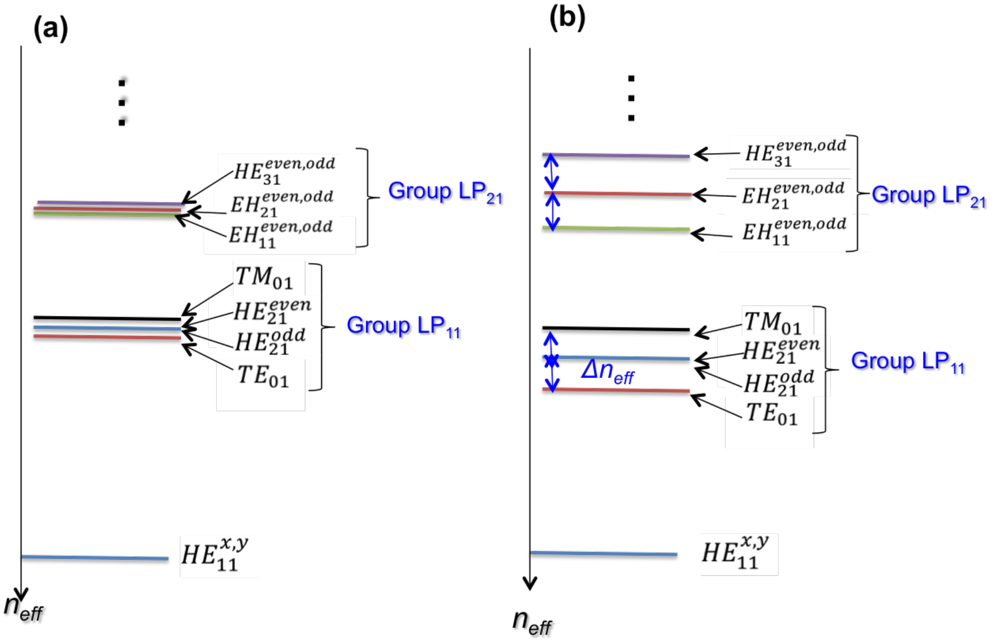

Figure 3.3: Concept of the effective index separation for the mode groups: LP_{11} and LP_{21}. **(a)** Conventional MMF with small effective index separation resulting in mode coupling. **(b)** Desired solution that leads a enough splitting amongst the modes into the groups LP_{11} and LP_{21}, that can be achieved by the design of a special index profile.

3.2.2. Fiber mode coupling

For conventional MMF with small refractive index differences between core and cladding, *almost no-degenerate* modes have almost equal effective index. In this case, OAM family is susceptible to strong mode coupling from perturbations. In this subsection, we mathematically describe mode coupling phenomenon.

Following the formulations of [9,61,66], we write the refractive index profile as $n(r,z) = n_0(r) + n_b(r,\phi,z)$, where n_0 is the fiber's ideal profile and n_b is a perturbation of index profile, which is separable into transverse $N_b(r,\phi)$, and longitudinal parts $f(z)$. The coefficient of power coupling between modes j and k is then determined by:

$$\langle P_{j,k}\rangle = \frac{\omega^2}{c^2}\Phi(k_{z,j} - k_{z,k})\left(\int\int r dr d\phi N_b E_j^* E_k\right)^2, \tag{3.18}$$

where ω and c are the frequency and speed of light, Φ is the spatial power spectrum of the autocorrelation of $f(z)$, which could be derived considering a small index perturbation proportional to Fourier coefficients related to perturbation periodicity. E_j is the normalized electric field of the j^{th} mode, and $N_b(r,\phi)$ is the transverse perturbation. If the spatial power spectrum of autocorrelation of $f(z)$ is assumed to be of Gaussian form, then:

$$\varPhi(k_{z,j}-k_{z,k}) = \sqrt{\pi}\sigma^2 L_c e^{-\left[\frac{1}{2}L_c(k_{z,j}-k_{z,k})\right]^2}, \tag{3.19}$$

where σ is the RMS deviation of $f(z)$, and L_c is its correlation length. The angular part of the perturbation p can be separated by:

$$N_b(r,\phi) = \sum_{p=-\infty}^{\infty} \widetilde{N_p}(r)e^{ip\phi}, \tag{3.20}$$

where $\widetilde{N_p}$ is the Fourier series coefficient of the perturbation corresponding to angular momentum

If the j^{th} and k^{th} modes are OAM states expressed as:

$$\varPsi_\ell = \hat{e}G(r)e^{i\ell\phi} \tag{3.21}$$

where $\hat{e}$ is a polarization, and $G(r)$ the field's radial envelope. Coupling from a mode with OAM ℓ_j to one with ℓ_k depends on the inner product between the fields $E_j = \varPsi_{\ell_\mathbf{j}}$, $E_k = \varPsi_{\ell_\mathbf{k}}$ and the perturbation. Thus, we can solve the overlap integral of equation 3.18, and simplify its angular part as:

$$\int\int rdrd\phi N_b E_j^* E_k = \int_0^a \widetilde{N_p}(r)G_j^*(r)G_k(r)rdr \sum_{p=-\infty}^{\infty} \underbrace{\int_0^{2\pi} e^{i(\ell_k-\ell_j+p)\phi}d\phi,}_{angular\ \ part} \tag{3.22}$$

which vanishes unless

$$p - (\ell_j - \ell_k) = 0 \tag{3.23}$$

In equation (3.19), $\varPhi$ achieves maximum value for $\Delta n_{eff} = n_{eff_j} - n_{eff_k}$, and maximum exchange of power between modes will be achieved when they are phase matched. In theory, two degenerate modes will never couple if the integral of equation (3.18) is zero. However, in practice, any real perturbation will have some Fourier spectrum in both azimuthal and radial coordinates, like in equation (3.19), thus, coupling between *almost degenerate* modes is expected.

From the point of view of phase matching, only strong coupling between the spin-orbit aligned states, (e.g. two $V_{l,m}^+$ states) would be expected. In view of coupling strength relative to the integral of equation (3.18), coupling is likely between spin-orbit anti-aligned states $V_{l,m}^{+}$ and $W_{l,m}^{-}$, since any perturbation will be sufficient to couple $\hat{\sigma}^{+}$ and $\hat{\sigma}^{-}$. This latter is even less likely between OAM states coming from two *quasi non-degenerate modes* ($HE_{l+1,m}$ and $EH_{l-1,m}$), which are OAM states with opposite orbital charges $+\ell$ and $-\ell$.

Let us introduce an expression in order to quantify the "*mode purity*", which measures the ability of a perturbed OAM mode of remaining uncoupled with other OAM modes. If we calculate the "*mode purity*" for each perturbed OAM mode, we obtain the *OAM spectra*, also know as *OAM charge weight distributions* as:

$$C_i = \int\int E(x,y,z)\Psi_i^*(x,y,z)dxdy \tag{3.24}$$

where $|C_i|^2$ is the *OAM charge weight* and $\sum|C_i|^2 = 1$ is expected. $E(x,y,z)$ is the normalized electric field of the achieved mode in a perturbed fiber (e.g. in presence of ellipticity of ring, twists or fiber bending). $\Psi_i(x,y,z)$ is the normalized electric field of eigenmodes in an ideal unperturbed fiber. Equation (3.24) is a simplified version of the equation (3.18) considering all field components to extend its validity to the high contrast case, but now taking into account the perturbed fields, instead of the perturbation itself as was previously done. Note that if both fields are unperturbed C_i=0, which means that the modes are perfectly orthogonal, and they are uncoupled. This equation is used to estimate the mode coupling and crosstalk in presence of perturbations such as fiber bending that will be described in the next section.

3.2.3. Model of a bent fiber

Bent waveguides have been modeled using an exact approach that uses full-vectorial finite-element method in a local cylindrical coordinate system to describe bending loss and modal distribution of the fields [67]. Likewise, other approach has been proposed in [68] to model bending losses in optical waveguides, using *transformation optics* (TO) technique. We use the latter technique (TO) to model a bent fiber shown in Figure 3.4. The bending plane is parallel to the xz plane with R being the bending radius defined from the origin to the center of the waveguide.

TO considers that light propagation along a bent fiber located in the xyz coordinates (see Figure 3.4a), is equivalent to light propagation along a straight fiber located in a

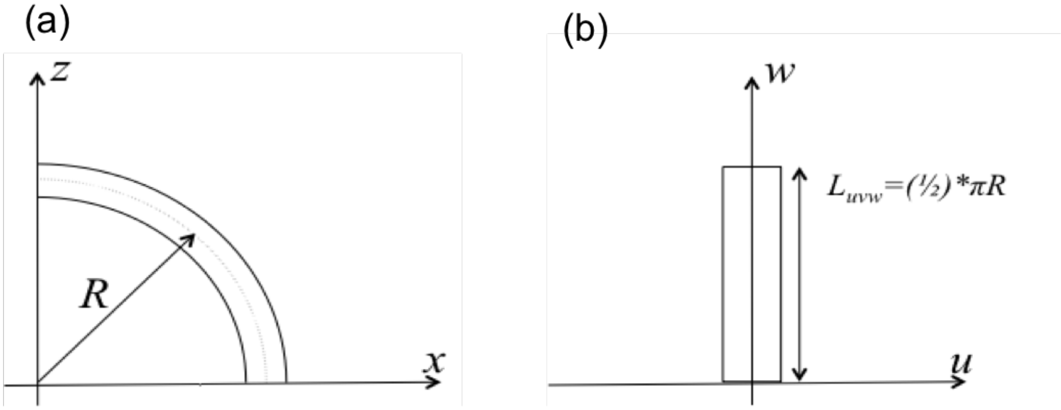

Figure 3.4: **(a)** Top view of a fiber's core with a bending radius R in xy plane **(b)** Top view of the transformed straight waveguide νw plane. Adapted from [68]

new coordinate system $u\nu w$ (see Figure 3.4b), through a coordinate transformation T:

$$T : u + jw = Rln\left(\frac{x + jz}{R}\right) \tag{3.25}$$

If we apply this transformation to the first quadrant in the xyz coordinates, we can use the formula given in [69]:

$$\frac{\epsilon_i}{\epsilon} = \frac{\mu_i}{\mu} = Q_u Q_\nu Q_w / Q_i^2 \tag{3.26}$$

$$\epsilon_i = \epsilon Q_u Q_\nu Q_w / Q_i^2 \qquad \mu_i = \mu Q_u Q_\nu Q_w / Q_i^2 \tag{3.27}$$

$$Q_i^2 = (\partial x/\partial i)^2 + (\partial y/\partial i)^2 + (\partial z/\partial i)^2 \qquad (i = u, \nu, w) \tag{3.28}$$

and the transformation equation (3.25) to rewrite the permittivity and permeability as tensors in the new coordinate system $u\nu w$:

$$\frac{\epsilon_i}{\epsilon} = \frac{\mu_i}{\mu} = \begin{bmatrix} 1 & 0 & 0 \\ 0 & e^{2u/R} & 0 \\ 0 & 0 & 1 \end{bmatrix} \tag{3.29}$$

This approach is based on the form invariance property of the Maxwell equations in any coordinate system, that leads to the scalability of the permittivity and permeability by a common factor in this new coordinate system. Thus, in a bent fiber one can solve the eigenmodes supported by the straight fiber in uvw by taking into account this scaling shown in equation (3.29), and to use the effective index of the eigenmodes n_{eff} and transformation for eigenvector $E_x = E_u/Q_u$, where $Q_u = e^{u/R}$ in our case. This model was implemented in Comsol 5.1® to compute perturbed fields of equation (3.24).

4. VORTEX FIBERS

As aforementioned in section (3.21), the OAM mode instability problem in step-index fibers, as shown in Figure 3.3 arises from the *near-degeneracy* amongst higher order vector modes described in section (2.2). OAM modes are ideally orthogonal but are easily coupled under small perturbations, limiting their propagation to short fiber lengths on the order of a few centimeters [53–55]. In this chapter, we describe a class of specialty fibers, introduced by [8]. One of them is all-solid, and fabricated in silica and doped silica, and it is able of lifting the degeneracy amongst the modes belonging to LP_{11}(first-high order modes), which is formed by the vector modes: TM_{01}, TE_{01}, and $HE_{21}^{even,odd}$. Likewise, another special fiber with a part of air-core is able of lifting the degeneracy, but amongst groups of high-order modes [9]. We explain the reasoning behind untypical refractive index profile in these fibers, called *vortex fibers*, from now on. Then, we numerically solve the vector equation (2.18) using the finite element method implemented in Comsol 5.1® to compute modal effective indices, the modal dispersion, as well as modal field distributions. We will show that in these fibers, there is a large separation among effective indices within the mode group considered *near-degenerate*, that can be several orders of magnitude higher than in conventional fibers, indicating in this manner, a reduction of mode coupling according to the theory described in section (3.2). Before we go further, let us analyze in detail these vortex fiber designs, as our start point.

4.1. DESIGN OF VORTEX FIBER

Near-degeneracy among modes within a group is related to the polarization correction term $\delta\beta$ of the equation (2.13) obtained by means of a first-order perturbative analysis. Thus, for example, we calculate the scalar propagation constants of a LP_{lm} group, which are identical in scalar approximation, and then, the real propagation constants of the vector modes belonging to this group can be obtained through a vector correction (see Table 2.3) and the equations (2.22) and (2.23). The magnitude of splitting depends on the index contrast Δ and the radial gradient of the field $\mathrm{d}F_l/\mathrm{d}R$. We can intuitively guess that an increase in Δ would increase the mode splitting, and therefore it would lift the degeneracy within of the group of modes. However, only an increase of Δ is not enough to lift the degeneracy because the modes become increasingly confined and the field amplitudes dramatically decrease at waveguide boundary, reducing the $\mathrm{d}F_l/\mathrm{d}R$ term of the equations (2.22) and (2.23), that also should be taken into account (See details of this concept in [70]).

In particular, we focus on the first order LP_{11} group or *OAM family* of $\ell = 1$. The vector correction of the propagation constants β for the scalar solution are given by (see Table 2.3):

$$\delta\beta_{TE_{01}} = 0 \tag{4.1}$$

$$\delta\beta_{TM_{01}} = 2(I_1 + I_2) \tag{4.2}$$

$$\delta\beta_{HE_{21}^{even,odd}} = I_1 - I_2 \tag{4.3}$$

where I_1 and I_2 were given by equations (2.22) and (2.23), and may be rewritten as in [8]:

$$I_1 = \frac{\delta n_{max}}{2a^2 n_{co}\beta} \int rE(r)\frac{\partial E(r)}{\partial r}\frac{\partial(\frac{\Delta}{n}/\Delta n_{max})}{\partial r}\mathrm{d}r \tag{4.4}$$

$$I_2 = \frac{\delta n_{max}}{2a^2 n_{co}\beta} \int E^2(r)\frac{\partial(\frac{\Delta}{n}/\Delta n_{max})}{\partial r}\mathrm{d}r \tag{4.5}$$

where $E(r)$ is the electric field profile for the scalar mode, a is the size of the waveguiding core, $\Delta n(r)/\Delta n_{max}$ is the normalized index profile of the fiber. An index profile that lifts the degeneracy should to maximize $\Delta n(r)/\Delta n_{max}$ while also maximizing the field $E(r)$ and the field-gradient $\frac{\partial E(r)}{\partial r}$ at index step fibers.

We start by first considering a conventional fiber with step index profile. If we observe the Figure 4.1a this index profile does not maximize the electric field $E(r)$ or mode intensity $|E(r)|^2$ (in red) for the scalar LP_{11} mode. This condition is also not satisfied only by increasing the relative index contrast $\Delta N/\Delta N_{max}$. Then, we conclude that a waveguide whose profile mirror that mode itself (seeFigure 4.1b) can accomplish the condition of high mode intensity close to the waveguide transition regions (boundaries), maximizing $\frac{\partial E(r)}{\partial r}$ as well as $E(r)$. This is indeed what equations (4.1) - (4.5) demand- i.e large separation in propagation constants requires large I_1 and I_2 values, which can be obtained when LP_{11} (or any higher order mode) power and its derivates resides close to index boundary. This yields a fiber designed to have large degeneracy splittings. [70].

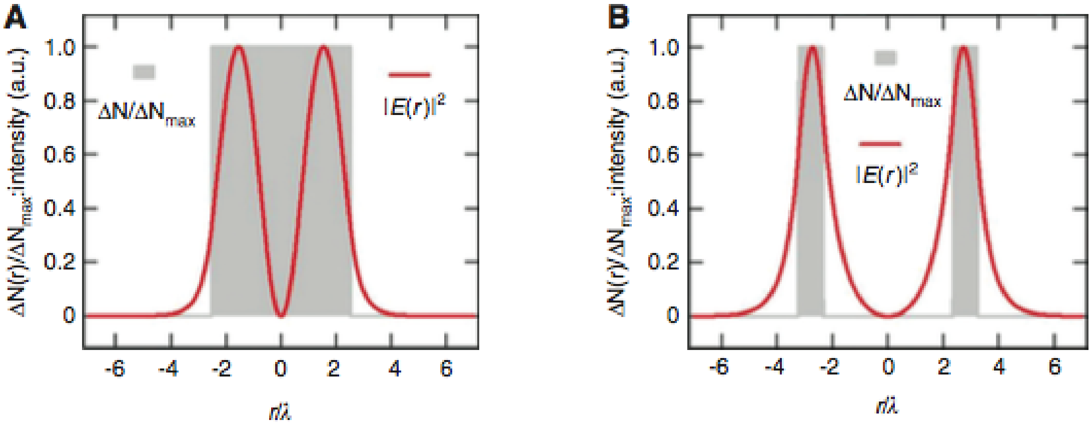

Figure 4.1: Normalized index profile (gray background), and corresponding mode intensity $|E(r)|^2$ for the scalar LP_{11} mode (red) for **(a)** conventional step-index fiber, and **(b)** the ring-fiber (mirror design). ©2009 IEEE. With permission from [8]

This concept was demonstrated for the first time by Ramachandran in 2009 [8], and based on this design goal of having vector modes *almost non-degenerate* with $\Delta n_{eff} > 10^{-4}$ has been possible. It can be applied in ring-fiber designs to propagate higher order modes or OAM modes of $\ell > 1$ with great stability [9,11]. Several ring fibers have been designed for stable propagation of optical vortices [9,11,41,60,71–74]. In particular, we are interested in the designs of [10]: *solid design* that splits the first group of higher order mode (LP_{11} group, or OAM family of $\ell = 1$); and in [9]: *air-core design* that splits highest order mode to enable propagation of OAM *families* of $\ell = \pm 6, \pm 7, \pm 8$.

4.2. ALL-SOLID VORTEX FIBER: NUMERICAL ANALYSIS

4.2.1. $OAM_{\pm 1}$, TM_{01} *and* TE_{01} *modes*

An optical microscope image (see Figure 4.2a) shows of the cleaved end-face of the all-solid vortex fiber. It is specified using the convention dk110OD, like dk11OD105, in which the number 105 is proportional to the core size (see [11] pag. 28). The inset shows the fiber core region surrounded by a trench and a ring region. Figure 4.2b shows the measured refractive index profile reported in [3, 11]. We will show that this fiber propagates the two polarizations of the fundamental mode HE_{11} (denoted LP_{01} in the scalar approximation), and the modes $HE_{21}^{even,odd}$, TM_{01}, TE_{01} belonging to the first mode group LP_{11}. Besides, the index profile has a characteristic high-index ring that serves to inhibit the near-degeneracy between $HE_{21}^{even,odd}$ and TM_{01}, TE_{01} modes that are usually coupled in conventional step-index fibers. $HE_{21}^{even,odd}$ modes yields an OAM states of $\ell = \pm 1$, called by simplicity $OAM_{\pm 1}$.

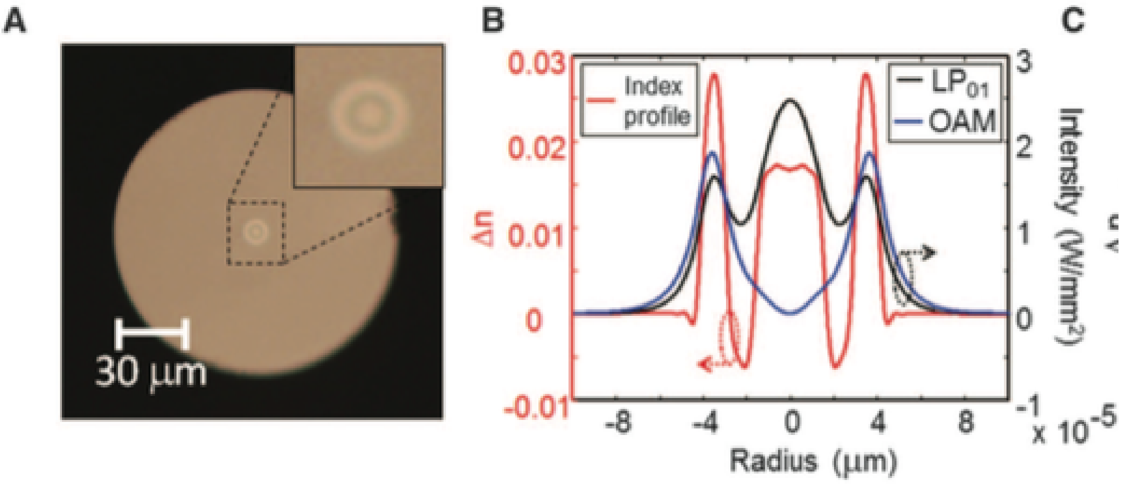

Figure 4.2: **(a)**Microscope image of the end-face of the all-solid vortex fiber **(b)**. Measured refractive index (red line), and numerically calculated mode profiles LP_{01} (black line), and OAM_1. With permission from [11] ©Boston University, and from [3] AAAS, respectively.

In order to study the modal properties of this fiber, we use the finite element method implemented in Comsol 5.1® software to numerically solve vector wave equation (2.3) for the vortex fiber. Using an interpolated index profile take from the measured profile shown in Figure 4.2b, we draw the waveguide structure in Comsol 5.1®, which consists of a solid core surrounded by circular concentric rings (see Figure 4.2a). The full-structure was discretized by triangular elements of a size smaller than the wavelength, and a perfect match layer (PML) of 1 μm was used to truncate the computational domain after 52.5 μm. We compute the effective index as a function of the ligth wavelength, and the modal field distribution of the propagated modes.

We find out a separation of approximately 3×10^{-3} (at 1550 nm) with respect to the fundamental HE_{11} mode, as well as a separation of approximately 1.1×10^{-4} between nearest neighbor first order modes (see Figure 4.3). Our results are in agreement with the reported in [3, 11]

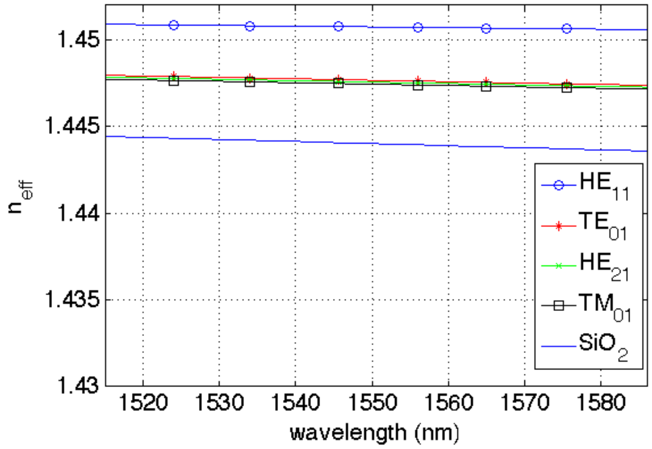

(a)Effective index as a function of light wavelength - solid vortex fiber dk11OD105

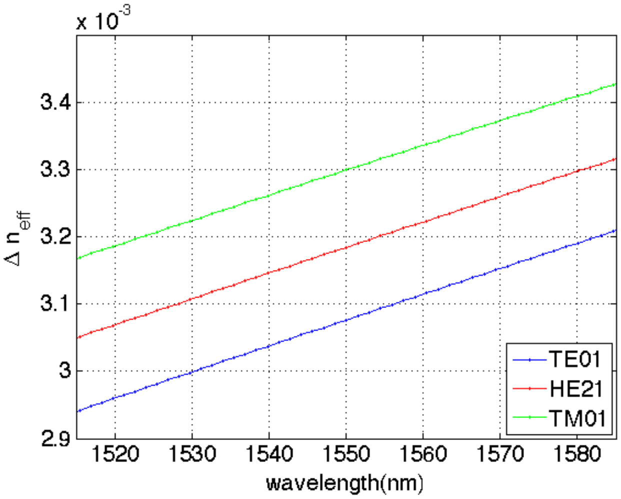

(b)Δn_{eff} as a function of light wavelength - solid vortex fiber dk11OD105

Figure 4.3: Numerically computed effective index of the all-solid vortex fiber dk110D105 as a function of light wavelength.**(a)** Effective index of the fundamental mode (HE_{11}) and the first-order mode **(b)**. Numerically calculated effective index differences of the first-order modes TE_{01}, HE_{21}, and TM_{01} with respect to the fundamental mode (HE_{11}). This figure was made with the help of [12].

We also obtain the mode profiles as is shown in Figure 4.4. Note that fundamental mode ($HE_{1,1}$) does not have a typical profile anymore as in the case of the conventional step- index fiber; which is Gaussian-like. The HE_{21} mode intensity profile resembles a doughnut shape due to refractive index ring structure.

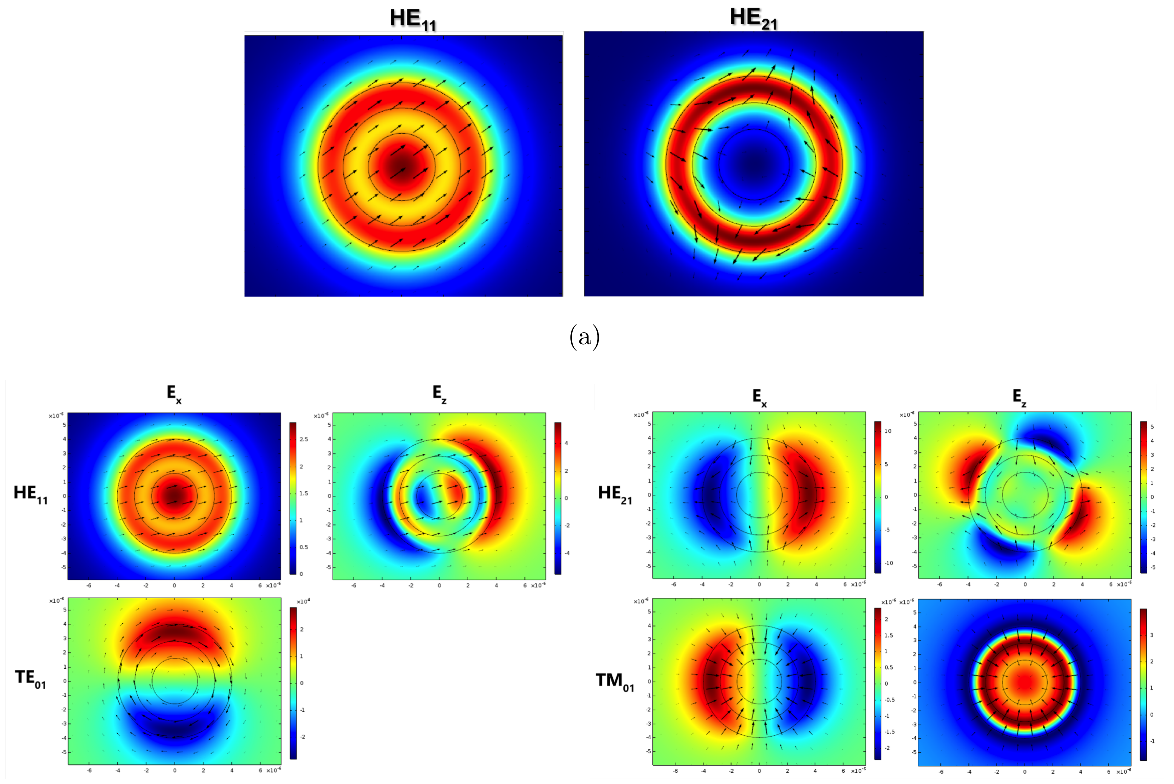

(a)

(b) (c)

Figure 4.4: Mode profiles in 2D case.**(a)** Mode intensity profile proportional to the *Poynting vector* for the HE_{11} and HE_{21}. Arrows indicate the electric field distributions. **(b)** Electric field profiles E_x and E_z for the HE_{11} and TE_{01} modes. **(b)** Electric field profiles E_x and E_z for the HE_{21} and TM_{01} modes.

The Figure 4.5 reveals the phase profiles (see equation (3.10)) for OAM_0 and OAM_1 modes. We observe no change in the phase distribution for OAM_0 as was expected. Instead, OAM_1 possesses an helicoidal phase distribution, in which the blue corresponds to $-pi$ and red to pi radians, so there is an azimuthal dependence of the phase showed in the equation (3.10) for non-zero OAM fiber states.

We also obtain the radial electric field $E(r)$ and its derivative (see Figure (4.6)). We

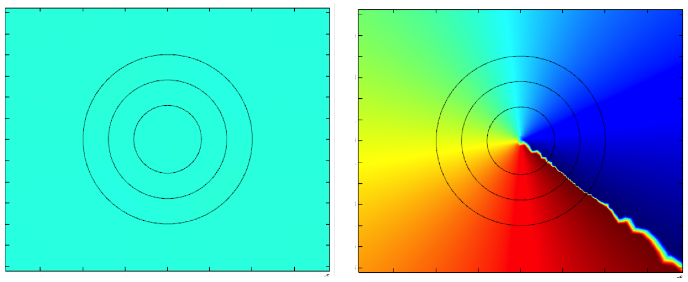
(a)
(b)

Figure 4.5: Phase profile for **(a)** OAM_0 **(b)**OAM_1 modes.

find out a high mode intensity close to the waveguide transition regions (boundaries), maximizing $\frac{\partial E(r)}{\partial r}$, as well as, maximizing $E(r)$. These conditions are satisfied in this vortex fiber, which is necessary to produce a split between the vector modes of the first group LP_{11} as was described in section 4.1.

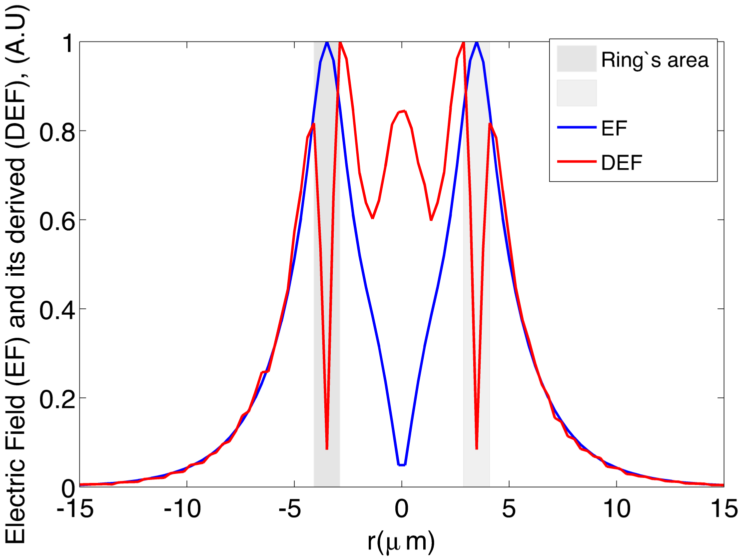

Figure 4.6: Radial electric field (EF) and its radial derived (DEF) in the ring's area

4.2.2. Effect of increasing the ring's width

Let us analyze the modal behavior in vortex fibers with large ring width. We focus in the telecom wavelength of 1550 nm. We increase the ring diameter to achieve the index profile reported in [11] pag.32 (see fiber named dk110OD160) in which higher order modes are now guided. Figure 4.7a shows guiding of higher order modes belonging to

LP_{11} group: TE_{01}, HE_{21} and TM_{01}; LP_{21} group: HE_{31} andEH_{11}; LP_{02} group: HE_{12}; and LP_{31} group: HE_{41} and EH_{21}.

We can observe that Δn_{eff} between HE_{11} modes and the vector modes belonging to LP_{11} group decrease as a consequence of the increase in the modal content. Additionally LP_{21} and LP_{31} groups can generate OAM_2 and OAM_3 modes, respectively, however, they have a Δn_{eff} of approximately 2×10^{-5} indicating higher mode coupling among its vector modes, which suggests that they remain still *almost degenerate*, preventing in this manner a stable propagation in long lengths.

Based on the simulations for the vortex fiber with a large ring, we can infer about two important observations. First, it is reasonable for now to conclude that the mode coupling can be higher in all-solid vortex fibers of a larger ring, as well as the number of available OAM states becomes larger, but most of them can be unstable. Second, in an ideal case, this all-solid vortex fiber should only propagate a few modes to avoid a higher coupling with highest order modes.

4.2.3. OAM Spectra

Regarding the quantification of the mode coupling strength, we compute the OAM *spectra* using the equation (3.24). We consider bend radius of 2 and 5 cm to obtain perturbed electric fields by using the model of the subsection (3.2.3). Note that the equation (3.24) gives a "*mode purity*" of zero value (C_i=0) as long as both fields are unperturbed. We compute equation (3.24) for two unperturbed fields combining possible several cases and notice that in the most of the cases it yields a value of $\sim$ 120 dB, indicating a perfect orthogonality between the modes, or equivalently a mode of high purity.

The *spectra* was obtained using an own code in Matlab® that numerically compute the perturbed and unperturbed electric fields obtained from Comsol®. Table 4.1 shows the values in dB units indicating the coupling strength between perturbed OAM_1, HE_{11_y}, and HE_{11_x} modes corresponding to first columns, and unperturbed TE_{01}, TM_{01} and OAM_{-1} modes corresponding to the first rows. We observe that mode coupling is more intense to small bend radius of 2 cm.

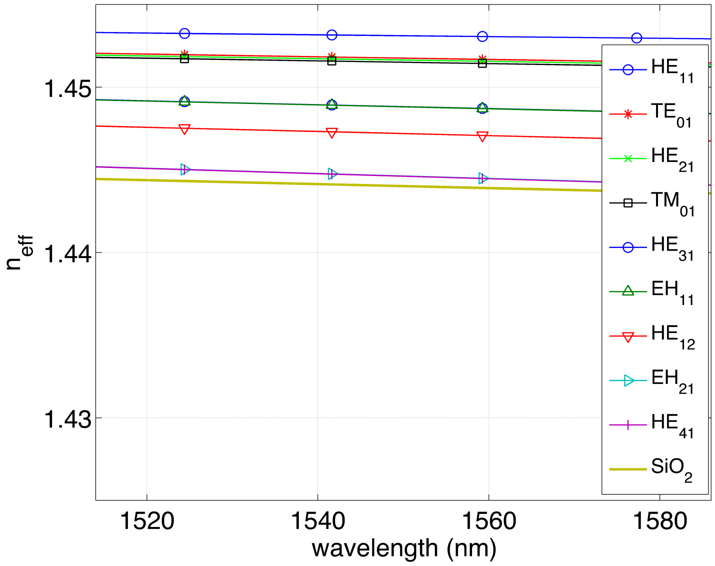

(a)Effective index as a function of light wavelength - solid vortex fiber dk11OD160

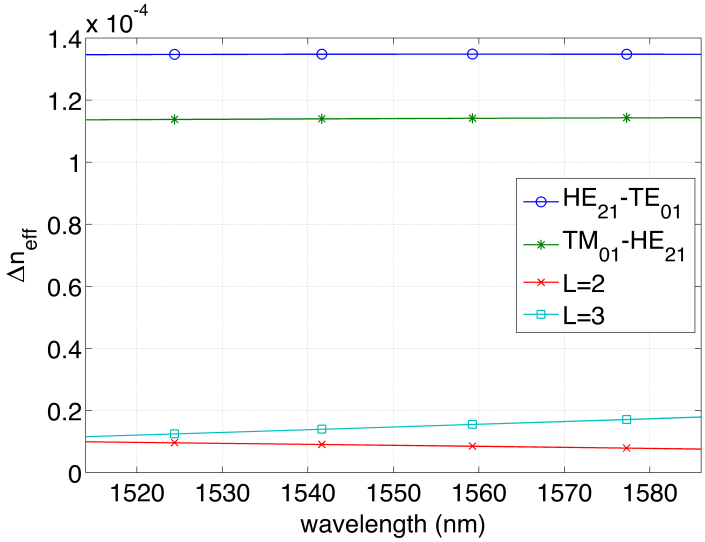

(b)Δn_{eff} as a function of light wavelength - solid vortex fiber dk11OD160

Figure 4.7: Numerically computed effective index of the all-solid vortex fiber (dk110D160) as a function of light wavelength. **(a)** Effective index for guided modes in the vortex fiber. **(b)** Effective index differences for guided modes in the vortex fiber. This figure was made with the help of [12].

We also observe high coupling strengths of values around 0 dB between the modes with the same orbital charge ℓ, which means that the propagation is not affected by the bend. Otherwise, a lower coupling strength for the OAM modes of opposite orbital charge (ℓ=1 and ℓ=-1 highlighted by green). These results are relevant because allow affirming that the propagation of OAM modes is very stable even under great perturbations like bends, remaining coupled with itself and uncoupled with the others.

Table 4.1: OAM *Spectra* of the all-solid vortex fiber dk100OD105. Perturbed modes are indicated in the first column. Fiber was bent with radii of **(a)** 5 cm and **(b)** 2 cm.

(a)Fiber bent with 5 cm

	TE_{01}	TM_{01}	OAM_{-1}	OAM_1
OAM_{-1}	-45	-39	-0.005	-58
OAM_1	-47	-39	-58	-0.005
HE_{11_y}	-30	-103	-33	-33
HE_{11_x}	-111	-73	-78	-78

(b)Fiber bent with 2 cm

	TE_{01}	TM_{01}	OAM_{-1}	OAM_1
OAM_{-1}	-29	-23	-0.05	-48
OAM_1	-31	-24	-48	-0.05
HE_{11_y}	-22	-96	-25	-25
HE_{11_x}	-120	-65	-70	-70

4.3. AIR-CORE DESIGN: NUMERICAL ANALYSIS

Figure 4.8a shows the an image of the cleaved end-face of a sample of the air-core vortex fiber, and Figure 4.8b the measured index profile.

In this subsection, we describe the air- core vortex fiber that also enables conservation of OAM. The air-core acts as a repulsive barrier, forcing the mode field to encounter large index step between ring and cladding, yielding high mode confinement and also satisfying the criteria mentioned in section 4.1. This design allows one to lift the *near-*

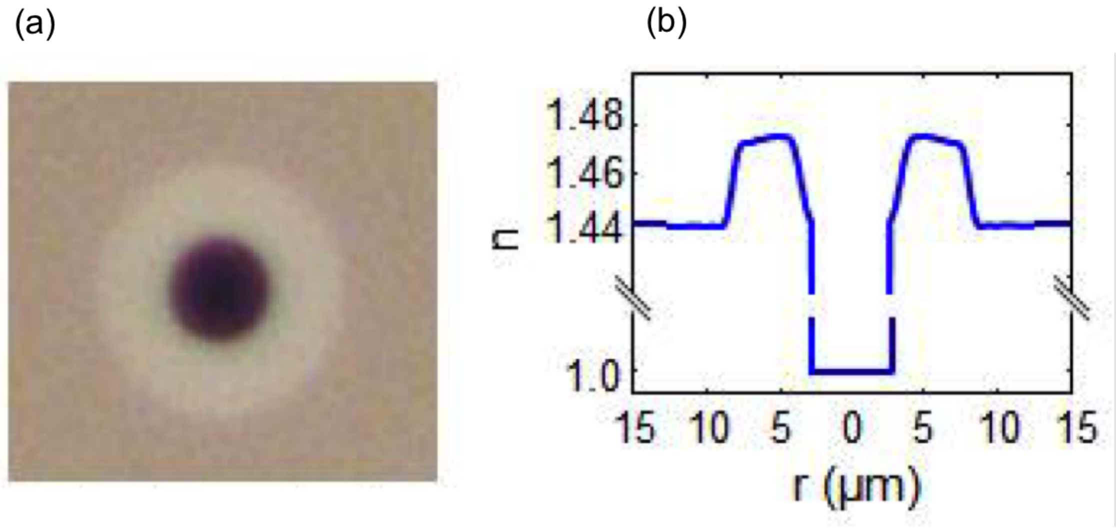

Figure 4.8: **(a)** Microscope image and **(b)** measured index profile for the air-core fiber. With permission from [9]. Copyright 2015 Optical Society of America

degeneracy among modes of the same group, or OAM states with the same $|\ell|$ (opposite orbital charges $+\ell$ and $-\ell$), though the state with OAM and SAM aligned remain degenerate with each other, but separate from those with OAM and SAM anti-aligned [9]. This fiber supports stable OAM modes with large $|\ell|$, with low sensitivity to be coupled in fiber bends.

4.3.1. Lifting the modal degeneracy of highest order modes

Practical communication distances have been achieved over fibers only for the special case of the lowest order $\ell = 1$ OAM states [3], however, ideally a multimodal system to multiplex modes should have a large number of states. There is a fundamental problem to exploit the infinite-dimensional basis allowed by OAM states because it is required a medium in which this modal degeneracy is addressed. This air-core fiber was conceived to face this problem because allows increasing the stable OAM modes.

We simulate this fiber using the finite element method implemented in Comsol 5.1®, by using a step index profile shown in Figure 4.8b to draw the waveguide structure. The full-structure was discretized by triangular elements of size smaller than the wavelength, and a perfect match layer (PML) of λ was used to truncate the computational domain after 48.75 μm. We compute the effective index as a function of the wavelength of light, and also obtain the modal field distribution of the propagated modes. We find up to 32 propagating modes including $TE_{0,m}$, $TM_{0,m}$ and hybrid modes $HE_{l+1,m}$ and $EH_{l-1,m}$, some are shown in Figure (4.9).

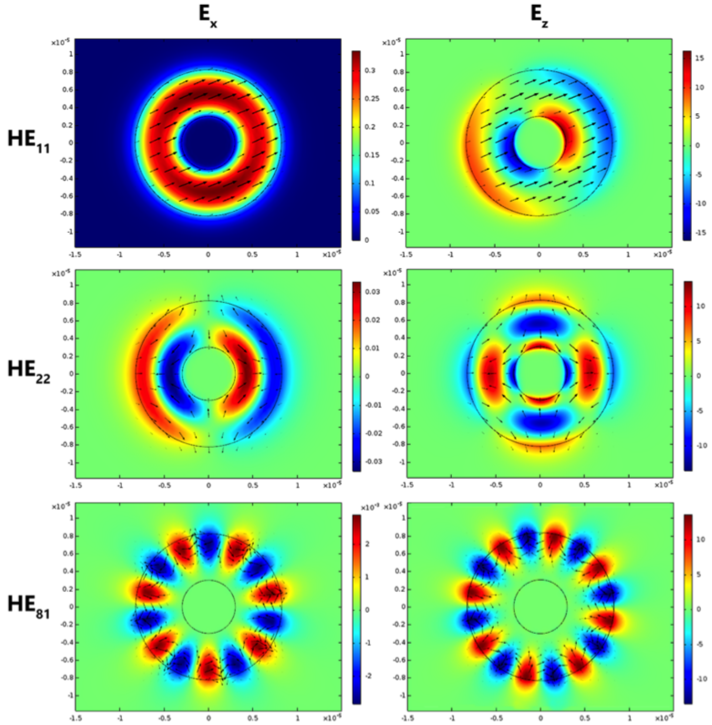

Figure 4.9: Vector modes propagate in the air-core vortex fiber. The fundamental mode HE_{11} is confined on the ring possessing a linear polarization. This fiber can support $HE_{m,2}$ modes with second radial order, like the mode HE_{22}. Also, it can support $HE_{m,1}$ modes of our interest to shape the OAM basis. This figure was made with the help of [12]

We find up to 16 OAM modes coming from $V^{+}_{l,m}$ and $W^{+}_{l,m}$, in a broad window wavelength from 1450 nm up to 1570 nm as shown in Figure 4.10a. We observe an n_{eff} splitting amongst highest order OAM states, which are *near-degenerate*. According to the phenomenological reasons described in the section (3.2) only OAM modes with $\ell = \pm 6, \pm 7, \pm 8$ are stable, since Δn_{eff} are large enough above 10^{-4} as shown by the red circles in Figure 4.10b, whose values are shown in Table 4.2. Below ℓ =6, for which OAM states are also supported, the n_{eff} splitting is too small and LP-like behavior is expected. This Δn_{eff} is slightly different from the already reported by [9], likely due to small changes in the simulated geometry, and core or cladding indices.

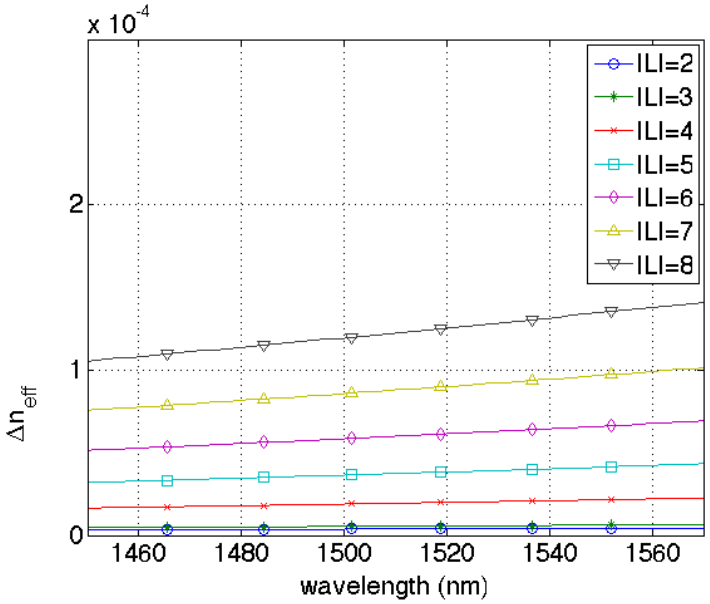

(a)Effective index as a function of the light wavelength - air core fiber

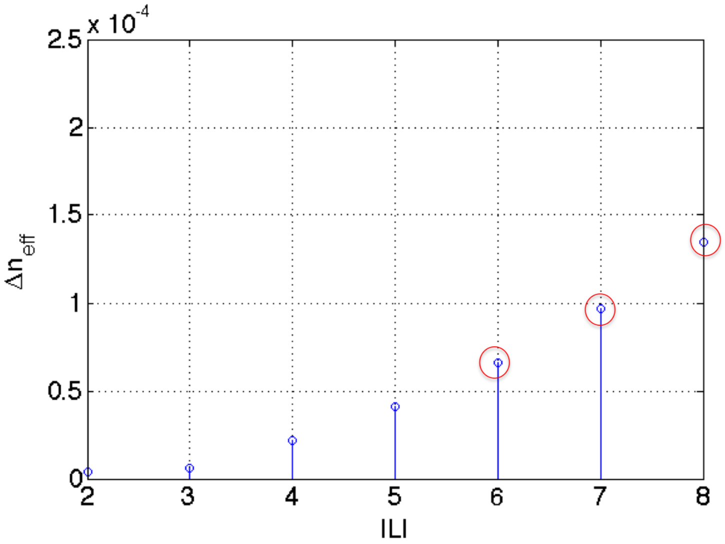

(b)Δn_{eff} vs. L=ℓ at a telecom wavelength of 1550 nm - air -core fiber

Figure 4.10: Effective index for OAM modes with $L = \pm\ell$ in an air core fiber. **(a)** Effective index difference as a function of light wavelength. **(b)** Effective index difference vs. $\pm\ell$ at a telecom wavelength of 1550 nm for the air-core vortex fiber. This figure was made with the help of [12].

Table 4.2: Effective index differences to assess the *degeneracy* among OAM modes. The differences were computed between OAM modes with opposite orbital charges $+\ell$ and $-\ell$, which means the same $\pm|\ell|$ ((+) indicates spin-orbit aligned, and (-) indicates spin-orbit anti-aligned)

Modes	Δn_{eff}
$OAM_{+6} - OAM_{-6}$	$\sim 0.65959x10^{-4}$
$OAM_{+7} - OAM_{-7}$	$\sim 0.96692x10^{-4}$
$OAM_{+8} - OAM_{-8}$	$\sim 1.3455x10^{-4}$
$OAM_{+8} - OAM_{7}$	$\sim 3.786x10^{-3}$
$OAM_{+7} - OAM_{6}$	$\sim 0.3073x10^{-3}$

OAM spatial phase distribution is presented in Figure 4.11. Each state possesses total angular momentum $\mathbf{J}$, which have orbital ℓ, and spin σ parts, that can be both positive or negative. Thus, 4 OAM states for every $|L| = |\ell|$ are expected. In Figure 4.11 we also show the OAM modes with orbital charges $\pm\ell$, which can be excited by a circular polarization $\pm\sigma$ (left or right handed), that represents the SAM, yielding in this case, 12 OAM states.

We also compute the modal dispersions obtained by a numerical implementation of the second derivative: $\partial^2\beta/\partial\omega^2$, using an own code in Matlab®. Figure 4.12 shows the modal dispersion for OAM modes with orbital charges of $\ell = 6, 7$. These values are very similar to already reported in [9]. Dispersion values at these wavelengths are in order of magnitude quite similar to the standard singlemode fiber (e.g. 18 ps/nm km at 1550 nm). This fact means that the OAM modes in this air-core vortex fiber can be used as channels in optical communication systems multiplexed by modes without troubles introduced by impairments associated with high dispersion values that limits transmission at hight-rates.

4.3.2. Accidental degeneracies

In order to increase the volume of OAM states, a large index contrast, and also an increase in the ring width are the most obvious alternatives. In this way, as mode volume is increased, the number of $m = 2$ modes increases too. In an ideal fiber,

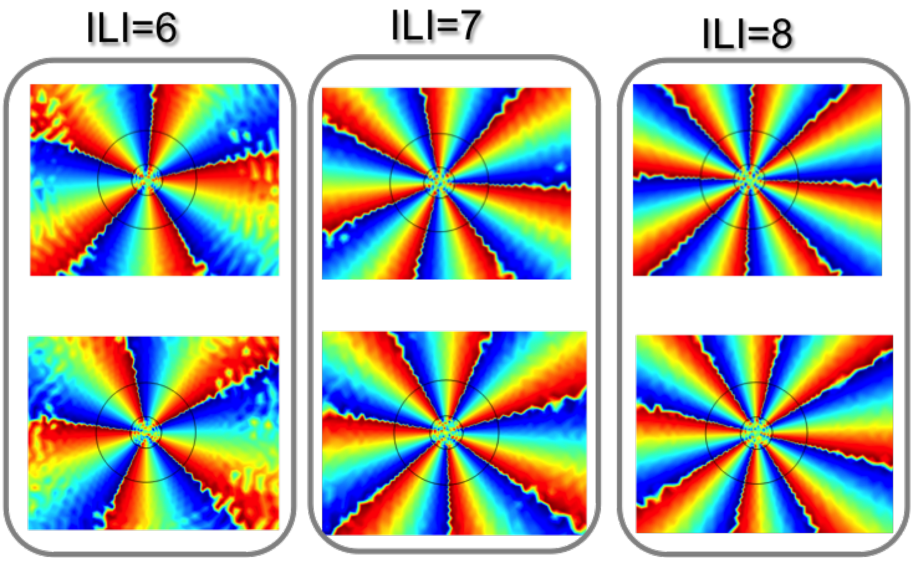

Figure 4.11: Stable OAM states propagated in the simulated air-core vortex fiber. Each SAM $\sigma = \pm 1$ produce two possible states for each OAM modes, yielding in this case up to 12 OAM states.

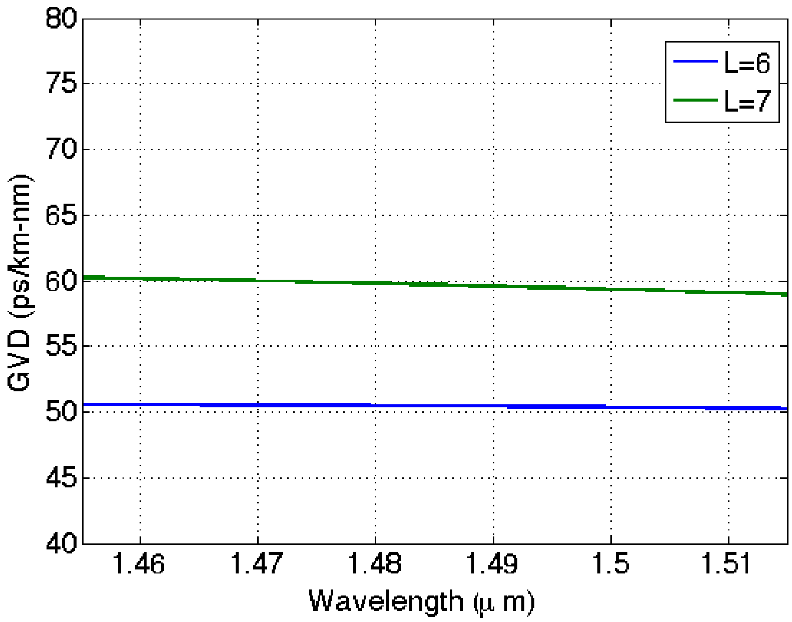

Figure 4.12: Modal dispersion for the ℓ=6, and 7 across C-band for the air-core fiber. See Ref [9]. This figure was made with the help of [12]

desired OAM states should come from hybrid modes $HE_{l+1,m}$ and $EH_{l-1,m}$ with any azimuthal order l, and with this condition: $(l, m) = (\ell, 1)$, which means only one radial order. Modes with higher radial number ($m > 1$) should be suppressed because they can lead to "*accidental degeneracies*" in which a mode with a number $(\ell, 1)$ may be degenerate with a mode with a number $(\ell, m > 1)$, over some wavelength range. Modes of different azimuthal symmetry have no anti-crossing that would prevent these accidental degeneracies. However, in particular, the modes of same azimuthal symmetry and different radial order could be easily coupled due to accidental degeneracies, as well as by the similarity of the field distributions, that leads to values of the overlap integral in equation (3.22) different from zero. This effect would destroy the fiber's ability to transmit higher-order OAM states with $m = 1$ over long distances.

An example of an "*accidental degeneracies*" between modes with radial order of $m = 1$ and $m = 2$ is shown in Figure 4.13 for the simulated air-core fiber, where we should be avoided the operation in regions in which the modes with $m = 2$ are closely spaced in n_{eff} to desired OAM modes with $m = 1$.

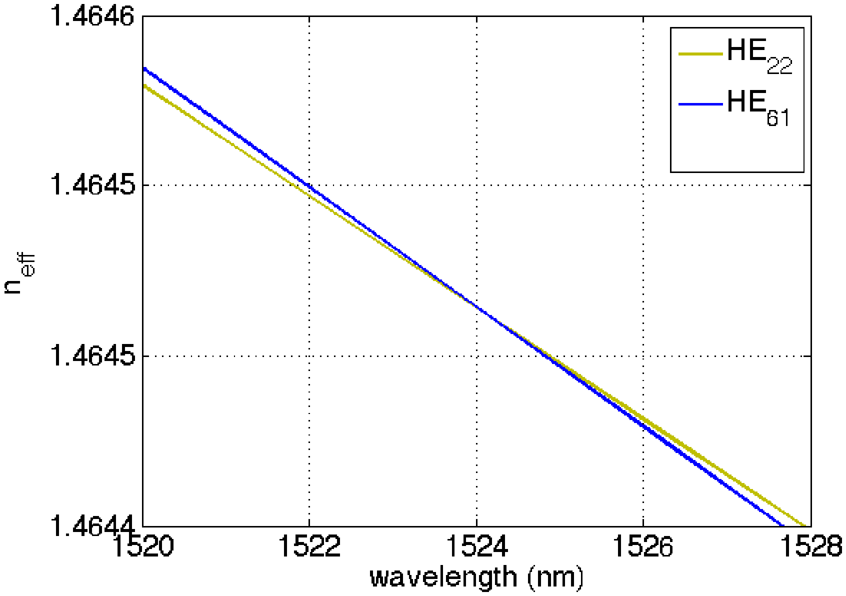

Figure 4.13: Accidental degeneracy between the (l,m)=(6,1) and (2,2) modes near to 1523 nm in the air-core vortex fiber. This figure was made with the help of [12].

The most apparently obvious design methodology for suppressing $m > 1$ coupling is to make a thin, higher contrast ring, for which the $m > 1$ states simply are not guided [9].

Although this alternative can be very efficient by inhibiting modes of $m > 1$, higher index contrast only is achieved either by including dopants as Germanium (Ge) in the ring, or Fluor (F) in the cladding respectively, which imply an increase in the fiber's loss. Alternatively, thinner rings lead to very confined fields and field gradients, which result in high scattering losses. Recent work has theoretically proposed such waveguide [73], and experimental work has claimed OAM propagation over a few centimeters length [60], likely due to high losses. On the other hand, high index contrast and a very thin ring lead to differences in electromagnetic continuity conditions between **s** and **p** polarized electromagnetic fields promoting the spin-orbit coupling, a fundamental effect that prevents km-scale OAM state propagation [13].

4.3.3. OAM Spectra

We compute by using an own code in Matlab® the *OAM spectra* for the air-core fiber simulated here. We consider fiber bend radii of 1 and 5 cm to obtain perturbed electric fields. As was shown for the solid vortex fiber, we also compute equation (3.24) for two unperturbed fields combining possible several cases and notice that in most of the cases it yields a value of above 120 dB, indicating again perfect orthogonality among the modes, or equivalently a mode of high purity.

The values of the Table 4.3 (in dB units) show that the coupling strength (OAM charge weight) increase as bending radii decrease. We stress that: (a) there are lower coupling strengths (less than -67 dB at a bend radius of 1cm) between anti-aligned ($W^{+}_{l,m}$) and aligned ($W^{+}_{l,m}$) OAM modes (modes with opposite orbital charges $+\ell$ and $-\ell$), which are highlighted by the color. (b): Otherwise, there are higher coupling strengths between pairs of anti-aligned ($W^{+}_{l,m}$) or aligned ($W^{+}_{l,m}$) OAM modes (modes with the same sign between their orbital charges $+\ell$ or $-\ell$) reaching values of up to -19 dB at a bend radius of 1cm. (c): In addition, a coupling strength around -0.01 dB at a bend radius of 5 cm (highlighted in gray), between OAM modes with the same orbital charge $+\ell$ or $-\ell$ shows that the propagation of the OAM modes is not affected by the bends. These results are in agreement with the already described in the subsection 3.2.2.

Table 4.3: *Spectra* of the air-core vortex fiber between OAM modes. Fiber was bent radii of **(a)** 5 cm and **(b)** 1 cm. Perturbed modes are in the first column

(a)Fiber bent with 5 cm

	ℓ_6	ℓ_7	ℓ_{-6}	ℓ_{-7}
ℓ_{-6}	-76	-83	-0.012	-32
ℓ_{-7}	-73	-91	-32	-0.010
ℓ_6	-0.012	-32	-78	-74
ℓ_7	-32	-0.010	-82	-93

(b)Fiber bent with 1 cm

	ℓ_6	ℓ_7	ℓ_{-6}	ℓ_{-7}
ℓ_{-6}	-83	-71	-0.29	-19
ℓ_{-7}	-60	-67	-19	-0.26
ℓ_6	-0.32	-19	-83	-59
ℓ_7	-19	-0.26	-67	-78

4.3.4. Spin-orbit coupling in air-core vortex fibers

High electric fields at the air-silica boundary cause spin angular momentum (SAM with left or right circular polarization, $\hat{\sigma}_{\pm}$) to couple with OAM, a form of spin-orbit interaction [13, 75]. An example of spin-orbit interaction can be observed in Figure 4.14 that compares the polarization structures of the $HE_{1,1}$ modes of "*low-contrast*" and "*high-contrast*" fibers. Both structures are ring fibers with a core radius of 16 μm and ring width of 4 μm; the low-contrast structure has a silica core and cladding, while the high contrast structure has an air-core. The black arrows show the polarization, which is by construction linear at each point in the space in a "*low-contrast*" fiber, and azimuthal in a "*high-contrast*" fiber. The red ellipses depict the polarization states of the superposition of $HE^{odd}_{l+1,m} + HE^{even}_{l-1,m}$, which give rise to spatially uniform circular polarization in the low-contrast case, but spatially varying elliptical polarization in the high contrast case [13].

The low-contrast example illustrates that when spin-orbit coupling is weak an external circularly polarized sources can be used to efficiently excite the OAM modes. Otherwise,

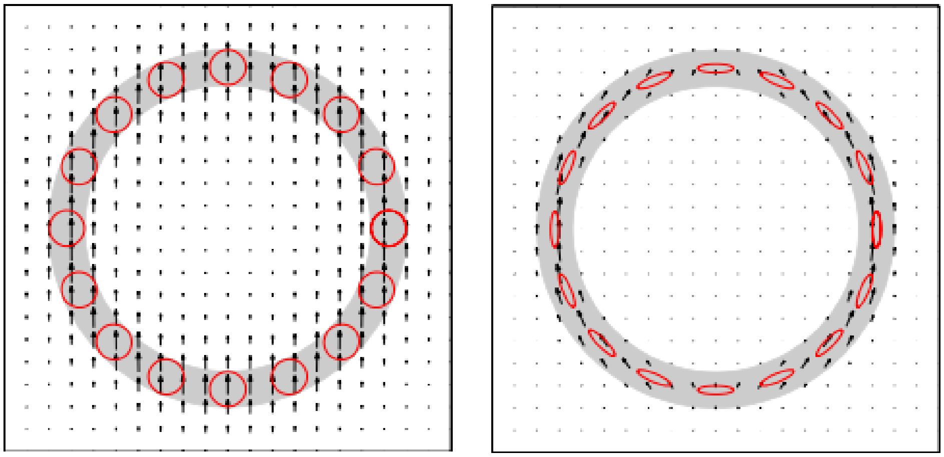
(a) (b)

Figure 4.14: Comparison between $HE_{1,1}$ fields of **(a)** low-contrast and **(b)** high-contrast fibers.©2014 IEEE. With permission [13]

when spin-orbit coupling is strong this effect prevents an efficient excitation of OAM modes with external circularly polarized sources.

This effect comes from the fact that the modes in an air-core fiber are not weakly guided, and have no direct counterpart in paraxial optics [13], therefore, orbital part $e^{i\phi\ell}$ and spin part $\hat{\sigma}_{\pm}$ are not decoupled anymore (see equations (3.10) and (3.11)). With high field amplitudes and index contrast, a full vectorial solution should be addressed. Then, for $|\ell| > 2$ OAM states can be written:

$$\overrightarrow{e_t;l} = \left\{ \begin{array}{l} e^{\pm(\ell+1)\phi} \cdot \left[e_{r;\ell,AA}(r)\hat{r} \mp i e_{\phi;\ell,AA}(r)\hat{\phi} \right] \cdot e^{i\beta_{L,AA}} \cdot z \\ e^{\pm(\ell+1)\phi} \cdot \left[e_{r;\ell,A}(r)\hat{r} \mp i e_{\phi;\ell,A}(r)\hat{\phi} \right] \cdot e^{i\beta_{L,A}} \cdot z \end{array} \right\} \tag{4.6}$$

where r and ϕ are the radial and azimuthal unit vectors, and e_r and e_ϕ are the field amplitudes in the corresponding directions. AA is spin-orbit anti-aligned states (sign of SAM and OAM opposite), and A is spin-orbit aligned states (sign of SAM and OAM being the same). Under paraxial and weakly guided approximation, OAM fields were described with an uniform (circular) polarization (see equations (3.10) and (3.11)), but using a full-vectorial solution the fields are spatially non-uniform, with an ellipticity $| e_\phi/e_r|$, as shown in Figure 4.15, where in the paraxial case this ratio approaches unity, exhibiting again uniformly polarized fields [14]. Figure 4.15 shows the field distribution for an $|\ell| = 2$ spin-orbit (SO) aligned (A) as well as spin-orbit (SO) anti-aligned (AA) modes.

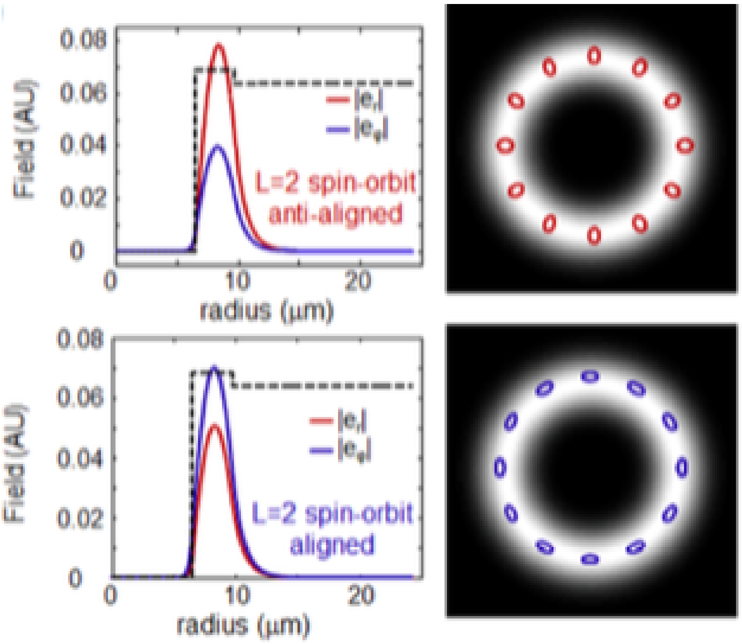

Figure 4.15: 1D and 2D plots of the electric field of the $|\ell| = 2$ states for the SO aligned and SO anti-aligned fields of a simulated air-core fiber with an air-core radius of 6.5 μm, ring width of 3.25 μm and index contrast $n_{ring} - n_{cladding} = 0.04$. Unequal radial and azimuthal field component yield a spatially varying elliptical polarization state. With permission of [14]. Copyright 2015 Optical Society of America

Lower ℓ -state are more likely to experience spin-orbit coupling, due to the larger $n_{air} - n_{ring}$, and consequently tend to be more TE orTM like, exhibiting azimuthal (TE case) and radial (TM case) polarizations (see Figure 4.16) [14, 75].

Note that the SO aligned modes are almost azimuthally polarized, while the anti-aligned modes are almost radially polarized. Then the equation (4.7) may also be rewritten as:

$$\overrightarrow{e_t;l} = \left\{ \begin{array}{l} e^{\pm(\ell-2)\phi} \cdot e_{r;\ell,AA}(r) \cdot \\ \frac{1}{2}\left[\hat{\sigma}^{+} e^{i\phi}\left(1 \mp \left|\frac{e_{\phi;\ell,AA}(r)}{e_{r;\ell,AA}(r)}\right|\right) + \hat{\sigma}^{-} e^{i\phi}\left(1 \pm \left|\frac{e_{\phi;\ell,AA}(r)}{e_{r;\ell,AA}(r)}\right|\right)\right] \cdot e^{i\beta_{L,AA}} \cdot z \\ \\ e^{\pm(\ell+2)\phi} \cdot e_{r;\ell,A}(r) \cdot \\ \frac{1}{2}\left[\hat{\sigma}^{+} e^{i\phi}\left(1 \pm \left|\frac{e_{\phi;\ell,A}(r)}{e_{r;\ell,A}(r)}\right|\right) + \hat{\sigma}^{-} e^{i\phi}\left(1 \mp \left|\frac{e_{\phi;\ell,A}(r)}{e_{r;\ell,A}(r)}\right|\right)\right] \cdot e^{i\beta_{L,A}} \cdot z \end{array} \right\} \qquad (4.7)$$

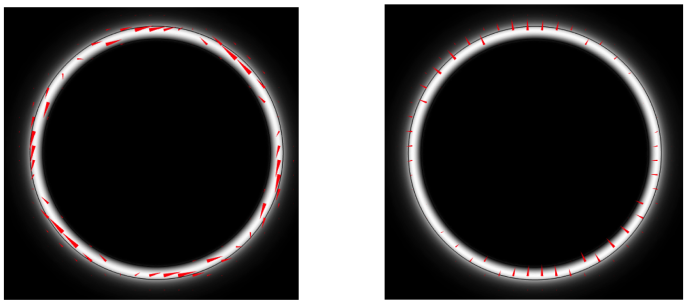

(a)ℓ=+2. Azim shape (b)ℓ=-2. Radial shape

Figure 4.16: 2D plots of the electric field of $|\ell| = 2$ states for the **(a)** SO aligned that yields a TE-like (azimuthal) electric field, and **(b)** SO anti-aligned that yields a TM-like (radial) fields of a simulated air-core fiber with an air-core radius of 25 μm, ring width of 2.5 μm and index contrast $n_{ring} - n_{cladding} = 0.02$.

in terms of the separable component of the polarization $\hat{\sigma}_{\pm}$, where we can observe that OAM modes have an extra component with $\ell = \pm 2$, which means that for OAM modes with the same **J**, and in non-paraxial regime a spin-orbit coupled pair with $|\ell|= 2$ can exist. This fact could lead to an increase in the OAM basis by joining the conventional OAM eigenmodes with their spin states AA and A, and spin-orbit coupled eigenmodes (i.e., with $|\ell|= 2$) showed in equation 4.7. This effect was already used as an alternative increasing the number of available OAM state in air-core fibers [75]. However, this implies an external decoupling between OAM states by using external processing like MIMO-DSP. This is another reason why high index contrasts in this kind of fibers, and thinner rings are not feasible alternatives to increase the number of available OAM states in vortex fibers. For this, we propose in this doctoral work to use metamaterials as a new alternative to achieve more uncoupled OAM states and increasing of OAM states as well.

5. DESIGN OF A METAMATERIAL-BASED VORTEX FIBER

The results of the last section are our starting point. We use the geometry and the index profiles of both all solid and air-core vortex fibers, and we will demonstrate that by replacing the silica-cladding with a metamaterial but preserving ring width, it is possible to reach a better performance. The goal is to try to increase the number of stable OAM modes with $m = 1$, as well as the effective index differences between modes in a *near-degenerate group*, and also reduce the number of OAM modes with $m > 1$ by preserving the ring width to avoid the phenomena of spin-orbit coupling. In addition, high index contrast between the ring and cladding that leads to high losses in this class of fiber should be avoided too. This trade-off seems to be still one of the open problems to be tackled in the scientific community, and our proposal consists in using metamaterials to achieve this goal. In the following subsections, we describe its advantages in the change of the modal behavior in photonic structures, and in the reduction of modal bending loss compared to other options like increasing the index contrast, bandgap effect, and nanoscaled slots. Finally, we show the results of our designs of vortex fibers using an anisotropy-engineered dielectric metamaterial.

5.1. ANISOTROPY-ENGINEERED DIELECTRIC METAMATERIAL

Metamaterials seek to extend conventional materials by using artificially designed and fabricated structural units with the required effective properties and functionalities. The central guiding principle in all metamaterials consists of fabricating a medium composed of unit cells far below the size of the wavelength. The unique resonances of the unit cell based on its structure and material composition as well as coupling between the cells lead to a specific macroscopic electromagnetic response [15]. These nanostructures have been optimized to achieve a range of exotic electromagnetic responses, including negative magnetic permeability (magnetic metal, $\mu < 0$) [76], negative refractive index ($n < 0$) [77], zero refractive index ($n \sim 0$) [78], optical chirallity [79, 80], and hyperbolicity [81].

Recently, however, metamaterials composed of dielectric structures, completely *transparent building blocks* in which light does not couple to plasmons or optical phonons, have been demonstrated to achieve all four quadrants of electromagnetic responses: $\epsilon > 0$, $\mu > 0$; $\epsilon < 0$, $\mu > 0$; $\epsilon > 0$, $\mu < 0$; $\epsilon < 0$, $\mu < 0$, where ϵ is electric permittivity showed in Figure 5.1.

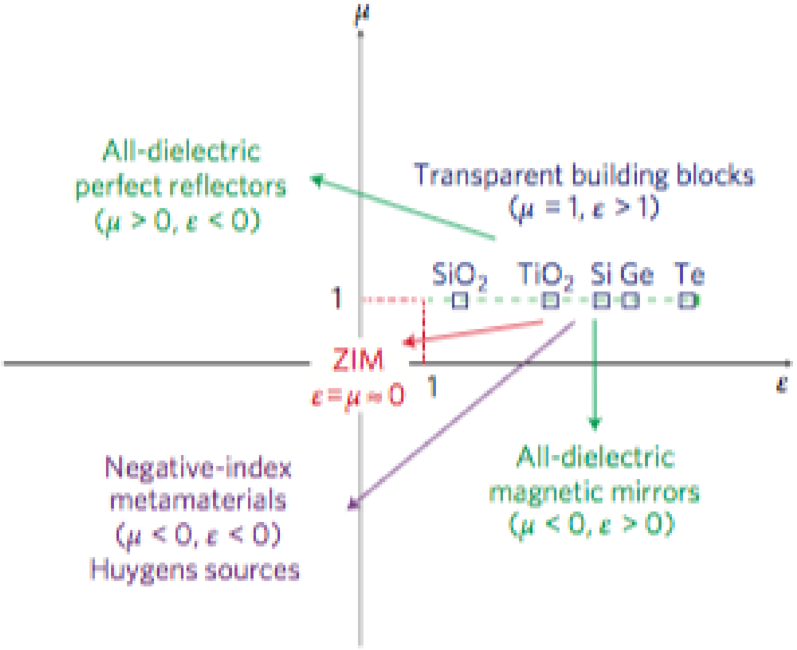

Figure 5.1: Electric permittivity ϵ and magnetic permeability μ form four quadrants that represent the entire range of the isotropic electromagnetic response. All four quadrants can be covered by designing specific all-dielectric metamaterials. ZIM is zero-index material. With permission from Macmillan Publishers Ltd. [15]. Copyright 2016

Dielectric photonic waveguides can be classified according to two fundamental principles governing them, one that utilizes the large index contrast between media to confine light within nanoscale slots [82, 83], and another that uses Bragg reflection of waves int the bandgap photonic crystal [84, 85]. The waveguide modes in the latter are not scattered at sharp bends and they can be confined within low index core.

A new approach that consists of dielectric metamaterials used as cladding or substrate fabricated in transparent building blocks of SiO_2, TiO_2, Si, Ge, Te (see the first quadrant showed in Figure 5.1) have recently been proposed as an alternative to light confinement at the nanoscale [17], and selective confinement of modes in optical waveguides (it was demonstrated by us in [86]).

Another unique aspect of all-dielectric metamaterials lies in the large amount of possibilities for engineering the anisotropy of the media. Unlike natural materials, where the difference between principal refractive indices for the two possible polarizations (extraordinary and ordinary) rarely exceeds 10%, all-dielectric metamaterials can be engineered to have much higher index contrast [17].

The use of dielectric metamaterials as cladding or substrate rely on controlling the optical momentum of evanescent waves to manipulate propagating waves. The control of evanescent waves is explained in [87] by means of the relaxed total internal reflection (TIR). This phenomenon is governed by Snell's law and occurs when an optical ray traverses a flat interface between two different isotropic dielectrics, light is partly reflected back to the first medium and refracted in the second medium. If $n_1 > n_2$ ($n_{1,2}$ the refractive index of the two dielectrics) and the incident angle is greater than the critical angle ($\theta_c = \sin^{-1}(n_2/n_1)$), light is totally reflected back to the first medium and evanescently decays in the second medium (See Figure 5.2a)

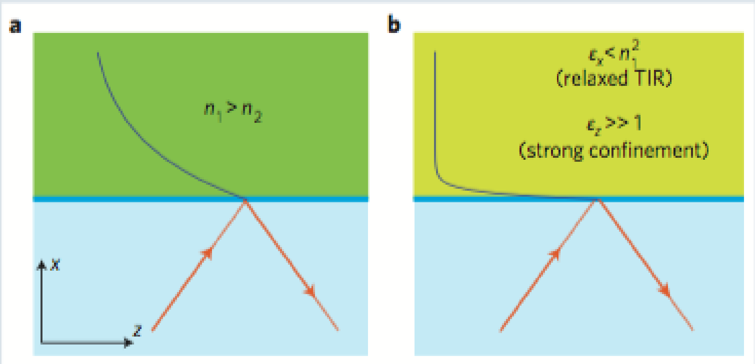

Figure 5.2: **a** TIR in an isotropic medium. **b** Relaxed TIR in an anisotropic medium. With permission from Macmillan Publishers Ltd. [15]. Copyright 2016

However, if the second medium is anisotropic and the incident light is p-polarized like in the case of the the transverse magnetic (TM) mode in a planar waveguide, the TIR condition is reduced to $n_1 > n_{2x}$, a condition called relaxed TIR because it leaves a degree of freedom to choose the refractive index in the other direction [17, 87]. By increasing the refractive index in the parallel direction ($n_{2z} \gg 1$), it is possible to control the momentum and skin depth of the evanescent waves in the second medium [16]:

$$k_{2x}^{\perp} = \frac{n_{2z}}{n_{2x}} \sqrt{(k_0 n_{2x})^2 - (k_z^{\parallel})} \tag{5.1}$$

where $k_z^{\parallel} = n_1 k_0 \mathrm{sin}\theta$ is the tangential momentum of light and θ is the incident angle. Increasing n_{2z}/n_{2x} gives rise to reduced skin-depth in the second medium (See Figure (5.2)b), where $n_{2x} < n_1$ to satisfy TIR condition. Note that n_{2z} can be even greater than n_1, achieving strong confinement for $n_{2z} \gg 1$. Thus, by increasing the anisotropy of the cladding, it is possible to change the modal behavior in any waveguide (circular or square) by controlling evanescent waves through transforming the momentum of light [16]. Claddings with strong anisotropy can be engineered using lossless all-dielectric blocks using the materials showed in Figure 5.1.

A detailed explanation using full analytical mode calculations of 1D, 2D waveguides is provided in the supplementary material in [17]. We stress in two points: (a) in a 1D planar waveguide the TM mode is affected by the presence of the anisotropy-engineered dielectric metamaterial, while TE modes are not, and for the TM mode the electric field component E_z decreases while E_x increases in the core, indicating high confinement; (b) in a 2D circular waveguide the first HE_{11} or fundamental mode can propagate without cut-off if $\epsilon_z > \epsilon$, and becomes a quasi-transverse electromagnetic mode (TEM), also E_z and H_z components of hybrid modes $HE_{l+1,m}$ and $EH_{l-1,m}$ decrease by increasing ϵ_z, so high confinement is expected. These points imply that the enhanced confinement and the changes in the modal behavior (i.e. slow light, reduction of bending loss, reduction of mode coupling, increase of the number of modes, etc) do not require a high effective mode index, in contrast to the conventional approach. Therefore, substrate or cladding fabricated in anisotropy-engineered dielectric metamaterials provide a novel strategy by means of an additional degree of freedom: controlling evanescent field momentum, that would enable mode matching in photonic devices and fibers.

As an example, let us consider an optical waveguide in silicon, which at optical communication wavelength around 1550 nm has the highest refractive index among lossless dielectrics. Thus, it is widely accepted that the silicon core surrounded by vacuum (highest index contrast) is the best waveguide to confine light better than silicon surrounded by any other lossless material (Figure 5.1a). However, if we surround the silicon core with an anisotropy-engineered dielectric metamaterial as demonstrated in Figure 5.3b, the waveguide can confine the fundamental mode HE_{11} better than silicon-vacuum waveguide. To satisfy relaxed TIR condition, we should have $\epsilon_x = \epsilon_y < \epsilon_{Si}$ for strong confinement, and ϵ_z should be as large as possible, therefore it is demonstrated that claddings of high anisotropy are better in terms of confinement than vacuum [16].

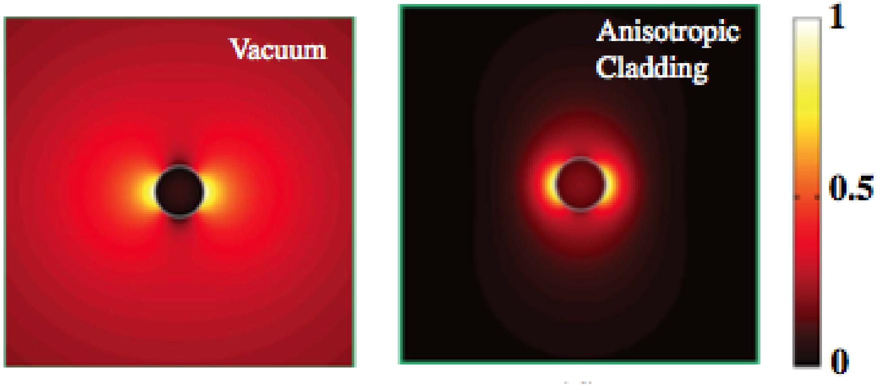

(a) (b)

Figure 5.3: **(a)** The x-component of the electric field of HE_{11} mode for silicon-air waveguide. The core radius is $r = 0.07\lambda$. Less than 2% of the power is confined inside the silicon core. **(b)** The x-component of the electric field of HE_{11} mode for the same waveguide surrounded by an anisotropic cladding $\epsilon_x = \epsilon_y < \epsilon_{Si} = 1.2$ and $\epsilon_z = 12$. The cladding helps to confine up to 30% of the total power inside the core, and also HE_{11} mode becomes in TEM. With permission from [16]. Copyright 2015 Optical Society of America

5.1.1. Practical realization of all-dielectric metamaterials of anisotropy-engineered

We can realize anisotropic metamaterials by artificially structured media using available lossless dielectrics. One practical way is embedding periodic thin high index nanorods of a subwavelength size in a low index host dielectric, or visceversa, thin nanorods of air embedded into a high index dielectric [18], as Figure 5.3 shows.

The periodicity is much lower than the operating wavelength to ensure that the structure behaves as a homogeneous material and it is far away form its band-gap. Metamaterial cladding in Figure 5.4 can be accurately described by an effective refractive index,

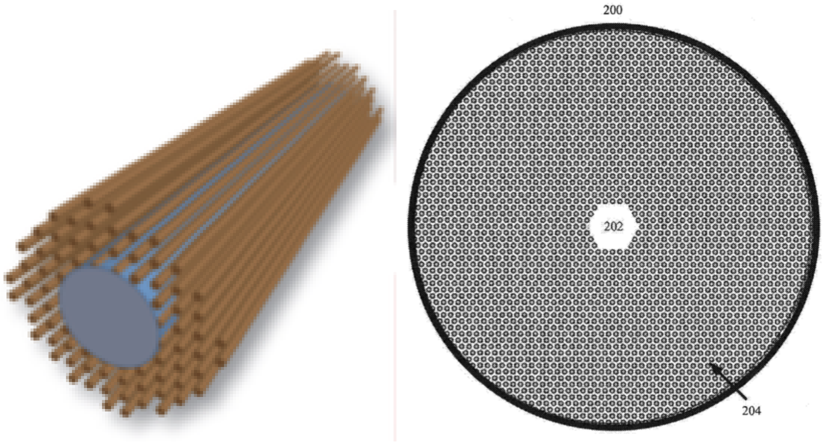

(a) (b)

Figure 5.4: An example of a metamaterial cladding consisting of **(a)** high index nanorods embedded in low index dielectric. With permission from [17]. Copyright 2014 Optical Society of America. **(b)** low index nanorods, may be air holes, embedded in high index dielectric. With permission from [18] USPTO©

which is independent of the periodicity and is calculated using the Maxwell-Garnett approximation. Effective relative permittivity normal $\epsilon_\perp$ and parallel $\epsilon_\parallel$ to the nanorods axes for sub-wavelength conditions in an uniaxial configuration is [17]:

$$\epsilon_\parallel = \rho\epsilon_d + (1-\rho)\epsilon_h \tag{5.2}$$

$$\epsilon_\perp = \frac{(1+\rho)\epsilon_d\epsilon_h + (1-\rho)\epsilon_d\epsilon_h}{(1-\rho)\epsilon_d + (1+\rho)\epsilon_h} \tag{5.3}$$

where ϵ_d and ϵ_h are permittivity of the dielectric nanorods and host, respectively, and ρ is the fill-fraction of a nanorods in its unit-cell of the proposed cylindrical waveguide.

We adopt the telecom wavelength 1550 nm in the design of our metamaterial cladding. We decide to use air holes ($\epsilon_{air} = 1$) inside silica ($\epsilon_{silica} \sim 2.07$) in order to simplify the fabrication process [18], as well as achieve low propagation loss in long lengths. However, any couple of materials could be used to design a cladding of metamaterial as was shown in the first quadrant in Figure 5.1 to the case of using transparent material blocks, or other materials as is shown in the proposal of [88–90].

5.1.2. Fabrication Techniques

A method of manufacturing the optical fiber with a cladding of metamaterial is described in [18]. This is based on the construction of successive performs to split and join smaller segments to finally built the metamaterial. In some preforms, the rods used within the preforms may be hollow, and the preform may be fabricated using bonded glass capillaries. In this case, the hollow regions are subwavelength in diameter. The fabrication steps are sketched in Figure 5.5). In order to fabricate our cladding, we can use bonded glass capillaries of silica to shape our metamaterial.

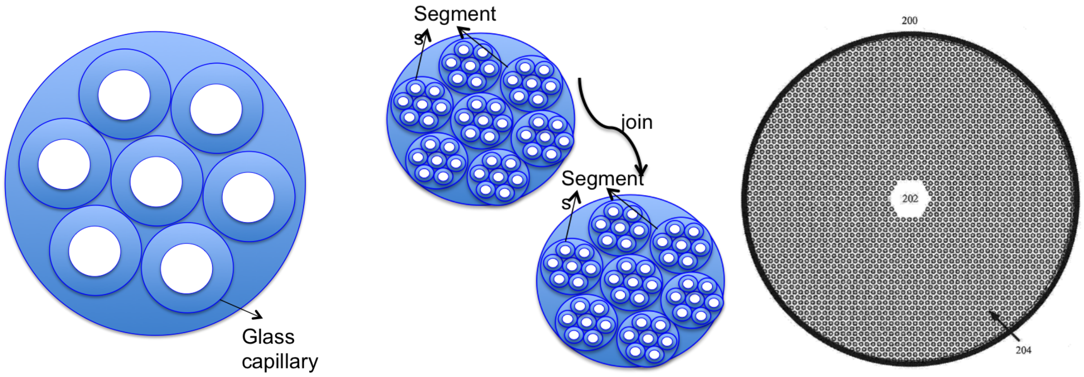

(a) (b) (c)

Figure 5.5: **(a)**The first fiber preform that consists of bonded glass capillaries of silica into a glass (also silica) substrate to produce a first optical fiber. **(b)** The second fiber preform comes from the first optical fiber that was divided into segments and then are assembled to shape the metamaterial. **(c)** Fiber with a cladding in metamaterial using the fabrication process of **(a)** and **(b)**. **(c)** is used with permission from [18] USPTO©

This fabrication technique could be used to produce an OAM fiber with either a solid core (section 4.2) or an air-core (section 4.3), and a cladding with metamaterial. In this particular, the metamaterial cladding can be performed in a multistep process that involves the creation of two sets of optical fiber configurations [18] (see Figure 5.5b). Metamaterial cladding with a desired size can be assembled enclosing the OAM core (solid or air). In some claddings, the lattice may be a regular hexagonal array, a rectangular array, or other regularly shaped array. We adopt a spatial pattern of a multilayer order to conserve circular symmetry following the pixelated configuration described in [91], however, any configuration adopted does not affect the homogenization provided by effective refractive index approximation.

Based on this fabrication process, we report a numerical study on OAM optical fibers with fine inclusions of air holes inside the cladding. We refer to such fibers as a metamaterial optical fiber, which can conceptually be considered as an extension from the previously published microstructured optical fibers [85], and pixelated fibers [91].

Cladding metamaterials can have optical properties not obtainable in naturally existing bulk materials, including artificial anisotropy as well as graded material properties. Therefore, incorporation of metamaterials in optical fiber designs can produce a new range of fiber properties [92,93]. Particularly here, we will show how certain propagation modes can be achieved in an OAM fiber, and also how they can change the fiber's modal behavior with the help of a cladding of metamaterial. We emphasize that we decide to use a cladding of metamaterial instead of a microstructure cladding with large holes, because our simulations show that in the latter there is a high birefringence between the even and odd solutions of the highest order modes, inhibiting in this manner the propagation of OAM modes. Therefore, we will show the results of the full-structure calculation in order to get more realistic results to propose a producible sample.

5.2. DESIGN OF A SOLID-CORE VORTEX FIBER WITH ANISOTROPY-ENGINEERED METAMATERIAL CLADDING

In this subsection, we describe the performance of a solid-core vortex fiber with anisotropy-engineered metamaterial cladding through numerical analysis in Comsol 5.1®. Several simulations were implemented varying the size of the hole into the cladding order to reach a cladding configuration to split even more the vector modes of the group of the first order LP_{11}. Figure 5.6 shows an image of one of those possible configurations, now replacing the conventional cladding in silica by a cladding in a metamaterial that consists of multilayered arrays of air holes into the silica. This configuration in multilayer with small holes parallel to the concentric rings was chosen in order to avoid likely birrefringence for high order modes, which were observed for other of configurations, like hexagonal microstructure or and in some cases with larger holes. Following the suggestion in [16], we find out that 8 alternated layers are enough to obtain our desired solution. The core of this fiber have a size $r_{co} + D_1 + D_2$, and its index profile follows the distribution presented in [3, 11] or Figure 4.2.

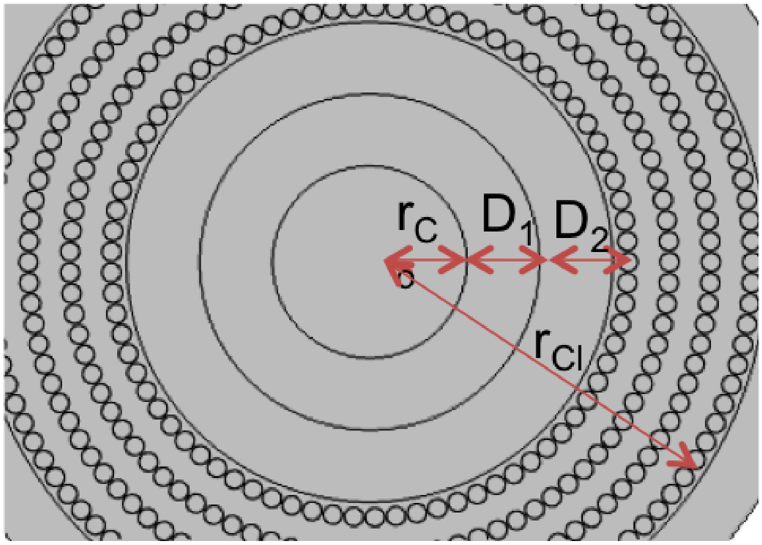

Figure 5.6: Comsol 5.1® image of the transverse section of a solid-vortex fiber with anisotropy-engineered claddng

Table 5.1 shows the geometric parameters of the chosen configuration. The full-structure was discretized by triangular elements of a size smaller than the wavelength, and a perfect match layer (PML) of 1 μm was used to truncate the computational domain after 52.5 μm.

Table 5.1: Geometric parameters of the full structure shown in Figure 5.1

Parameters	Name	Value
r_{cl}	Cladding radii	15.75 μm
r_{co}	Core radii	1.6 μm
D_1	Trench width	1.2 μm
D_2	Ring width	1.2 μm
N	Number of layers	8
d	Air-hole diameter	0.31 μm
L	Distance between successive holes	0.34 μm
D_l	Distance between successive layers	0.68 μm

We compute the effective index as a function of light wavelength, and the modal field distribution of the propagated vector and OAM modes. Similarly to the conventional solid vortex fiber, our proposed fiber also propagates the two polarizations of the fundamental mode HE_{11} (denoted LP_{01} in the scalar approximation), and the modes $HE_{21}^{even,odd}$, TM_{01}, TE_{01} belonging to the first mode group LP_{11}.

Based on the geometric parameters of the full-structure, we can apply the homogenization approach given by equations (5.2) and (5.3) as is shown in Table 5.2. Note that the air-hole diameter is only one order of magnitude less than the wavelength, in order to relax the fabrication process.

Table 5.2: Equivalent parameters obtained from homogenization approach of the full-structure applied for our proposed solid-vortex fiber with metamaterial cladding

Parameters	Value
$n_{x,y}$ or $n(r)$	1.232
n_z	1.309
ρ	0.3

We expect that the anisotropy-engineered index profile for the cladding inhibits, even more, the near-degeneracy between the modes of the first group ($OAM_{\pm 1}$ group). This is because $\epsilon_{x,y}$ (proportional to the transverse component of the index $n(r)$, or $n_{x,y}$) are lower than ϵ_{silica}, promoting a change in the modal behavior of the structure by maximizing the index contrast between the cladding and ring, which is a requirement according to the theory described in the section 4.1. In this case, a modal change is manifested by increasing the index separation between the modes within the same group. In addition, we also expect a small reduction of the z-component of electric or magnetic fields of the hybrid modes $HE_{l+1,m}$ and $EH_{l-1,m}$ due to the confinement promoted by the anisotropy of the metamaterial, bringing as consequence a reduction in the bending loss of the modes propagated into the ring of the vortex fiber (see [86]).

5.2.1. Lifting of the $OAM_{\pm 1}$ degeneracy, and reduction of the HE_{11} bending loss

In order to check the hypothesis mentioned above, we compared the results already obtained for the conventional solid vortex fiber with respect to our proposal. We find out a separation of 1×10^{-2} (at 1550 nm) with respect to the fundamental HE_{11} mode for our proposal, which is almost one order of magnitude higher with the value of 3×10^{-3} obtained for a conventional vortex fiber (see again Figure 4.3a), that is now inserted in Figure 5.7. Also, a separation of 8.5×10^{-4} between nearest neighbor first order modes is higher than the reported for the conventional solid vortex fiber, which means a lifting in the degeneracy of the $OAM_{\pm 1}$ group (see again Figure 4.3b), that is now inserted in Figure 5.8.

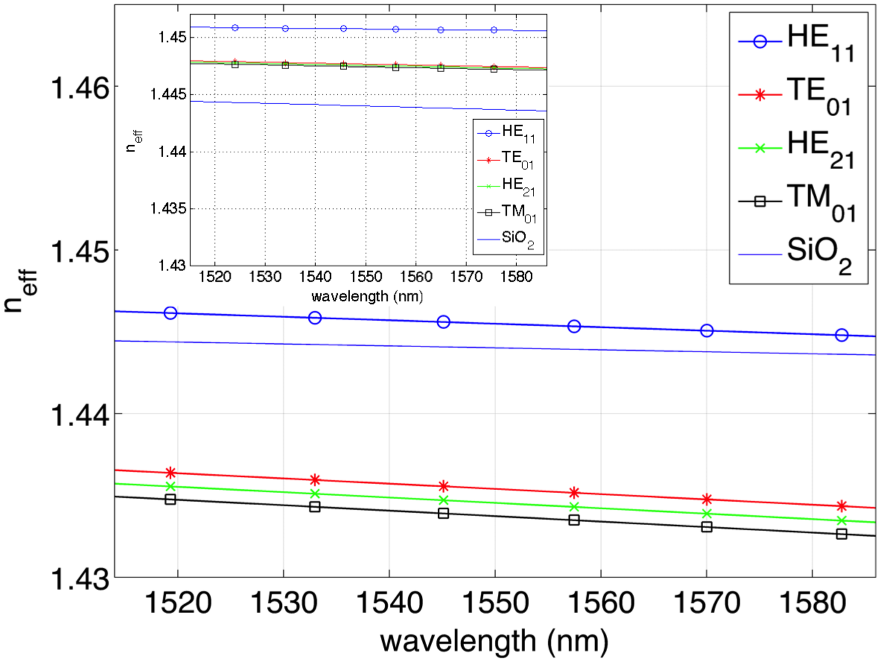

Figure 5.7: Numerically computed effective index as a function of light wavelength for the modes propagated in the solid-vortex fiber with the cladding of metamaterial (our proposal). Figure inset shows the results for the conventional solid-vortex fiber dk110OD105. This figure was made with the help of [12]

Regarding the intensity and phase distribution profiles of the OAM_0 and $OAM_{\pm 1}$, this is very similar to the profiles shown in Figure 4.4 and 4.5 for the conventional solid vortex fiber. We also stress that an increase in the effective index difference means a better performance of the fiber due to a likely reduction of mode coupling for longer lengths as was explained in subsection 3.2. Mode coupling strength will be quantified by means of the *spectra* (see subsection 5.2.2).

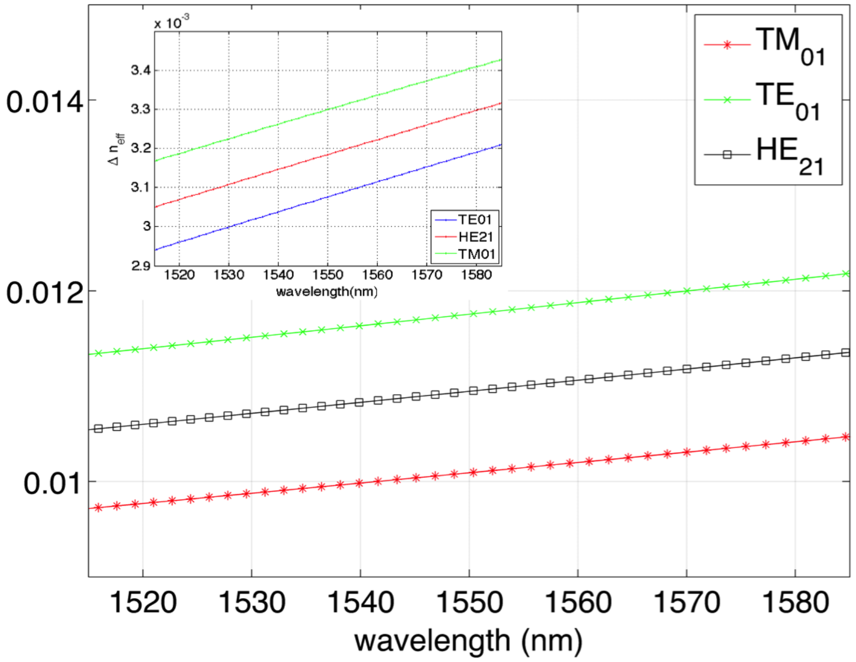

Figure 5.8: Numerically computed effective index difference as a function of light wavelength for the modes propagated in the solid-vortex fiber with the cladding of metamaterial (our proposal). Figure inset shows the results for the conventional solid-vortex fiber dk110OD105. This figure was made with the help of [12]

Besides, we observe a higher modal confinement, which is the relation between the power into the core divided by the total power into the fiber (P_{core}/P_{total}), also know as the confinement factor (CF)) for the HE_{11} y-polarized mode in the solid vortex fiber of metamaterial cladding, and negligible bending loss (approximately 0 $dB/90^o$) at lower bending radius as is shown in Table 5.3.

Note that in the conventional solid vortex fiber the HE_{11} y-polarized is not propagated for bending radius (BR) less than 1 cm (see Table 5.4). This phenomenon is quite similar to what happens in the strip and channel optical waveguides in SOI platform, in which the quasi-TE mode (approximately x-polarized) is less sensitive to bending loss than the quasi-TM mode (approximately y-polarized).

The authors have proposed a novel configuration that uses uniaxial metamaterials to confine and reduce the bending loss of the quasi-TM mode in the strip and channel optical waveguides [86]. In our case, the proposed metamaterial cladding (also uniaxial

Table 5.3: CF for HE_{11} y-polarized mode as a function of the bending radius (BR) for the solid vortex fibers. The second column shows the CF for the HE_{11} y-polarized in the solid vortex fiber with a cladding of metamaterial of anisotropy-engineered (our proposal), and the third column shows the CF for the HE_{11} y-polarized in the conventional solid vortex fiber.

BR	CF HE_{11} y-pol (our proposal)	CF HE_{11} y-pol (conventional)
0.1 cm	99.32%	It's not propagated
0.5 cm	99.70%	It's not propagated
1 cm	99.71%	61.57%
5 cm	99.71%	62.87%

type) yields a similar effect by confining the $HE_{1,1}$ y-polarized mode (analogous to quasi-TM mode y-polarized) in this vortex fiber.

As was shown for the conventional solid-core vortex fiber, we also obtain the radial electric field $E(r)$ for the HE_{21} mode, for the solid-core vortex fiber with metamaterial (our proposal), (see Figure 5.9b). We compare both, finding out that there are a high mode intensities close to the waveguide transition regions (boundaries), maximizing $\frac{\partial E(r)}{\partial r}$, as well as, maximizing $E(r)$ over the high index ring. These conditions are satisfied in our proposal too, which are necessary produce a split between the vector modes of the first group LP_{11} as was described in section 4.1.

5.2.2. OAM Spectra

We compare the mode coupling strength of this fiber with the anisotropy-engineered cladding with respect to the values obtained for the conventional OAM solid vortex fiber through the OAM *spectra.* We consider a bend radius of 2 and 5 cm to obtain the perturbed electric fields.

As was shown for the conventional fibers of solid and air-core, we compute equation (3.24) for two unperturbed fields combining possible several cases, and notice that in most of the cases it yields a value of -120 dB, indicating a perfect orthogonality between the modes, or equivalently a mode of high purity.

Table 5.4: Evolution of the HE_{11} y-polarized mode (modulus of Poynting vector) as a function of the bending radius (BR). The second column shows the evolution of the HE_{11} y-polarized in the solid vortex fiber with a cladding of metamaterial of anisotropy-engineered (our proposal), and the third column shows the evolution of the HE_{11} y-polarized in the conventional solid vortex fiber.

BR	HE_{11} y-pol (our proposal)	HE_{11} y-pol (conventional)
0.1 cm	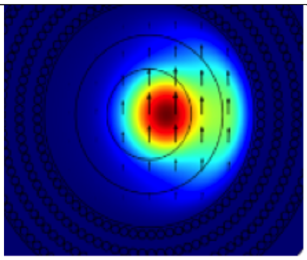	It's not propagated
0.5 cm	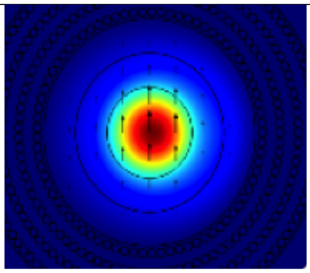	It's not propagated
1 cm	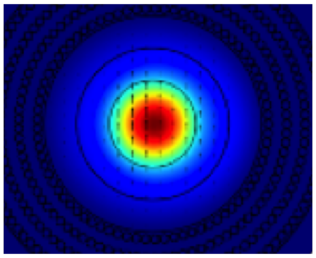	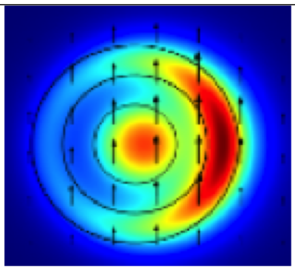
5 cm	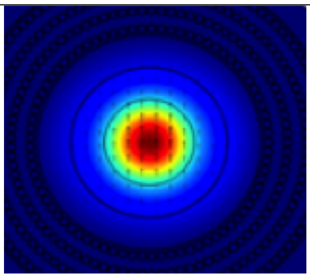	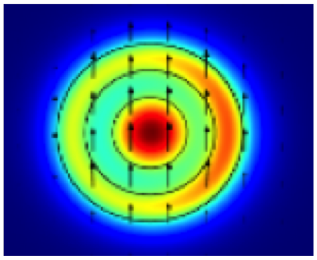

Table 5.5 shows the values in dB units indicating the coupling strength between perturbed OAM_1, HE_{11_x} and HE_{11_y} modes, and unperturbed TE_{01}, TM_{01} and OAM_{-1} modes, where perturbed modes corresponds to the first columns, and unperturbed

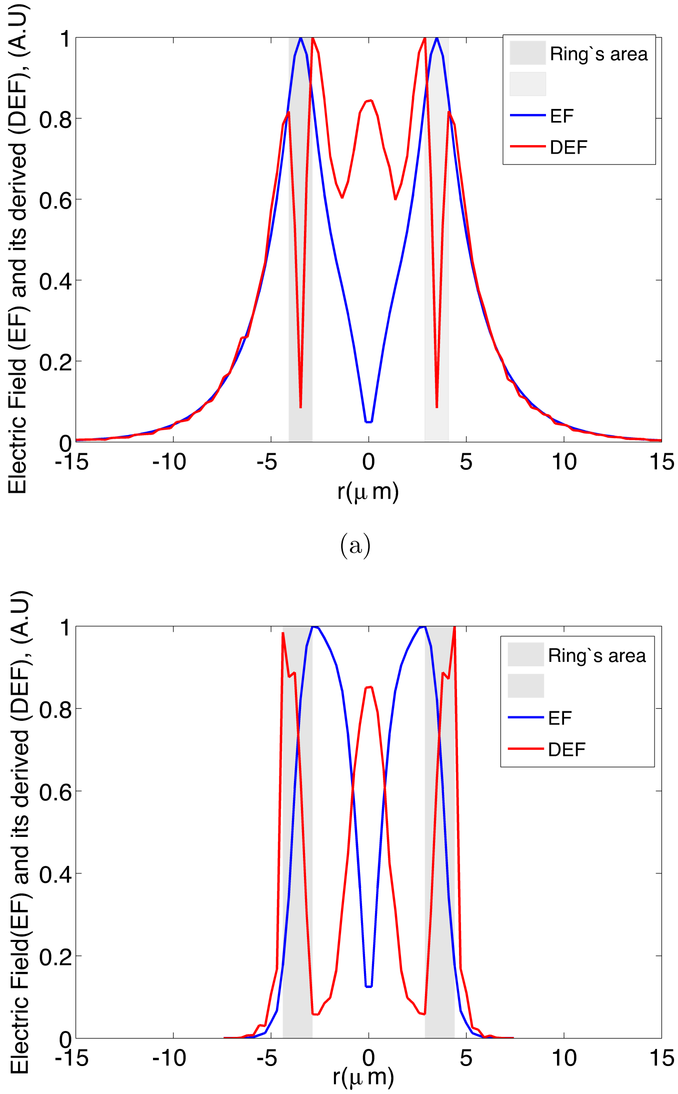

(a)

(b)

Figure 5.9: Radial electric field (EF) and its radial derived (DEF) in the ring area for **(a)** conventional solid core vortex fiber and **(b)** solid-core vortex fiber with the cladding of metamaterial (our proposal)

modes corresponds to the first rows. We observe high coupling strengths of values around 0 dB between the modes with the same orbital charge ℓ, which means that the propagation is not affected by the bend. Otherwise, a lower coupling strength for the OAM modes of opposite orbital charge (ℓ=1 and ℓ=-1 highlighted by green) in the conventional solid-core vortex fiber is observed. In this case, there is a reduction of 15 dB in the coupling strength compared with the conventional vortex fiber bent with 2 cm.

Values highlighted by the colors indicate the coupling strength of the OAM_1 mode with the modes corresponding to the first group $TE_{0,1}$, and $TM_{0,1}$, and with the anti-aligned mode OAM_{-1}. A lower coupling strength for all modes is showed in the case of solid-vortex fiber with the metamaterial cladding, in special between the OAM modes with opposite orbital charge (ℓ=1 and ℓ=-1), or the pair aligned (OAM_1) and anti-aligned (OAM_1) (see the explanation in section 3.2.2 pag. 56.)

5.2.3. Lifting of the $OAM_{\pm1}$ and $OAM_{\pm2}$ degeneracies in vortex solid-core fiber with metamaterial cladding with larger ring

Let us compare the modal behavior in both conventional solid already described in the subsection 4.2.2. (fiber named as dk110OD160), and vortex fibers with anisotropy-engineered cladding (our proposal), and with a larger ring, in which highest order modes are now guided (see Figure 4.7a).

Regarding the vortex fiber with the metamaterial cladding, $n_{x,y}$ is lower than the silica (SiO_2) refractive index, therefore there is an increase in the transverse index contrast ($\Delta n(r) = n_{ring} - n_{x,y}$) that produces an increase in the number of propagated modes, some of them quite unstable ($\Delta n_{eff} < 10^{-4}$) as shown in Figure 5.11b. The last four modes ($TM_{0,2}$, $HE_{2,2}$, $TE_{0,2}$, $EH_{2,1}$) possess a second radial order $m = 2$ and, in addition, the $HE_{2,2}$, and $EH_{2,1}$ modes are still *almost degenerated*, therefore they can not be used in the vortex fiber (see subsection 4.3.2).

Figure 4.7b shows that OAM modes with $\ell > 1$ also remain *almost degenerate* in the conventional solid vortex fiber, and therefore they are not considered in the OAM basis. However, we observe that OAM_2 is not longer *almost degenerated*, reaching a Δn_{eff} of approximately 3.5×10^{-4} at 1550 nm, caused by the presence of the metamaterial cladding (see Figure 5.11a). This fact leads us to conclude about of using metamaterials as cladding in this kind of fibers. We have demonstrated that OAM modes lift the degeneracy in vortex fibers with rings of larger width by using a cladding of metamaterial.

Table 5.5: OAM *Spectra* of the all-solid vortex fiber dk100OD105 for OAM_1, HE_{11_x}, HE_{11_y} modes. The fiber was bent radii of **(a)** 5 cm and **(b)** 2 cm. OAM *Spectra* of the all-solid vortex fiber with anisotropy-engineered cladding (AEC) (our proposal) for OAM_1, $HE_{1,1_x}$, $HE_{1,1_y}$ modes. The fibers are bent with **(c)** 5 cm and **(d)** 2 cm. Perturbed modes are indicated in the first column

(a)Vortex fiber bent with 5 cm

	TE_{01}	TM_{01}	OAM_{-1}	OAM_1
OAM_{-1}	-45	-39	-0.005	-58
OAM_1	-47	-39	-58	-0.005
HE_{11_y}	-30	-103	-33	-33
HE_{11_x}	-111	-73	-78	-78

(b)Vortex fiber bent with 2 cm

	$TE_{0,1}$	$TM_{0,1}$	OAM_{-1}	OAM_1
OAM_{-1}	-29	-23	-0.05	-48
OAM_1	-31	-24	-48	-0.05
$HE_{1,1_y}$	-22	-96	-25	-25
$HE_{1,1_x}$	-120	-65	-70	-70

(c)Vortex fiber with AEC bent with 5 cm

	$TE_{0,1}$	$TM_{0,1}$	OAM_{-1}	OAM_1
OAM_{-1}	-53	-55	-0.002	-64
OAM_1	-53	-56	-64	-0.002
$HE_{1,1_y}$	-37	-129	-41	-41
$HE_{1,1_x}$	-111	-72	-77	-77

(d)Vortex fiber with AEC bent with 2 cm

	$TE_{0,1}$	$TM_{0,1}$	OAM_{-1}	OAM_1
OAM_{-1}	-53	-55	-0.002	-63
OAM_1	-53	-55	-63	-0.002
$HE_{1,1_y}$	-37	-129	-41	-41
$HE_{1,1_x}$	-111	-73	-77	-77

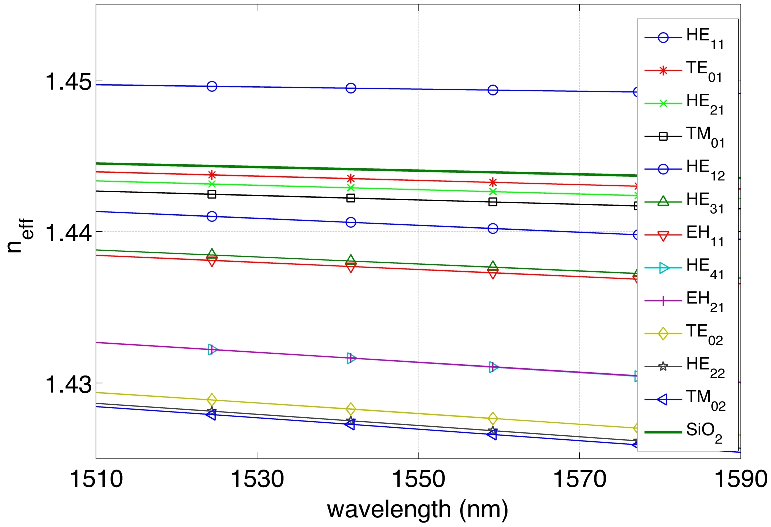

(a)Solid vortex fiber of metamaterial cladding. SiO_2 is the green-line

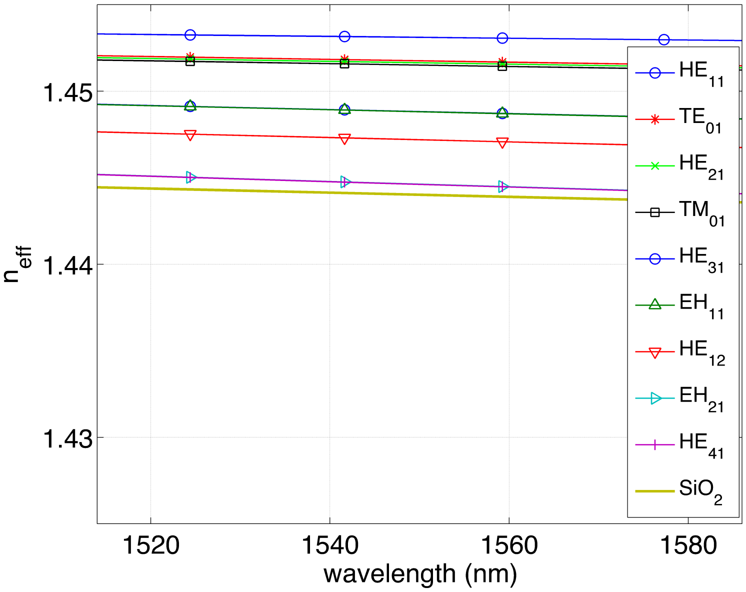

(b)Conventional solid vortex fiber. Cladding is SiO_2 (yellow-line)

Figure 5.10: Effective index as a function of light wavelength for guided modes in **(a)** the solid vortex fibers with the metamaterial cladding. **(b)** conventional solid vortex fiber dk110OD160. This figure was made with the help of [12]

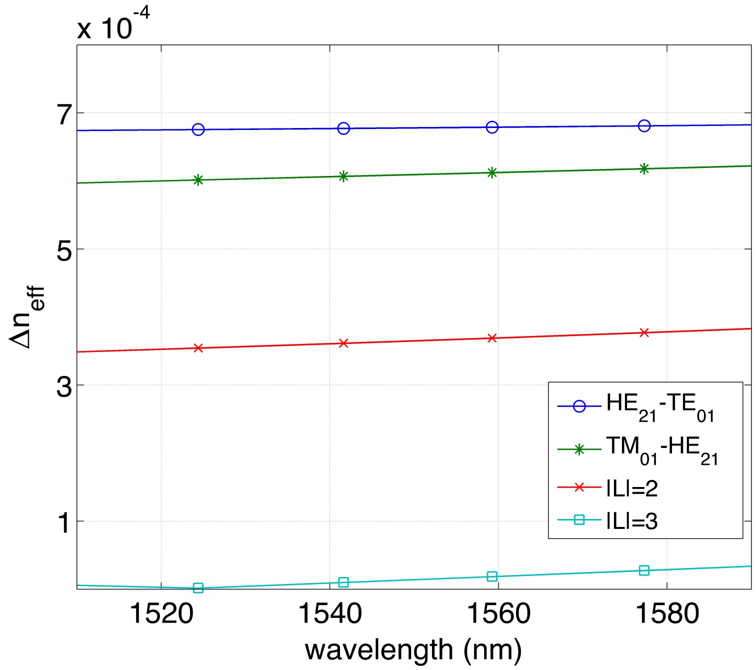

(a)Solid vortex fiber of metamaterial cladding

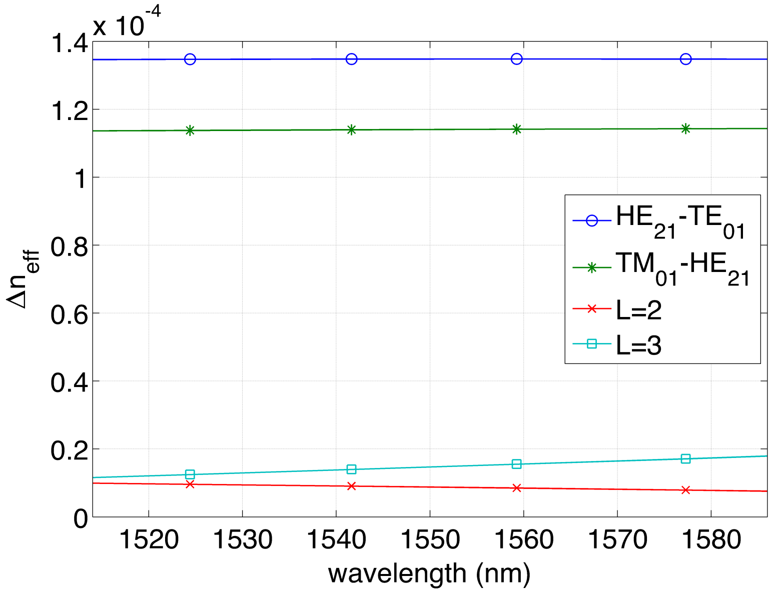

(b)Conventional solid vortex fiber

Figure 5.11: Effective index difference as a function of light wavelength for guided modes in **(a)** the solid vortex fibers with the metamaterial cladding, **(b)** conventional solid vortex fiber dk110OD160. This figure was made with the help of [12]

5.2.4. Comparison between conventional and metamaterial-based vortex solid-core fiber

Based on the results of the conventional solid, and our proposal, a design of cladding in anisotropic metamaterials with two possible refractive indexes in transverse and longitudinal direction can be considered as a new degree of freedom to design vortex fibers. We believe that the reduction of the coupling strength is a consequence of both the increase in the effective index among the vector modes within the group, as well as the anisotropy of the metamaterial that increases the effective index in longitudinal direction improves the mode confinement [86] preserving its modal profile when OAM modes are propagated in the bends. By using this design, it is possible to preserve the width and the refractive index contrast between the ring and cladding, in order to avoid both higher loss caused by the addition of dopants in the cladding or ring structure, and the generation of spin-orbit coupled modes, in special for OAM modes of low order. The mains advantage of this design can be thus summarized:

- The HE_{11} y-polarized mode can be propagated with bending radii less than 1 cm in our proposed OAM fiber with cladding of anisotropy-engineered metamaterial, which means a better robustness to fiber bends.
- A reduction in the coupling strength of 22 dB, and 31 dB between the $TE_{0,1}$ and the $OAM_{\pm1}$ modes, and $TM_{0,1}$ and the $OAM_{\pm1}$ modes, respectively, are achieved in our proposal which likely means a better performance of these fibers to transmit uncoupled channels over long lengths. The reduction in the mode coupling strengths is a consequence of lifting the degeneracy amongst the modes of the $OAM_{\pm1}$ group.
- Our proposal of a metamaterial cladding with engineered anisotropy could be used as an alternative lifting the degeneracy of highest order modes propagated in rings of larger width.

5.3. DESIGN OF AN AIR-CORE VORTEX FIBER WITH ANISOTROPY-ENGINEERED METAMATERIAL CLADDING

In this subsection, we describe the performance of an air-core vortex fiber with anisotropy-engineered metamaterial cladding through numerical analysis. Several simulations were performed in Comsol 5.1® varying the hole size into the cladding in order to reach a cladding configuration to split even more the vector modes of the last mode groups. The Figure 5.6 shows one of those possible configurations, now replacing the conventional cladding in silica with a metamaterial.

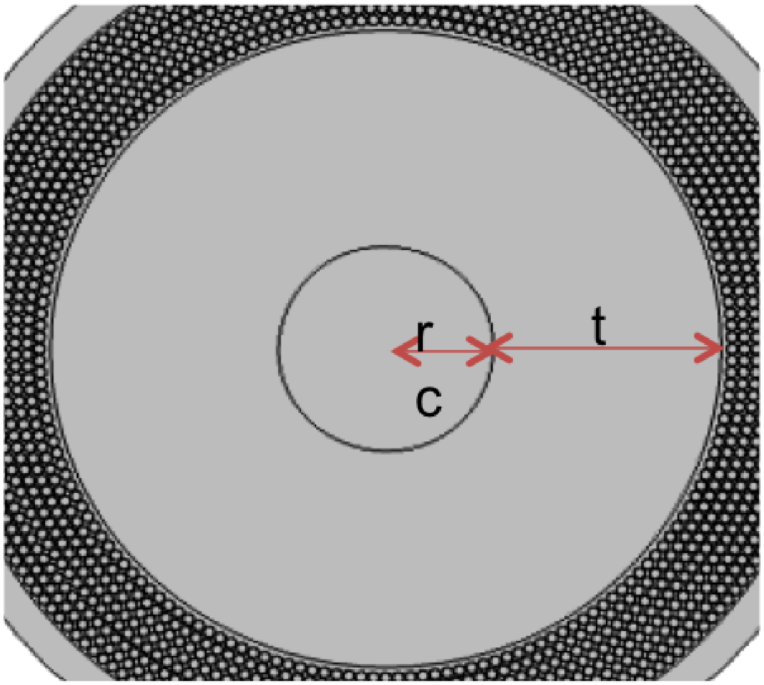

Figure 5.12: Comsol 5.1® image of the transverse section of an air-core vortex fiber with anisotropy-engineered cladding

Table 5.5 shows the geometric parameters of the chosen configuration. The full-structure was discretized by triangular elements of sizes smaller than the wavelength, and a perfect match layer (PML) of 1 μm was used to truncate the computational domain after 42.5 μm. We compute through the effective index as a function of light wavelength, and the modal field distribution of the propagated vector and OAM modes. Similarly to the conventional air-vortex fiber, our proposal inhibits, even more, the near-degeneracy between the modes of the last groups of propagated modes.

Based on the geometric parameters of the full-structure, we can apply the homogenization approached given by equations (5.2) and (5.3) (see Table 5.6). Note that the air-hole diameter is only almost two orders of magnitude smaller than the light wavelength, satisfying in this way the homogenization criterion. However, we simulate the

Table 5.6: Geometric parameters of the full-structure (our proposal) shown in Figure (5.12)

Parameters	Name	Value
t	Ring thickness	6.5 μm
r_c	Air-core radius	3 μm
l	Air hole diameter	0.31 μm
l	Distance between successive holes	0.34 μm
D_l	Distance between layers	0.34 μm
N	Number of layers	8

full-structure to get more realistic results.

Table 5.7: Equivalent parameters obtained from homogenization approach of the full-structure applied for the anisotropy-engineered cladding of the air-core vortex fiber (our proposal).

Parameters	Value
$n_{x,y}$ or $n(r)$	1.086
n_z	1.148
ρ	0.65

5.3.1. The increase the modal volume, and lifting in the degeneracy of the highest OAM modes

Let us compare the modal behavior of both conventional air-core (already described in the subsection 4.2.3), and air-core vortex fibers with anisotropy-engineered cladding. We show that higher order modes are also guided as is shown in Figure 5.13.

We show a comparison between the modal content in the air-core fiber in Figure 5.13a and the fiber with metamaterial cladding (our proposal). Figure 5.13b shows the effective index for the propagated modes at a telecom wavelength 1550 nm. We find up to 32 propagates mode for the conventional air-core vortex fiber, and up to 36 propagated modes for our proposed vortex fiber of metamaterial cladding.

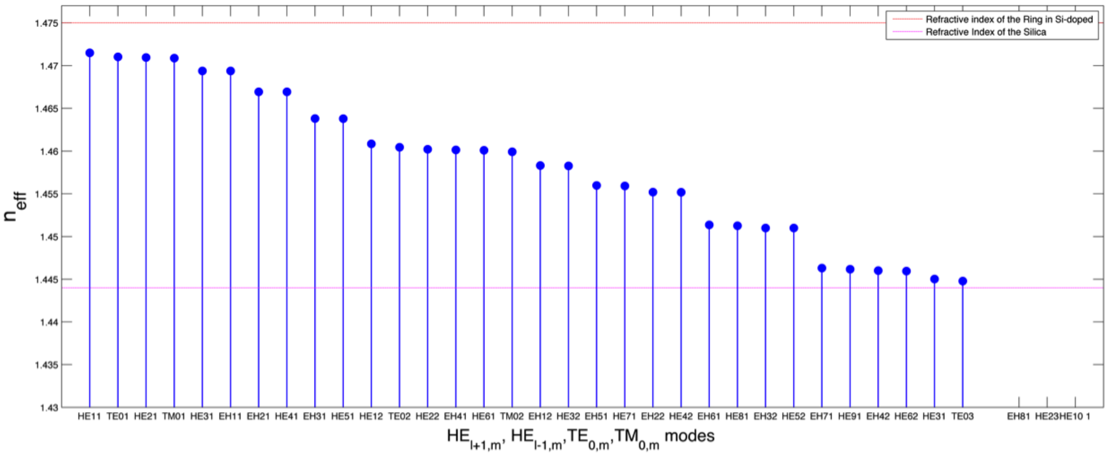

(a)Conventional air-core vortex fiber

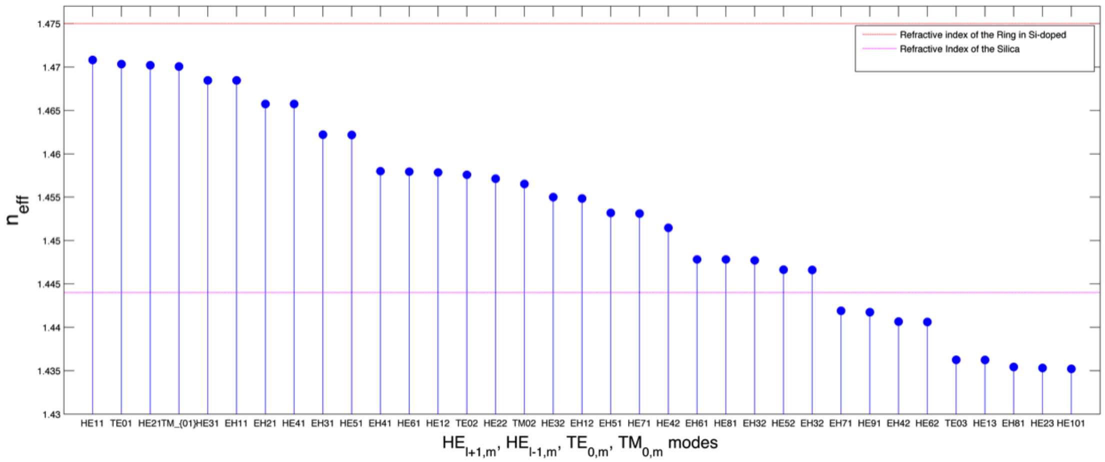

(b)Air core vortex fiber of metamaterial cladding

Figure 5.13: Modal content of the air-core vortex fibers **(a)** Conventional air-core vortex fiber **(b)** Air-core vortex fiber of metamaterial cladding with anisotropy-enginerred (our proposal). This figure was made with the help of [12]

In the vortex fiber of metamaterial cladding, we find one additional mode $HE_{10,1}$ that could be used to propagate an additional OAM mode in a broad range of wavelengths from 1450 nm to 1570 nm (see Figure 5.14b), as long as the criterion of low-mode coupling is satisfied. We find up to 9 $HE_{\ell+1,m}$ modes including HE_{11} mode, and 8 $EH_{\ell-1,m}$ modes that can produce up to 16 aligned and anti-aligned OAM modes in a window wavelengths as shown in Figure (5.14)c. However, for our proposal, the

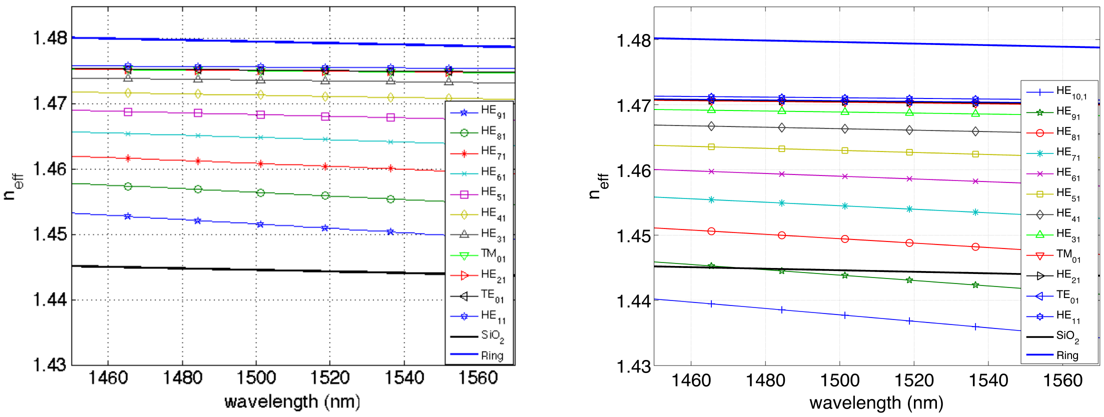

(a)Conventional air-core vortex fiber (b)Air-core vortex fiber of AEC

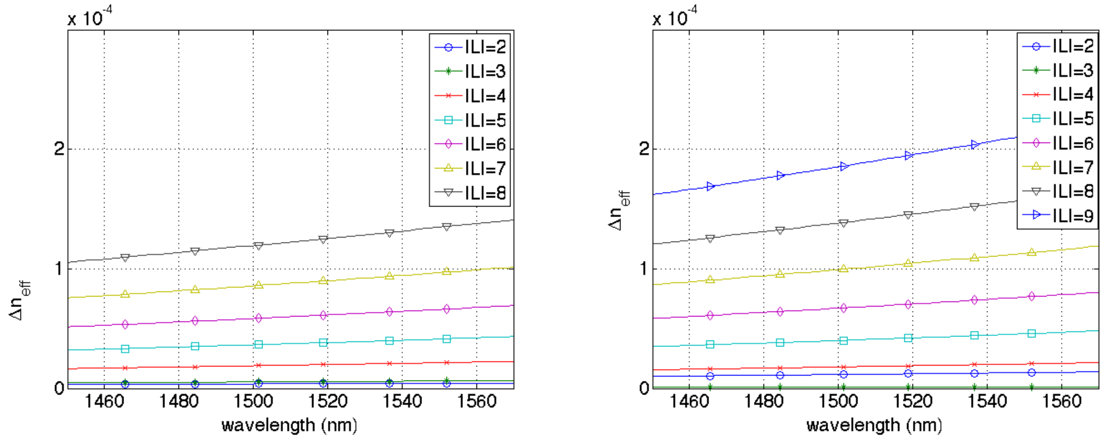

(c)Conventional air-core vortex fiber (d)Air-core vortex fiber of AEC

Figure 5.14: Effective index as a function of light wavelength: **(a)** Modes $HE_{\ell+1,1}$, $TE_{0,1}/TM_{0,1}$ in the conventional air-core vortex fiber. **(b)** modes $HE_{\ell+1,1}$, TE_{01}/TM_{01} in the air-core vortex fiber of engineered-anisotropy cladding (AEC). (our proposal). Effective index difference as a function of light wavelength: **(c)** conventional air-core vortex fiber. **(d)** air-core vortex fiber of engineered-anisotropy cladding (AEC). This figure was made with the help of [12]

additional $HE_{10,1}$ can generate the OAM_9 mode, which can also be propagated in this fiber because it satisfies the criterion of low-mode coupling ($\Delta n_{eff} > 10^{-4}$) as is shown in Figure 5.14d.

According to the phenomenological reasons described in section 3.2, the OAM modes with $\ell = \pm 6, \pm 7, \pm 8$ are stable in conventional air-core fiber. Note that now for our proposal the ± 9 mode is also stable, since Δn_{eff} are large enough as is shown in Figure 5.15 and Table 5.7. There is also increase in the Δn_{eff} amongst mode groups for our proposal as is shown by the red circles of the Figure 5.15. Below $\ell = 6$, for which OAM states are also supported, the n_{eff} splitting is too small and LP-like behavior is obtained.

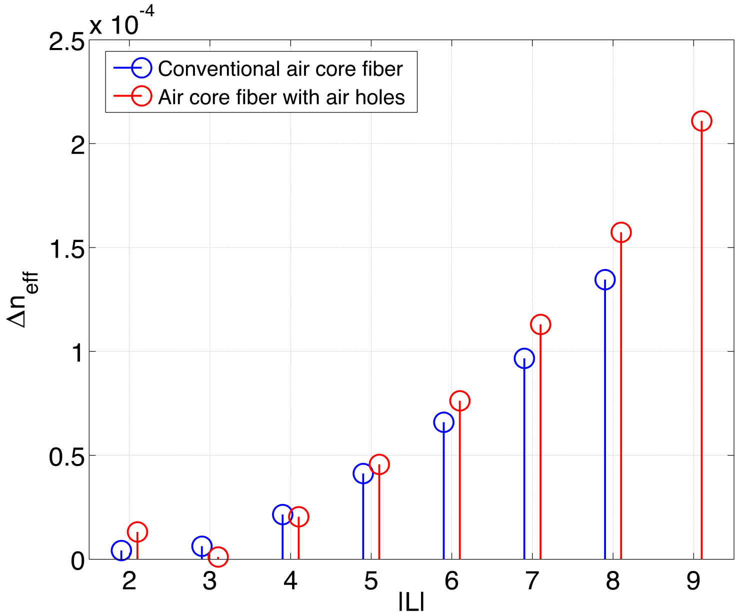

Figure 5.15: Effective index difference Vs. ℓ at a telecom wavelength 1550 nm for the air-core vortex fiber of metamaterial cladding (our proposal).

We also compute the modal dispersions obtained by a numerical implementation of the second derivative: $\partial^2\beta/\partial\omega^2$, in Matlab®. Figure 5.17a shows the modal dispersion for an OAM_{+6} ($\ell = 6$), which is, in order of magnitude, similar to the conventional air-core vortex fiber (maximum value of around +60 ps/nm·km as is shown in Figure 4.12) and the standard SMF in the same wavelengths (+18 ps/nm·km). Thus, this fiber can operate in optical communication systems similar to the conventional air-core vortex fiber.

Additionally, we show that "*accidental degeneracies*" can occur between modes with radial order $m = 1$ and $m = 2$ (see Figure 5.17b) for the simulated air-core vortex fiber with anisotropy-engineered cladding. The operation in regions in which the modes with $m = 2$ are closely spaced in n_{eff} to desired OAM modes with $m = 1$ should be avoided.

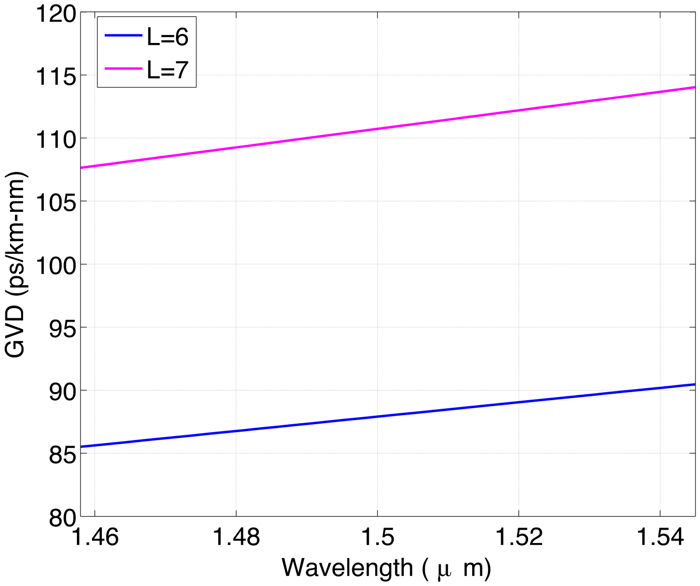

Figure 5.16: Modal dispersion for the $\ell = 6$, and 7 across C-band for the air-core fiber of metamaterial cladding (our proposal).

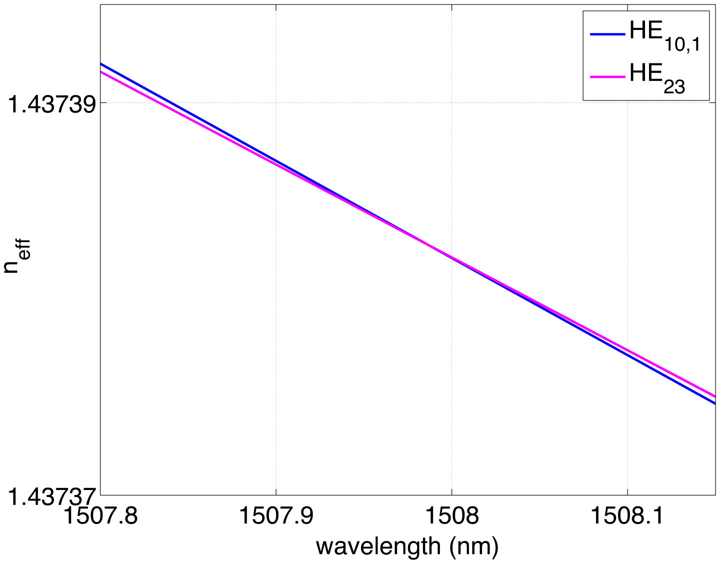

Figure 5.17: Accidental degeneracy between the (l,m)=(10,1) and (3,2) modes near to 1510 nm in the air-core vortex fiber with metamaterial approach (our proposal)

5.3.2. OAM Spectra

We compare the mode coupling strength of this fiber with the anisotropy-engineered cladding with respect to the values obtained for the conventional OAM air-core vortex fiber through the OAM *spectra*.

We also consider radii of 1 and 5 cm to obtain the perturbed electric fields. As was shown for the conventional vortex fibers of solid and air-core, we also compute equation (3.24) for two unperturbed fields combining possible cases. Notice that in the most of the cases it yields a value of around -120 dB, indicating a perfect orthogonality among the modes, or equivalently a mode of high purity.

Table 5.7 shows the values in dB units indicating the coupling strength between aligned $(+\ell)$ and anti-aligned $(-\ell)$ modes, where the first columns are corresponding to perturbed fields, and the first rows are corresponding to unperturbed fields. We observe that mode coupling is more intense for the conventional vortex fiber at a bending radius of 1 cm.

We stress that: (a) there are lowest coupling strengths in our proposed fiber (values are highlighted by the colors) than in the conventional vortex fiber. They are less intense reaching lowest values of up to -107 dB at a bend radius of 1cm, between anti-aligned $(W^{+}_{l,m})$ and aligned $(W^{+}_{l,m})$ OAM modes, which indicates high orthogonality. (b): In addition, we observe higher coupling strengths (values in gray) between OAM modes with the same orbital charge $+\ell$ or $-\ell$, showing that the propagation of the OAM modes is less affected by the bends in our proposed fiber.

5.3.3. Are the hybrid modes ($HE_{l+1,m}$ and $EH_{l-1,m}$) more stable than OAM modes?

Regarding the stability of OAM modes and the reason why these are preferably used in vortex fiber than the vector modes, we compare the mode coupling strength between OAM and vector modes through the OAM *spectra*. We consider a small bend radius of 1 cm to obtain the perturbed electric fields. Let us consider the mode OAM_7 formed by the HE^{even}_{81} and HE^{odd}_{81} modes, and the mode OAM_{-7} formed by the EH^{even}_{61} and EH^{odd}_{61} modes. This way, there are 8 possible accounts of equation (3.24). First, the

Table 5.8: *Spectra* of the air-core vortex fiber between an aligned and anti-aligned OAM modes. Conventional air-core vortex fiber was bent a radii of **(a)** 5 cm and **(b)**1 cm, and the air-core vortex fiber with anisotropic-engineered cladding (AEC) was bent radii of **(a)** 5 cm and **(b)**1 cm

(a)Vortex fiber bent 5 cm

	ℓ_6	ℓ_7	ℓ_{-6}	ℓ_{-7}
ℓ_{-6}	-76	-83	-0.012	-32
ℓ_{-7}	-73	-91	-32	-0.010
ℓ_6	-0.012	-32	-78	-74
ℓ_7	-32	-0.010	-82	-93

(b)Vortex fiber bent 1 cm

	ℓ_6	ℓ_7	ℓ_{-6}	ℓ_{-7}
ℓ_{-6}	-83	-71	-0.29	-19
ℓ_{-7}	-60	-67	-19	-0.26
ℓ_6	-0.32	-19	-83	-59
ℓ_7	-19	-0.26	-67	-78

(c)Vortex fiber with AEC bent 5 cm

	ℓ_6	ℓ_7	ℓ_{-6}	ℓ_{-7}
ℓ_{-6}	-94	-90	-0.07	-34
ℓ_{-7}	-60	-100	-34	-0.08
ℓ_6	-0.019	-34	-67	-81
ℓ_7	-34	-0.007	-76	-70

(d)Vortex fiber with AEC bent 1 cm

	ℓ_6	ℓ_7	ℓ_{-6}	ℓ_{-7}
ℓ_{-6}	-76	-75	-0.25	-21
ℓ_{-7}	-46	-107	-21	0.23
ℓ_6	0.23	-21	-48	-68
ℓ_7	-21	0.18	-62	-79

overlap integral given by equation (3.24), considering the pair of unperturbed OAM modes with $\ell = \pm 7$, gives a coupling strength value of -116 dB, indicating that the modes are highly orthogonal or remain highly pure.

In our example, the *spectra* was computed for both: between OAM_7 and OAM_{-7} states (see Table 5.8), and between their *almost non-degenerates* pair: $HE^{even,odd}_{\ell+1,1}$ and $EH^{even,odd}_{\ell-1,1}$, with $k_{z,HE^{even,odd}_{\ell+1,1}} \neq k_{z,EH^{even,odd}_{\ell-1,1}}$ (see Table 5.8)

Table 5.9: *Spectra* between an aligned and anti-aligned OAM_{+7} and OAM_{-7} modes. The fiber was bent 1cm to produce

	ℓ_7	ℓ_{-7}
ℓ_{-7}	-79	-0.26
ℓ_7	0.26	-67

Table 5.10: *Spectra* between an aligned and anti-aligned OAM_{+7} and OAM_{-7} modes. The fiber was bent 1 cm

	$HE^{even}_{8,1}$	$HE^{odd}_{8,1}$	$EH^{even}_{6,1}$	$EH^{odd}_{6,1}$
$HE^{even}_{8,1}$	-0.3	-22	-28	-30
$HE^{odd}_{8,1}$	-22	-0.3	-30	-28
$EH^{even}_{6,1}$	-43	-48	-0.3	-17
$EH^{odd}_{6,1}$	-48	-42	-17	-0.3

Considering that modes in the columns are unperturbed modes, we observe that the mode coupling is more intense between hybrid modes than OAM modes. A reduction of approximately 30 dB was found between the aligned and anti-aligned OAMs modes with the same state $\pm\ell$, with respect to the computed value between their non-degenerated pairs (see highlighted values by the colors). We can conclude that OAM modes are more stable to external perturbations like fiber bending than the vector modes, which is an additional reason why the OAM modes are preferred instead vector or LP modes.

5.3.4. Comparison between conventional and metamaterial-based vortex air-core fiber

The mains advantage of this design can be summarized thus:

- An increase of up to an additional OAM mode is achieved in our proposal of air-core vortex fiber with metamaterial cladding. In this design, the $HE_{10,1}$ is now propagated in a broad wavelength range from 1450 to 1530 nm. This optical mode is not propagated in conventional air-core vortex fiber with the same ring size.

- An increase in the effective index difference is observed in our design with respect to the conventional one, which means a lifting in the degeneracy of hybrid modes with the same radial order (m), which leads to a reduction in the mode coupling strength as was shown in the OAM *spectra* (see Table 5.7) that would allow the use of OAM modes as independent uncoupled channels over quite long lengths.

- Non-degenerate modes $HE_{l+1,m}$ and $EH_{l-1,m}$ are more strongly coupled by external perturbations than OAM modes. A significative reduction of approximately 30 dB was computed in air-core fibers, which leads us to conclude that OAM modes have more stable propagation in vortex fiber than conventional hybrid modes.

CONCLUSIONES

In this doctoral work, we have numerically modeled a new design of vortex fiber with a cladding made of dielectric metamaterial that could potentially increase the capacity and the length of future optical communication links. Our design of an anisotropic cladding with two possible refractive indexes in transverse (x, y) and longitudinal (z) directions can be considered as a new degree of freedom to improve the performance of the vortex fiber. Based on our results, we conclude that a reduction in the transverse indexes (n_x, n_y) enabled by the configuration of the metamaterial cladding leads to an increase the modal content. Moreover, an increase in the longitudinal index (n_z) leads to a higher modal confinement (see our contribution in [86] attached here from pg. 129-132), preserving the modal profile of OAM modes after the propagation in the bending, resulting in a lower coupling strength under this perturbation. This phenomenon had not been reported to achieve better performance in vortex fibers, and it is part of the claims of a patent still pending by the authors (see [94] attached here from pag. 133-171). This is our main contribution to the state of the art, so we have proposed by the first time the use of metamaterials with intuitive designs (arrangements of multilayers and nanorods) to modify the modal behavior in photonic structures (planar and circular waveguides) under perturbations like the bends.

In this dissertation, we first theoretically studied the modes of a multimode fiber with a step index profile using a weakly guiding approximation. We prove that a linear combination of hybrid vector modes $HE^{even}_{\ell+1,m}$, $HE^{odd}_{\ell+1,m}$ and $EH^{even}_{\ell-1,m}$, $EH^{odd}_{\ell-1,m}$ with $\pi/2$ a nonuniform way. For this new design, we drew inspiration from the proposal of metamaterial cladding introduced by Jahani in 2015 [16] that modify the modal behavior of photonic structures. We numerically studied the mode properties in the vortex fiber with silica cladding introduced by the first time for Ramachandran and its group [8], and then in vortex fiber with a cladding made of a metamaterial with air holes into the silica. We show that by replacing the silica cladding with the metamaterial there is an increase in separation of the effective index in the almost degenerated vector modes of the mode groups, as well as an increase in the number of propagated modes. The improvement of our design can be explained and summarized:

- *Reduction of the coupling strength*: We believe that the reduction of the coupling strength between OAM modes is a consequence of both the increase in the effective index among the vector modes within the group as well as due to the anisotropy of the metamaterial that promotes an increase in the confinement of the OAM modes propagated into the bends. This effect is not possible just through the increase of the index contrast [86, 94].
- *Stability of the OAM modes to external perturbations*: We have investigated the bend sensitivity effects, and demonstrated that the OAM modes exhibit a more reduced coupling strength under external perturbation like bending than the vector modes (see subsection 5.24). This fact results in three very important remarks:

a) Vortex fibers are one of the most promising candidates for a stable propagation of modes in long fiber lengths.

b) Vortex fibers would be interesting to be implemented in possible applications of OAM-MDM on a short range (less than 100 m) where low bending loss sensitivity and coupling is mandatory. The potential applications could be data centers, where fiber optics cable are becoming dominant due to higher bandwidth, and smaller lightweight compared with twisted pair copper cables [95].

c) Regarding to the claims defended by Zhao and his group in [96] in which they affirm that "*OAM is not a new degree of freedom*", because OAM are a subset of the LG modes in free-space, or a subset of vector modes HE/EH in fiber, which is equivalent to having a linear combination among them, we agree with them. In addition, they also state that "*Any advantage that may exist for OAM modes can also be exploited using these other sets of modes*", which in principle is true in the sense that having N vector modes is equal than having N linearly polarized (LP) or OAM modes. However, they also affirm that OAM modes in fiber haven't any advantage because "*When choosing a basis set for communications, one should consider first whether the set is complete, and second how convenient the set is for implementation in the application at hand, regardless of whether the basis set includes OAM modes*". In this affirmation, they do not take into account the convenience of using OAM modes in fibers instead of vector or LP modes. We show that the OAM modes exhibit uniform polarizations (linear or circular) allowing easier generation and external excitation when compared to vector modes, and the external perturbations like bending easily destroy the orthogonality of the vector and LP basis set, but not of the OAM basis set. Although in a guided medium as optical fiber the OAM could not be considered as a *new degree of freedom*, the OAM basis is the most *convenient* set to send independent channels in fiber communication system multiplexed by modes.

- *Preservation of the ring width*: In our proposal, we have demonstrated that it is possible to preserve the ring width and the refractive index contrast, in order to avoid either higher loss caused by addition of dopants in the cladding/ring structure, or the generation of spin-orbit coupled modes, in special for OAM modes of low order.
- *MIMO-DSP vs OAM modes with low crosstalk*: In our proposed vortex fiber there is an increase in the number of supported modes with a reduced coupling strength (see OAM *Spectra*), which means lower cross-talk among mode groups avoiding MIMO-DSP processing. This is in agreement with the goal of having all-photonic communication networks enabling low power consumption. In communication networks that require MIMO-DSP the complexity and power consumption increase in a nonlinear manner with the number of modes [97,98], and also there is an increase of the nonlinear effects due to cross-phase modulation coming from a very low differential group delay required by MIMO [1].

Thesis content and Main contributions

The main contributions of this doctoral work are summarized:

- The reduction of bending loss for the TM mode in planar waveguides (see our published work in [86].
- The increase in the confinement and reduction of bending loss for the $HE_{1,1}$ y-polarized mode in the proposed solid-vortex fiber (see our patent pending in [94], and pag. 92 in chapter 5).
- The reduction of the coupling strengths, and the increase in the number of modes in our proposed vortex fibers (see our patent pending in [94], and pag. 96, 99, 103, 104 and 107 in chapter 5).
- The design of vortex polymer optical fibers with low coupling strengths between OAM modes under perturbations like bends. This new design is a proposal to increase the

capacity of optical communications systems of short range (see the manuscript to be submitted to the list of publications).

- The performing of our own code to numerically compute the OAM *spectra*, taking into account the high-index contrast cases by means of the introduction of the z-components of the electric and magnetic fields. This code allows obtaining the coupling strengths between any pair of modes. To the best of our knowledge, we have numerically shown by the first time the robustness of the OAM modes with respect to the hybrid modes (see pag. 108). These results show the advantages of this technology in multiplexing of signals in MDM systems, and the implications of the increase of the capacity of these multiplexing systems using OAM instead others modal basis like based on LP-modes, or vector modes.
- The performing of our own code to numerically compute the total dispersion in fibers and waveguides by means of numerical derivates. This code was implemented and validated for bent waveguides (see our published work in [99]).

Future works

- *Fabrication and experimental tests*: As a nearest future work, we propose the fabrication of our vortex fiber in order to experimentally demonstrate the performance of our design using the techniques described in the appendix: "*Modal Content Measurement*".
- *Optimization tools to design vortex fibers with other class of metamaterials*: We have presented the metamaterials as a new degree of freedom to design vortex fiber. As a future work, we propose the construction of an optimizing tool that allows the introduction of other materials (e.g. nanorods or layer of Silicon and Germanium as in [16]) in the metamaterial design (that may be non-intuitive) to obtain vortex fiber designs targeted to other functions, such as modified reduced slope dispersion, with a specific crosstalk value, or other specific designs.
- *Reduce slope dispersion*: Total dispersion (material+waveguide) should be lower across the C-band, however, we have found that in our proposal this values is relatively large. A modified version of vortex fiber will try to reduce the dispersion to allow better performance for WDM-OAM systems. The authors have had experience in engineered-dispersion for bent planar waveguides made of glass (see pag. 172-187 [99]). Thus, this concept could extend to design our vortex fibers.

- *Fibers in plastic and polymer*: As mentioned above, the vortex fibers are potential candidates to be implemented in optical communication systems of short range (less than 100 m). The authors have been working in this kind of vortex fibers by using polymers in an air-core design, and expect to publish the results as soon as possible (see in the appendix the publications). Fibers for short range applications are fabricated in plastic and polymers [95]. We propose the extension of this concept to design fibers in plastic or polymer, which can be easily fabricated with microstructured cladding, to operate in other wavelengths
- *Integrated optic*: As a still open problem we propose the design of integrated optical devices to coupled this vortex fibers to a chip. Currently, OAM mode excitation is made using spatial light modulators (SLM), which hinders its scalability.

Thus far, from our point of view, the design of fibers to support many modes with low crosstalk is perhaps one of the most critical barriers to unlock the all-photonic systems multiplexed by modes, and our proposal stands as an alternative to advance in this pathway. Every solution described in this thesis (MCF, Vortex Fibers, MIMO-DSP in MMF, OAM-MDM) has its pros and cons, nevertheless none of them can be considered as a definitive solution beyond conventional multiplexing techniques to overcome the capacity crunch predicted by the scientific community.

BIBLIOGRAPHY

[1] R. J. Essiambre and R. W. Tkach, "Capacity trends and limits of optical communication networks," *Proceedings of the IEEE*, vol. 100, no. 5, pp. 1035–1055, May 2012.

[2] D. J. Richardson, J. M. Fini, and L. E. Nelson, "Space-division multiplexing in optical fibres," *Nat Photon*, vol. 7, no. 5, pp. 354–362, 05 2013. [Online]. Available: http://dx.doi.org/10.1038/nphoton.2013.94

[3] N. Bozinovic, Y. Yue, Y. Ren, M. Tur, P. Kristensen, H. Huang, A. E. Willner, and S. Ramachandran, "Terabit-scale orbital angular momentum mode division multiplexing in fibers," *Science*, vol. 340, no. 6140, pp. 1545–1548, 2013. [Online]. Available: http://science.sciencemag.org/content/340/6140/1545

[4] L. Allen, M. Padgett, and M. Babiker, "The orbital angular momentum of light," *PROGRESS IN OPTICS, VOL XXXIX*, vol. 39, pp. 291–372, 1999.

[5] A. E. Willner, H. Huang, Y. Yan, Y. Ren, N. Ahmed, G. Xie, C. Bao, L. Li, Y. Cao, Z. Zhao, J. Wang, M. P. J. Lavery, M. Tur, S. Ramachandran, A. F. Molisch, N. Ashrafi, and S. Ashrafi, "Optical communications using orbital angular momentum beams," *Adv. Opt. Photon.*, vol. 7, no. 1, pp. 66–106, Mar 2015. [Online]. Available: http://aop.osa.org/abstract.cfm?URI=aop-7-1-66

[6] S. M. Barnett, L. Allen, R. P. Cameron, C. R. Gilson, M. J. Padgett, F. C. Speirits, and A. M. Yao, "On the natures of the spin and orbital parts of optical angular momentum," *Journal of Optics*, vol. 18, no. 6, p. 064004, 2016. [Online]. Available: http://stacks.iop.org/2040-8986/18/i=6/a=064004

[7] A. Snyder and J. Love, *Optical Waveguide Theory*, ser. Science paperbacks. Springer US, 1983. [Online]. Available: https://books.google.co.in/books?id=gIQB_hzB0SMC

[8] S. Ramachandran, P. Kristensen, and M. F. Yan, "Generation and propagation of radially polarized beams in optical fibers," *Opt. Lett.*, vol. 34, no. 16, pp. 2525–2527, Aug 2009. [Online]. Available: http://ol.osa.org/abstract.cfm?URI=ol-34-16-2525

[9] P. Gregg, P. Kristensen, and S. Ramachandran, "Conservation of orbital angular momentum in air-core optical fibers," *Optica*, vol. 2, no. 3, pp. 267–270, Mar 2015. [Online]. Available: http://www.osapublishing.org/optica/abstract.cfm?URI=optica-2-3-267

[10] S. Ramachandran, N. Bozinovic, P. Gregg, S. Golowich, and P. Kristensen, "Optical vortices in fibres: A new degree of freedom for mode multiplexing," in *European Conference and Exhibition on Optical Communication.* Optical Society of America, 2012, p. Tu.3.F.3. [Online]. Available: http://www.osapublishing.org/abstract.cfm?URI=ECEOC-2012-Tu.3.F.3

[11] N. Bozinovic, *Orbital angular momentum in optical fibers, PhD.Tesis.* Boston University, 2013.

[12] M. Corato-Zanarella, "Preeliminary study of oam fibers," *Unicamp Master Student 2017. Fapesp Scientific Initiation*, Private Communication, 2017.

[13] S. Golowich, "Asymptotic theory of strong spin-orbit coupling in optical fiber," *Opt. Lett.*, vol. 39, no. 1, pp. 92–95, Jan 2014. [Online]. Available: http://ol.osa.org/abstract.cfm?URI=ol-39-1-92

[14] S. Ramachandran, P. Gregg, P. Kristensen, and S. E. Golowich, "On the scalability of ring fiber designs for oam multiplexing," *Opt. Express*, vol. 23, no. 3, pp. 3721–3730, Feb 2015. [Online]. Available: http://www.opticsexpress.org/abstract.cfm?URI=oe-23-3-3721

[15] S. Jahani and Z. Jacob, "All-dielectric metamaterials," *Nat Nano*, vol. 11, no. 1, pp. 23–36, 01 2016. [Online]. Available: http://dx.doi.org/10.1038/nnano.2015.304

[16] ——, "Photonic skin-depth engineering," *J. Opt. Soc. Am. B*, vol. 32, no. 7, pp. 1346–1353, Jul 2015. [Online]. Available:

http://josab.osa.org/abstract.cfm?URI=josab-32-7-1346

[17] ——, "Transparent subdiffraction optics: nanoscale light confinement without metal," *Optica*, vol. 1, no. 2, pp. 96–100, Aug 2014. [Online]. Available: http://www.osapublishing.org/optica/abstract.cfm?URI=optica-1-2-96

[18] R. Byren and V. Shkunov, "Low-latency, hollow-core optical fiber with total internal reflection mode confinement," Apr. 2 2015, uS Patent App. 14/042,913. [Online]. Available: http://www.google.com/patents/US20150093085

[19] C. Schulze, A. Dudley, D. Flamm, M. Duparr?, and A. Forbes, "Measurement of the orbital angular momentum density of light by modal decomposition," *New Journal of Physics*, vol. 15, no. 7, p. 073025, 2013. [Online]. Available: http://stacks.iop.org/1367-2630/15/i=7/a=073025

[20] E. B. Desurvire, "Capacity demand and technology challenges for lightwave systems in the next two decades," *Journal of Lightwave Technology*, vol. 24, no. 12, pp. 4697–4710, Dec 2006.

[21] E. Desurvire, C. Kazmierski, F. Lelarge, X. Marcadet, A. Scavennec, F. Kish, D. Welch, R. Nagarajan, C. Joyner, R. Schneider, S. Corzine, M. Kato, P. Evans, M. Ziari, A. Dentai, J. Pleumeekers, R. Muthiah, S. Bigo, M. Nakazawa, D. Richardson, F. Poletti, M. Petrovich, S. Alam, W. Loh, and D. Payne, "Science and technology challenges in xxist century optical communications," May 2011, article for the 50th anniversary of the invention of the LASER. [Online]. Available: http://eprints.soton.ac.uk/200955/

[22] J. Berthold, A. A. M. Saleh, L. Blair, and J. M. Simmons, "Optical networking: Past, present, and future," *Journal of Lightwave Technology*, vol. 26, no. 9, pp. 1104–1118, May 2008.

[23] R. W. Tkach, "Scaling optical communications for the next decade and beyond," *Bell Labs Technical Journal*, vol. 14, no. 4, pp. 3–9, Winter 2010.

[24] M. Gao, J. Kurumida, and S. Namiki, "Wide range operation of regenerative optical parametric wavelength converter using ase-degraded 43-gb/s rz-dpsk signals," *Opt. Express*, vol. 19, no. 23, pp. 23 258–23 270, Nov 2011. [Online].

Available: http://www.opticsexpress.org/abstract.cfm?URI=oe-19-23-23258

[25] P. P. Mitra and J. B. Stark, “Nonlinear limits to the information capacity of optical fibre communications,” *Nature*, vol. 411, no. 6841, pp. 1027–1030, 06 2001. [Online]. Available: http://dx.doi.org/10.1038/35082518

[26] R. J. Essiambre, G. Kramer, P. J. Winzer, G. J. Foschini, and B. Goebel, “Capacity limits of optical fiber networks,” *Journal of Lightwave Technology*, vol. 28, no. 4, pp. 662–701, Feb 2010.

[27] T. Morioka, Y. Awaji, R. Ryf, P. Winzer, D. Richardson, and F. Poletti, “Enhancing optical communications with brand new fibers,” *IEEE Communications Magazine*, vol. 50, no. 2, pp. s31–s42, February 2012.

[28] C. M. Smith, N. Venkataraman, M. T. Gallagher, D. Muller, J. A. West, N. F. Borrelli, D. C. Allan, and K. W. Koch, “Low-loss hollow-core silica/air photonic bandgap fibre,” *Nature*, vol. 424, no. 6949, pp. 657–659, 08 2003. [Online]. Available: http://dx.doi.org/10.1038/nature01849

[29] S. Golowich, N. Bozinovic, P. Kristensen, P. Gregg, and S. Ramachandran, “Orbital angular momentum states for mode division multiplexing in optical fiber,” in *2013 IEEE Photonics Society Summer Topical Meeting Series*, July 2013, pp. 109–110.

[30] Y. Jung, V. A. J. M. Sleiffer, N. Baddela, M. N. Petrovich, J. R. Hayes, N. V. Wheeler, D. R. Gray, E. N. Fokoua, J. P. Wooler, N. H. L. Wong, F. Parmigiani, S. U. Alam, J. Surof, M. Kuschnerov, V. Veljanovski, H. de Waardt, F. Poletti, and D. J. Richardson, “First demonstration of a broadband 37-cell hollow core photonic bandgap fiber and its application to high capacity mode division multiplexing,” in *Optical Fiber Communication Conference and Exposition and the National Fiber Optic Engineers Conference (OFC/NFOEC), 2013*, March 2013, pp. 1–3.

[31] H. Huang, G. Milione, M. P. J. Lavery, G. Xie, Y. Ren, Y. Cao, N. Ahmed, T. An Nguyen, D. A. Nolan, M.-J. Li, M. Tur, R. R. Alfano, and A. E. Willner, “Mode division multiplexing using an orbital angular momentum mode sorter and mimo-dsp over a graded-index few-mode optical

fibre," *Scientific Reports*, vol. 5, p. 14931, 2015. [Online]. Available: http://www.ncbi.nlm.nih.gov/pmc/articles/PMC4598738/

[32] P. J. Winzer, "Energy-efficient optical transport capacity scaling through spatial multiplexing," *IEEE Photonics Technology Letters*, vol. 23, no. 13, pp. 851–853, July 2011.

[33] ——, "Scaling optical fiber networks: Challenges and solutions," *Opt. Photon. News*, vol. 26, no. 3, pp. 28–35, Mar 2015. [Online]. Available: http://www.osa-opn.org/abstract.cfm?URI=opn-26-3-28

[34] Y. Ding, F. Ye, C. Peucheret, H. Ou, Y. Miyamoto, and T. Morioka, "On-chip grating coupler array on the soi platform for fan-in/fan-out of mcfs with low insertion loss and crosstalk," *Opt. Express*, vol. 23, no. 3, pp. 3292–3298, Feb 2015. [Online]. Available: http://www.opticsexpress.org/abstract.cfm?URI=oe-23-3-3292

[35] B. Stern, X. Zhu, C. P. Chen, L. D. Tzuang, J. Cardenas, K. Bergman, and M. Lipson, "On-chip mode-division multiplexing switch," *Optica*, vol. 2, no. 6, pp. 530–535, Jun 2015. [Online]. Available: http://www.osapublishing.org/optica/abstract.cfm?URI=optica-2-6-530

[36] A. W. Snyder and J. Love, *Optical Waveguide Theory*, 1st ed. Springer, 1983. [Online]. Available: http://www.amazon.com/Optical-Waveguide-Theory-Science-Paperbacks/dp/0412099500%3FSubscriptionId%3D13CT5CVB80YFWJEPWS02%26tag%3Dws%26linkCode%3Dxm2%26camp%3D2025%26creative%3D165953%26creativeASIN%3D0412099500

[37] I. Giles, A. Obeysekara, R. Chen, D. Giles, F. Poletti, and D. Richardson, "Fiber lpg mode converters and mode selection technique for multimode sdm," *IEEE Photonics Technology Letters*, vol. 24, no. 21, pp. 1922–1925, Nov 2012.

[38] L. Gruner-Nielsen, Y. Sun, J. W. Nicholson, D. Jakobsen, K. G. Jespersen, R. Lingle, and B. Palsdottir, "Few mode transmission fiber with low dgd, low mode coupling, and low loss," *Journal of Lightwave Technology*, vol. 30, no. 23, pp. 3693–3698, Dec 2012.

[39] R. A. Panicker and J. M. Kahn, “Algorithms for compensation of multimode fiber dispersion using adaptive optics,” *Journal of Lightwave Technology*, vol. 27, no. 24, pp. 5790–5799, Dec 2009.

[40] K.-P. Ho and J. M. Kahn, “Statistics of group delays in multimode fiber with strong mode coupling,” *J. Lightwave Technol.*, vol. 29, no. 21, pp. 3119–3128, Nov 2011. [Online]. Available: http://jlt.osa.org/abstract.cfm?URI=jlt-29-21-3119

[41] Y. Yan, L. Zhang, J. Wang, J.-Y. Yang, I. M. Fazal, N. Ahmed, A. E. Willner, and S. J. Dolinar, “Fiber structure to convert a gaussian beam to higher-order optical orbital angular momentum modes,” *Opt. Lett.*, vol. 37, no. 16, pp. 3294–3296, Aug 2012. [Online]. Available: http://ol.osa.org/abstract.cfm?URI=ol-37-16-3294

[42] P. Gregg, P. Kristensen, and S. Ramachandran, “13.4km oam state propagation by recirculating fiber loop,” *Opt. Express*, vol. 24, no. 17, pp. 18 938–18 947, Aug 2016. [Online]. Available: http://www.opticsexpress.org/abstract.cfm?URI=oe-24-17-18938

[43] T. Hayashi, T. Taru, O. Shimakawa, T. Sasaki, and E. Sasaoka, “Design and fabrication of ultra-low crosstalk and low-loss multi-core fiber,” *Opt. Express*, vol. 19, no. 17, pp. 16 576–16 592, Aug 2011. [Online]. Available: http://www.opticsexpress.org/abstract.cfm?URI=oe-19-17-16576

[44] PolettiF., W. V., P. N., BaddelaN., N. FokouaE., H. R., G. R., LiZ., SlavikR., and R. J., “Towards high-capacity fibre-optic communications at the speed of light in vacuum,” *Nat Photon*, vol. 7, no. 4, pp. 279–284, 04 2013. [Online]. Available: http://dx.doi.org/10.1038/nphoton.2013.45

[45] M. N. Petrovich, F. Poletti, J. Wooler, A. Heidt, N. K. Baddela, Z. Li, D. R. Gray, R. Slavík, F. Parmigiani, N. Wheeler, J. Hayes, E. N. Fokoua, L. Grüner-Nielsen, B. Pálsdóttir, R. Phelan, B. Kelly, M. Becker, N. MacSuibhne, J. Zhao, F. C. G. Gunning, A. Ellis, P. Petropoulos, S. ul Alam, and D. Richardson, “First demonstration of 2μm data transmission in a low-loss hollow core photonic bandgap fiber,” in *European Conference and Exhibition on Optical Communication.*

Optical Society of America, 2012, p. Th.3.A.5. [Online]. Available: http://www.osapublishing.org/abstract.cfm?URI=ECEOC-2012-Th.3.A.5

[46] L. Allen, S. Barnett, and M. . . Padgett, *Optical Angular Momentum*. CRC Press, 2016. [Online]. Available: https://books.google.co.uk/books?id=kZjSBQAAQBAJ

[47] A. E. Siegman, *Lasers*. University Science Books, 1986. [Online]. Available: https://books.google.com.br/books?id=1BZVwUZLTkAC

[48] S. Franke-Arnold, L. Allen, and M. Padgett, "Advances in optical angular momentum," *Laser & Photonics Reviews*, vol. 2, no. 4, pp. 299–313, 2008. [Online]. Available: http://dx.doi.org/10.1002/lpor.200810007

[49] J. H. Poynting, "The wave motion of a revolving shaft, and a suggestion as to the angular momentum in a beam of circularly polarised light," *Proceedings of the Royal Society of London A: Mathematical, Physical and Engineering Sciences*, vol. 82, no. 557, pp. 560–567, 1909. [Online]. Available: http://rspa.royalsocietypublishing.org/content/82/557/560

[50] R. A. Beth, "Mechanical detection and measurement of the angular momentum of light," *Phys. Rev.*, vol. 50, pp. 115–125, Jul 1936. [Online]. Available: http://link.aps.org/doi/10.1103/PhysRev.50.115

[51] M. Padgett, J. Courtial, and L. Allen, "Light's orbital angular momentum," *Physics Today*, vol. 57, no. 5, pp. 35–40, May 2004. [Online]. Available: http://eprints.gla.ac.uk/1968/

[52] M. Padgett, "Light's twist," *Proceedings of the Royal Society of London A: Mathematical, Physical and Engineering Sciences*, vol. 470, no. 2172, 2014. [Online]. Available: http://rspa.royalsocietypublishing.org/content/470/2172/20140633

[53] P. Z. Dashti, F. Alhassen, and H. P. Lee, "Observation of orbital angular momentum transfer between acoustic and optical vortices in optical fiber," *Phys. Rev. Lett.*, vol. 96, p. 043604, Feb 2006. [Online]. Available: http://link.aps.org/doi/10.1103/PhysRevLett.96.043604

[54] G. Volpe and D. Petrov, “Generation of cylindrical vector beams with few-mode fibers excited by laguerre–gaussian beams,” *Optics Communications*, vol. 237, no. 1–3, pp. 89–95, 7 2004. [Online]. Available: http://www.sciencedirect.com/science/article/pii/S0030401804003669

[55] G. K. L. Wong, M. S. Kang, H. W. Lee, F. Biancalana, C. Conti, T. Weiss, and P. S. J. Russell, “Excitation of orbital angular momentum resonances in helically twisted photonic crystal fiber,” *Science*, vol. 337, no. 6093, pp. 446–449, 2012. [Online]. Available: http://science.sciencemag.org/content/337/6093/446

[56] B. Saleh and M. Teich, *Fundamentals of Photonics*, ser. Wiley Series in Pure and Applied Optics. Wiley, 2013. [Online]. Available: https://books.google.com.br/books?id=Qfeosgu08u8C

[57] K. Okamoto, *Fundamentals of Optical Waveguides*, ser. Optics and photonics. Academic Press, 2000. [Online]. Available: https://books.google.com.br/books?id=Igfx0KJc7ZoC

[58] S. M. Barnett and R. Loudon, “The enigma of optical momentum in a medium,” *Philosophical Transactions of the Royal Society of London A: Mathematical, Physical and Engineering Sciences*, vol. 368, no. 1914, pp. 927–939, 2010. [Online]. Available: http://rsta.royalsocietypublishing.org/content/368/1914/927

[59] J. Jackson, *Classical electrodynamics*. Wiley, 1975. [Online]. Available: https://books.google.de/books?id=_7rvAAAAMAAJ

[60] C. Brunet, P. Vaity, Y. Messaddeq, S. LaRochelle, and L. A. Rusch, “Design, fabrication and validation of an oam fiber supporting 36 states,” *Opt. Express*, vol. 22, no. 21, pp. 26 117–26 127, Oct 2014. [Online]. Available: http://www.opticsexpress.org/abstract.cfm?URI=oe-22-21-26117

[61] D. Marcuse, *Theory of dielectric optical waveguides*, ser. Quantum electronics–principles and applications. Academic Press, 1974. [Online]. Available: https://books.google.co.uk/books?id=kZwxAAAAIAAJ

[62] J. M. Kahn, K.-P. Ho, and M. B. Shemirani, “Mode coupling effects in

multi-mode fibers," in *Optical Fiber Communication Conference.* Optical Society of America, 2012, p. OW3D.3. [Online]. Available: http://www.osapublishing.org/abstract.cfm?URI=OFC-2012-OW3D.3

[63] A. Galtarossa, L. Palmieri, A. Pizzinat, M. Schiano, and T. Tambosso, "Measurement of local beat length and differential group delay in installed single-mode fibers," *J. Lightwave Technol.*, vol. 18, no. 10, p. 1389, Oct 2000. [Online]. Available: http://jlt.osa.org/abstract.cfm?URI=jlt-18-10-1389

[64] W.-P. Huang, "Coupled-mode theory for optical waveguides: an overview," *J. Opt. Soc. Am. A*, vol. 11, no. 3, pp. 963–983, Mar 1994. [Online]. Available: http://josaa.osa.org/abstract.cfm?URI=josaa-11-3-963

[65] R. Olshansky, "Mode coupling effects in graded-index optical fibers," *Appl. Opt.*, vol. 14, no. 4, pp. 935–945, Apr 1975. [Online]. Available: http://ao.osa.org/abstract.cfm?URI=ao-14-4-935

[66] A. Bjarklev, "Microdeformation losses of single-mode fibers with step-index profiles," *Journal of Lightwave Technology*, vol. 4, no. 3, pp. 341–346, Mar 1986.

[67] K. Kakihara, N. Kono, K. Saitoh, and M. Koshiba, "Full-vectorial finite element method in a cylindrical coordinate system for loss analysis of photonic wire bends," *Opt. Express*, vol. 14, no. 23, pp. 11 128–11 141, Nov 2006. [Online]. Available: http://www.opticsexpress.org/abstract.cfm?URI=oe-14-23-11128

[68] Z. Han, P. Zhang, and S. I. Bozhevolnyi, "Calculation of bending losses for highly confined modes of optical waveguides with transformation optics," *Opt. Lett.*, vol. 38, no. 11, pp. 1778–1780, Jun 2013. [Online]. Available: http://ol.osa.org/abstract.cfm?URI=ol-38-11-1778

[69] J. B. Pendry, D. Schurig, and D. R. Smith, "Controlling electromagnetic fields," *Science*, vol. 312, no. 5781, pp. 1780–1782, 2006. [Online]. Available: http://science.sciencemag.org/content/312/5781/1780

[70] S. Ramachandran, S. Golowich, M. F. Yan, E. Monberg, F. V. Dimarcello, J. Fleming, S. Ghalmi, and P. Wisk, "Lifting polarization degeneracy of modes by fiber design: a platform for polarization-insensitive microbend fiber

gratings," *Opt. Lett.*, vol. 30, no. 21, pp. 2864–2866, Nov 2005. [Online]. Available: http://ol.osa.org/abstract.cfm?URI=ol-30-21-2864

[71] Y. Yan, J. Wang, L. Zhang, J.-Y. Yang, I. M. Fazal, N. Ahmed, B. Shamee, A. E. Willner, K. Birnbaum, and S. Dolinar, "Fiber coupler for generating orbital angular momentum modes," *Opt. Lett.*, vol. 36, no. 21, pp. 4269–4271, Nov 2011. [Online]. Available: http://ol.osa.org/abstract.cfm?URI=ol-36-21-4269

[72] Y. Yue, L. Zhang, Y. Yan, N. Ahmed, J.-Y. Yang, H. Huang, Y. Ren, S. Dolinar, M. Tur, and A. E. Willner, "Octave-spanning supercontinuum generation of vortices in an as2s3 ring photonic crystal fiber," *Opt. Lett.*, vol. 37, no. 11, pp. 1889–1891, Jun 2012. [Online]. Available: http://ol.osa.org/abstract.cfm?URI=ol-37-11-1889

[73] S. Li and J. Wang, "Multi-orbital-angular-momentum multi-ring fiber for high-density space-division multiplexing," *IEEE Photonics Journal*, vol. 5, no. 5, pp. 7 101 007–7 101 007, Oct 2013.

[74] ——, "Supermode fiber for orbital angular momentum (oam) transmission," *Opt. Express*, vol. 23, no. 14, pp. 18 736–18 745, Jul 2015. [Online]. Available: http://www.opticsexpress.org/abstract.cfm?URI=oe-23-14-18736

[75] P. Gregg, P. Kristensen, A. Rubano, S. Golowich, L. Marrucci, and S. Ramachandran, "Spin-orbit coupled, non-integer oam fibers: Unlocking a new eigenbasis for transmitting 24 uncoupled modes," in *Conference on Lasers and Electro-Optics.* Optical Society of America, 2016, p. JTh4C.7. [Online]. Available: http://www.osapublishing.org/abstract.cfm?URI=CLEO_AT-2016-JTh4C.7

[76] A. N. Grigorenko, A. K. Geim, H. F. Gleeson, Y. Zhang, A. A. Firsov, I. Y. Khrushchev, and J. Petrovic, "Nanofabricated media with negative permeability at visible frequencies," *Nature*, vol. 438, no. 7066, pp. 335–338, 11 2005. [Online]. Available: http://dx.doi.org/10.1038/nature04242

[77] V. M. Shalaev, "Optical negative-index metamaterials," *Nat Photon*, vol. 1, no. 1, pp. 41–48, 01 2007. [Online]. Available: http://dx.doi.org/10.1038/nphoton.2006.49

[78] M. Silveirinha and N. Engheta, “Design of matched zero-index metamaterials using nonmagnetic inclusions in epsilon-near-zero media,” *Phys. Rev. B*, vol. 75, p. 075119, Feb 2007. [Online]. Available: http://link.aps.org/doi/10.1103/PhysRevB.75.075119

[79] M. Hentschel, M. Schaferling, T. Weiss, N. Liu, and H. Giessen, “Three dimensional chiral plasmonic oligomers,” *Nano Letters*, vol. 12, no. 5, pp. 2542–2547, 2012, pMID: 22458608. [Online]. Available: http://dx.doi.org/10.1021/nl300769x

[80] E. Plum, J. Zhou, J. Dong, V. A. Fedotov, T. Koschny, C. M. Soukoulis, and N. I. Zheludev, “Metamaterial with negative index due to chirality,” *Phys. Rev. B*, vol. 79, p. 035407, Jan 2009. [Online]. Available: http://link.aps.org/doi/10.1103/PhysRevB.79.035407

[81] H. N. S. Krishnamoorthy, Z. Jacob, E. Narimanov, I. Kretzschmar, and V. M. Menon, “Topological transitions in metamaterials,” *Science*, vol. 336, no. 6078, pp. 205–209, 2012. [Online]. Available: http://science.sciencemag.org/content/336/6078/205

[82] V. R. Almeida, Q. Xu, C. A. Barrios, and M. Lipson, “Guiding and confining light in void nanostructure,” *Opt. Lett.*, vol. 29, no. 11, pp. 1209–1211, Jun 2004. [Online]. Available: http://ol.osa.org/abstract.cfm?URI=ol-29-11-1209

[83] W. S., C. M. B., CounyF., BenabidF., M. A., K. C., C. H. B., and F. L., “Field enhancement within an optical fibre with a subwavelength air core,” *Nat Photon*, vol. 1, no. 2, pp. 115–118, 02 2007. [Online]. Available: http://dx.doi.org/10.1038/nphoton.2006.81

[84] T. F. Krauss, “Planar photonic crystal waveguide devices for integrated optics,” *physica status solidi (a)*, vol. 197, no. 3, pp. 688–702, 2003. [Online]. Available: http://dx.doi.org/10.1002/pssa.200303117

[85] J. D. Joannopoulos, P. R. Villeneuve, and S. Fan, “Photonic crystals: putting a new twist on light,” *Nature*, vol. 386, no. 6621, pp. 143–149, 03 1997. [Online]. Available: http://dx.doi.org/10.1038/386143a0

[86] C. M. Serpa-Imbett and H. E. Hernandez-Figueroa, "Novel bending loss reduction technique for the tm mode in soi-based waveguides," *IEEE Photonics Technology Letters*, vol. 28, no. 8, pp. 872–875, April 2016.

[87] S. Jahani and Z. Jacob, "Breakthroughs in photonics 2014: Relaxed total internal reflection," *IEEE Photonics Journal*, vol. 7, no. 3, pp. 1–5, June 2015.

[88] D. Pratap, S. A. Ramakrishna, J. G. Pollock, and A. K. Iyer, "Anisotropic metamaterial optical fibers," *Opt. Express*, vol. 23, no. 7, pp. 9074–9085, Apr 2015. [Online]. Available: http://www.opticsexpress.org/abstract.cfm?URI=oe-23-7-9074

[89] M. M. Hasan, D. S. Kumar, M. R. C. Mahdy, D. N. Hasan, and M. A. Matin, "Robust optical fiber using single negative metamaterial cladding," *IEEE Photonics Technology Letters*, vol. 25, no. 11, pp. 1043–1046, June 2013.

[90] E. J. Smith, Z. Liu, Y. Mei, and O. G. Schmidt, "Combined surface plasmon and classical waveguiding through metamaterial fiber design," *Nano Letters*, vol. 10, no. 1, pp. 1–5, 2010, pMID: 19368372. [Online]. Available: http://dx.doi.org/10.1021/nl900550j

[91] A. Baz, G. Bouwmans, L. Bigot, and Y. Quiquempois, "Pixelated high-index ring bragg fibers," *Opt. Express*, vol. 20, no. 17, pp. 18 795–18 802, Aug 2012. [Online]. Available: http://www.opticsexpress.org/abstract.cfm?URI=oe-20-17-18795

[92] M. Yan, N. A. Mortensen, and M. Qiu, "Engineering modes in optical fibers with metamaterial," *Frontiers of Optoelectronics in China*, vol. 2, no. 2, p. 153, 2009. [Online]. Available: http://dx.doi.org/10.1007/s12200-009-0024-x

[93] S. Atakaramians, A. Argyros, S. C. Fleming, and B. T. Kuhlmey, "Hollow-core waveguides with uniaxial metamaterial cladding: modal equations and guidance conditions," *J. Opt. Soc. Am. B*, vol. 29, no. 9, pp. 2462–2477, Sep 2012. [Online]. Available: http://josab.osa.org/abstract.cfm?URI=josab-29-9-2462

[94] M. C.-Z. Claudia Milena Serpa-Imbett and H. E. Hernandez-Figueroa, "Fibras vortex com revestimento de metamaterial anisotrópico. no. pedido

br1020170084973," *INPI (Instituto Nacional da Propiedade Intelectual)*, pp. 1–20, April 2017. [Online]. Available: https://gru.inpi.gov.br/pePI/jsp/patentes/PatenteSearchBasico.jsp

[95] C. Kachris and I. Tomkos, "A survey on optical interconnects for data centers," *IEEE Communications Surveys Tutorials*, vol. 14, no. 4, pp. 1021–1036, Fourth 2012.

[96] N. Zhao, X. Li, G. Li, and J. M. Kahn, "Capacity limits of spatially multiplexed free-space communication," *Nat Photon*, vol. 9, no. 12, pp. 822–826, 12 2015. [Online]. Available: http://dx.doi.org/10.1038/nphoton.2015.214

[97] S. Ö. Arik, D. Askarov, and J. M. Kahn, "Effect of mode coupling on signal processing complexity in mode-division multiplexing," *Journal of Lightwave Technology*, vol. 31, no. 3, pp. 423–431, Feb 2013.

[98] D. C. Kilper and H. Rastegarfar, "Energy challenges in optical access and aggregation networks," *Philosophical Transactions of the Royal Society of London A: Mathematical, Physical and Engineering Sciences*, vol. 374, no. 2062, 2016. [Online]. Available: http://rsta.royalsocietypublishing.org/content/374/2062/20140435

[99] J. D. Marconi, M. L. F. Abbade, C. M. Serpa-Imbett, and E. A. M. Fagotto, "Ultra-broadband two-pump optical parametric amplifier in tellurite waveguides with engineered dispersion," *Opt. Express*, vol. 25, no. 4, pp. 4268–4283, Feb 2017. [Online]. Available: http://www.opticsexpress.org/abstract.cfm?URI=oe-25-4-4268

[100] N. Bozinovic, S. Golowich, P. Kristensen, and S. Ramachandran, "Control of orbital angular momentum of light with optical fibers," *Opt. Lett.*, vol. 37, no. 13, pp. 2451–2453, Jul 2012. [Online]. Available: http://ol.osa.org/abstract.cfm?URI=ol-37-13-2451

[101] S. Golowich, N. Bozinovic, P. Kristensen, and S. Ramachandran, "Complex mode amplitude measurement for a six-mode optical fiber," *Opt. Express*, vol. 21, no. 4, pp. 4931–4944, Feb 2013. [Online]. Available: http://www.opticsexpress.org/abstract.cfm?URI=oe-21-4-4931

[102] J. W. Nicholson, A. D. Yablon, S. Ramachandran, and S. Ghalmi, “Spatially and spectrally resolved imaging of modal content in large-mode-area fibers,” *Opt. Express*, vol. 16, no. 10, pp. 7233–7243, May 2008. [Online]. Available: http://www.opticsexpress.org/abstract.cfm?URI=oe-16-10-7233

[103] D. M. Nguyen, S. Blin, T. N. Nguyen, S. D. Le, L. Provino, M. Thual, and T. Chartier, “Modal decomposition technique for multimode fibers,” *Appl. Opt.*, vol. 51, no. 4, pp. 450–456, Feb 2012. [Online]. Available: http://ao.osa.org/abstract.cfm?URI=ao-51-4-450

ANEXOS

A. PUBLICATIONS

My publications can be consulted online in:

1. SCOPUS: By the Scoups IDs: 56689999700, 55832754600.
2. ORCID: By the Orcid ID: 0000-0002-1420-0084
3. COLCIENCIAS-CvLac: By my name: Claudia Milena Serpa Imbett

Journal Publications, Patent and Conference papers derived from this doctoral work are listed as follow:

A. Journal Publications

1. **Claudia M. Serpa-Imbett**, and Hugo E. Hernandez-Figueroa. "*Novel Bending Loss Reduction Technique for the TM Mode in SOI-Based Waveguides*". Photonic Technology Letters. Vol. 28, no. 8, April 15, 2016. DOI: 10.1109/LPT.2016.2515263. Impact Factor: 1.945. (see the paper attached from pag. 129-132)
2. Jorge D. Marconi, Marcelo l. F. Abbade, **Claudia M. Serpa-Imbett**, and Eric a. M. Fagotto. "*Ultra-broadband two-pump optical parametric amplifier in tellurite waveguides with engineered dispersion*". Optics Express. 4268, Vol. 25, No. 4, 20 Feb 2017. DOI: 10.1364/OE.25.004268. Impact Factor: 3.148. (see the paper attached from pag. 172-187)

B. Manuscript to be submitted in a Journal

1. Jose A. Borda-Hernandez, **Claudia M. Serpa-Imbett**, and Hugo E. Hernandez-Figueroa. "*Vortex Polymer Optical fiber with 72 OAM states*". To be submitted to Journal of Lightwave Technology. Impact Factor: 2.567.

C. Patent

1. **Claudia Milena Serpa-Imbett**, Mateus Corato-Zanarella and Hugo E. Hernandez-Figueroa. "*Fibras Vortex com Revestimento de Metamaterial Anisotrópico*". No. Pedido BR1020170084973. INPI (Instituto Nacional da Propiedade Intelectual) Brazil. (Patent Pending). Search online in: https://gru.inpi.gov.br/pePI/jsp/patentes/PatenteSearchBasico.jsp. (see the document attached from pag. 133-171)

D. Conference works

1. **C. Serpa** and H. E. Hernandez-Figueroa. "*Reduction of Bending Loss for the TM mode in a strip-waveguide using a metamaterial in SOI-based platform,*" in Latin America Optics and Photonics Conference, (Optical Society of America, 2016), paper LTu2A.3. DOI: 10.1364/LAOP.2016.LTu2A.3

2. J.D. Marconi, M. Abbade, **C. M. Serpa-Imbett**, J. Cordoba-Ramirez, and E. Fagotto, "*Broadband two-pump parametric amplifier in engineered dispersion tellurite waveguides,*" in Latin America Optics and Photonics Conference, (Optical Society of America, 2016), paper LTu4A.11.DOI: 10.1364/LAOP.2016.LTu4A.11.

3. E. LAMILLA, I. Aldaya, **C. M. Serpa**, P. Jarshel, and P. C. Dainese, "*Modal Content in a 7-cell Hollow-Core Photonic Bandgap Fiber and its Dependence with Offset Launch Conditions,*" in Latin America Optics and Photonics Conference, (Optical Society of America, 2016), paper LTu3C.3. DOI: 10.1364/LAOP.2016.LTu3C.3

4. O. Florez Peñaloza, P. F. Jarschel, **C. Serpa**, C. M. Cordeiro, and P. C. Dainese, "*Brillouin Scattering in Silica Microwires,*" in Latin America Optics and Photonics Conference, OSA Technical Digest (online) (Optical Society of America, 2014), paper LTh2A.3.

5. **C. M. Serpa-Imbett**, J. Marin-Alfonso, C. Gomez-Santamaria, L. Betancur and F. Amaya-Fernandez. "*Performance comparison of a fiber optic communication system based on optical OFDM and an optical OFDM-MIMO with Alamouti code by using numerical simulations*". Proc. SPIE 9043, 2013 International Conference on Optical Instruments and Technology: Optoelectronic Devices and Optical Signal Processing, 90430F (December 23, 2013); DOI: 10.1117/12.2035687.

6. **C. M. Serpa-Imbett**, J. Marin-Alfonso, C. Gomez-Santamaria, L. Betancur and F. Amaya-Fernandez, "*Performance of spatially multiplexed systems based on numerical simulations of OFDM-MIMO in a two-core fiber with low coupling, and a few mode fiber with high DGD*". Microwave and Optoelectronics Conference (IMOC), 2013 SBMO/IEEE MTT-S International, Rio de Janeiro, 2013, pp. 1-4. DOI: 10.1109/IMOC.2013.6646484.

7. **C. M. Serpa-Imbett**, J. Marin-Alfonso, L. Betancurt and F. Amaya-Fernandez, "*Theoretical investigation of pilot allocation for pilot-aided phase channel estimation in optical-orthogonal frequency division multiplexed fiber system*". Communications and Computing (COLCOM), 2013 IEEE Colombian Conference on, Medellin, 2013, pp. 1-5. DOI: 10.1109/ColComCon.2013.6564830.

Novel Bending Loss Reduction Technique for the TM Mode in SOI-Based Waveguides

Claudia M. Serpa-Imbett, *Student Member, IEEE*, and Hugo E. Hernandez-Figueroa, *Senior Member, IEEE*

***Abstract*— A new approach to reduce the bending loss of the fundamental quasi-transverse magnetic mode in optical waveguides is presented. A much lower bending loss is achieved by designing waveguides that use as substrate or cladding an anisotropic metamaterial made of multilayers of thin films of germanium and porous silica instead of a conventional silica substrate or cladding. We numerically demonstrate a reduction in the bending loss of up to ∼3 dB/90° for a silicon-on-insulator (SOI) waveguide of the standard core size (500 x 220 nm), as well as, up to ∼10 dB/90° for a sub-wavelength SOI waveguide of core size (372 × 186 nm), even considering the high absorption of the germanium layers in the cladding, both designed to operate at 1550 nm.**

***Index Terms*— Anisotropic media, integrated optics, silicon on insulator (SOI), optical bent waveguides, metamaterial.**

I. INTRODUCTION

MINIATURIZATION and dense photonic integration of optical devices on small chips using elements, such as, ring resonators, and complex waveguide interconnections, can be enabled by using small bends [1], however, it is mandatory that bending losses must be drastically reduced. These losses depend on polarization in planar waveguides with high index contrast, such as the ones fabricated using Silicon-on-Insulator (SOI) platforms. In SOI bent waveguides, operating at 1550 nm, the fundamental quasi-Transverse Electric (TE) mode is more confined and exhibits lower losses than the fundamental quasi-Transverse Magnetic (TM) mode. This behavior is not compensated just increasing the index contrast in the waveguide, and becomes much more evident for small bend radii, in the order of few micrometers, when the latter leaks much more power into the substrate/cladding than the former [2], [3]. This prevents the realization of dual-polarized highly integrated photonics circuits.

Several schemes have been proposed to confine the fundamental quasi-TM mode in 90 deg bent waveguides, e.g., in [4], multilayer in air trenches and silicon-strip mirrors were adopted for bent waveguides with low index contrast; and in [5], almost lossless bends were designed using waveguide with anisotropic epsilon near-zero metamaterials; therefore it is evident that non-conventional strategies – i. e., other than just increasing the index contrast – are required to be explored.

In this letter, we extend the new strategy for light confinement introduced by S. Jahani and Z. Jacob in [6], to reduce the bending loss in optical waveguides. This consists of controlling the momentum of evanescent waves in waveguides using as cladding an anisotropic metamaterial (AMM). They recently showed that if a dielectric 1D-cross-section waveguide is embedded into a transparent anisotropic metamaterial cladding, the fundamental TM mode can be tightly confined inside the core irrespective of core size; similarly, in 2D-cross-section waveguides, the HE_{11} mode in an optical fiber can also be confined using that kind of cladding [6], [7]. Here, we will demonstrate that such AMM can also reduce the bending loss of the fundamental quasi-TM mode of SOI waveguides.

II. BENDING LOSS AND CONFINEMENT FACTOR IN BENT WAVEGUIDES

We used the recently proposed transformation optics (TO) technique [8], [9] to compute the waveguide bending loss and modal confinement of light propagating through a 90 deg bend shown in Fig. 1. TO considers that the light propagation along a bent waveguide is equivalent to the light propagation along a straight waveguide, through a coordinate transformation that leads to rewrite the permittivity and permeability as tensors in the new coordinate system. So, one can solve the eigenmodes supported by the straight waveguide in the new coordinate system by taking into account the anisotropic material parameters, and to use the effective index of the eigenmodes to calculate the bending loss, BL for a 360° turn with a length of $2\pi R$, of each mode given by the equation:

$$BL = 1 - \exp(-n_2 k_0 2\pi R) \tag{1}$$

where, n_2 is the imaginary part of the computed mode effective index, k_0 is the light propagation constant in vacuum, and R is the bend radius.

We are also interested in the mode distribution of the bent waveguides to see how much the quasi-TE and quasi-TM modes are leaking to the surrounding medium. This leaky behavior is quantified through the confinement factor, CF, which is the net power of the mode in the core, P_{core}, respect to the total power in the waveguide, P_{total}, $(CF = P_{core}/P_{total})$.

Manuscript received October 25, 2015; revised December 3, 2015; accepted December 29, 2015. Date of publication January 8, 2016; date of current version March 10, 2016. This work was supported by the Brazilian C&T Institute FOTONICOM through National Council of Technological and Scientific Development under Project 574017/2008-9 and Fundação de Amparo à Pesquisa do Estado de São Paulo under Project 2008/57857-2. The work of C. M. Serpa-Imbett was supported by a Scholarship from Colombian Agency Enlaza Mundos and Brazilian Agency Coordenação de Aperfeiçoamento de Pessoal de Nível Superior.

C. M. Serpa-Imbett was with Pontificia Bolivariana University, Medellín 80305, Colombia. She is now with the Department of Communications, School of Electrical and Computer Engineering, University of Campinas, Campinas 13083-852, Brazil (e-mail: claumise@decom.fee.unicamp.br).

H. E. Hernandez-Figueroa is with the Department of Communications, School of Electrical and Computer Engineering, University of Campinas, Campinas 13083-852, Brazil (e-mail:hugo@decom.fee.unicamp.br).

Color versions of one or more of the figures in this letter are available online at http://ieeexplore.ieee.org.

Digital Object Identifier 10.1109/LPT.2016.2515263

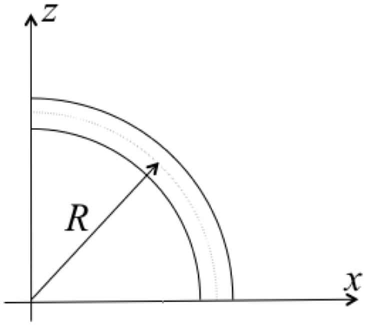

Fig. 1. Top view of a waveguide's core forming a 90 deg bend with radius R.

III. SIMULATION OF BENT WAVEGUIDES

Adopting a wavelength of 1550 nm, we consider the light propagating along a waveguide forming a 90 deg bend. The top view of the bend waveguide is schematically shown in Fig. 1. The bend plane is parallel to the xz plane with R being the bending radius defined from the origin to the center of the waveguide.

We will investigate two cases: a conventional strip-type waveguide and a sub-wavelength (SW) channel-type waveguide illustrated in Figs. 2(a) and 5(a), respectively. Following the confinement scheme here proposed, the substrate of the former and the cladding of the latter will be replaced by an AMM, which consists of a periodic multilayer combination, with piled layers parallel to the xz plane, made of high-index and low-index dielectrics with layer thicknesses and periodicities well below the wavelength of the light to ensure that the structure behaves as a homogeneous material, far away from its band-gap.

Effective medium theory for this super-lattice predicts a homogenized medium independent to the periodicity [10]. The anisotropic material has the dielectric tensor components given by:

$$\varepsilon_{\parallel} = \varepsilon_{high}\rho + \varepsilon_{low}(1-\rho) \tag{2}$$

$$1/\varepsilon_{\perp} = \rho/\varepsilon_{high} + (1-\rho)/\varepsilon_{low} \tag{3}$$

where $\varepsilon_{\parallel}$ and $\varepsilon_{\perp}$ are the dielectric constant parallel and perpendicular, respectively, and ρ is the fill fraction of the high-index material [6], [11]. In our simulation, we use an AMM alternating high-index thin films of Ge ($n_{Ge} \approx 4.3$, $k_{Ge} \approx 0.01$) [12], and ultra low-index porous silica ($n_{SiO2\_Pou} \approx 1.05$, $k_{SiO2\_Pou} \approx 0$). Layers of porous silica have been deposited on Si substrate as antireflection coatings eliminating Fresnel reflection from an air interface over a broad range of optical wavelengths [13]. We emphasize that the band-edge loss at 1550 nm of germanium is not a fundamental impediment in the performance of our structure [6]. For an optimal fill fraction of $\rho = 0.7$ is achieved a maximum anisotropy $(\varepsilon_{z/}\varepsilon_{x})$ at 1550 nm. Multilayer effective medium theory predicts a uniaxial anisotropic medium with dielectric permittivity of $\varepsilon_z \approx 10.2$ and extinction coefficient $k_z \approx 0.008$, and $\varepsilon_y \approx 3.8$, $k_x \approx 0$, where $\varepsilon_{y=}\varepsilon_x$, $k_x = k_y$. This AMM is depicted in Figs. 2(b) and 5(b).

The bend radius varies from 2 μm up to 10 μm, therefore, we use uniaxial PMLs (Perfectly Matched Layers) with thickness of 1 μm to truncate the right and bottom edges of the computational window since the radiated mode field will leak into these two directions [2], [9].

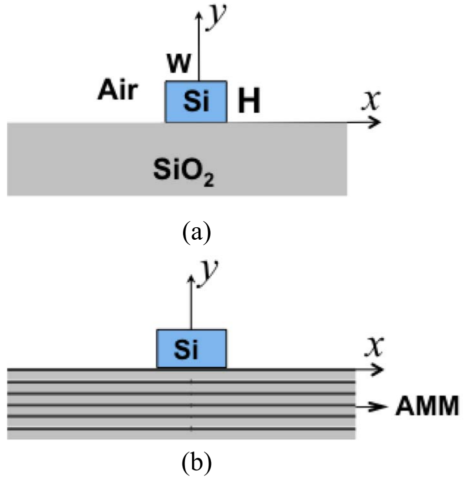

(a)

(b)

Fig. 2. Cross-section of the strip-type waveguide with (a) silica-substrate (conventional), and (b) AMM-substrate (our proposal).

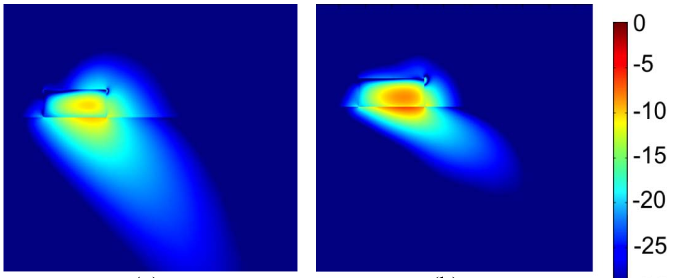

(a) (b)

Fig. 3. MPV for the fundamental quasi-TM mode in Log-scale. For a bend strip-type waveguide with (a) silica-substrate (conventional) and (b) AMM-substrate (our proposal). Bend radius of 2 μm.

IV. NUMERICAL RESULTS

A. Strip-Type Waveguides

We consider a SOI strip-type waveguide with a standard core size (W × H) of 500 × 220 nm in silicon ($n_{Si} \approx 3.48$) lying on top of a silica ($n_{SiO2} \approx 1.46$) substrate, and air as the top cladding. We have chosen this waveguide because is widely adopted in the fabrication of SOI photonic circuits [2]. To improve the mode confinement of this SOI waveguide we propose a new geometry, which consists of replacing the substrate's material, silica, by the AMM previously described. The cross sections of the two waveguides are schematically shown in Fig. 2.

Fig. 3 shows the computed cross-section distribution of the modulus of the Poynting Vector (MPV) in the propagation direction z for the fundamental quasi-TM mode in Log-scale, for a bend radius of 2 μm. The strong leaky behavior for the silica-substrate waveguide, Fig. 3(a), is in agreement with the results reported in [2], however, much less leakage is observed for the AMM-substrate waveguide, Fig. 3(b).

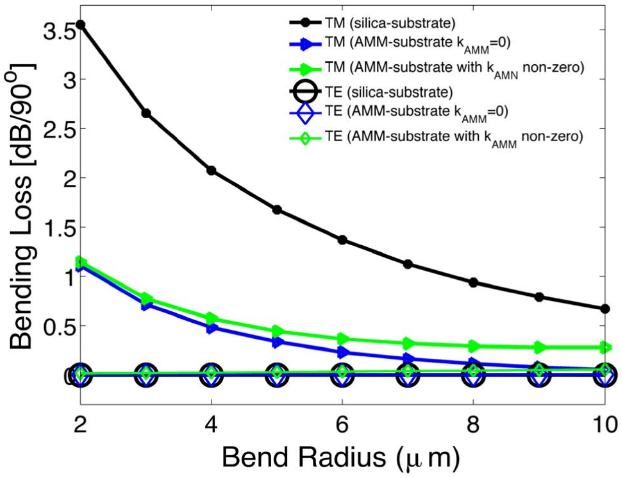

Fig. 4. BL curves as a function of the bend radius for the strip-type waveguides.

We find that the fundamental quasi-TM mode has a *CF* of 38% in the straight silica-substrate waveguide, in contrast to 57% for the straight AMM-substrate waveguide, i.e., 1.5 times more confined. However, this *CF* value decreases to 23% when the silica-substrate waveguide is bent with a radius of 2 μm, but in contrast, the AMM-substrate waveguide's *CF* for that radius goes down to 43%, which is even superior to the straight silica-substrate waveguide's *CF*.

A reduction in bending loss is expected as a consequence of the increase in the confinement. This loss is assessed through Eq. 1. Fig. 4 shows the *BL* for 90° turns as a function of the radius for both the fundamental quasi-TE, and fundamental quasi-TM modes. We observe that for either the silica-substrate or the AMM-substrate, the former exhibits a negligible bending loss for all computed bend radii. The latter, as expected, exhibits a much higher bending loss, however, we observe a loss reduction of about 2.5 dB/90° at a bend radius of 2 μm for the AMM-substrate when compared to the silica-substrate. As it is shown in Fig. 4 (green line), the germanium absorption of the AMM cladding does not significantly affect the performance of the structure. This is due to the high confinement of TM mode on the core, which is a consequence of the presence of the metamaterial.

Besides that, for both substrates *BL* decreases when the bend radius increases. Almost negligible *BL* is attained for the AMM-substrate when the bend radius is about 10 μm, in contrast considering the silica-substrate for that bend radius, the fundamental quasi-TM mode's *BL* is still high, approximately 0.7 dB/90°.

B. Channel-Type Waveguide

We also consider a sub-wavelength (SW) SOI channel-type waveguide inspired on the approach described in [7], with a core size (W×H) of 372 × 186 nm made of silicon ($n_{Si} \approx 3.48$) and embedded into silica ($n_{SiO2} \approx 1.46$). To improve the mode confinement of this SOI waveguide a new geometry is proposed here, which consists of replacing the cladding's material, silica, by the AMM described in Section III. The cross sections of the two waveguides are schematically shown in Fig. 5.

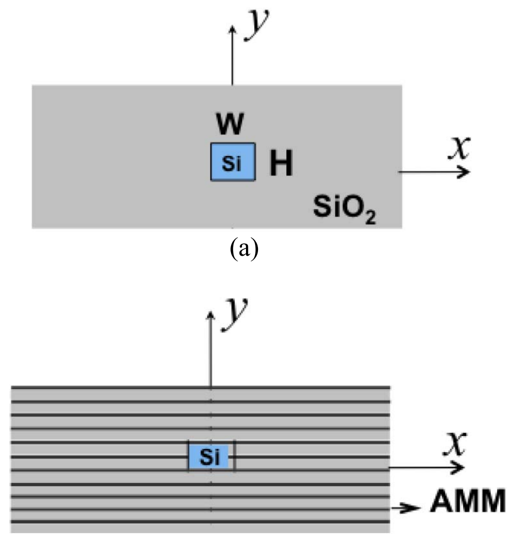

(a)

(b)

Fig. 5. Cross-sections of the SW channel-type waveguide with (a) silica-cladding, and (b) AMM-cladding (our proposal).

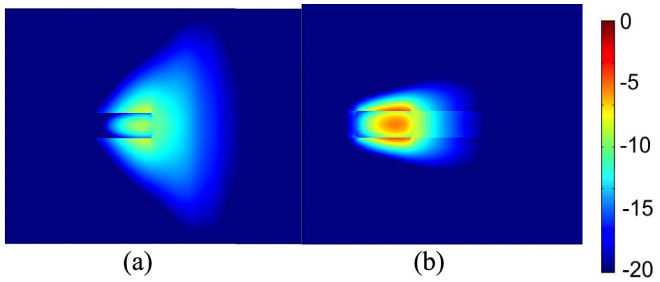

(a) (b)

Fig. 6. MPV for the fundamental quasi-TM mode in Log-scale. For a bend channel-type waveguide with (a) silica-substrate (conventional) and (b) AMM-substrate (our proposal). Bend radius of 2 μm.

Fig. 6 shows the computed MPV's cross-section distribution for the fundamental quasi-TM mode in Log-scale, for a bend radius of 2 μm. As before, leaky behavior is more noticeable for the silica-cladding waveguide, see Fig. 6(a), than for the AMM-cladding waveguide, see Fig. 6(b).

We find that the fundamental quasi-TM mode has a *CF* of 7% in the straight silica-cladding waveguide, in contrast to 93% for the straight AMM-cladding waveguide, i.e., 13.3 times more confined. However, this *CF* value decreases to 6% when the silica-cladding waveguide is bent with a radius of 2 μm, but in contrast, the AMM-cladding waveguide's *CF* for that radius goes down to 28%, which is 4 times superior to the straight silica-substrate waveguide's *CF*.

Fig. 7(a) shows the *BL* for 90° turns as a function of the radius for both the fundamental quasi-TE and quasi-TM modes.

As in the strip-type waveguides we also observe a negligible BL for the fundamental quasi-TE polarized mode for either silica-cladding or AMM-cladding waveguides. The fundamental quasi-TM polarized mode exhibits a high *BL*, even higher

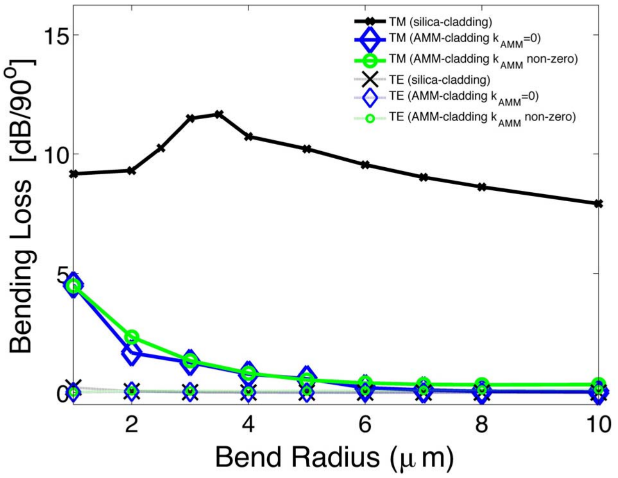

Fig. 7. BL curves as a function of the bend radius for the channel-type waveguides.

compared with the strip-type waveguides analyzed previously, however, we observe a significant loss reduction of about 8 dB/90° at a bend radius of 2 μm using our proposed AMM-cladding waveguide. As it is shown in Fig. 7 (green line), the germanium absorption of the AMM cladding does not significantly affect the performance of the structure. In this case, the TM mode is almost 13.3 times more confined as consequence of the presence of the metamaterial, therefore is much more negligible the effect of the germanium absorption in this SW structure than in the standard structure.

One can see an increase of the bending loss for greater bending radii for the silica-cladding waveguide. This is a typical situation for SW SOI waveguides, which feature a trade-off between the mode confinement and the propagation loss [9]. We can conclude that our proposed AMM-cladding waveguide drastically reduces *BL*: more than 5 dB/90° for all analyzed bending radii. This effect comes from the fact that the evanescent field is more influenced by the presence of the AMM in waveguides at SW core scale, than the waveguides of larger core size [6].

V. CONCLUSION

In summary, we have shown that it is possible to confine the fundamental quasi-TM mode in bent waveguides using bend radii of few micrometers, by using the AMM strategy presented here. We have compared the *CF* and the *BL* as a function of the bend radius for waveguides with a 90 deg bend. We have shown that there is a dramatic reduction of bending loss in the two types of SOI waveguides analyzed with a negligible effect of the germanium absorption in both structures. This scheme would allow us to use both TE and TM polarizations, improving in this way the performance of a wide variety of optical integrated devices.

ACKNOWLEDGMENT

The authors thank Dr. Lucas Heitzmann Gabrielli and Dr. Jorge Diego Marconi for the fruitful discussions.

REFERENCES

[1] C. Manolatou, S. G. Johnson, S. Fan, P. R. Villeneuve, H. A. Haus, and J. D. Joannopoulos, "High-density integrated optics," *J. Lightw. Technol.*, vol. 17, no. 9, pp. 1682–1692, Sep. 1999.

[2] K. Kakihara, N. Kono, K. Saitoh, and M. Koshiba, "Full-vectorial finite element method in a cylindrical coordinate system for loss analysis of photonic wire bends," *Opt. Exp.*, vol. 14, no. 23, pp. 11128–11141, Nov. 2006.

[3] Y. A. Vlasov and S. J. McNab, "Losses in single-mode silicon-on-insulator strip waveguides and bends," *Opt. Exp.*, vol. 12, no. 8, pp. 1622–1631, Apr. 2004.

[4] L. Li, G. P. Nordin, J. M. English, and J. Jiang, "90° bends in low index contrast waveguides," *Proc. SPIE*, vol. 4987, pp. 106–112, Jun. 2003.

[5] J. Luo, P. Xu, H. Chen, B. Huo, L. Gao, and Y. Lai, "Realizing almost perfect bending waveguides with anisotropic epsilon-near-zero metamaterials," *Appl. Phys. Lett.*, vol. 100, no. 22, pp. 221903-1–221903-5, 2012.

[6] S. Jahani and Z. Jacob, "Transparent subdiffraction optics: Nanoscale light confinement without metal," *Optica*, vol. 1, no. 2, pp. 96–100, 2014.

[7] S. Jahani and Z. Jacob, "Photonic skin-depth engineering," *J. Opt. Soc. Amer. B*, vol. 32, no. 7, pp. 1346–1353, 2015.

[8] J. B. Pendry, D. Schurig, and D. R. Smith, "Controlling electromagnetic fields," *Science*, vol. 313, pp. 1780–1782, Jun. 2006.

[9] Z. Han, P. Zhang, and S. I. Bozhevolnyi, "Calculation of bending losses for highly confined modes of optical waveguides with transformation optics," *Opt. Lett.*, vol. 38, no. 11, pp. 1778–1780, Jun. 2013.

[10] G. W. Milton, *The Theory of Composites*. Cambridge, U.K.: Cambridge Univ. Press, 2002.

[11] P. B. Catrysse and S. Fan, "Transverse electromagnetic modes in aperture waveguides containing a metamaterial with extreme anisotropy," *Phys. Rev. Lett.*, vol. 106, no. 22, pp. 223902-1–223902-4, 2011.

[12] D. E. Aspnes and A. A. Studna, "Dielectric functions and optical parameters of Si, Ge, GaP, GaAs, GaSb, InP, InAs, and InSb from 1.5 to 6.0 eV," *Phys. Rev. B*, vol. 27, no. 2, pp. 985–1009, 1983.

[13] J. Q. Xi *et al.*, "Optical thin-film materials with low refractive index for broadband elimination of Fresnel reflection," *Nature Photon.*, vol. 1, no. 3, pp. 176–179, 2007.

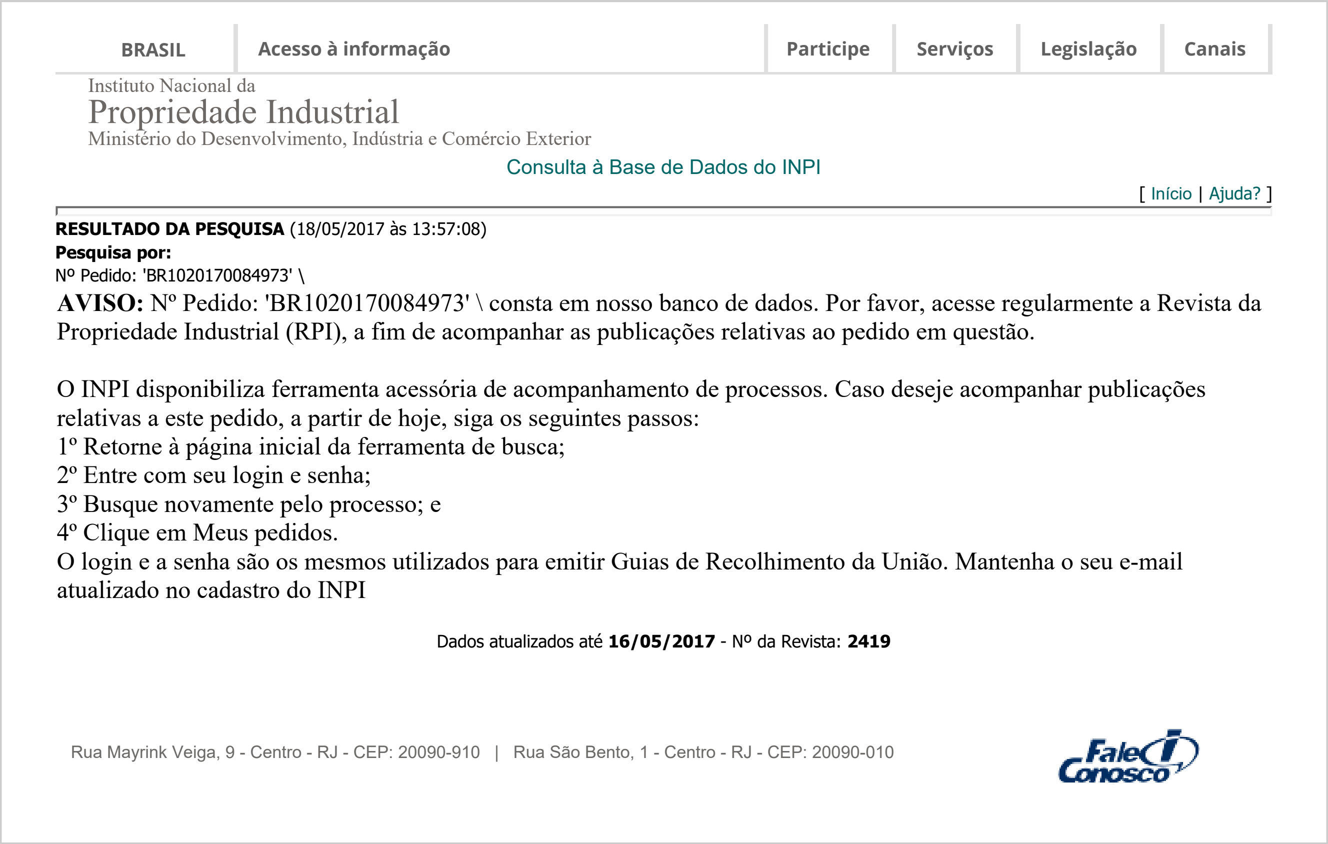

Instituto Nacional da
Propriedade Industrial
Ministério do Desenvolvimento, Indústria e Comércio Exterior

Consulta à Base de Dados do INPI

RESULTADO DA PESQUISA (18/05/2017 às 13:57:08)
Pesquisa por:
Nº Pedido: 'BR1020170084973' \

AVISO: Nº Pedido: 'BR1020170084973' \ consta em nosso banco de dados. Por favor, acesse regularmente a Revista da Propriedade Industrial (RPI), a fim de acompanhar as publicações relativas ao pedido em questão.

O INPI disponibiliza ferramenta acessória de acompanhamento de processos. Caso deseje acompanhar publicações relativas a este pedido, a partir de hoje, siga os seguintes passos:
1º Retorne à página inicial da ferramenta de busca;
2º Entre com seu login e senha;
3º Busque novamente pelo processo; e
4º Clique em Meus pedidos.
O login e a senha são os mesmos utilizados para emitir Guias de Recolhimento da União. Mantenha o seu e-mail atualizado no cadastro do INPI

Dados atualizados até **16/05/2017** - Nº da Revista: **2419**

Rua Mayrink Veiga, 9 - Centro - RJ - CEP: 20090-910 | Rua São Bento, 1 - Centro - RJ - CEP: 20090-010

< Uso exclusivo do INPI >

INPI INSTITUTO NACIONAL DA PROPRIEDADE INDUSTRIAL
PROTOCOLO GERAL
AUGUSTUL
25/04/2017 018170000989
15:04 DESP
BR 10 2017 008497 3

Espaço reservado para o protocolo | Espaço reservado para a etiqueta | Espaço reservado para o código QR

INPI INSTITUTO NACIONAL DA PROPRIEDADE INDUSTRIAL

INSTITUTO NACIONAL DA PROPRIEDADE INDUSTRIAL
Sistema de Gestão da Qualidade
Diretoria de Patentes

DIRPA	Tipo de Documento: **Formulário**	**DIRPA**	Página: **1/3**
Título do Documento: **Depósito de Pedido de Patente**		Código: **FQ001**	Versão: **01**
		Procedimento: **DIRPA-PQ006**	

Ao Instituto Nacional da Propriedade Industrial:
O requerente solicita a concessão de um privilégio na natureza e nas condições abaixo indicadas:

1. Depositante (71):

1.1 Nome: UNIVERSIDADE ESTADUAL DE CAMPINAS - UNICAMP

1.2 Qualificação: PESSOA JURÍDICA DE DIREITO PÚBLICO, AUTARQUIA ESTADUAL

1.3 CNPJ/CPF: 46.068.425/0001-33

1.4 Endereço Completo: CIDADE UNIVERSITÀRIA "ZEFERINO VAZ"

1.5 CEP: 13083-970

1.6 Telefone: 19 3521-5015 1.7 Fax: 19 3521-5210

1.8 E-mail: patentes@inova.unicamp.br

☒ continua em folha anexa

2. Natureza: ☒ Invenção ☐ Modelo de Utilidade ☐ Certificado de Adição

3. Título da Invenção ou Modelo de Utilidade (54):

"FIBRAS VORTEX COM REVESTIMENTO DE METAMATERIAL ANISOTRÓPICO"

☐ continua em folha anexa

4. Pedido de Divisão: do pedido Nº **Data de Depósito:**

5. Prioridade: ☐ Interna (66) ☐ Unionista (30)

O depositante reivindica a(s) seguinte(s):

País ou Organização do depósito	Número do depósito (se disponível)	Data de depósito

☐ continua em folha anexa

6. Inventor (72):

☐ Assinale aqui se o(s) mesmo(s) requer(em) a não divulgação de seus nome(s), neste caso não preencher os campos abaixo.

6.1 Nome: CLÁUDIA MILENA SERPA IMBETT

6.2 Qualificação: COLOMBIANA,SOLT

6.3 CPF: 236.916.558-82

6.4 Endereço Completo: RUA MAL. HERMES DA FONSECA, 66, EM CAMPINAS - SP

6.5 CEP: 13084-517

6.6 Telefone: 19 9989.49882 6.7 FAX:

6.8 E-mail: claumiseimbett@gmail.com

☒ continua em folha anexa

---

7. Declaração de divulgação anterior não prejudicial. ☐
Artigo 12 da LPI – período de graça.
Informe no item 11.13 os documentos anexados, se houver.

---

8. Declaração na forma do item 3.2 da Instrução Normativa nº 17/2013:

☐ Declaro que os dados fornecidos no presente formulário são idênticos ao da certidão de depósito ou documento equivalente do pedido cuja prioridade está sendo reivindicada.

---

9. Procurador (74):

9.1 Nome: FERNANDA LAVRAS COSTALLAT SILVADO

9.2 CNPJ/CPF: 295.166.068-57 9.3 API/OAB: 210.899

9.4 Endereço Completo: PROCURADORIA GERAL DA UNICAMP, EM CAMPINAS - SP

9.5 CEP: 13083-970

9.6 Telefone: 19 3521-4771 9.7 FAX: 19 3521-4944

9.8 E-mail: proc-geral@pg.unicamp.br

☐ continua em folha anexa

---

10. Listagem de sequências biológicas.
Informe nos itens 11.9 ao 11.12 os documentos anexados, se houver. ☐

11. Documentos Anexados:

(Assinale e indique também o número de folhas):
(Deverá ser indicado o número total de somente uma das vias de cada documento).

		Documentos Anexados	folhas
☒	11.1	Guia de Recolhimento da União (GRU).	1
☒	11.2	Procuração.	1
☐	11.3	Documentos de Prioridade.	
☐	11.4	Documento de contrato de trabalho.	
☒	11.5	Relatório descritivo.	24
☒	11.6	Reivindicações.	2
☒	11.7	Desenho(s) (se houver). Sugestão de figura a ser publicada com o resumo: nº, 1 por melhor representar a invenção (sujeito à avaliação do INPI).	6
☒	11.8	Resumo.	1
☐	11.9	Listagem de sequências em arquivo eletrônico: _____nº de CDs ou DVDs (original e cópia).	
☐	11.10	Código de controle alfanumérico no formato de código de barras referente às listagem de sequências.	
☐	11.11	Listagem de sequências em formato impresso.	
☐	11.12	Listagem de sequências - Declaração de acordo com a Resolução INPI nº 70/2013.	
☐	11.13	Outros (especificar)	

12. Total de folhas anexadas: 35 **fls.**

13. Declaro, sob as penas da Lei que todas as informações acima prestadas são completas e verdadeiras.

CAMPINAS, SP, EM 04.04.2017
Local e Data

Assinatura e Carimbo

FERNANDA LAVRAS COSTALLAT SILVADO
Procuradora de Universidade Subchefe
Matrícula nº 309279
OAB/SP nº 210.899

1 Continuação dos dados do depositante/interessado:

1.2 Qualificação: UNIVERSIDADE ESTADUAL DE CAMPINAS – UNICAMP, pessoa jurídica de direito público, autarquia estadual devidamente inscrita no CNPJ sob nº 46.068.425/0001-33 e isenta de inscrição estadual.

1.4 Endereço completo: Cidade Universitária "Zeferino Vaz" – Distrito de Barão Geraldo, em Campinas – SP – CEP 13083-970

6. Dados dos outros dois inventores:

6.1 Nome**: MATEUS CORATO ZANARELLA**
6.2 Qualificação: brasileiro, solteiro, estudante de graduação
6.3 CPF Nº 429.285.928-06
6.4 Endereço completo: Rua Ângelo Lavezzo, 111, Centro, em Amparo - SP
6.5 CEP: 55199-257
6.6 Telefone: (19) 9925.77395
6.7 FAX: (19)
6.8 E-Mail: mateuscorato@gmail.com

6.1 Nome**: HUGO ENRIQUE HERNANDEZ FIGUEROA**
6.2 Qualificação: brasileiro, casado, prof. universitário
6.3 CPF Nº 907.776.387-20
6.4 Endereço completo: Av. Albert Einstein, 400, Cidade Universitária "Zeferino Vaz", Distrito de Barão Geraldo, em Campinas - SP
6.5 CEP: 13083-852
6.6 Telefone: (19) 9925.77395
6.7 FAX: (19)
6.8 E-Mail: hugoehf@gmail.com

FIBRAS VORTEX COM REVESTIMENTO DE METAMATERIAL ANISOTRÓPICO

Campo da invenção:

[1] A presente invenção se insere na área de engenharia de telecomunicações e refere-se mais precisamente a uma nova configuração / geometria de fibra óptica para promover a propagação de mais modos com menos interferência. Nesta nova geometria, aumentou-se o número de modos de OAM (momento angular orbital, do inglês: *orbital angular momentum*) - ou seja, do tipo que utiliza feixes de laser em forma de rosca conhecidos como vórtices ópticos - em relação às geometrias convencionais das fibras de OAM (núcleo sólido e oco) visando, principalmente, a obtenção de melhores valores de pureza de modos sob perturbações externas - tais como curvatura - quando comparado aos resultados conseguidos com o uso das fibras do atual estado da técnica.

[2] Cabe ressaltar que a principal aplicação dessa invenção são comunicações Ópticas baseadas em fibra óptica, multiplexação espacial, multiplexação por modos numa fibra óptica usando modos OAM, e geração e propagação de modos OAM usando fibras vórtice (ou vortex).

Fundamentos da invenção:

[3] Conforme é de conhecimento dos versados no assunto, o Amplificador Dopado com Érbio (EDFA, do inglês: *Erbium Doped Fiber*) e as tecnologias de Multiplexação por Comprimento de Onda (WDM, do inglês: *wavelength-division multiplexing*) desenvolvidos na década de 1990 permitiram a transmissão de grandes quantidades de dados nos sistemas de comunicações ópticas atuais. Aplicações de Internet, como vídeo-sob-demanda (VOD, do inglês: *video-on-demand*) em alta definição, transmissão de vídeo de ultra alta definição e

cinema digital, geram um crescimento exponencial para a demanda de largura de banda nas redes de comunicações ópticas. Assim, presume-se que em breve a demanda atingirá o assim chamado "limite de Shannon" não-linear, que é o limite de capacidade teórica da fibra monomodo de sílica convencional.

[4] Ocorre que se estimarmos um crescimento anual de 30% a 60% da demanda, em um período de 5 a 10 anos seriam necessários sistemas comerciais operando acima do "limite de Shannon", o que causaria um colapso nas transmissões devido à inevitável crise de esgotamento de capacidade das redes ópticas. A fim de evitar que se chegue a tal situação, a comunidade científica tem procurado outras opções, e uma delas considera a antiga noção de que as fibras podem suportar facilmente centenas de modos espaciais. Esta tecnologia de multiplexação é chamada de Multiplexação por Divisão de Espaço (SDM, do inglês: *Space-Division Multiplexing*) é a candidata mais promissora para a superação da crise de capacidade das redes ópticas.

[5] O termo "Multiplexação por Divisão de Espaço", no entanto, inclui dois conceitos diferentes: o primeiro relacionado com a transmissão de informações através de várias fibras paralelas ou, em outras palavras, através de fibras de múltiplos núcleos (MCFs, do inglês: *multicore fibers*); e o segundo envolvendo a utilização de múltiplos caminhos de dados em uma única fibra - ou seja, a transmissão de informações usando diferentes modos, por meio do uso de fibras multimodo (MMF, do inglês: *multi-mode fibers*) ou fibras com poucos modos (FMF, do inglês: *few-mode fibers*) conforme pode ser observado na **Figura 1** anexa. Isto é chamado

de Multiplexação por Divisão de Modo (MDM, do inglês: *Mode-Division Multiplexing*) e apresenta um grande potencial para aumentar a capacidade das redes ópticas já que, como no caso das tecnologias de WDM, uma única fibra é usada para transmitir múltiplos canais independentes.

[6] Na Multiplexação por Divisão de Modos, cada modo pode transportar um canal de dados independente e a ortogonalidade permite uma (de)multiplexação eficiente. Dentre os vários conjuntos de bases modais conhecidos, o mais significativo para a solução do problema técnico em questão se baseia no momento angular orbital (OAM) da luz. Outras são baseadas em feixes vetoriais cilíndricos (CVBs, do inglês: *cylindrical vector beams*) e feixes similares a Hermite-Gauss (HG) gerados por diferentes combinações lineares de CVBs, também conhecidos como modos linearmente polarizados (LP, do inglês: *linearly polarized*). Esses conjuntos são suportados por fibras multimodo de tipos diferentes (núcleo sólido ou oco) para enlaces ópticos curtos e longos, como foi recentemente demonstrado em vários trabalhos. Essa nova tecnologia apresenta duas alternativas: o uso de fibras especiais que permitem a transmissão de modos OAM com baixo acoplamento entre si (baixo *crosstalk)*, sem necessitar de processamento digital de sinais (DSP, do inglês: *digital signal processing*) externo baseado em técnicas de múltiplas entradas e múltiplas saídas (MIMO, do inglês: *multiple-input multiple-output)*; e o uso de fibras simples como as FMFs, mas necessitando de processamento MIMO para separar os canais. Ambas as opções têm sido exploradas nos últimos anos, porém, a fim de alcançar um sistema de comunicação totalmente fotônico, deve-se evitar o

processamento digital de sinais.

[7] Um dos principais desafios para tornar essa tecnologia mais atraente está em permitir a integração com outras tecnologias, tais como WDM. A capacidade de integração conta com o conceito de paralelismo óptico, que foi introduzido para os formatos de modulação em quadratura, nos quais a fase e a amplitude do sinal são modulados independentemente, em um ou nos dois estados possíveis da polarização da luz. Mesmo considerando todas as estratégias atualmente adotadas para melhorar a capacidade dos sistemas de comunicação, no futuro próximo nenhuma delas poderá fornecer um caminho sustentável para superar a crise de capacidade óptica. Para dimensionar redes ópticas para as próximas décadas, o paralelismo óptico deve ser estendido para a única dimensão física que ainda não foi explorada: o espaço.

[8] No caso de vários caminhos ópticos (modos ou núcleos) que viajam numa fibra, há dois cenários a se considerar. O primeiro refere-se ao regime de acoplamento forte (tipicamente comprimentos > km): este esquema poderia ser implementado em fibras com um grande número de modos, que poderiam compartilhar, por exemplo, o mesmo amplificador óptico. O inconveniente neste caso é a complexidade dos esquemas de DSP MIMO para contornar o acoplamento entre os modos, que inevitavelmente se intensifica com o aumento no número de modos. O design das fibras deve ser mais complexo para alcançar um baixo atraso diferencial de grupo (*differential group delay*) e acopladores de modos mais complexos são necessários.

[9] O segundo cenário é o do Regime de acoplamento

fraco (tipicamente <km): o acoplamento (*crosstalk*) é menor e fibras mais simples podem ser utilizadas, mas o número de caminhos espaciais possíveis é limitado a uns poucos. O *crosstalk* entre os sinais poderia ser compensado por métodos computacionais que utilizam algoritmos de feedback de óptica adaptativa, os quais "revertem" o efeito do acoplamento enviando uma superposição adequada de modos na entrada, de forma que a saída seja o modo desejado. Entretanto, esta abordagem é limitada, já que o acoplamento é um processo aleatório que pode se alterar em intervalos de tempo da ordem de milésimos de segundo em fibras convencionais.

[10] Portanto, o método adaptativo pode ser problemático em sistemas de longa distância, nos quais o atraso de propagação do sinal pode ser de dezenas de milissegundos.

Estado da técnica

[11] Alguns documentos do estado da técnica já descrevem tentativas de minimizar o problema do limite de capacidade e instabilidade de transmissão como, por exemplo, o documento US20150093085, que revela uma fibra óptica (200) com núcleo de ar (202) revestido com metamaterial (204) dielétrico de geometria cilíndrica com seção transversal circular, ilustrado na **Figura 2** anexa. No entanto, o documento propõe uma conformação geométrica para fibra óptica para a propagação exclusiva de modos HE/EH, TM e TE sendo que, nesse caso, a fibra óptica não é capaz de propagar modos com momento angular orbital (OAM) estavelmente conforme o proposto na invenção em questão. Além disso, a fibra revelada no documento US20150093085 obrigatoriamente tem núcleo de ar (200) e, assim, para uma propagação no

núcleo, o metamaterial (204) do revestimento deve ter índice de refração transversal sempre menor do que 1; complementarmente, o núcleo (202) da fibra do documento citado tem que ser *subwavelength*, ou seja, seu tamanho tem que ser menor do que o comprimento de onda. Tais condições acabam por limitar demasiadamente as possibilidades de uso e capacidade da fibra.

[12] O documento WO2010127676 descreve uma fibra óptica que compreende uma região de núcleo obrigatoriamente oco se estendendo ao longo do eixo longitudinal e um revestimento de metamaterial circundando o núcleo. Diferentemente da invenção aqui proposta, tal configuração permite apenas a propagação de modos HE/EH, TM e TE - ou seja, não propaga modos com momento angular orbital (OAM) estavelmente, e o metamaterial é empregado como revestimento. Na invenção ora proposta, o núcleo da fibra pode ser sólido ou oco (ar), possui adicionalmente um anel de maior índice de refração onde são propagados os modos OAM e o metamaterial é empregado como revestimento, o que proporciona resultados diferentes.

[13] O documento US20160363726 refere-se a uma estrutura de guia de onda de núcleo oco para guiar um sinal eletromagnético, compreendendo: um material de núcleo compreendendo um índice de refração predeterminado, e uma estrutura de revestimento disposto sobre o material de núcleo, onde a estrutura de revestimento tem um índice de refração que é menor do que uma unidade, sendo que o revestimento compreende uma estrutura metamaterial de epsilon-quase-zero (ENZ, do inglês: epsilon-near-zero). No entanto, assim como ocorre com as anterioridades citadas acima, a estrutura em questão não permite a propagação

estável de modos com momento angular orbital (OAM) porque a fibra não tem a configuração do perfil de índice ora proposto e, nesse sentido, cabe esclarecer que a fibra óptica do presente pedido, além de permitir a propagação estável de modos OAM, também pode utilizar metamaterial ENZ.

[14] Percebe-se, assim, que o atual estado da técnica carece de soluções efetivas para promover o aumento da capacidade de transmissão das fibras ópticas e viabilizar o aumento do número de modos de OAM propagados e, simultaneamente, viabilizar uma propagação mais estável desses modos de OAM quando são submetidos a perturbações. Para solucionar esses problemas, a presente invenção propõe a adoção de um perfil de índice que compreende um metamaterial como revestimento externo/final em fibras de vórtice que podem ter núcleo sólido ou oco, proporcionando ainda grande amplitude de modos de uso e fabricação.

<u>Objetivos e vantagens da invenção:</u>

[15] Em função do exposto acima, e sabendo que a fibra óptica multimodo (MMF) é empregada em distâncias curtas e que o acoplamento entre os modos impede a propagação estável da informação, a presente invenção objetiva-se a solucionar o problema técnico da atual limitação na capacidade de transmissão das fibras ópticas conhecidas e dos problemas futuros que tal limitação pode impor às redes de transmissão tendo em vista o aumento de demanda atual e projetada para os próximos anos - que indica a iminência de um colapso indesejado.

[16] Conforme é do conhecimento dos versados no tema, existem fibras especiais que permitem a propagação estável de modos por longos comprimentos. Uma propagação estável

significa que a forma do modo não muda e ele não se acopla significativamente com outros modos para a distância de propagação relevante em questão. Tais fibras especiais são conhecidas como "fibras vórtice" (ou vortex), que, conforme estudos já realizados, propagam modos tipo OAM de forma estável por distâncias que podem ser de até dezenas de km.

[17] Em função disso, é um dos principais objetivos da presente invenção revelar a conjugação da utilização dessa nova classe de fibra multimodo (MMF) chamada de fibra vórtice com metamateirais anisotrópicos em sua fabricação - mais precisamente como material de revestimento externo.

[18] Portanto, é um dos principais objetivos da presente invenção apresentar meios para promover o aumento da capacidade de sistemas futuros de transmissão de dados baseados em fibras.

[19] É outro dentre os objetivos da invenção propor uma nova abordagem do design das ditas fibras de vórtice que, uma vez empregando metamateriais como revestimento, possa reduzir o acoplamento entre modos e aumentar o número de modos OAM propagados, além de permitir uma propagação mais estável desses modos quando a fibra estiver sob perturbações. Tais fibras vórtice, dado o design especial aqui proposto, serão capazes reduzir o acoplamento entre modos que impede a propagação estável de modos em fibras perturbadas, diminuindo, assim, a necessidade de equalização eletrônica externa e permitindo, consequentemente, uma propagação estável por comprimentos mais longos.

[20] No pedido de patente em questão, propõe-se uma extensão na abordagem de design dessa classe de fibras por meio da utilização de metamateriais anisotrópicos como

revestimento, com o intuito de diminuir ainda mais o acoplamento entre modos, aumentar o número de modos propagáveis de forma estável e melhorar sua estabilidade frente a perturbações que, lembre-se, ocorrem com frequência.

Breve descrição da invenção:

[21] Os objetivos acima mencionados são alcançados através do objeto da presente invenção: uma fibra óptica compreendendo ao menos um núcleo (10), ao menos um anel (20) intermediário e ao menos um revestimento de metamaterial (30), caracterizado pelo fato de que a dita fibra óptica (1) é uma fibra multimodo de vórtice que compreende: pelo menos um núcleo (10) sólido ou preenchido com ar; pelo menos um anel (20) intermediário adjacente ao núcleo (10), e ao menos uma camada distal de revestimento de metamaterial (30) adjacente à superfície externa do pelo menos um anel (20) intermediário, sendo que o dito revestimento de metamaterial (30) compreende um metamaterial anisotrópico dielétrico.

[22] Segundo uma concretização preferencial da invenção, o dito núcleo (10) deve apresentar índice de refração menor que o índice de refração do material do anel (20) intermediário.

[23] Preferencialmente o revestimento de metamaterial (30) será compreendido por células unitárias compostas por materiais isotrópicos dielétricos e pode ser pelo menos um substrato cooperante com cilindros (50) ou nano-bastões dispostos na porção interna no dito substrato - sendo que os ditos cilindros (50) ou nano-bastões cooperam com o substrato em duas ou mais camadas concêntricas e uniformes ou sendo dispostos de maneira não-uniforme na seção transversal da

fibra óptica (1). Cabe esclarecer que opcionalmente o metamaterial (30) pode ser produzido com um substrato de sílica, e os cilindros (50) podem ser ocos (preenchidos com ar) sem que com isso se fuja do escopo de proteção aqui reivindicada.

[24] Alternativamente ao menos uma parte do núcleo (10) pode ser preenchida com metamaterial, sendo que a invenção também pode compreender ao menos um anel (20) intermediário fabricado em metamaterial.

Breve descrição das figuras:

[25] Para obter uma total e completa visualização do objeto desta invenção, são apresentadas as figuras as quais se faz referências, conforme se segue.

[26] A **Figura 1** mostra diversos exemplos de seções transversais de uma fibra monomodo e de fibras multimodos (MMF) conhecidas no atual estado da técnica;

[27] A **Figura 2** mostra outro exemplo de construção do atual estado da técnica utilizando revestimento de metamaterial para o núcleo de uma fibra óptica;

[28] A **Figura 3** mostra a seção transversal de uma fibra óptica de acordo com uma concretização preferencial da invenção, compreendendo uma fibra óptica multimodo do tipo vórtice (ou vortex) para a transmissão de modos OAM com um revestimento externo (30) de metamaterial anisotrópico dielétrico;

[29] A **Figura 4** mostra um gráfico de quadrantes que combinam possibilidades de permissividade elétrica ε e permeabilidade magnética μ, listando elementos que podem ser utilizados para projetar metamateriais dielétricos específicos que podem ser empregados como revestimento das

fibras ópticas da presente invenção;

[30] A **Figura 5** ilustra um exemplo de casca de metamaterial consistindo em nano-bastões de alto índice de refração embutidos em um material dielétrico de baixo índice;

[31] A **Figura 6** mostra um detalhe ampliado de uma concretização preferencial da presente invenção, ilustrando o revestimento (30) e anel de fibra (20);

[32] A **Figura 7.1** mostra um gráfico que permite observar a diferença de índice efetivo em relação ao modo fundamental HE_{11} versus o comprimento de onda calculado numericamente para fibras vórtice com núcleo sólido e medidas geométricas de uma fibra de vórtice convencional. Já a **Figura 7.2** exibe os mesmos resultados para uma fibra vórtice de mesmas dimensões, mas com metamaterial como revestimento;

[33] A **Figura 8.1** mostra um gráfico que representa a diferença de índice efetivo entre os modos $HE_{l+1,1}$ e $EH_{l-1,1}$ para uma fibra convencional com núcleo de ar, enquanto a **Figura 8.2** mostra a mesma diferença obtida para uma fibra com revestimento em metamaterial conforme uma concretização da presente invenção que apresenta núcleo de ar (oco) e com as dimensões de uma fibra vórtice convencional, e

[34] A **Figura 9** mostra um gráfico que representa a diferença de índice efetivo entre os modos $HE_{l+1,1}$ e $EH_{l-1,1}$ no comprimento de onda das telecomunicações, 1550 nm, calculado numericamente para as ditas fibras com núcleo de ar, permitindo observar o aumento de mais um modo para a fibra vórtice com revestimento em metamaterial.

Descrição detalhada da invenção:

[35] A fim de auxiliar na compreensão da descrição a seguir, serão citados abaixo alguns conceitos importantes

para conhecimento do campo da invenção:

- Equalização: o termo *equalização* se refere a ajustar o sinal de saída distorcido para que seja o mais parecido possível ao sinal original. No caso em questão, as distorções do sinal que sai da fibra são geralmente oriundas do acoplamento entre os modos OAM.

-Fibras vórtice (ou vortex): são um tipo de fibra multimodo (MMF) que, dado o seu design especial, são capazes de reduzir o acoplamento entre modos OAM, diminuindo assim a necessidade de equalização eletrônica externa.

- Metamaterial: compreende uma distribuição cuidadosamente projetada de estruturas elementares que resulta num material artificial com propriedades efetivas não encontradas em materiais convencionais. Para isso, fabrica-se um meio composto por células unitárias (elementos) muito menores do que o comprimento de onda no qual o guia de onda (neste caso, a fibra óptica) opera.

- Acoplamento de modos: termo utilizado para denotar o intercâmbio de energia entre os modos de propagação de uma fibra, neste caso entre os modos OAM. Acoplamento modal é um dos principais fenômenos de propagação em fibras multimodo que impede uma propagação estável ou sem intercâmbio de energia entre os modos em fibras multimodo perturbadas. Como, na prática, sempre há perturbações, este problema está sempre presente.

- Degenerescência modal: dois modos são ditos degenerados quando possuem o mesmo índice efetivo, embora tenham distribuições espaciais diferentes. Quebrar a degenerescência entre modos significa aumentar a diferença entre seus índices efetivos até que estes possam ser considerados distintos para todos os efeitos práticos. De forma empírica, pode-se dizer que a degenerescência entre dois modos é quebrada quando a diferença de seus índices é $>10^{-4}$, o que permite uma propagação dos modos sem acoplamento significativo por distâncias da ordem de 1000 m. Modos vetoriais são as soluções exatas das equações de Maxwell que modelam a propagação de ondas eletromagnéticas num guia de onda. No caso em questão, uma fibra óptica é considerada um guia de onda circular. Como as fibras ópticas são guias de onda que confinam e propagam luz, estas soluções são consideradas distribuições espaciais de luz que viajam com uma velocidade de propagação inversamente proporcional ao índice efetivo. Em fibras ópticas multimodo convencionais de baixo contraste, ocorrem degenerescências entre diversos modos vetoriais. Nas fibras vórtice (também um tipo de fibra multimodo) os índices efetivos dos modos são mais separados quando comparados com os de uma fibra multimodo convencional. Na fibra vórtice proposta na invenção aqui revelada, a separação aumenta ainda mais com a presença do metamaterial no revestimento.

- Sistemas multiplexados por modos: um sistema multiplexado envia simultaneamente sinais pelo mesmo canal. Num sistema multiplexado por modos os sinais são os modos que compartilham o mesmo canal, que é a fibra óptica.

- Estruturas fotônicas: são estruturas que manipulam e guiam a luz, dentre as quais se encontram os guias de onda, como as fibras ópticas; já os sistemas fotônicos representam a mistura de estruturas fotônicas em um sistema de transmissão de luz.

- Momento angular orbital ou OAM: momento angular é uma quantidade física associada à rotação. No caso da luz, o momento angular pode ser separado em spin e orbital. O momento angular spin está associado às polarizações circulares esquerda e direita, nas quais o vetor campo elétrico E rotaciona ao redor do eixo principal do feixe. O momento angular orbital (OAM), por outro lado, está relacionado com a rotação do vetor de Poynting (S), que mede o fluxo de potência do feixe de luz, e com o perfil de fase do feixe. A luz pode ter ambos os tipos de momento angular e, no caso das fibras ópticas de vórtice, o OAM pode ser propagado estavelmente por distâncias longas.

- Modo OAM em fibra óptica: O modo OAM numa fibra óptica vem de combinações de modos híbridos $HE_{l+1,m}$ (par e ímpar) e $EH_{l-1,m}$ (par e ímpar) com uma diferença de fase de π/2 rad conforme as equações abaixo:

$$V_{l,m}^{\pm} = HE_{l+1,m}^{par} \pm HE_{l+1,m}^{ímpar} = \hat{\sigma}^{\pm} F_{l,m}(r) e^{\pm il\phi} e^{i\beta_{HE} z}$$
$$W_{l,m}^{\pm} = EH_{l-1,m}^{par} \mp EH_{l-1,m}^{ímpar} = \hat{\sigma}^{\pm} F_{l,m}(r) e^{\mp il\phi} e^{i\beta_{EH} z}$$

Sendo que $\hat{\sigma}^{\pm} = \hat{x} \pm i\hat{y}$ é a polarização da luz, que pode ser direita ou esquerda, e l é a carga topológica do modo OAM, relacionada à rotação do vetor de Poynting. Dois modos OAM que se propagam por uma fibra perfeita são não-acoplados, ou seja, a correlação entre seus campos eletromagnéticos (dada pela "integral de *overlap*" entre os campos) é zero ou, na escala logarítmica, <-120 dB para todos os efeitos práticos. O acoplamento entre os modos ocorre quando a fibra é perturbada; assim, um modo OAM pode ter uma correlação com outro modo OAM diferente de zero.

- Número de estados de OAM utilizáveis: significa o número de modos OAM que podem ser excitados e usados em um sistema de comunicação óptica ou de sensores. É necessário avaliar o número de modos OAM que não se acoplam facilmente, calculando a diferença de índice efetivo entre os modos adjacentes. Idealmente o valor desta diferença tem que ser da ordem de 10^{-4} ou maior; se o valor fosse menor que 10^{-4} o modo OAM não seria utilizável porque se acoplaria facilmente com outros modos durante a propagação. Portanto, número de estados OAM utilizáveis são os modos OAM que têm uma diferença de índice efetivo da ordem de 10^{-4} ou maior entre os modos adjacentes, sendo excitados com polarização circular direita ou esquerda.

[36] O objeto da presente invenção passará a ser mais detalhadamente descrito e explicado com base nas figuras, que possuem caráter meramente exemplificativo e não limitativo, posto que adaptações e modificações podem ser feitas sem que, com isso, se fuja do escopo da proteção reivindicada.

[37] Conforme é possível observar através da **Figura 3** anexa, a presente invenção refere-se, mais especificamente, a uma fibra óptica multimodo (1) vórtice (ou vortex) para a transmissão de modos OAM por longas distâncias e com baixo acoplamento, sendo que na concretização preferencial da presente invenção a dita fibra óptica (1) compreende basicamente um núcleo (10), um anel intermediário (20) e um revestimento de metamaterial (30). Nessa configuração, o núcleo (10) pode ser sólido ou preenchido com ar (oco) e deve apresentar índice de refração menor que o índice de refração do material do anel (20) intermediário - sendo, portanto, variável.

[38] O revestimento de metamaterial (30) é, de acordo com uma concretização preferencial da presente invenção, constituído por células unitárias compostas por materiais isotrópicos dielétricos. No entanto, outros tipos de materiais podem ser utilizados em sua composição, conforme o gráfico ilustrado na **Figura 4** anexa. Nela é possível observar que a combinação das possibilidades de permissividade elétrica $\boldsymbol{\varepsilon}$ e permeabilidade magnética $\boldsymbol{\mu}$ formam quatro quadrantes que representam toda a gama de resposta eletromagnética isotrópica, sendo que todos os quatro quadrantes podem ser utilizados para projetar materiais dielétricos específicos possíveis de serem usados, com vantagem, no revestimento da fibra óptica da invenção em questão. Cabe esclarecer que o quadrante superior esquerdo engloba todos os dielétricos que são refletores perfeitos, para os quais $\boldsymbol{\mu > 0}$ e $\boldsymbol{\varepsilon < 0}$. No quadrante superior direito são situados os materiais transparentes para os quais $\boldsymbol{\mu = 1}$ e $\boldsymbol{\varepsilon > 1}$. O quadrante inferior direito situa materiais com $\boldsymbol{\mu < 0}$ e $\boldsymbol{\varepsilon > 0}$ que inclui todos os materiais dielétricos magnéticos espelhados, e o quadrante inferior esquerdo envolve os metamateriais de índice negativo com $\boldsymbol{\mu < 0}$ e $\boldsymbol{\varepsilon < 0}$ e fontes do Princípio de Huygens.

[39] Os metamateriais (30) podem ser confeccionados de duas maneiras:

(i) incorporando nano-bastões delgados (31), com tamanho de ordem menor que o comprimento de onda de alto índice de refração em um substrato dielétrico (32) de baixo índice, ou vice-versa, conforme ilustrado na **Figura 5** anexa; ou

(ii) intercalando camadas dielétricas de índices de refração diferentes.

[40] Conforme já fora citado anteriormente no presente relatório, os metamateriais (30) apresentam uma distribuição de estruturas que resulta em um material artificial que, portanto, é oriundo da fabricação de um meio composto por células unitárias (elementos) muito menores do que o comprimento de onda no qual o guia de onda (fibra óptica) opera. A periodicidade das ditas células unitárias é muito menor do que o comprimento de onda em que o guia será usado para assegurar que a estrutura se comporte como um material homogêneo efetivo. O revestimento de metamaterial (30) da **Figura 5** tem um comportamento anisotrópico, o que significa que possui índices de refração diferentes para eixos distintos: paralelo ou perpendicular ao eixo de propagação. Os índices de refração podem ser descritos com precisão por um índice de refração efetivo (ou equivalente), que é independente da periodicidade e é calculado usando a aproximação de Maxwell-Garnett. Os cálculos das permissividades relativas paralela e perpendicular ao eixo são dados pelas equações abaixo:

$$\epsilon_{|} = \rho\epsilon_d + (1-\rho)\epsilon_h$$

$$\epsilon_{\perp} = \frac{(1+\rho)\epsilon_d\epsilon_h + (1-\rho)\epsilon_d\epsilon_h}{(1-\rho)\epsilon_d + (1+\rho)\epsilon_h}$$

[41] Nas equações acima $\boldsymbol{\varepsilon_d}$ e $\boldsymbol{\varepsilon_h}$ são as permissividades dos nano-tubos (ou camadas) dielétricos e do substrato, respectivamente, e ρ é a fração da área ocupada pelos ditos nano-tubos. Os respectivos índices de refração transversal e longitudinal são calculados por $n_{\perp} = \sqrt{\epsilon_{\perp}}$ e $n_{||} = \sqrt{\epsilon_{||}}$.

[42] Um aspecto único dos metamateriais (30) com

células unitárias dielétricas reside na ampla gama de possibilidades que eles permitem para projetar anisotropias de meios. Ao contrário dos materiais naturais, nos quais os índices de refração principais para as duas polarizações possíveis (extraordinária e ordinária) raramente excedem 10%, os metamateriais totalmente dielétricos podem ser projetados para ter um contraste de índice muito maior, o que possibilita, na invenção em questão, modificar o comportamento dos modos da fibra óptica multimodo (1) de vórtice quando o metamaterial (30) é utilizado como revestimento.

[43] Com a utilização da fibra óptica multimodo (1) da presente invenção, espera-se que os modos de alta ordem apresentem uma menor sensibilidade a curvaturas (acarretando menores acoplamentos) e que o número de modos da fibra aumente sem ter que aumentar o raio do anel (20), devido ao maior contraste de índice de refração entre o revestimento de metamaterial (30) e o anel (20) da fibra (1) e à anisotropia do revestimento.

[44] Em uma concretização preferencial da presente invenção que se encontra ilustrada na **Figura 6** anexa, o metamaterial (30) é composto por um substrato de sílica com cilindros de ar (50) embutidos formando multicamadas. Essa configuração pode também ser estendida para outros tipos de metamateriais (30), como cilindros de outros materiais ou multicamadas dielétricas. A fibra (1) foi projetada para elevar o contraste entre os índices de refração do anel (20) (n_{anel}) e $n_{\perp}$ do revestimento, permitindo aumentar o número de modos da fibra. Além disso, a anisotropia dada por $n_{||}$ permite intensificar ainda mais o confinamento dos modos, diminuindo

suas sensibilidades a perturbações, como as curvaturas. Vale notar que este efeito não pode ser conseguido unicamente pela dopagem da fibra (1).

[45] Com a construção aqui proposta, observou-se que as diferenças de índice efetivo entre os modos de alta ordem aumentaram em comparação com a fibra de revestimento isotrópico e que a sensibilidade dos modos a curvaturas diminuiu, acarretando menores acoplamentos. Assim, a introdução de um metamaterial (30) como revestimento na fibra óptica (1) tipo vórtice permite modificar a resposta modal da fibra.

[46] A seguir serão reveladas algumas das concretizações possíveis da presente invenção:

- Configuração 1: fibra óptica multimodo (1) de vórtice para a propagação de modos OAM projetada com parte do núcleo (10) de ar ou sólido, anel (20) intermediário sólido e revestimento (30) em metamaterial que pode ser feito de muitas configurações conforme gráfico da **Figura 4**;

- Configuração 2: fibra óptica multimodo (1) de vórtice para a propagação de modos OAM projetada com parte do núcleo (10) em metamaterial, anel (20) intermediário sólido e revestimento (30) em metamaterial que pode ser feito de muitas configurações conforme gráfico da **Figura 4**;

- Configuração 3: fibra óptica multimodo (1) de vórtice para a propagação de modos OAM projetada com parte do núcleo (10) de ar ou sólido, anel (20) intermediário em metamaterial e revestimento (30) em metamaterial que pode ser feito de muitas configurações conforme gráfico da **Figura 4**;

- Configuração 4: o metamaterial das configurações 1, 2 e 3 pode ter uma fração da área ocupada pelos nano-bastões (ou camadas) que podem ter distribuição uniforme ou não-uniformes na secção transversal da fibra óptica multimodo (1).

[47] Cabe mencionar que durante a elaboração da invenção a concretização descrita na Configuração 1 acima foi testada. O revestimento (30) foi feito com nano-bastões de ar dentro de um substrato de sílica (SiO_2) dispostos em forma de multicamadas. O material escolhido para o anel medial (20) foi a sílica dopada, sendo que as medidas geométricas do diâmetro do núcleo (10), do anel medial (20) e do revestimento (30) foram escolhidas do estado da técnica. À época, os inventores encontraram resultados que permitem concluir que a concretização proposta supera significativamente o desempenho obtido pelo uso das fibras vórtice convencionais com revestimento sólido, posto que:

- a diferença de índice efetivo entre os modos adjacentes aumentou, conservando as medidas geométricas da fibra óptica multímodo tipo vórtice convencional do estado da técnica (1), mas trocando o revestimento pelo metamaterial.

- o acoplamento modal da fibra óptica multimodo (1) de acordo com uma concretização preferencial da presente invenção perturbada mecanicamente com curvaturas de 1 a 5 cm diminui quando comparado com a fibra vórtice convencional e não revestida com metamaterial.

- o número de modos OAM utilizáveis da fibra revestida de metamaterial é maior, tanto pelo aumento da diferença entre índices efetivos quanto pelo maior contraste entre o índice de refração do anel e o índice de refração transversal do revestimento em metamaterial, permitindo a propagação de mais modos.

[48] Durante os testes foram simuladas duas fibras ópticas (1) de vórtice com revestimento em metamaterial (30). A primeira com o núcleo (10) sólido e com as medidas geométricas da fibra vórtice convencional. A segunda, uma fibra óptica (1) de vórtice com núcleo (10) de ar e com as medidas geométricas da fibra vórtice convencional.

[49] Na primeira fibra óptica (1) de vórtice com núcleo sólido e revestimento em metamaterial testada observou-se que a fibra com revestimento (30) em metamaterial apresenta maiores diferenças de índices efetivos quando comparada com a fibra convencional, conforme pode ser melhor observado através dos gráficos das **Figuras 7.1 e 7.2** anexas, na qual o gráfico (60) mostra, para fins comparativos, os resultados obtidos com o uso de uma fibra óptica convencional. A diferença de índice efetivo é duas ordens de grandeza maior para a fibra óptica (1) de vórtice revestida com metamaterial (30).

[50] Além disso, observou-se nesse primeiro teste uma modificação no acoplamento modal entre os modos OAM_1, conforme representado nas tabelas abaixo, que mostram os valores de acoplamento modal entre um modo OAM_1 e os modos OAM_{-1}, TE_{01} e TM_{01} quando a fibra (1) é perturbada com um raio de curvatura de 2 centímetros. As linhas se referem aos modos que foram perturbados pela curva e os valores no interior da tabela são, em dB, os coeficientes de acoplamento com os modos indicados nas colunas. Os resultados empregando a fibra óptica multimodo (1) revestida com metamaterial (conforme o revelado na presente invenção) permitem observar uma diminuição no acoplamento para o modo OAM_1 em relação aos modos TE_{01}, TM_{01} e OAM_{-1} de até 22, 31 e 22 dB, respetivamente.

Fibra multimodo Vortex sólida convencional			
	TE_{01}	TM_{01}	OAM_{-1}
OAM$_1$	**-31**	**-24**	**-48**
HE$_{11y}$	-22	-96	-25
HE$_{11x}$	-120	-65	-70

Fibra multimodo Vortex sólida com revestimento em metamaterial			
	TE_{01}	TM_{01}	OAM_{-1}
OAM$_1$	**-53**	**-55**	**-70**
HE$_{11y}$	-37	-129	-41
HE$_{11x}$	-111	-73	-77

[51] Similarmente, na segunda fibra óptica (1) de vórtice com revestimento em metamaterial testada durante a concepção da invenção observou-se a ocorrência de maiores diferenças de índices entre os modos $HE_{l+1,m}$ e $EH_{l-1,m}$ quando comparada à convencional (Fig. 8.1), sendo que tais dados se encontram ilustrados nas **Figuras 8.1 e 8.2** anexas. Neste caso, as fibras possuíam núcleo de ar.

[52] Complementarmente observa-se que o gráfico representado na Figura 9 anexa indica a diferença de índice efetivo dos modos $HE_{l+1,m}$ em relação aos modos $EH_{l-1,m}$ no comprimento de onda 1550 nm das telecomunicações, calculado numericamente para as fibras vórtice (30) com núcleo de ar testadas. Tal gráfico permite observar, também, o aumento de mais dois modos HE (par e ímpar) e dois modos EH (par e ímpar) (70) (Figura 9) para a fibra vórtice com revestimento em metamaterial, resultando em mais quatro estados OAM utilizáveis.

[53] As tabelas apresentadas a seguir mostram valores de acoplamento modal entre os modos OAM$_{+7}$ em relação aos modos OAM$_{-7}$ quando a fibra é perturbada com uma curvatura de 1 cm. As linhas se referem aos modos que foram perturbados pela curva e os valores no interior da tabela são, em dB, os

coeficientes de acoplamento com os modos indicados nas colunas. As diferenças nos resultados da tabela entre a fibra vórtice de núcleo de ar convencional e a fibra vórtice de núcleo de ar com o revestimento em metamaterial permitem observar uma significativa diminuição no acoplamento entre os modos.

Fibra multimodo Vortex com núcleo de ar - convencional		
	ℓ_{7}	ℓ_{-7}
ℓ_{-7}	**-67 dB**	
ℓ_{7}		**-78 dB**

Fibra multimodo Vortex com núcleo de ar e revestimento em metamaterial		
	ℓ_{7}	ℓ_{-7}
ℓ_{-7}	**-107 dB**	
ℓ_{7}		**-79 dB**

[54] Nota-se que a principal diferença da presente invenção em relação ao atual estado da técnica é a utilização de metamateriais como revestimento para reduzir o acoplamento entre os modos OAM quando sujeitos a perturbações e aumentar o número de modos propagados. Essa nova geometria fornece uma fibra vórtice mais robusta às perturbações externas. Conforme demostrado, as simulações de fibra OAM usando metamateriais mostram uma redução de até 30 dB no acoplamento entre modos OAM.

[55] Conclui-se, portanto, que a invenção aqui revelada soluciona o problema da dificuldade de aumento de capacidade em sistemas futuros de comunicação baseada em fibras ópticas, de forma versátil (posto permitir a utilização de uma grande gama de metamateriais como material de revestimento), simples e altamente eficaz.

[56] Os versados na arte valorizarão os conhecimentos aqui apresentados e poderão reproduzir a invenção nas

modalidades apresentadas e em outras variantes, abrangidas no escopo das reivindicações anexas.

REIVINDICAÇÕES

1. Fibra óptica compreendendo ao menos um núcleo (10), ao menos um anel (20) intermediário e ao menos um revestimento de metamaterial (30), **CARACTERIZADO** pelo fato de que a dita fibra óptica (1) é uma fibra óptica multimodo de vórtice que compreende:

- pelo menos um núcleo (10) sólido ou preenchido com ar;
- pelo menos um anel (20) intermediário adjacente ao núcleo (10), e
- ao menos uma camada distal de revestimento de metamaterial (30) adjacente à superfície externa do pelo menos um anel (20) intermediário,

sendo que o dito revestimento de metamaterial (30) compreende um metamaterial anisotrópico dielétrico.

2. Fibra óptica de acordo com a reivindicação 1, **CARACTERIZADA** pelo fato de compreender pelo menos um núcleo (10) com índice de refração menor que o índice de refração do material do anel (20) intermediário.

3. Fibra óptica de acordo com a reivindicação 1, **CARACTERIZADA** pelo fato de que o revestimento de metamaterial (30) é compreendido por células unitárias compostas por materiais isotrópicos dielétricos.

4. Fibra óptica de acordo com a reivindicação 1, **CARACTERIZADA** pelo fato de que o revestimento de metamaterial (30) compreende pelo menos um substrato cooperante com cilindros (50) ou nano-bastões dispostos na porção interna no dito substrato.

5. Fibra óptica de acordo com a reivindicação 4, **CARACTERIZADA** pelo fato de que os ditos cilindros (50) ou nano-bastões cooperam com o substrato em duas ou mais camadas

concêntricas e de distribuições uniformes.

6. Fibra óptica de acordo com a reivindicação 4, **CARACTERIZADA** pelo fato de que os ditos cilindros (50) ou nano-bastões são dispostos de maneira não-uniforme na seção transversal da fibra óptica (1).

7. Fibra óptica de acordo com a reivindicação 1, **CARACTERIZADA** pelo fato de que o revestimento de metamaterial (30) compreende múltiplas camadas dielétricas de índices de refração diferentes intercaladas, sendo que as camadas podem ser uniformes ou não-uniformes.

8. Fibra óptica de acordo com a reivindicação 4, **CARACTERIZADA** pelo fato de que o metamaterial (30) compreende um substrato de sílica.

9. Fibra óptica de acordo com a reivindicação 4, **CARACTERIZADA** pelo fato de os cilindros (50) serem ocos.

10. Fibra óptica de acordo com a reivindicação 1, **CARACTERIZADA** pelo fato de compreender ao menos uma parte do núcleo (10) preenchida com metamaterial.

11. Fibra óptica de acordo com a reivindicação 1, **CARACTERIZADA** pelo fato de compreender ao menos um anel (20) intermediário fabricado em metamaterial.

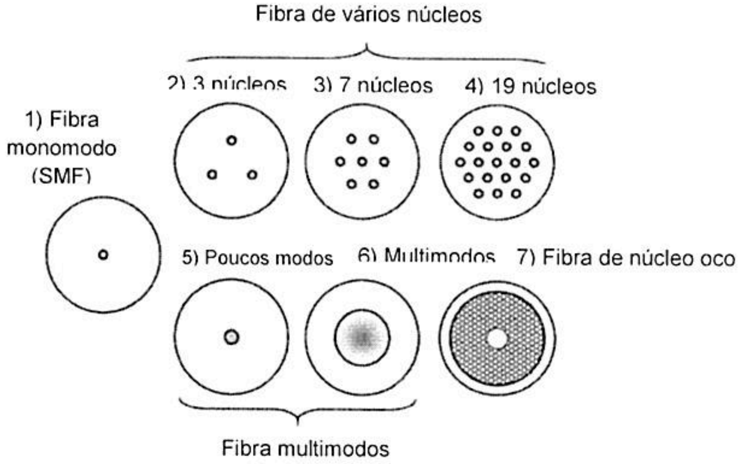

(Estado da Técnica)

FIG. 1

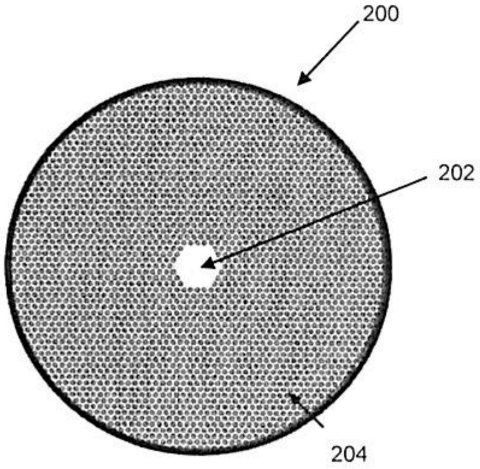

(Estado da Técnica)

FIG. 2

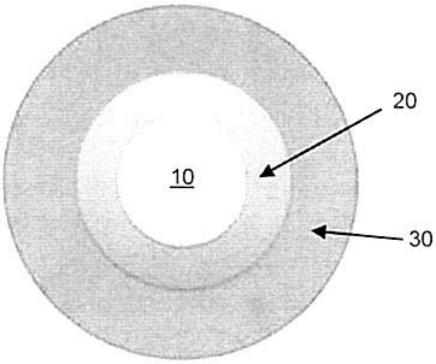

20
10
30

FIG.3

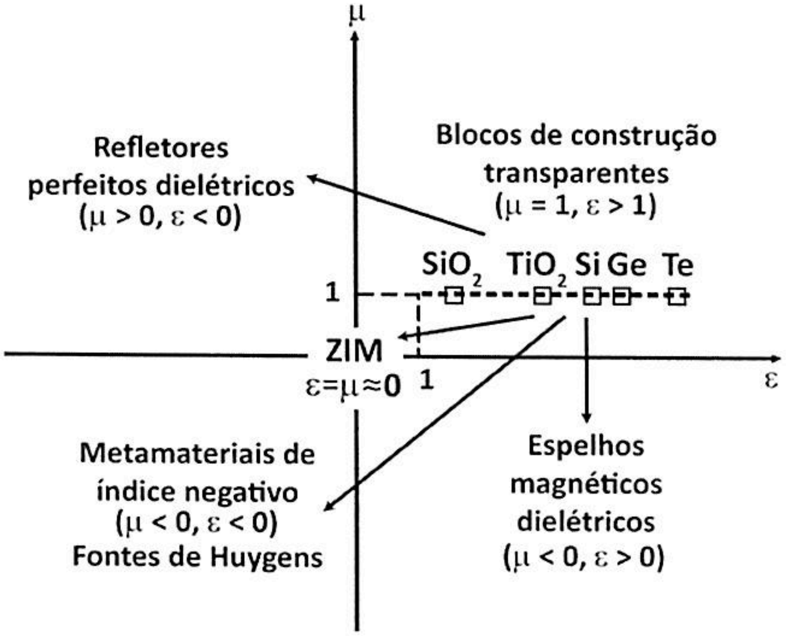

μ
Refletores perfeitos dielétricos (μ > 0, ε < 0)
Blocos de construção transparentes (μ = 1, ε > 1)
SiO$_2$
TiO$_2$
Si
Ge
Te
1
ZIM
ε=μ≈0
1
ε
Metamateriais de índice negativo (μ < 0, ε < 0) Fontes de Huygens
Espelhos magnéticos dielétricos (μ < 0, ε > 0)

FIG.4

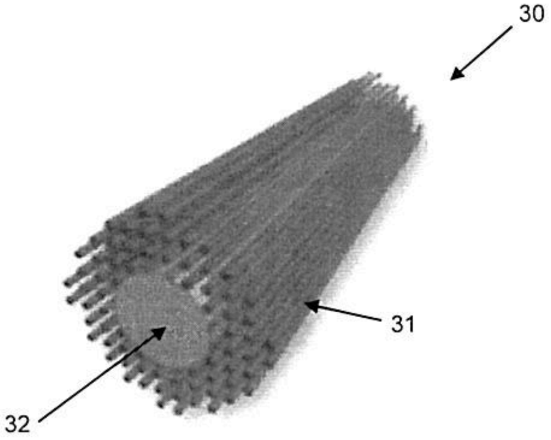

FIG. 5

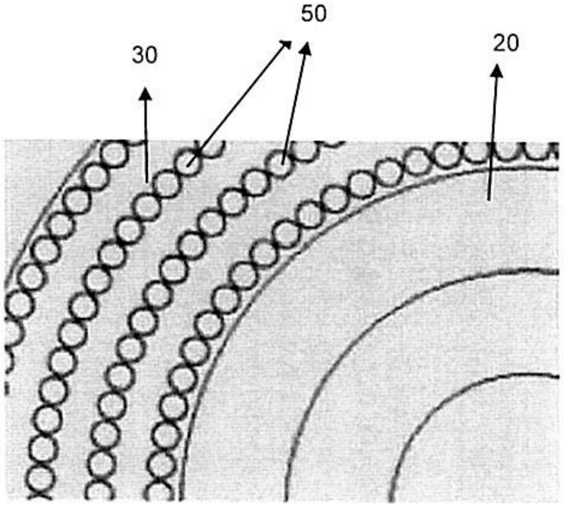

FIG. 6

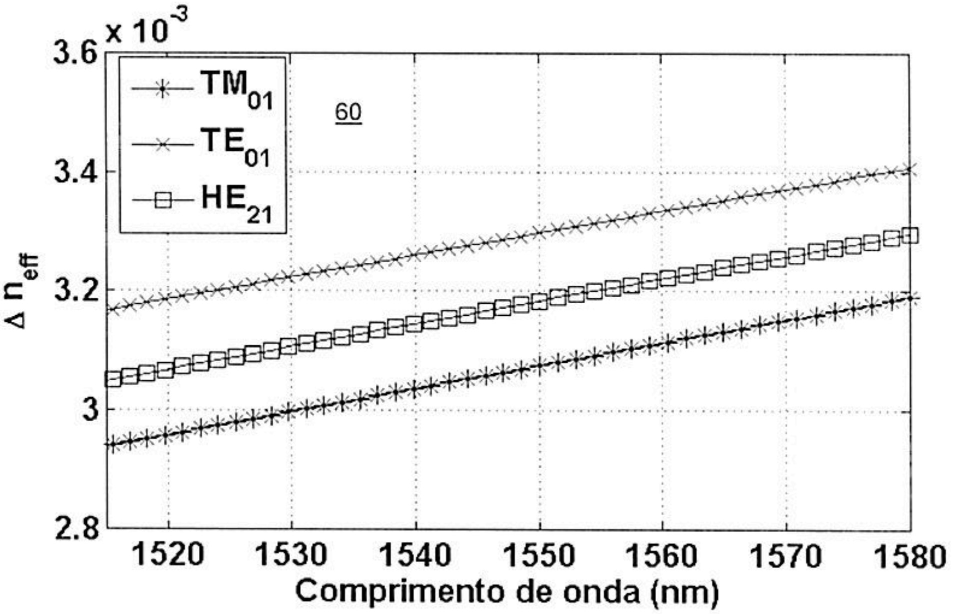
x 10^-3
3.6
3.4
3.2
3
2.8
Δ n_eff
TM01
TE01
HE21
60
1520
1530
1540
1550
1560
1570
1580
Comprimento de onda (nm)

FIG. 7.1

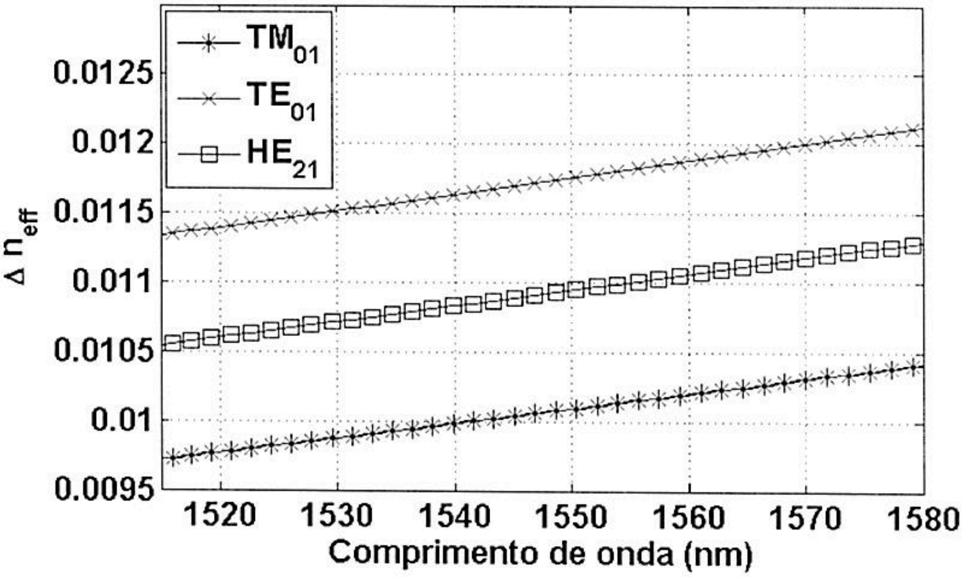
0.0125
0.012
0.0115
0.011
0.0105
0.01
0.0095
Δ n_eff
TM01
TE01
HE21
1520
1530
1540
1550
1560
1570
1580
Comprimento de onda (nm)

FIG. 7.2

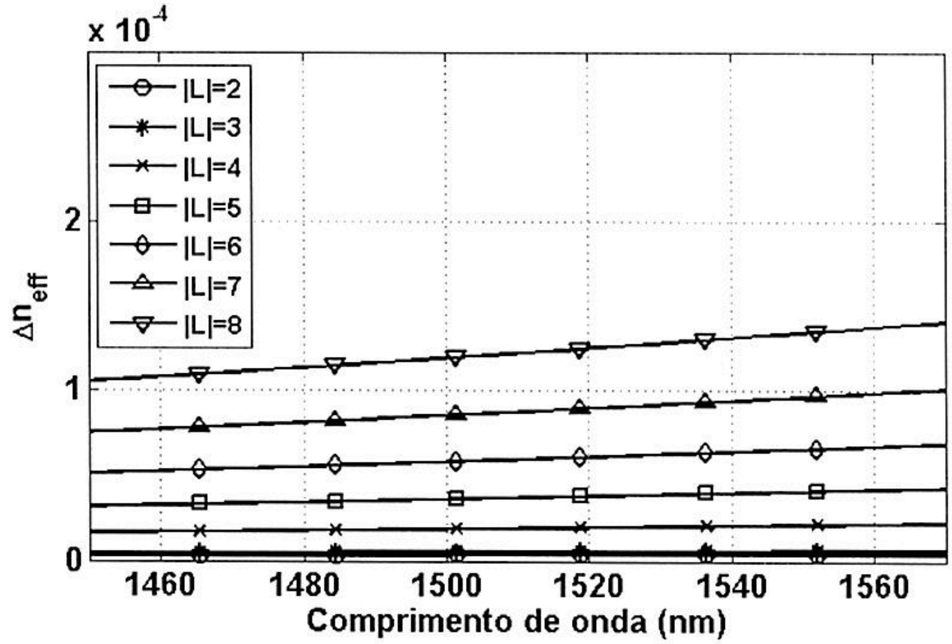
x 10^-4
Δn_eff
0
1
2
1460
1480
1500
1520
1540
1560
Comprimento de onda (nm)
|L|=2
|L|=3
|L|=4
|L|=5
|L|=6
|L|=7
|L|=8

FIG. 8.1

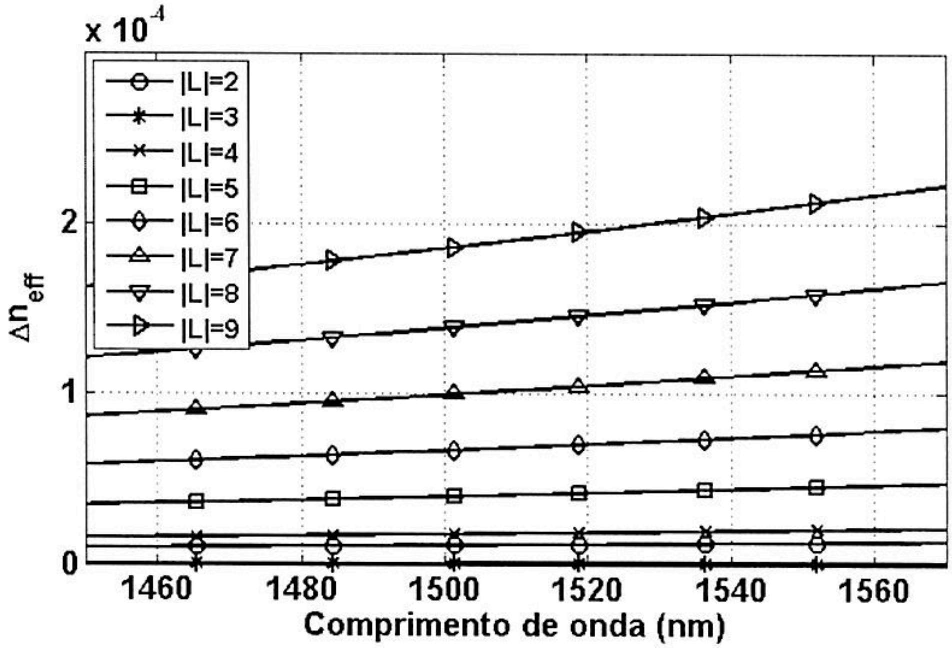
x 10^-4
Δn_eff
0
1
2
1460
1480
1500
1520
1540
1560
Comprimento de onda (nm)
|L|=2
|L|=3
|L|=4
|L|=5
|L|=6
|L|=7
|L|=8
|L|=9

FIG. 8.2

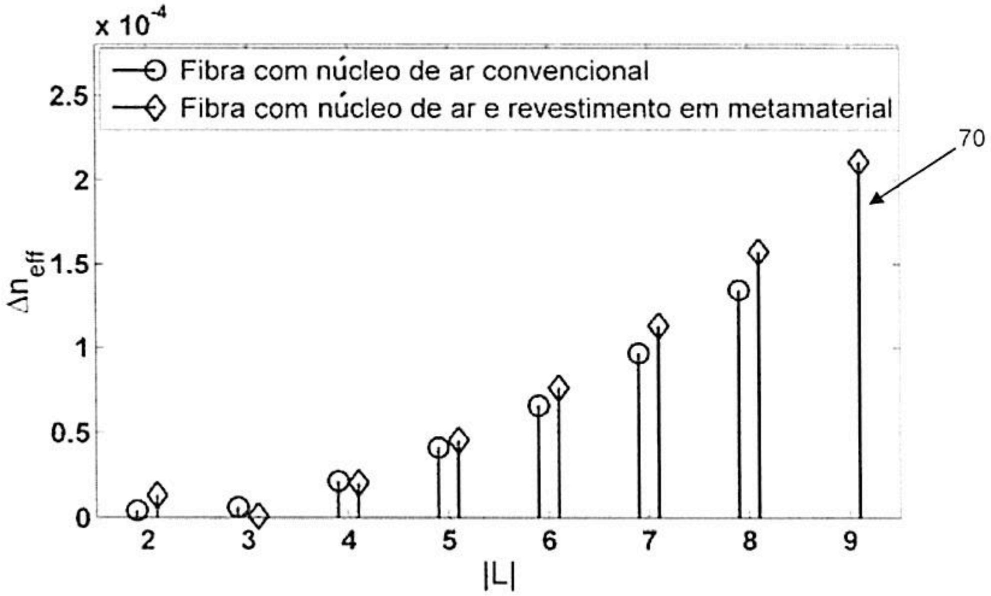
x 10^-4
Fibra com núcleo de ar convencional
Fibra com núcleo de ar e revestimento em metamaterial
70
2.5
2
1.5
1
0.5
0
Δn_eff
2
3
4
5
6
7
8
9
|L|

FIG. 9

Resumo

FIBRAS VORTEX COM REVESTIMENTO DE METAMATERIAL ANISOTRÓPICO

A presente invenção se insere na área de engenharia de telecomunicações e refere-se mais precisamente a uma nova configuração / geometria de fibra ótica para promover uma redução no acoplamento dos modos OAM e, assim, aumentar tanto o número de modos OAM propagados quanto permitir uma propagação de baixo acoplamento entre os modos OAM quando sujeitos perturbações. Para tanto, a invenção compreende uma fibra óptica (1) multimodo de vórtice compreendendo: pelo menos um núcleo (10) sólido ou preenchido com ar; pelo menos um anel (20) intermediário adjacente ao núcleo (10), e ao menos uma camada distal de revestimento de metamaterial (30) adjacente à superfície externa do pelo menos um anel (20) intermediário, sendo que o dito revestimento de metamaterial (30) compreende um metamaterial anisotrópico dielétrico.

Research Article Vol. 25, No. 4 | 20 Feb 2017 | OPTICS EXPRESS 4268

Optics EXPRESS

Ultra-broadband two-pump optical parametric amplifier in tellurite waveguides with engineered dispersion

JORGE D. MARCONI,[1,*] MARCELO L. F. ABBADE,[2] CLAUDIA M. SERPA-IMBETT,[3] AND ERIC A. M. FAGOTTO[4]

[1] *Centro de Engenharia, Modelagem e Ciências Sociais Aplicadas, Universidade Federal do ABC, UFABC, SP, Brazil*
[2] *São Paulo State University (UNESP),Campus of São João da Boa Vista, SP, Brazil*
[3] *School of Electrical Engineering and Computer Science, Unicamp, Campinas, SP, Brazil*
[4] *School of Electrical Engineering, PUC-Campinas, Campinas, SP, Brazil*
[*] *jorge.marconi@ufabc.edu.br*

Abstract: The capacity of communication networks may be significantly improved by simply enhancing the optical amplifier bandwidth. This paper presents a numerical investigation of an ultra-broadband, low-ripple, two-pump-optical parametric amplifier (2P-OPA) that employs a tellurite glass buried-channel type nano-waveguide as nonlinear medium. The nano-waveguide was designed as a 25-cm-long Archimedean spiral that occupies a footprint of only ~2.5 mm^2, with a ~0.7 μm^2 effective cross section. Its zero-dispersion wavelength is ~1550 nm, the nonlinear coefficient is ~3000 W^{-1} km^{-1}, and the attenuation coefficient is ~0.5 dB/m (1100 to 1900 nm). Simulations suggest a 2P-OPA based on such waveguide will be able to amplify 243 QPSK input channels modulated at 56 Gbps over 102 nm bandwidth, over metropolitan area network scales.

OCIS codes: (190.0190) Nonlinear optics; (190.4970) Parametric oscillators and amplifiers; (130.0130) Integrated optics; (130.3120) Integrated optics devices; (130.4310) Nonlinear.

References and links

1. P. Bayvel, R. Maher, T. Xu, G. Liga, N. A. Shevchenko, D. Lavery, A. Alvarado, and R. I. Killey, "Maximizing the optical network capacity," Phil. Trans. R. Soc. A **374**(2062), 20140440 (2016).
2. A. D. Ellis, N. M. Suibhne, D. Saad, and D. N. Payne, "Communication networks beyond the capacity crunch," Phil. Trans. R. Soc. A **374**(2062), 20150191 (2016).
3. J. X. Cai, Y. Sun, H. Zhang, H. G. Batshon, M. V. Mazurczyk, O. V. Sinkin, D. G. Foursa, and A. Pilipetskii, "49.3 Tb/s transmission over 9100 km using C+L EDFA and 54 Tb/s transmission over 9150 km using hybrid-Raman EDFA," J. Lightwave Technol. **33**(15), 2724–2734 (2015).
4. R. J. Essiambre and R. W. Tkach, "Capacity trend and limits of optical communication networks," Proc. IEEE **100**(5), 1035–1055 (2012).
5. R. J. Essiambre, G. J. Foschini, G. Kramer, and P. J. Winzer, "Capacity limits of information transmission in optically-routed fiber networks," Bell Labs Tech. J. **14**(4), 149–162 (2010).
6. R. J. Essiambre, G. Kramer, P. J. Winzer, G. J. Foschini, and B. Goebel, "Capacity limits of optical fiber networks," J. Lightwave Technol. **28**(4), 662–701 (2010).
7. J. Berthold, A. A. M. Saleh, L. Blair, and J. M. Simmons, "Optical networking: past, present, and future," J. Lightwave Technol. **26**(9), 1104–1118 (2008).
8. E. B. Desurvire, "Capacity demand and technology challenges for lightwave systems in the next two decades," J. Lightwave Technol. **24**(12), 4697–4710 (2006).
9. D. C. Kilper and H. Rastegarfar, "Energy challenges in optical access and aggregation networks," Phil. Trans. R. Soc. A **374**(2062), 20140435 (2016).
10. S. Beppu, K. Kasai, M. Yoshida, and M. Nakazawa, "2048 QAM (66 Gbit/s) single-carrier coherent optical transmission over 150 km with a potential SE of 15.3 bit/s/Hz," Opt. Express **23**(4), 4960–4969 (2015).
11. J. Sakaguchi, W. Klaus, J. M. D. Mendinueta, B. J. Puttnam, R. S. Luís, Y. Awaji, N. Wada, T. Hayashi, T. Nakanishi, T. Watanabe, Y. Kokubun, T. Takahata, and T. Kobayashi, "Large spatial channel (36-core x 3 mode) heterogeneous few-mode multicore fiber," J. Lightwave Technol. **34**(1), 93–103 (2016).
12. F. Poletti, M. N. Petrovich, and D. J. Richardson, "Hollow-core photonic bandgap fibers: technology and applications," Nanophotonics **2**(5–6), 315–340 (2013).

#279786 https://doi.org/10.1364/OE.25.004268
Journal © 2017 Received 31 Oct 2016; revised 31 Jan 2017; accepted 1 Feb 2017; published 16 Feb 2017

13. J. M. Chavez Boggio, A. Guimarães, F. A. Callegari, J. D. Marconi, and H. L. Fragnito, “Q penalties due to pump phase modulation and pump RIN in fiber optic parametric amplifiers with non-uniform dispersion,” Opt. Commun. **249**(4–6), 451–472 (2005).
14. J. M. Chavez Boggio, J. D. Marconi, S. R. Bickham, and H. L. Fragnito, “Spectrally flat and broadband double-pumped fiber optical parametric amplifiers,” Opt. Express **15**(9), 5288–5309 (2007).
15. L. Zhang, T.-H. Tuan, H. Kawamura, K. Nagasaka, T. Suzuki, and Y. Ohishi, “Broadband optical parametric amplifier formed by two pairs of adjacent four-wave mixing sidebands in a tellurite microstructured optical fibre,” J. Opt. **18**(5), 055502 (2016).
16. P. S. Maji and P. R. Chaudhuri, “Gain and bandwidth investigation in a near-zero ultra-flat dispersion PCF for optical parametric amplification around the communication wavelength,” Appl. Opt. **54**(11), 3263–3272 (2015).
17. D. Bigourd, P. B. d’Augerès, J. Dubertrand, E. Hugonnot, and A. Mussot, “Ultra-broadband fiber optical parametric amplifier pumped by chirped pulses,” Opt. Lett. **39**(13), 3782–3785 (2014).
18. S. K. Chatterjee, S. N. Khan, and P. R. Chaudhuri, “Two-octave spanning single pump parametric amplification at 1550 nm in a host lead-silicate binary multi-clad microstructure fiber: influence of multi-order dispersion engineering,” Opt. Commun. **332**, 244–256 (2014).
19. M. W. Lee, T. Sylvestre, M. Delqué, A. Kudlinski, A. Mussot, J.-F. Gleyze, A. Jolly, and H. Maillotte, “Demonstration of an all-fiber broadband optical parametric amplifier at 1 µm,” J. Lightwave Technol. **28**(15), 2173–2178 (2010).
20. J. M. Chavez Boggio, S. Moro, E. Myslivets, J. R. Windmiller, N. Alic, and S. Radic, “155-nm continuous-wave two-pump parametric amplification,” IEEE Photonics Technol. Lett. **21**(10), 612–614 (2009).
21. T. Toroundinis and P. Andrekson, “Broadband single-pumped fiber-optic parametric amplifiers,” IEEE Photonics Technol. Lett. **19**(9), 650–652 (2007).
22. H. Hu, R. M. Jopson, A. H. Gnauck, M. Dinu, S. Chandrasekhar, C. Xie, and S. Randel, “Parametric amplification, wavelength conversion, and phase conjugation of a 2048-Tbit/;s WDM PDM 16-QAM signal,” J. Lightwave Technol. **33**(7), 1286–1291 (2015).
23. N. El Dahdah, D. S. Govan, M. Jamshidifar, N. J. Doran, and M. E. Marhic, “Fiber optical parametric amplifier performance in a 1-Tb/s DWDM communication system,” IEEE J. Sel. Top. Quantum Electron. **18**(2), 950–957 (2012).
24. X. Liu, R. M. Osgood Jr., Y. A. Vlasov, and W. M. J. Green, “Mid-infrared optical parametric amplifier using silicon nanophotonic waveguides,” Nat. Photonics **4**, 557–560 (2010).
25. M. A. Foster, A. C. Turner, J. E. Sharping, B. S. Schmidt, M. Lipson, and A. L. Gaeta, “Broad-band optical parametric gain on a silicon photonic chip,” Nature **441**(7096), 960–963 (2006).
26. A. Pasquazi, Y. Park, J. Azaña, F. Légaré, R. Morandotti, B. E. Little, S. T. Chu, and D. J. Moss, “Efficient wavelength conversion and net parametric gain via four wave mixing in a high index doped silica waveguide,” Opt. Express **18**(8), 7634–7641 (2010).
27. J. J. Leal, R. Narro-Garcia, H. Desirena, J. D. Marconi, E. Rodrigues, K. Linganna, and E. De la Rosa, “Spectroscopic properties of tellurite glasses co-doped with Er3+ and Yb3+,” J. Lumin. **162**(13195), 72–80 (2015).
28. K. S. Bindra, H. T. Bookey, A. K. Kar, B. S. Wherrett, X. Liu, and A. Jha, “Nonlinear optical properties of chalcogenide glasses: Observation of multiphoton absorption,” Appl. Phys. Lett. **79**(13), 1939–1941 (2001).
29. S. Shen, A. Jha, X. Liu, M. Nafataly, K. Bindra, H. J. Bookey, and A. K. Kar, “Tellurite glasses for broadband amplifiers and integrated optics,” J. Am. Ceram. Soc. **85**(6), 1391–1395 (2002).
30. A. Jha, *Inorganic Glasses for Photonics* (John Wiley & Sons, 2016), Chap. 7.
31. M. E. Marhic, *Fiber Optical Parametric Amplifiers, Oscillators, and Related Devices* (Cambridge University, 2007), Ch. 3.
32. X. Guan, Y. Ding, and L. H. Frandsen, “Ultra-compact broadband higher order-mode pass filter fabricated in a silicon waveguide for multimode photonics,” Opt. Lett. **40**(16), 3893–3896 (2015).
33. S. Khan, J. Chiles, J. Ma, and S. Fathpour, “Silicon-on-nitride waveguides for mid-and near- infrared integrated photonics,” Appl. Phys. Lett. **102**(12), 121104 (2013).
34. C. Schulze, D. Flamm, S. Unger, S. Schröter, and M. Duparré, “Measurement of higher-order mode propagation losses in effectively single mode fibers,” Opt. Lett. **38**(23), 4958–4961 (2013).
35. Y. Jung, Y. Jeong, G. Brambilla, and D. J. Richardson, “Adiabatically tapered splice for selective excitation of the fundamental mode in a multimode fiber,” Opt. Lett. **34**(15), 2369–2371 (2009).
36. J. M. O. Daniel, J. S. P. Chan, J. W. Kim, J. K. Sahu, M. Ibsen, and W. A. Clarkson, “Novel technique for mode selection in a multimode fiber laser,” Opt. Express **19**(13), 12434–12439 (2011).
37. N. Bhatia, K. C. Rustagi, and J. John, “Single LP(0,n) mode excitation in multimode fibers,” Opt. Express **22**(14), 16847–16862 (2014).
38. F. Dubois, P. Emplit, and O. Hugon, “Selective mode excitation in graded-index multimode fiber by a computer-generated optical mask,” Opt. Lett. **19**(7), 433–435 (1994).
39. J. Wilde, C. Schulze, R. Brüning, M. Duparré, and S. Schröter, “Selective higher order fiber mode excitation using a monolithic setup of a phase plate at fiber facet,” Proc. SPIE **9343**, 2078993 (2015).
40. L. W. Luo, N. Ophir, C. P. Chen, L. H. Gabrielli, C. B. Poitras, K. Bergmen, and M. Lipson, “WDM-compatible mode-division multiplexing on a silicon chip,” Nat. Commun. **5**, 3069 (2014).
41. M. Baas, G. Li, and E. Van Stryland, *Handbook of Optics Vol. IV* (Mc Graw Hill, 2010), Ch. 3.

42. I. Savelli, F. Desevedavy, J. C. Jules, G. Gadret, J. Fatome, B. Kibler, H. Kawashima, Y. Ohishi, and F. Smektala, “Management of OH absorption in tellurite optical fibers and related supercontinuum generation,” Opt. Mater. **35**(8), 1595–1599 (2013).
43. R. Kitamura, L. Pilon, and M. Jonasz, “Optical constants of silica glass from extreme ultraviolet to far infrared at near room temperature,” Appl. Opt. **46**(33), 8118–8133 (2007).
44. K. Kakihara, N. Kono, K. Saitoh, and M. Koshiba, “Full-vectorial finite element method in a cylindrical coordinate system for loss analysis of photonic wire bends,” Opt. Express **14**(23), 11128–11141 (2006).
45. K.-Y. Yang, Y.-F. Chau, Y.-W. Huang, H.-Y. Yeh, and D. Ping Tsai, “Design of high birefringence and low confinement loss photonics crystal fibers with five rings hexagonal and octagonal symmetry air-holes in fiber cladding,” J. Appl. Phys. **109**(9), 093103 (2011).
46. V. Finazzi, T. M. Monro, and D. J. Richardson, “Small-core silica holey fibers: nonlinearity and confinement loss trade-offs,” J. Opt. Soc. Am. B **20**(7), 1427 (2003).
47. G. P. Agrawal, *Fiber Optic Communication Systems* (John Wiley & Sons, 2002), Ch. 2.
48. K. Okamoto, *Fundamental of Optical Waveguides* (Academic, 2006), Ch. 4.
49. B. E. A. Saleh and M. C. Teich, *Fundamentals of Photonics* (John Wiley & Sons, 2007), Ch. 8.
50. S. F. Mansour, E. Sayed Yousef, M. Y. Hassaan, and A. M. Emara, “The influence of oxides on the optical properties of tellurite glass,” Phys. Scr. **89**(11), 115812 (2014).
51. V. Mishra, S. Pratap, R. haldar, and S. K. Varshney, “Sub-wavelength dual capillaries-assisted chalcogenide optical fibers: unusual modal properties in mid-IR (2-5 mm) spectral range,” IEEE J. Sel. Top. Quantum Electron. **22**(2), 4401906 (2016).
52. S. Afshar V and T. M. Monro, “A full vectorial model for pulse propagation in emerging waveguides with subwavelength structures part I: Kerr nonlinearity,” Opt. Express **17**(4), 2298–2318 (2009).
53. G. P. Agrawal, *Nonlinear Fiber Optics* (Academic, 2007), Ch. 2.
54. Q. Lin, O. J. Painter, and G. P. Agrawal, “Nonlinear optical phenomena in silicon waveguides: modeling and applications,” Opt. Express **15**(25), 16604–16644 (2007).
55. C. Koos, L. Jacome, C. Poulton, J. Leuthold, and W. Freude, “Nonlinear silicon-on-insulator waveguides for all-optical signal processing,” Opt. Express **15**(10), 5976–5990 (2007).
56. S. Lin and D. J. Costello, Jr., *Error Control Coding* (Pearson Prentice Hall, 2004).
57. J. M. Chavez Boggio, J. D. Marconi, and H. L. Fragnito, “Crosstalk in double-pumped fiber optics parametric amplifiers for wavelength division multiplexing systems,” Opt. Commun. **259**(1), 94–103 (2006).
58. J. D. Marconi, M. L. F. Abbade, C. M. Serpa-Imbett, J. Cordoba-Ramirez, and E. A. M. Fagotto, “Broadband two-pump parametric amplifier in engineered dispersion tellurite waveguides,” in *Latin America Optics and Photonics Conference*, 2016 OSA Technical Digest Series (Optical Society of America, 2016), paper LTu4A.11.

1. Introduction

Historically, there has been a growing demand for network bandwidth [1–8]. The dramatic increase in capacity (~1000 times in 10 years) provided by wavelength division multiplexing (WDM) technology and Erbium doped fiber amplifiers (EDFA) paved the road for telecommunication systems to overcome bandwidth need during the 1990s and part of the 2000s. After this period, advanced modulation formats and coherent detection associated with emerging digital signal processing (DSP) techniques allowed the aforementioned systems to support new bandwidth requirements.

However, present-day Internet services, which include high definition video streaming and games, besides potential new applications, as online medical services (for instance, personalized genetic medicine for diseases that require transmission of DNA information) [1], and the Internet of Things (IoT), with ~50 billion devices up to 2020 [1], will generate data traffic growth that will certainly exceed the current technology capacity in the next decade [4]. Considering a conservative estimation of bandwidth increase of 26% per year (~1 dB/year = 10 *log* 1.26), optical networks information traffic will grow more than 100 times throughout the two next decades. Furthermore, energy consumption and device footprint are also important issues that need to be addressed in the design of broadband-enabling equipment [9].

For these reasons, several efforts have been made to improve the optical communication systems capacity, which include: channel spectral efficiency (SE) increase [10], fibers for spatial division multiplexing (SDM) [11], fibers with very low nonlinear coefficients [12], hybrid Raman-EDFAs amplification [3] to extend the EDFA bandwidth, and improvement of reconfigurable add/drop multiplexers among others. By a rough estimation of the capacity enhancement due to such developments, the SE improvement leads to up to 5 dB (~3 times) [1, 10], the mitigation of fiber nonlinearities to 2 dB (1.6 times) [4], and the most significant contribution comes from SDM, 15 dB (~30 times) [11]. Hybrid Raman-EDFA amplification has led to a 3 dB (2 times) bandwidth extension. However, if the total spectral region of high transparency of standard single mode fibers could be used (1300 to 1700 nm) there would be an 11 dB (12 times) capacity improvement as compared to the EDFAs' 4 THz (~32 nm) C-band. Such an enhancement clearly depends upon the development of new broadband optical amplifiers, but it has the interesting advantage of not requiring the replacement of fiber infrastructure.

EDFAs and Raman amplifiers provide a fixed bandwidth amplification region and the latter present the benefit of being spectrally tunable. New broadband optical amplifiers should, however, simultaneously offer frequency tunability and variable bandwidth for deployment in different communication systems. Optical parametric amplifiers (OPAs) constitute an interesting class of devices with both of these features. They are based on the four-wave mixing (FWM) effect, which depends on the third-order susceptibility of the waveguide medium material. Actually, parametric amplifiers can be realized in one-pump (1P-OPA) or two-pump (2P-OPA) configurations [13, 14]. In both cases, several numerical and/or experimental analysis indicate that such amplifiers perform broadband amplification [15–21]. However, the spectra presented in these works are obtained by tuning and amplifying one single channel over the considered frequency range. Thus, they do not take into account the influence of channel crosstalk that is very important for practical communication systems. Other reports present systemic studies of fiber based OPAs [22,23] and, interestingly, consider the degradation caused by transmitting signals over multiple OPAs [23]. Nevertheless, in these situations the observed amplification bandwidths are restricted to 3 THz. It should also be noted that OPAs based on fibers, pumped with continuous lasers, need additional circuitry to suppress stimulated Brillouin backscattering [13, 20]. A possibility to overcome this problem is to use short-length waveguides as nonlinear medium. In this approach, silicon waveguides become attractive also because their nonlinearity is orders of magnitude higher than those of optical fibers [24, 25]. However, nonlinear two-photon absorption (TPA) and free-carrier absorption (FCA) limit silicon parametric gain in the 1550 nm window and the quality of modulated signals. The performance of glass OPA waveguides, has been also investigated for single channels in [26].

In this work, an ultra-broadband 2P-OPA based on tellurite glass nano-waveguide, which could be used in integrated photonics, is proposed. The device is intended to be tunable and to present variable bandwidth, reduced footprint and good energy efficiency. It was designed using a buried-channel type waveguide with a tellurite glass core and a SiO_2 cladding, following an Archimedean spiral structure to minimize the 2P-OPA area. The dispersive parameters of the nano-waveguide were conceived to offer low ripple and ultra-broad amplification bandwidth in the optical communications window. The choice for tellurite glass relies on its good thermomechanical properties [27], high nonlinearity, and negligible undesirable effects of TPA at telecommunication wavelengths [28–30] and FCA (tellurite glass is a dielectric material). A systemic analysis, with 243 channels (56 Gbps QPSK modulation format) being amplified, in a configuration where the 2P-OPA acts as an in-line optical amplifier, is also presented. The analysis includes bit error rate (BER) results, assuming that WDM signals are repeatedly attenuated and re-amplified. All these considerations are intended to provide a first systemic evaluation performance of tellurite OPAs. In fact, to the best of our knowledge, this is the first systematic literature report on the application of tellurite glass planar waveguides for parametric amplification.

The remaining of this paper is organized as follows. In Section 2, we present a brief theoretical review of OPA fundamentals. A detailed step-by-step description of the tellurite waveguide design is approached in Section 3. Section 4 shows simulation results that allow to assess the 2P-OPA performance for the transmission of WDM signals. Scenarios where the bandwidth of WDM channels are one, two or three times the bandwidth provided by EDFAs are considered. Finally, our conclusions are described in Section 5.

2. Brief theoretical description of OPAs

One and two-pump OPA configurations need to satisfy a nonlinear phase-matching condition in order that the parametric process efficiently builds up along the waveguide. In the case of the 1P-OPA, the pump frequency is close to the waveguide zero-dispersion wavelength, λ_0. For 2P-OPA, pumps are disposed near symmetrically over λ_0. Because of their higher amplification bandwidth and lower ripple, in this paper, we deal only with 2P-OPAs. In this case, the nonlinear interaction between pumps and signals also generate slave signals called idlers, which are located symmetrically to the average value of the pumps wavelength.

Considering the case of a lossless waveguide, it is possible to derive, from the propagation equations of the optical signals [31], the following expression for the parametric gain:

$$G = 1 + \left(\frac{x_0 \sinh x}{x} \right)^2, \tag{1}$$

where

$$x = x_0 \sqrt{1 - \left(\frac{\kappa}{2\gamma P_0} \right)^2}, \tag{2}$$

$x_0 = \gamma P_0 L$, γ is the nonlinear coefficient, $P_0 = 2\sqrt{P_1 P_2}$, P_1 and P_2 are the pump powers, $\kappa = \Delta\beta + \gamma(P_1 + P_2)$,

$\Delta\beta = \beta_2(\omega_c)[\Delta\omega_s^2 - \Delta\omega_P^2] + \dfrac{\beta_4}{12}(\omega_c)[\Delta\omega_s^4 - \Delta\omega_P^4] + \dfrac{\beta_6}{360}(\omega_c)[\Delta\omega_s^6 - \Delta\omega_P^6] + \ldots.$,

$\omega_c = \dfrac{(\omega_1 + \omega_2)}{2}$, ω_1 and ω_2 are the pump frequencies, $\Delta\omega_s = \omega_s - \omega_c$, ω_s is the signal frequency, $\Delta\omega_P = \omega_1 - \omega_c$ and $\beta_2(\omega_c)$, $\beta_4(\omega_c)$, $\beta_6(\omega_c)$, …, are the second-, fourth-, sixth-,… order dispersion parameters at frequency ω_c, respectively.

From Eqs. (1) and (2), it is clear that the parametric gain is maximum when the phase matching condition ($\kappa \sim 0$) is satisfied. This condition depends on the waveguide dispersion through the β_2, β_4, β_6, … parameters, which implies there are no fundamental physical constraints to the 2P-OPA gain bandwidth, such as the ones imposed by quantum transitions to EDFAs.

3. Waveguide design

The proposed waveguide is a buried-channel type, with a tellurite core and SiO_2 cladding. It follows an Archimedean spiral to minimize the device footprint. Figure 1 shows a schematic view of the waveguide. Its rectangular core cross section, 698 nm high (h) and 990 nm wide (w), was designed to maximize the parametric gain and to minimize the ripple by engineering the waveguide dispersion. This waveguide presents only two modes. We inform in advance that the higher order mode is weakly coupled to the waveguide and leaks to the cladding, because of curvature bends [32, 33] in our spiral structure. In addition to this, in the spectral range analyzed (from 1400 to 1700 nm), the higher order mode presents λ_0, at 1176 nm, for one polarization state and no λ_0 for the other. Thus, its phase matching condition is not satisfied and, therefore, the corresponding nonlinear interaction is negligible. Anyway, to prevent any influence from this higher order mode, we assume that light launched into the proposed waveguide passes through some device [32–40] that ensures only the waveguide fundamental mode is excited. For this reason, hereafter, we will treat the proposed waveguide as single mode. Since the spiral radius, R, changes along the waveguide length, it is necessary to find a minimum radius that concomitantly allows for low losses and for the required waveguide dispersion.

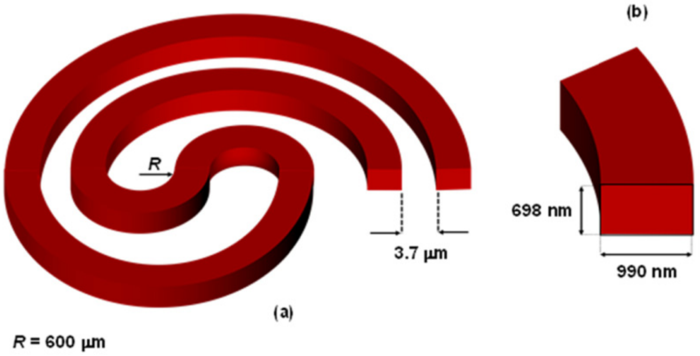

Fig. 1. a) Schematic design (not in scale) of the Archimedean spiral with their principal geometrical dimensions. b) Detail of the transversal cross sections with the high and the width of the waveguide that allow to obtain a λ_0 around 1550 nm.

The loss and the dispersion for the core and cladding materials were estimated through the following procedure. Firstly, for the core material, the refractive index was measured from a tellurite sample with composition (in mol%) 71%TeO_2– 22.5%WO_3 – 5%Na_2O – 1.5%Nb_2O_5 by using a Metricom model 2010/M prism coupling system. The experimental data were, then, fitted with a Sellmeier equation using the least square method, leading to a 0.9999 correlation coefficient. The obtained equation, which stands for the real part of the refractive index, is given by:

$$n(\lambda)=\sqrt{2.0016+2.2951\frac{\lambda^2}{\left(\lambda^2-0.046242\right)}+0.47334\frac{\lambda^2}{\left(\lambda^2-34.479\right)}}, \tag{3}$$

and it is is plotted in Fig. 2.

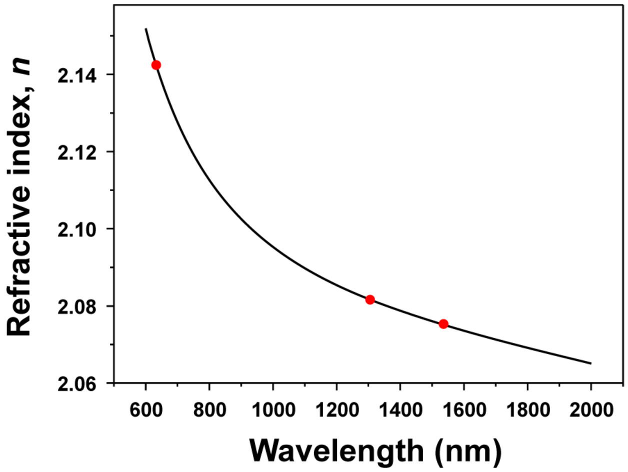

Fig. 2. Real part of tellurite refractive index as a function of wavelength. Dots are the experimental values.

The real part of the refractive index of the silica cladding was taken from [41]. The imaginary parts of the core and cladding refractive indexes were obtained from [42] and [43], respectively. All these data, along with the approach given in [44] and COMSOL Multiphysics® software, were used to calculate the waveguide effective refractive index, n_{eff}. Our calculations to estimate the waveguide losses showed that the light is no longer confined for $R < 70$ µm, for a wavelength range from 1100 up to 1900 nm. For $R > 70$ µm, the confinement loss [45, 46], by considering the material losses of the core (tellurite) and the cladding (SiO_2), was calculated as a function of the wavelength and plotted in Fig. 3. From this analysis, it is evident that the minimum radius imposed by losses is $R_L = 70$ µm.

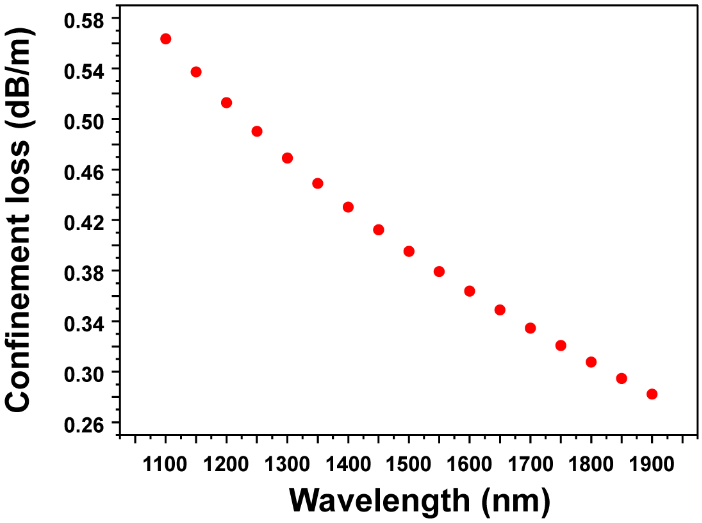

Fig. 3. Waveguide confinement losses.

Dispersion curves for the transverse electric (*TE*) (fundamental) and transverse magnetic (*TM*) modes, were calculated through the relations $\beta = k_0 n_{eff}$, $k_0 = \dfrac{2\pi}{\lambda}$, $\beta_2 = \dfrac{\partial^2 \beta}{\partial \omega^2}$, and $D = \left(-\dfrac{2\pi c}{\lambda^2}\right)\beta_2$ [47]. Figure 4(a) shows the dependence between dispersion and wavelength for R ranging from 30 to 800 µm, for *TE* mode. As R increases, the dispersion curves get closer to one another and there is no detectable variation for a minimum R imposed by dispersion of $R_D = 500$ µm. A very important feature for dispersion engineering is λ_0, whose spectral region in the considered waveguide is embraced by the two dotted vertical lines in Fig. 4(a). In Fig. 4(b), data from Fig. 4(a) are rearranged to show λ_0 as a function of R. It is seen that λ_0 increases rapidly for $R < 200$ µm. However, for $R > R_{\lambda 0}$, with $R_{\lambda 0}$ ~500 µm, λ_0 tends to a constant value of ~1550 nm that is very interesting for telecommunication applications. From Fig. 4(c) it is possible to observe a similar behavior for the *TM* mode, but in this case λ_0 is located at ~1400 nm.

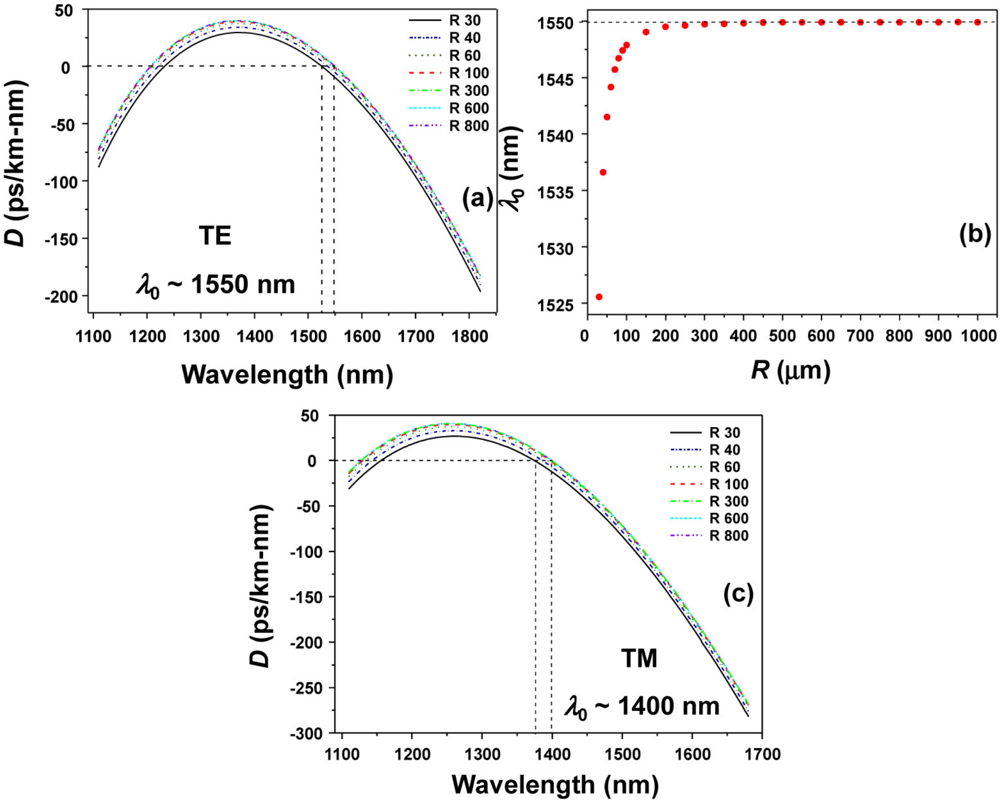

Fig. 4. a) Waveguide dispersion curves of the TE (fundamental) mode for 30 µm ≤ R ≤ 800 µm. b) ZDW as a function of the R. c) Dispersion curves of the TM mode for 30 µm ≤ R ≤ 800 µm.

The minimum radius, R_{min}, for the inner "*S*" of the waveguide Archimedean spiral (Fig. 1) must satisfy:

$$R_{min} \geq \max(R_L, R_D, R_{\lambda_0}), \tag{4}$$

where max(a_1,…, a_k) is a function that returns the largest value among a_1,…, a_k and k is an integer number. Consequently, from our previous discussion, we have R_{min} = 500 µm and, as indicated in Fig. 1, we adopted R = 600 µm with a safety margin of 100 µm.

Another fundamental feature to be assessed is the coupling loss between adjacent rounds of the spiral. It is necessary to calculate the minimum gap between successive rounds in order to minimize such loss. The situation to be considered is schematized in Fig. 5. Two parallel adjacent waveguides have their edges separated by a gap Γ. Assuming that initially light is only in waveguide *I* (mode TE_1), there will be a propagation distance, named coupling length, L_c, after which the energy is completely transferred from waveguide *I* to waveguide *II* (mode TE_2).

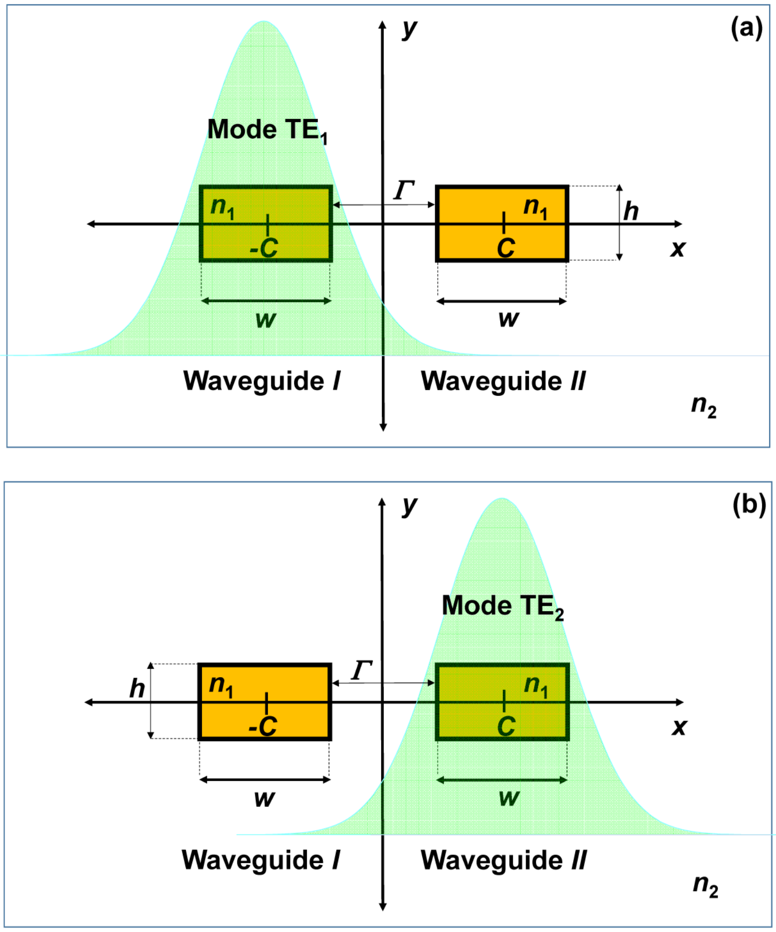

Fig. 5. a) Initially, the energy of the mode TE_1 is fully located in waveguide *I*. b) After a propagation distance equal to L_c, the energy is completely transferred to waveguide *II* (mode TE_2). The coefficients n_1 and n_2 are de refractive index of the core and the cladding, respectively.

It is possible to calculate the value of Γ that leads to $L_c >> L_s$, where L_s is the spiral length. Following the coupled-mode theory developed in [48], which considers adjacent single-mode waveguides, the coupling coefficient κ_{12}, obtained through an overlap integral between the waveguides field modes, is given by:

$$\kappa_{12} = \frac{\omega\varepsilon_0 (n_1^2 - n_2^2)\int_{-h}^{+h}\int_{C-w/2}^{C+w/2} \overline{E_1^*}\,\overline{E_2}\,dxdy}{\int_{-\infty}^{+\infty}\int_{-\infty}^{+\infty}\hat{k}\cdot\left(\overline{E_1^*}\times\overline{H_1}+\overline{E_1}\times\overline{H_1^*}\right)dxdy}, \qquad (5)$$

where κ_{12} is related to L_c as $L_c = \pi/(2\kappa_{12})$, ω is the angular frequency, ε_0 is the vacuum electric permittivity, n_1 and n_2 are, respectively, the core and the cladding refractive indices, and $\overrightarrow{E_1}$ and $\overrightarrow{H_1}$ are the uncoupled waveguide electric and magnetic fields related to mode TE_1 of waveguide *I*. Similarly, $\overrightarrow{E_2}$ and $\overrightarrow{H_2}$ are the uncoupled waveguide electric and magnetic fields related to mode TE_2 of waveguide *II*. The waveguide dimension parameters, h

and w, on the integral limits and the core center, C, are shown in Fig. 5. Equation (5) quantifies the coupling between TE_1 of waveguide I to TE_2 of waveguide II. The derivation of Eq. (5) assumes that the evanescent field of $\overrightarrow{E_1}$ in the region of waveguide II is considerably small. This condition is known as weak coupling and it is satisfied when the two waveguides are sufficiently separated. Under weak coupling, the spatial distributions of the modes, and their propagation constants, remain unchanged and only the field amplitudes vary [49].

Following the approach of [34] for a rectangular waveguide, the electric and magnetic fields involved in (5) are given by $\overrightarrow{E_1} = (Ex_1, Ey_1, 0)$, $\overrightarrow{E_2} = (Ex_2, Ey_2, 0)$, and $\overrightarrow{H_1} = (0, Hy_1, Hz_1)$. Furthermore, for a rectangular waveguide, we can also assume $|Ex_1| >> |Ey_1|$ and $|Ex_2| >> |Ey_2|$, leading to a coupling coefficient:

$$\kappa_{12} = \frac{\omega\varepsilon_0(n_1^2 - n_2^2)\int\limits_{-h}^{+h}\int\limits_{C-w/2}^{C+w/2} Ex_1^* Ex_2 \, dxdy}{2\int\limits_{-\infty}^{+\infty}\int\limits_{-\infty}^{+\infty} \Re e\left(Ex_1^* Hy_1\right) dxdy}. \tag{6}$$

Numerical results obtained for L_c as a function of Γ, for the TE mode, are presented in Fig. 6 for $\lambda = 1750$ nm. The minimum gap considered was $\Gamma = 1.5$ µm.

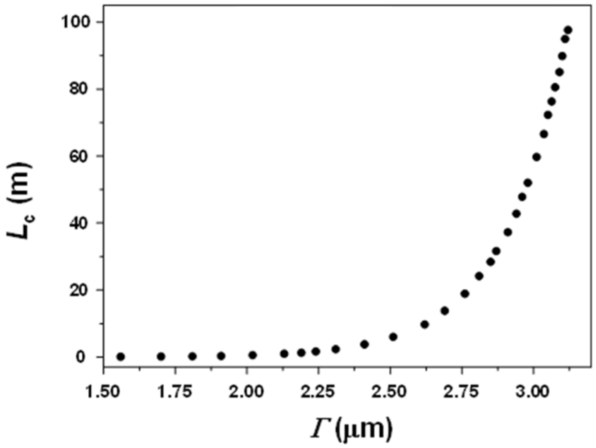

Fig. 6. Coupling length as a function of the gap width between adjacent waveguides.

In this case, as shown in Fig. 7, the magnitude of $\overrightarrow{E_1}$ is ~35 dB weaker in the region of waveguide II, which guarantees the weak coupling condition and assures the validity of Eq. (5). Longer wavelengths imply higher evanescent field magnitudes. Moreover, all of our systemic simulation results presented in Section 4 apply to wavelengths shorter than 1750 nm. Therefore, calculations for $\lambda = 1750$ nm in Fig. 7 ensure that the critical hypothesis of weak coupling holds for all of our simulations results.

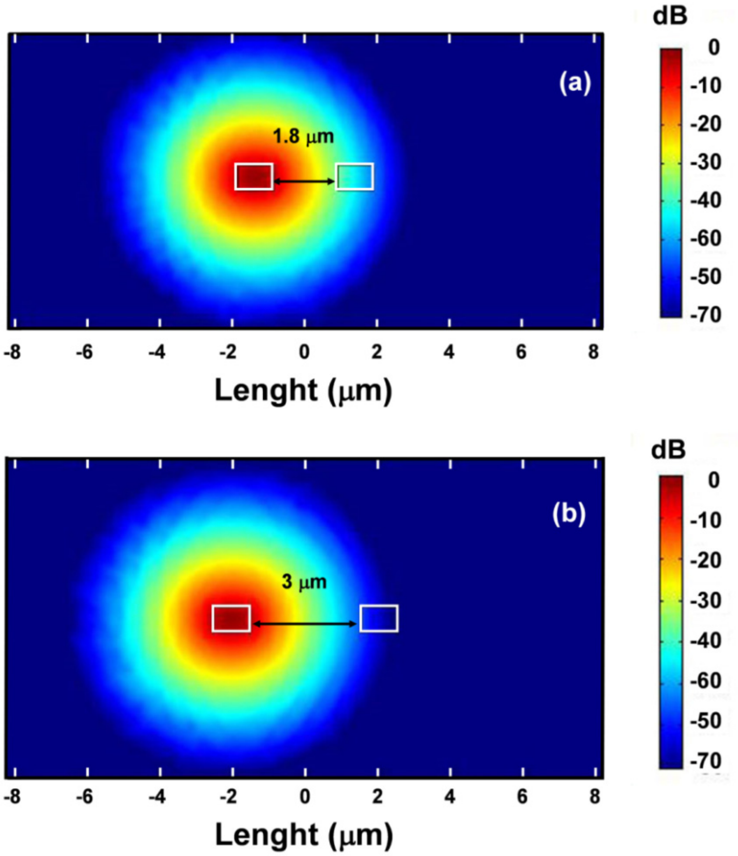

Fig. 7. a) Magnitude of the TE mode for a gap of 1.8 μm. b) 3 μm.

In order to define a limit for the minimum gap between adjacent spiral rounds, we note that for Γ ~3.1 μm, L_c ~100 m. This means that in the case of a hypothetical very long spiral, after 100 m of optical path, the optical power would be completely transferred from waveguide *I* to waveguide *II*, after 50 m only half of power would be transferred, and so on. Now, extrapolating the simulated points, it is found that, for Γ ~3.7 μm, L_c ~1 km. Considering that L_s is ~25 cm, the fraction of the optical power that will be transferred from waveguide *I* to waveguide *II*, after 25 cm of optical path, would be (L_s/L_c). 100 = 0.025% = –36 dB, which is considerably low. Then, Γ ~3.7 μm was taken as a reasonable value of the minimum gap between adjacent rounds of the spiral to allow for negligible coupling losses. This value implies the spiral should have 55 rounds to obtain L_s = 25 cm and that the outermost spiral round radius is 0.85 mm. As a consequence, the waveguide covers an area of ~2.5 mm^2.

This Γ ~3.7 μm value is a consequence of the high confinement of the fundamental *TE* mode as shown in Fig. 7. The color scale in dB indicates the modulus of the electric field for waveguide *I*. For a gap of 1.8 μm, the electric field from waveguide *I* drops ~45 dB in the region of waveguide II (Fig. 7(a)). The difference increases to ~60 dB or more for a gap of 3 μm (Fig. 7(b)).

Finally, considering an effective cross section area of ~0.7 μm^2 and a nonlinear refractive index n_2 ~5 · 10^{-19}m^2/W [50], the waveguide nonlinear parameter, as defined in [47], can be estimated as γ ~3000 W^{-1} km^{-1}. A more sophisticated approach would include the influence of the longitudinal component of the guided modes to compute γ [51, 52]. However, for the contrast index, waveguide dimensions, and spectral range considered in the simulations of the next section, the correction introduced by such approach should be relatively small as can be estimated from Fig. 5 of [52]. Under these conditions, it would only slightly increase our estimation of γ, which would lead to marginally lower pump powers to operate the OPA, with no significant change on the discussed waveguide properties.

4. 2P-OPA performance

The mathematical dependence between parametric gain and phase matching condition was pointed out in Section 2. In the present section, the use of the designed waveguide as a gain medium for a two-pump parametric amplifier (2P-OPA) is assessed. The nonlinear Schrödinger Equation (NLSE) properly describes the propagation of optical fields through the longitudinal direction of waveguides [53–55]. In order to simulate the performance of the proposed 2P-OPA we used VPItransmissionMaker software. In particular, a VPItransmissionMaker module, set with our engineered dispersion, was used to solve the NLSE through the split-step Fourier method. A constant waveguide attenuation of 0.5 dB/m was utilized. This value corresponds to the largest loss observed in the spectral range of interest for our simulations (Fig. 3). In accordance with our previous discussion, the nonlinear parameter was set to 3000 $(\mathrm{W{\cdot}km})^{-1}$. All signal channels were simulated with a pseudo-random bit sequence (PRBS) of length 2^{12}-1. A typical spectrum gain is shown in Fig. 8. The pumps were tuned at λ_{P1} = 1411.65 nm and λ_{P2} = 1687.7 nm (separation of 276 nm) with powers $P_{\mathrm{P1}} = P_{\mathrm{P2}}$ = 33 dBm, where P_{Pi} stands for the power of the pump placed at λ_{Pi} (i = 1, 2). A set of 243 input single polarization 56 Gbps quadrature phase shift keying (QPSK) modulated signal channels was placed from 1544.917 nm up to 1647.204 nm within the 50 GHz grid. The gain was ~16 dB with a ripple of ~4.5 dB, over a bandwidth of ~102 nm (12 THz), which is 3 times larger than the one obtained with C band EDFAs. The 2P-OPA optical signal-to-noise ratio (OSNR) was estimated by using the following procedure: (i) A given signal channel power was measured; (ii) Afterwards, the signal was suppressed and, then, at its frequency, the noise background power was measured; (iii) The 2P-OPA OSNR is just the ratio between these measurements, that is, 13.4 dB.

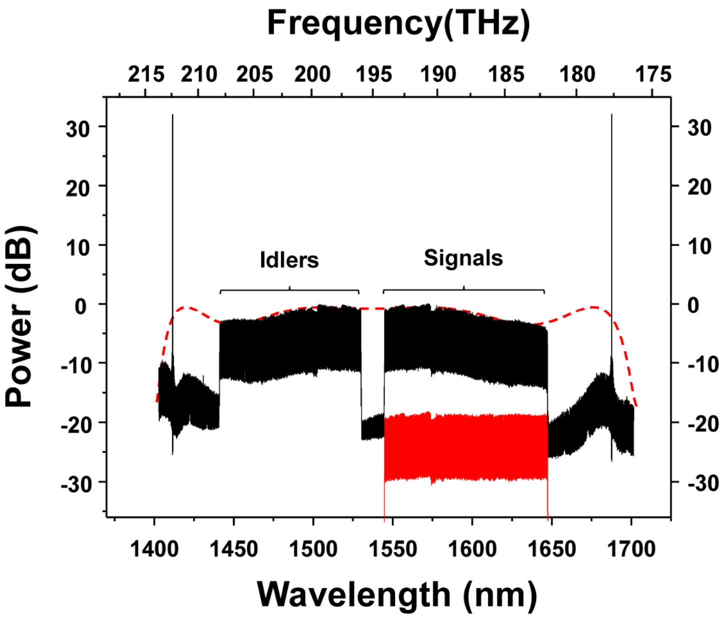

Fig. 8. 2P-OPA gain spectrum obtained for the designed waveguide. The dotted red line is the OPA gain obtained with the analytic model. The continuous red line is the OPA input set of channels.

Figure 8 also shows the gain spectra obtained with the analytic model presented in Section 2, with the same pump parameters used to solve the NLSE. The agreement between them is rather good. This fact is important because it clearly shows that some of the characteristics that determine the performance of the parametric amplifier, as gain, ripple and bandwidth, depend essentially on the phase matching condition, which relies on the dispersive properties of the waveguide. For instance, to calculate the analytic gain spectra, $\beta_2(\omega_c)$ can be written as $\beta_2(\omega_c) = \beta_3(\omega_c)\,(\omega_c - \omega_0) + \beta_4(\omega_c)\,(\omega_c - \omega_0)^2/2$, where $\omega_0 = (2\pi\, c)/\lambda_0$ and $\omega_c = ((\omega_1 + \omega_2)\,/2)$ (ω_1 and ω_2 are the pumps frequencies). This shows certain high-order dispersion parameters have a fundamental role for engineering the dispersion. The curves for $\beta_2(\omega)$, $\beta_3(\omega)$ and $\beta_4(\omega)$, the two last obtained through the derivatives of the $\beta_2(\omega)$, are shown in Fig. 9 (these curves were presented as a function of λ for sake of clarity). The values at $\lambda_c = (2\pi\, c)/\omega_c = 1537.34$ nm are $\beta_3(\lambda_c) = -0.67$ ps^3/km and $\beta_4(\lambda_c) = 0.007$ ps^4/km. The sixth order dispersion parameter is $\beta_6(\lambda_c) = 3.26\ 10^{-7}$ ps^6/km. Such a value is small enough to neglect the β_6 term in the expansion of $\Delta\beta$ ($\left|[(\beta_6(\omega_c)/360)[\Delta\omega_s^6 - \Delta\omega_p^6]/(\beta_4(\omega_c)/12)[\Delta\omega_s^4 - \Delta\omega_p^4]\right| \sim 10^{-2}$), and, furthermore, it has no significant effect on the parametric gain. The analytic curve, which takes into account only the contributions of $\beta_2(\omega)$, $\beta_3(\omega)$ and $\beta_4(\omega)$, matches quite well the spectral gain obtained by solving the NLSE. This allowed us to verify that the small spectral ripple obtained is a consequence of the positive values of $\beta_4(\omega)$ [14].

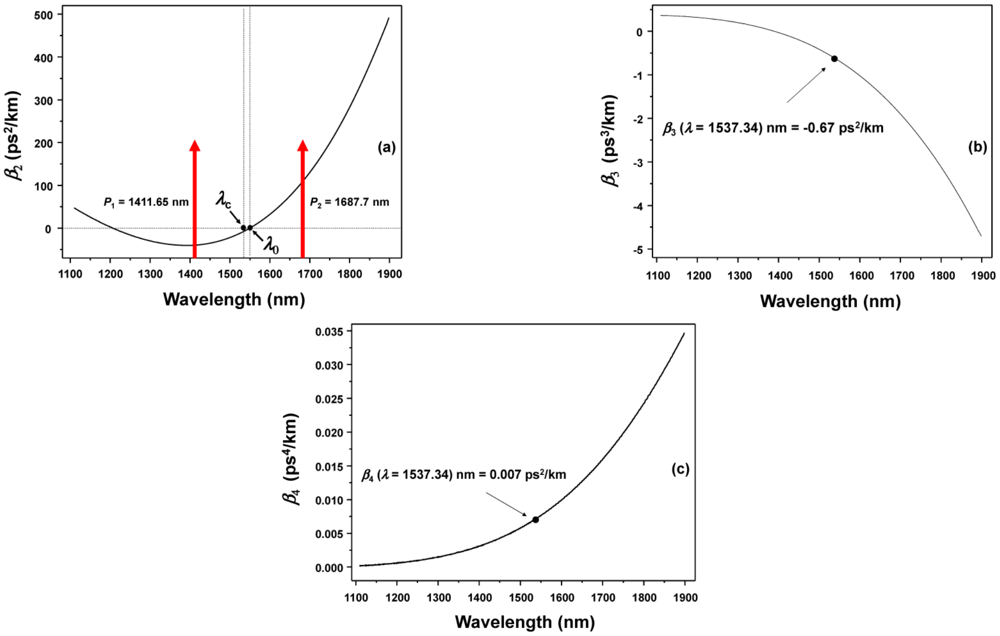

Fig. 9. Curves for: a) $\beta_2(\lambda)$. The red arrows show the pumps positions, and the black points the position of λ_c and λ_0. b) $\beta_3(\lambda)$. c) $\beta_4(\lambda)$. Dots indicate the values of $\beta_3(\lambda_c) = -0.67$ ps^3/km and $\beta_4(\lambda_c) = 0.007$ ps^4/km for $\lambda_c = 1537.34$ nm.

Figure 10 exhibits the bit error rates (BER) for 13, from 243 channels, spaced by ~1 THz. Firstly, the modulated channels with a power of ~-18 dBm were passed a single time by the 2P-OPA under consideration. At the amplifier output, the BERs were below 10^{-8} (Fig. 10(a)) and the signal power was around −1.5 dBm. Afterwards, we simulated a scenario where all signals were equalized and transmitted through consecutive 80-km-long spans of standard fiber, with an attenuation of ~0.18 dB/km, followed by a 2P-OPA. Since we are concerned with the amplifier performance, we assumed that the dispersion induced by the fiber spans was exactly compensated before the 2P-OPA. The curves in Fig. 10(a) show that after the sixth pass through the 2P-OPA, the BER is about ~10^{-2}, which can be turned into 10^{-15} by using forward error correction (FEC) mechanisms [56]. This propagation distance is compatible with the scale length of metropolitan area networks (MANs). For illustrative purposes, Fig. 10(b) shows the constellation diagrams for the best and the worst BER cases, after the first and the sixth passes. Under the considered simulation conditions, BER degradation is related to optical signal to noise ratio (OSNR) reduction and to the crosstalk that is inherent to parametric amplification [57]. The output spectrum at the sixth span output is shown in Fig. 11. After the sixth-pass, the OSNR is degraded by ~2.7 dB if compared to the first-pass.

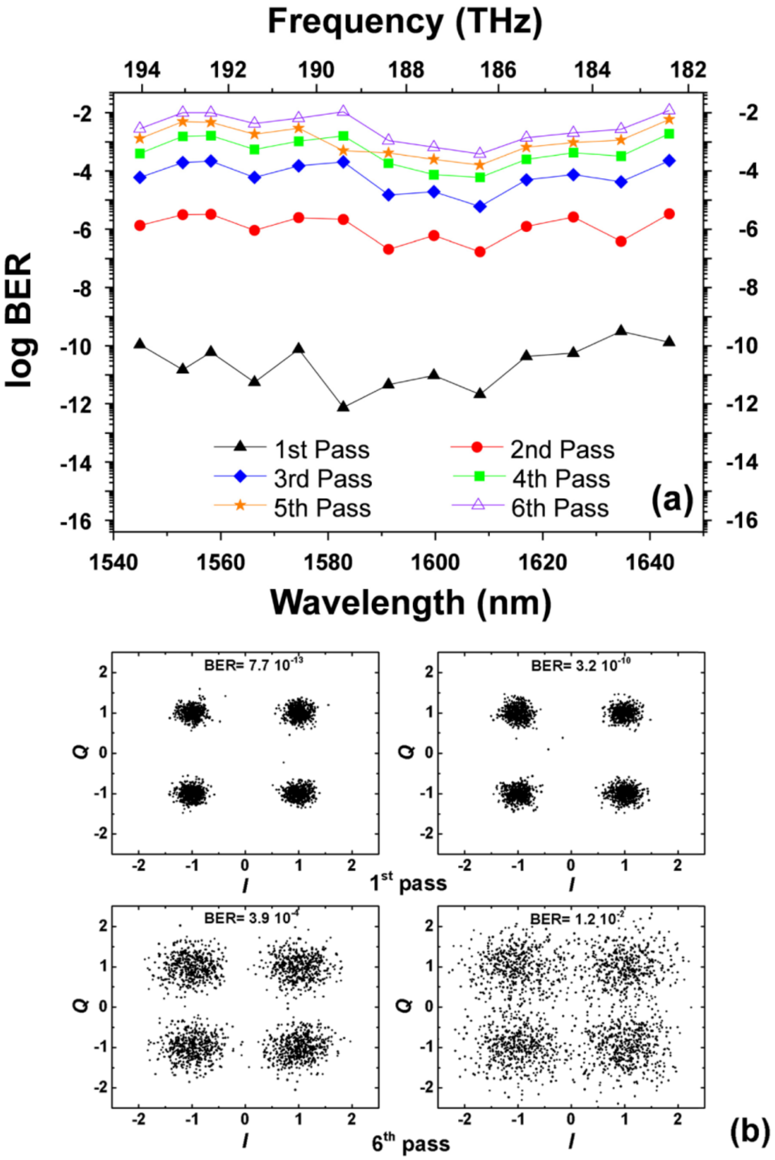

Fig. 10. a) BER performance for a 2P-OPA based on the designed tellurite waveguide. b) Constellation diagrams in the best and the worst BERs cases, for the 1st and the 6th passes.

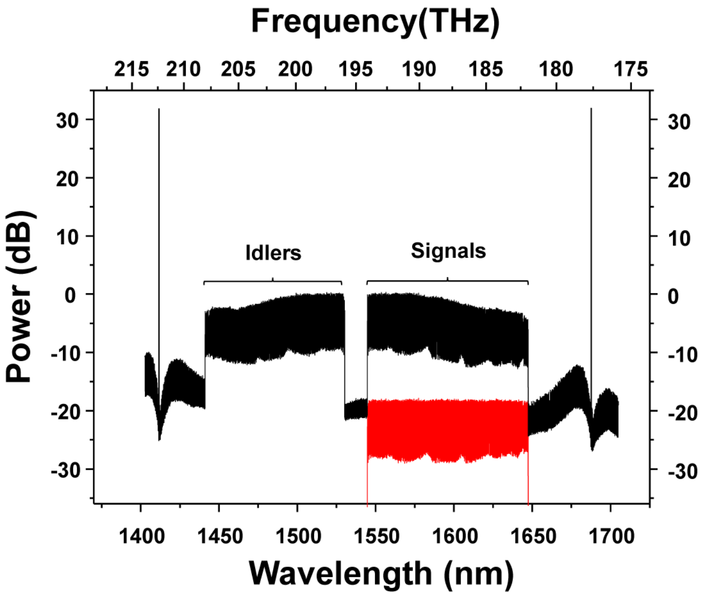

Fig. 11. Gain spectrum at the output of the sixth span of standard fiber followed by the sixth 2P-OPA. The continuous red line is the OPA input set of channels.

We also evaluated the 2P-OPA performance for 180 (9 THz or ~77.3 nm, as pointed out in our preliminary results [58])) and 100 (5 THz or ~43.9 nm) channels. In both cases, BERs were very low (below 10^{-16}) after the first pass and, thus, they can be considered error-free. Figure 12 shows a BER comparison for the case when signals underwent a second pass. Even in this situation, the BER values for 100 channels remain below 10^{-16}.

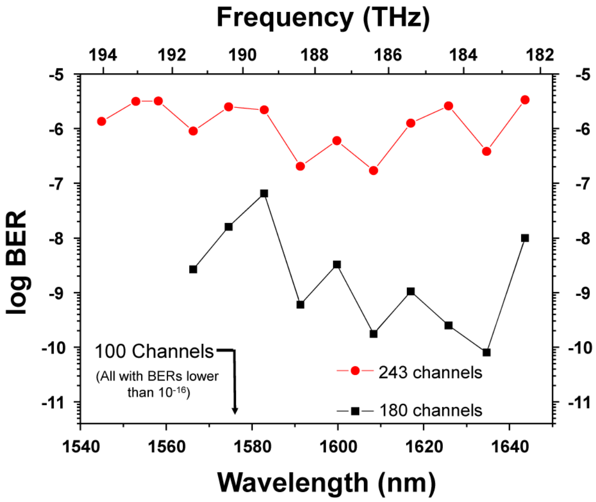

Fig. 12. 2P-OPA BER performance for different number of amplified 56 Gbps QPSK signals, spaced by 50 GHz.

These results are in agreement with previous findings that show how the crosstalk in 2P-OPAs increases with the number of amplified channels [57]. Such a crosstalk could be reduced by shortening the waveguide length and by increasing the pumps power or by manipulating the dispersive properties to minimize the spurious four-wave mixing products and other crosstalk mechanisms.

Therefore, our results suggest that the designed parametric amplifier may be used in networks with diameters larger than those of MANs, where the number of amplified channels is up to two times the one covered by conventional EDFAs. Alternatively, the device could be used for network with larger diameters if the number of channels could be reduced.

Currently, deployed commercial 100 Gbps WDM systems transmit 56 Gbps QPSK signals in two orthogonal polarizations. The analysis presented in this work is valid for one of such polarizations. A second amplifier or some polarization diversity scheme would be necessary to take the second polarization into account.

5. Conclusions

An ultra-broadband (~102 nm), low-ripple (~4.5 dB), small footprint (~2.5 mm^2), two-pump-optical parametric amplifier (2P-OPA) that employs a tellurite glass buried-channel type waveguide as nonlinear medium was numerically designed and investigated. This device is tunable and it can also be adjusted to exchange bandwidth by reach. The proposed waveguide was designed in an Archimedean spiral geometry to minimize the device footprint. For the dispersion calculations, the tellurite refractive index was obtained by fitting experimental data with a Sellmeier equation. The waveguide losses were of 0.5 dB/m and a 3.7 μm minimum gap between adjacent rounds of the spiral was adopted to keep coupling losses lower than 0.025%. Its nonlinear parameter was estimated as γ ~3000 W^{-1} km^{-1}, for a nonlinear refractive index n_2 ~5 x 10^{-19}m^2/W and an effective area of ~0.7 μm^2.

From an application point of view, our results suggest that the designed waveguide could amplify 243 QPSK 56 Gbps signals, spaced by 50 GHz, with an average gain of ~16 dB. The resulting amplification bandwidth is ~3 times larger than the one provided by C-band EDFAs, whereas a ripple of 4.5 dB is approximately the same. Results also suggest that signals could be propagated by around $6 \cdot 80$ km = 480 km, which correspond to a relatively large optical MAN. Longer reaches could be achieved by using DSP techniques to mitigate the influence of nonlinear crosstalk or by reducing the number of amplified channels.

In conclusion, the designed tellurite waveguide seems to be a very attractive medium for the realization of 2P-OPAs, which may become key devices for the development of the next generation of core networks. In fact, thanks to the OPAs tunability, four unities of the investigated device could be used in parallel to cover all the spectral region of SMF high transparency (1300 to 1700 nm) and to provide the 11 dB capacity improvement mentioned in Section 1, for MAN applications. A lower number of parallel 2P-OPAs could be used, if the waveguide dispersion is further engineered to reduce channel crosstalk or if DSP techniques are deployed to mitigate such effects. Furthermore, because of the tellurite glass high transparency and nonlinearity, thermal stability, and non-susceptibility to FCA and TPA, they have very strong potential for the development of photonic integrated circuits to be used in future optical communication systems.

Funding

Conselho Nacional de Pesquisa e Desenvolvimento (CNPq) (311137/2014-8, 311870/2014-7); Program INCT/FOTONICOM (CNPq 574017/2008-9 and FAPESP 2008/57857-2).

Acknowledgments

The Authors would like to thank Eng. Gabriel J. Suzigan for important discussions and VPIphotonics for providing academic licenses of the simulation software tools utilized in this work. We also like to express our deepest gratitude to Prof. H. L. Fragnito for providing access to Optical Communications Laboratory facilities at IFGW-UNICAMP.

B. MODAL CONTENT MEASUREMENTS

As most of the conventional light sources, coherent or incoherent, emit light in a fundamental mode LG_{00}, conversion to higher order modes to create OAM is needed. OAM modes can be created directly in fibers by using a grating [100], or externally by means of spatial-light modulators (SLM) [19], which then are used to excite the OAM modes in a vortex fiber. In order to confirm experimentally the propagation of OAM states in fibers it is very useful to use the interference with an expanded Gaussian beam producing spiral images thus as show in Figure B.1:

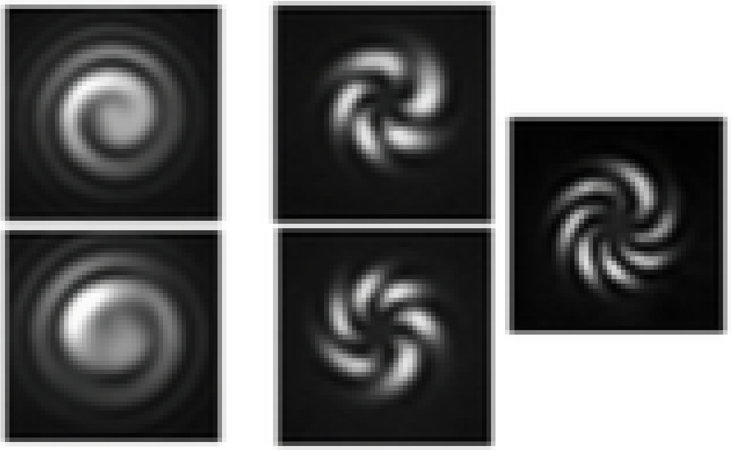

(a)ℓ=±1 (b)ℓ=5, 6 and 7

Figure B.1: **(a)** Interference of conventional solid vortex fiber output ℓ=±1 OAM states with a reference gaussian beam. **(b)** Interference of conventional air-core vortex fiber output ℓ= 5, 6 and 7 OAM states with a reference gaussian beam. With permission from [14]. Copyright 2015 Optical Society of America

These images indicate the existence of OAM modes, however, they are a poor metric to quantify the OAM mode purity. Even a mode that is up to 45% impure (almost 3 dB of coupling) could lead to visually "clean" spirals if the "*impurities*" are predominantly nearest-neighbors in $|\ell|$ [14]. There are several quantitative characterization tools that can be use to measure the mode purity such as: ring method [100], regression analysis [101], interferometric techniques [102], method based on correlation filters [19].

In previous chapters, we studied the performance of the conventional and metamaterial vortex fibers through their OAM *spectra* considering the most common perturbation in fiber: the bends. However, in a real fiber the mode coupling is also caused by possible fabrication defects, like core ellipticity and roughness, which would increase the coupling strength reported in the OAM *spectra*. In order to quantify the mode coupling strength we assemble two measurement techniques: spatially and spectrally modal interferometric method (S^2) to characterize modal content in optical fibers [102], and modal decomposition technique [19] to measure the coupling strength among OAM modes in free-space. We expect that these technique can be used to characterize the fabrication of our designs in a near future.

B.1. S^2 METHOD

Two or more modes propagating in an optical fiber form a spatial and spectral interference pattern if the modes have different group velocities. The S^2 imaging method analyzes this interference pattern and can detect weak high order modes (HOMs) interfering with the fundamental mode. A previous knowledge of the fiber properties is not necessary to fully quantify the modal shape of the different modes and their relative intensities and phases [102] (see Figure B.2).

Two electrical fields (the fundamental and a higher order mode) $E_1(x, y, \omega)$ and $E_2(x, y, \omega)$ propagating in an optical fiber are related in the following way:

$$E_2(x, y, \omega) = \alpha(x, y)E_1(x, y, \omega) \tag{B.1}$$

where $\alpha(x, y)$ is assumed to be independent of the wavelength at the given position.

We propagate the field assuming that the group delay difference between the modes is independent of frequency

$$E_2(x, y, \omega) = \alpha(x, y)E_1(x, y, \omega)e^{-i\omega\Delta\tau_b} \tag{B.2}$$

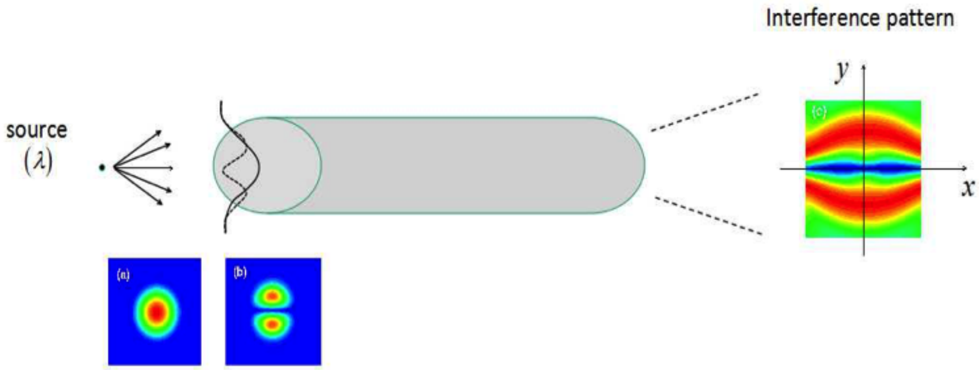

Figure B.2: Principles of operation of S^2 technique

where τ_b is the relatively group delay between the two modes. The spectral intensity pattern caused by interference between the two fields is given by:

$$I(x, y, \omega) = I_1(x, y, \omega)[1 + \alpha^2(x, y) + 2\alpha\cos(\omega\Delta\tau_b)] \tag{B.3}$$

The Fourier transform ($\mathcal{F}$) of the spectral intensity pattern $\mathcal{F}(I(x, y, \omega))$ is:

$$F(x, y, \tau) = (1 + \alpha^2(x, y)F_1(x, y, \tau) + \alpha(x, y))(F_1(x, y, \tau - \tau_b) + F_1(x, y, \tau + \tau_b)) \tag{B.4}$$

where F_1 is the Fourier transform of a single mode. We can then define the ratio $f(x, y)$ of the two modes with group delay τ_b and τ_0 as:

$$f(x, y) = \frac{F(x, y, \tau = \tau_b)}{F(x, y, \tau = \tau_0)} = \frac{\alpha(x, y)}{1 + \alpha^2(x, y)} \tag{B.5}$$

Finally we can write $\alpha(x, y)$ as follow:

$$\alpha(x, y) = \frac{1 - \sqrt{1 - 4f_2(x, y)}}{2f(x, y)} \tag{B.6}$$

The total intensity of each mode is the integral over the entire measurement wavelength range. The relative power of the higher order mode to the fundamental mode MPI can be written:

$$MPI = 10\log_{10}\left[\frac{\int\int I_2(x, y)dxdy}{\int\int I_1(x, y)dxdy}\right] \tag{B.7}$$

where I_1 and I_2 represent the intensity distribution of the fundamental and the higher order mode, respectively. If $\alpha(x, y)$ and τ_b are frequency dependent, Fourier integrals should be applied to equation (B.7)

Several experimental S^2 imaging systems have been demonstrated in different configurations, but we adopt the configuration reported in [103]. Our S^2 experiment consists of a tunable laser coupled to the fiber under test (FUT) using a SMF fiber (see Figure(B.3)). We have tested S^2 experiment using a hollow core Photonic-Bandgap Fiber (PBGF). Micropositioners with piezoelectric crystals are used to perform the coupling between FUT and the SMF. A power meter and InGaAs CCD camera were used to measure optical power and record images coming from the FUT.

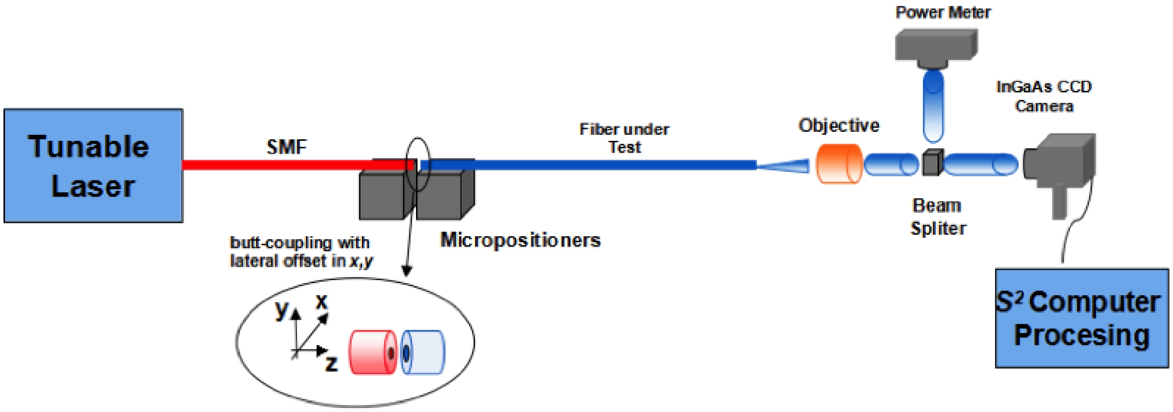

Figure B.3: S^2 experimental setup

We have verified the operation of our mathematical routines using numerical simulations in order to design our own S^2 code for image processing and also to get MPI value. This technique was assembled in the Fiber-Lab of the Department of Quantum Electronic Gleb Wataghin, Physic Institute, Campinas University (DEQ-Unicamp). We expect to use it to characterize the vortex fibers after the fabrication of our designs. We use a wideband tunable IR-laser operating around 1550 nm, a CCD camera in InGaAs of high sensitivity (less than 35 dB) to collect the images at the output of the fiber.

Finally, one of the measurement is presented in Figure (B.4). We obtained these images by means of a own code corresponding to the intensity and phase distributions of the higher order modes. MPI values (proportional to coupling strength with the fundamental mode) remain lower than 30 dB.

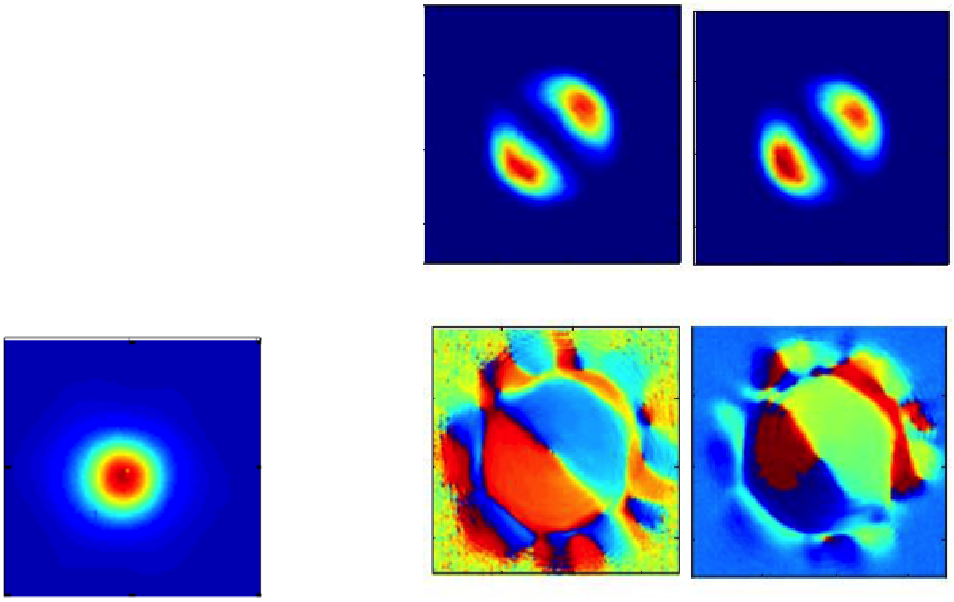

(a)Fiber output (b)HOM

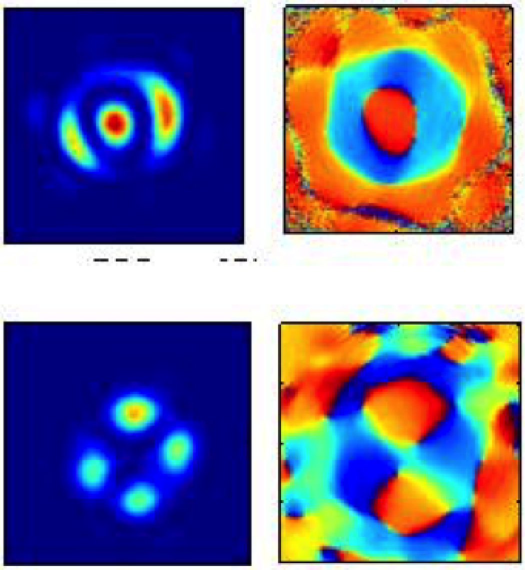

(c)HOM

Figure B.4: **(a)**The image at the output of the fiber which is processed to obtain the intensity and phase distributions of the modal content, and also the MPI values that represent the coupling strength between the fundamental and higher order modes (HOM). **(b)-(c)** Images of the intensity and phase distributions of the higher order modes recovered offline using our own processing algorithm

B.2. MODAL DECOMPOSITION TECHNIQUE

Modal decomposition is a powerful tool for the detailed investigation of laser field [19]. An optical field can be conceived as a composition of individual modes (Chapter 3 of [61]). Mathematically, any optical field can be expressed in terms of modes, which constitute orthogonal basis functions:

$$\mathbf{U}(\mathbf{r}) = \sum_{l=1}^{N} c_l \Psi_l(\mathbf{r}) \tag{B.8}$$

where $\mathbf{r}$=(x,y) is the spatial coordinates, $c_l = \rho_l e^{i\Delta\phi_l}$ is the complex expansion coefficient with complex amplitude ρ_l and intermodal phase $\Delta\phi_l$ with respect to a reference phase, $\Psi_l(\mathbf{r})$ is the lth mode field. Beam intensity $I(\mathbf{r})$ and phase $\phi_j(\mathbf{r})$ of each modes are:

$$\mathbf{I}(\mathbf{r}) = |\mathbf{U}(\mathbf{r})|^2 \tag{B.9}$$

$$\phi_j(\mathbf{r}) = arg[U_j(\mathbf{r})] \tag{B.10}$$

where U_j is the field component of the jth mode. The modal decomposition of a field of equation (B.9) can be performed all-optically by correlation filters [19]. Filters perform a correlation between incident field with modes that are encoded into the filter, which allws one to measure the power and relative phases of each mode based on the inner product measurement [19]. Correlation filters require the specific design of transmission functions in a holographic device. Measurements of the power of a distinct mode requires the complex conjugates of the modes encoded as transmission functions.

$$T_l(\mathbf{r}) = \Psi_l^*(\mathbf{r}) \tag{B.11}$$

Using this transmission function, the intensity on the Fourier plane of the correlation filters that is proportional to ρ_l^2, therefore the power of a mode can be measured by its intensity. Likewise, the by the superposition of the mode field with a reference field into the match filter:

$$T_l^{\cos}(\mathbf{r}) = [\Psi_0^*(\mathbf{r} + \Psi_l^*(\mathbf{r}]/\sqrt{2} \tag{B.12}$$

$$T_l^{\sin}(\mathbf{r}) = [\Psi_0^*(\mathbf{r} + i\Psi_l^*(\mathbf{r}]/\sqrt{2} \tag{B.13}$$

yields the intermodal phase $\Delta\phi_l$ computed by:

$$\Delta\phi_l = -arctan\left[\frac{2I_l^{\sin} - \rho_l^2 - \rho_0^2}{2I_l^{\cos} - \rho_l^2 - \rho_0^2}\right], \tag{B.14}$$

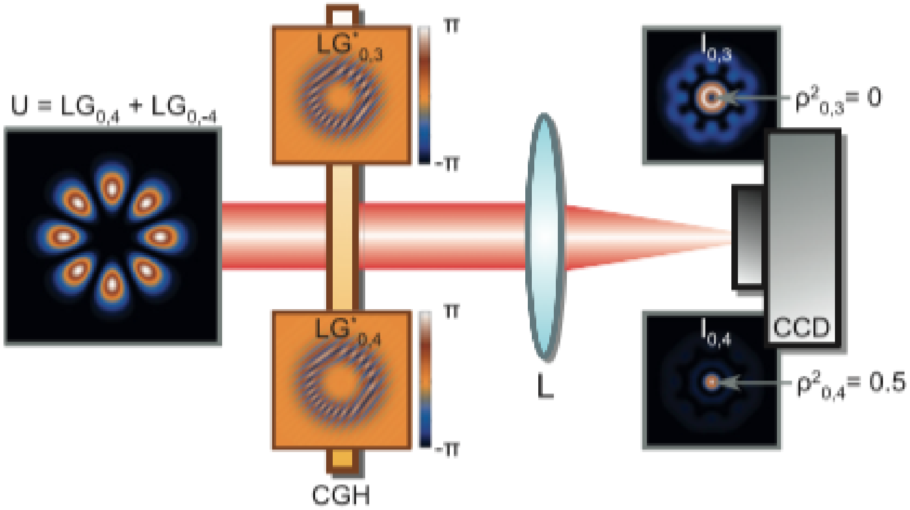

Figure B.5: S^2 experimental setup. Correlation filter technique. With permission from [19]. © IOP Publishing. All right reserved

where $I_l^{\sin}$ and $I_l^{\cos}$ depict the intensity signal T^2 to perform the phase measurement.

The procedure of inner product measurement is shown in Figure(B.5) As was showed in [19], consider for example a superposition of two equally weighted Laguerre-Gaussian (LG) modes $(LG_{0,4}+LG_{0,-4})/\sqrt(2)$. Then, displaying a transmission function $T=LG_{0,3}^*$ (e.g. encoded on an SLM) yields a zero intensity at the center of the optical axis in the Fourier plane. However, if the field of a mode is displayed as a transmission function of $T = LG_{0,4}^*$, a non-zero correlation signal is expected, yielding a relative modal power of $\rho_{0,4}^2$.

For any field with even a non-uniform polarization state, the correlation filters can be done by determination of the Stoke parameters $S_0 ... S_3$ of the beam, which requieres six (assuming completely polarized light) modal decomposition measurements with a quarter-wave plate and a polarizer oriented in an appropriated manner in front of the hologram:

$$S_0 = |U_x|^2+|U_y|^2= I(0^o) + I(90^o) \tag{B.15}$$

$$S_1 = |U_x|^2-|U_y|^2= I(0^o) - I(90^o) \tag{B.16}$$

$$S_2 = |U_x||U_y|\cos\delta = I(45^o) - I(135^o) \tag{B.17}$$

$$S_3 = |U_x||U_y|\sin\delta = I(45^o) - I(135^o) \tag{B.18}$$

where δ is the phase difference between U_x and U_y. Each field transmitted by a quarter-wave plate and a polarizer is modally decomposed and the beam intensity is reconstructed following equation (B.11). Accordingly, $I(\alpha)$ with $\alpha = 0^o, 45^o, 90^o, 135^o$ are the reconstructed intensity in each polarization state shown in equation (B.15-B.15). Performing the six modal decompositions, information of the optical field is complete: amplitude, phase and polarization distribution.

This technique was assembled in the Photonic-Lab of the FEEC-Unicamp by [12]. We expect use it to perform the OAM vortex fibers after of the fabrication of our designs. We use He-Ne laser and two SLMs (reflective, HoloEye, PLUTO-VIS, 1920x1080 pixels of pitch 8 μm) and a CCD camera operating in the visible to record the images.